Nanoparticles of Ni strongly embedded in porous silica : towards the design of efficient catalysts for lignin hydrogenolysis

Rita Raachini

Université Libanaise

École Doctorale
Sciences et Technologies
Doyen

THESE de doctorat en Cotutelle

Pour obtenir le grade de Docteur délivré par

Université Libanaise

Ecole Doctorale des Sciences et Technologie

Et Sorbonne Université

Ecole Doctorale de Physique et Chimie des Matériaux

Spécialité : Sciences des Matériaux

Présentée et soutenue publiquement par

RAACHINI Rita

Le 28 Novembre 2023

Nanoparticles of Ni strongly embedded in porous silica: towards the design of efficient catalysts for lignin hydrogenolysis

Membres du Jury

Mme Catherine ESPECEL, Professeur, Université de Poitiers	Rapporteure
M. Houssam RASSY, Professeur, Université Américaine de Beyrouth	Rapporteur
Mme Madona BOULOS, Professeur, Université Libanaise	Présidente du jury/Examinatrice
Mme Giulia FORNASIERI, Maître de conférences, Université Paris-Saclay	Examinatrice
M. Joseph SAAB, Professeur, Université Saint-Esprit de Kaslik	Examinateur
M. Serge THORIMBERT, Professeur, Sorbonne Université	Examinateur
Mme Maya BOUTROS, Professeur, Université Libanaise	Directrice de thèse
M. Franck LAUNAY, Professeur, Sorbonne Université	Directeur de thèse
Mme Madona LABAKI, Professeur, Université Libanaise	Invitée
Mme Brigitte ROUSSEAU, Maître de conférences, Sorbonne Université	Invitée

Acknowledgements

First, I would like to thank the Paris Ile-de-France Region (DiM RESPORE) and the Lebanese University for their financial support.

I am grateful that this work could be performed in collaboration between Sorbonne University (Laboratoire de Réactivité de Surface) and the Lebanese University (Laboratoire de Chimie-Physique des Matériaux).

I would like to express my sincere gratitude to my supervisors, Prof. Franck Launay and Prof. Maya Boutros for their encouragement, understanding, guidance, advice, patience and help in carrying out the work and overcoming the difficulties we encountered during these three years. Thank you for sharing your knowledge in the world of research. I have been very lucky to have the chance to work under your supervision.

I have also been lucky enough to have been involved in a number of fruitful collaborations. I would like to express my deepest gratitude to Dr. Brigitte Rousseau for sharing her knowledge of lignin with me and her help in characterizing this polymer.

It is a pleasure to thank Prof. Catherine Especel and Prof. Houssam Rassy for accepting to read my manuscript and give their objective opinion about this work. I am honored by the presence of Prof. Madona Boulos, Dr. Giulia Fornasieri, Prof. Joseph Saab and Prof. Serge Thorimbert as jury members to evaluate my work, and by the presence of Prof. Madona Labaki and Dr. Brigitte Rousseau as invited members.

Special thanks for Prof. Anne Bleuzen and Dr. Giulia Fornasieri for welcoming me in their Laboratory at Université Paris-Saclay for the preparation of the monoliths.

Thanks to all the members of the “Laboratoire de Chimie-Physique des Matériaux” directed by Prof. Mirvat Zakhour and to Prof. Michel Nakhl, director of the plateforme of Nanosciences and Nanotechnology, and to all the professors and staff members.

Moreover, I am also thankful to Prof. Helene Pernot, the director of the LRS and to all staff members and professors for facilitating my stay.

Thank you Cyril Thomas (H_2 chemisorption), Saremblé Guira (N_2-physisoprtion and H_2-TPR), Antoine Miche (XPS), Laetitia Valentin, Dalila Seghouane (ATG), Mohamed Selmane and Capucine Sassoye (XRD and PDF), Sandra Casale (TEM), Julie Noel (ICP-OES), Claire Troufflard and Régina Maruchenko (NMR), Annie Mettendorff, Aurélien Chervalier, Sonia M'Barek. Thanks to Ferdaous Ben Romdhane not only for TEM but also for being a close friend to me, for sharing laughter and for the deep talks.

My gratitude goes also toward my colleagues in France: Albert Issa, Ana Schuh Frantz, Walid Ait Mammar for sharing laughter in the afternoons in the lab. Special thanks to my sweetest friends I have met in France and became my second family: Valia, Melissa, Chantal, Christelle, Joelle Ch. and Joelle M. I cannot thank you enough for your love, moral support, advice and encouragement throughout not only my PhD studies by also my life.

My biggest thanks go to my family: Joseph, Rosette, Vanessa and Maria. No words can express the love and gratitude I have for you. Thanks for trusting me.

Abstract

Phenols may be obtained from lignin instead of petroleum. Here, improving lignin conversion by hydrogenolysis, while limiting side hydrogenation of produced phenols using nickel-based catalysts instead of noble metals, was our main concern. Porous materials made of highly dispersed nickel onto silica were synthesized by different pathways, characterized before and after reduction under H_2, then tested in the hydrogenolysis of three compounds bearing C-OAr bonds, as in the β-O-4 linkage of lignin, using isopropanol as H-donor. In a first series of materials, Ni was introduced by the impregnation of Aerosil 380 in the presence of ammonia and similar materials were prepared with Rh. The latter favored phenol formation but resulted in much slower C-OAr cleavage. In fact, the most active catalyst was found to be the Ni-based one, affording high phenol productivity reached by reducing the Ni-based catalyst at high temperature. Unlike Ni, no Rh-phyllosilicates were detected, this was related to the counterion of the precursor and the metal itself. Ni-Rh bimetallic materials prepared in a same way did not show any synergistic effect.

Secondly, designing highly dispersed nickel-based mesoporous monoliths with different pore structures (S_x) (wormlike, hexagonal or cubic pore structures) through an original sol-gel method was done. Differences were observed between the reduced forms of $Ni^{II}@S_x$, affording better yields with the more opened cubic structure. The resulting solids were compared to two materials obtained by the impregnation of either Aerosil 380 or a hexagonal silica monolith with Ni(II) in the presence of ammonia in order to study the effect of the support and the incorporation method. Under the conditions used, the best catalyst with respect to phenol selectivity, avoiding its hydrogenation to cyclohexanol, was Ni-based Aerosil 380. Lastly, the effect of adding a second metal with Ni (Co or Fe) by three methods was studied, *i.e.,* impregnation of Co or Fe on Ni@SBA-15 like monolith, a direct one-pot synthesis introduction or co-impregnation of both metals Ni and Co or Fe on a SBA-15 like monolith. The incorporation method of metals turned out to be a critical parameter for the catalytic activity. Incorporation of Co or Fe by “two-solvents” method on the Ni@SBA-15 like monolith led to the best phenol selectivity. In our hands, the hydrogenolysis of guaiacylglycerol-β-guaiacyl ether turned out to be more difficult than that of 2-phenoxy-1-phenylethanone and 2-phenoxy-1-phenylethanol.

Keywords : Nickel, Porous silica, Lignin, Hydrogenolysis, Phenol.

Résumé

Les phénols peuvent être obtenus à partir de la lignine plutôt qu'à partir du pétrole. Ici, notre principale préoccupation était d'améliorer la conversion de la lignine par hydrogénolyse, tout en limitant l'hydrogénation des phénols produits en utilisant des catalyseurs à base de Ni au lieu de métaux nobles. Des matériaux poreux constitués de Ni hautement dispersés sur de la silice ont été synthétisés via différentes méthodes, caractérisés avant et après réduction sous H_2, puis testés dans l'hydrogénolyse de trois composés comportant des liaisons C-OAr, mimant la liaison β-O-4 de la lignine, en utilisant l'isopropanol comme donneur d'hydrogène. Dans une première série de matériaux, le Ni a été introduit par imprégnation d'Aerosil 380 en présence d'ammoniaque et des matériaux similaires ont été préparés avec Rh. Le catalyseur à base de Rh favorise la formation de phénol mais le clivage des liaisons C-OAr est lent. Le catalyseur le plus actif s'est avéré être celui à base de Ni qui a permis d'atteindre une productivité importante en phénol si le nickel est réduit à haute température. Contrairement au Ni, des phyllosilicates de rhodium n'ont pas été détectés. Ceci est à relier au contre-ion dans le précurseur et au métal lui-même. Les matériaux bimétalliques (Ni/Rh) préparés par la même méthode n'ont pas permis de mettre en évidence une synergie entre les deux métaux.

Deuxièmement, des monolithes mésoporeux à base de nickel hautement dispersé de différentes structures de pores (S_x) (vermiculaire, hexagonale ou cubique) ont été synthétisés par voie sol-gel. Des différences d'activité catalytique ont été observées entre les formes réduites de $Ni^{II}@S_x$ mettant en avant de meilleurs rendements avec la structure cubique. Les solides obtenus ont été comparés à deux matériaux obtenus par imprégnation de la silice Aerosil 380 ou d'un monolithe de silice hexagonale par du nickel en présence d'ammoniaque afin d'étudier l'effet du support et de la méthode d'incorporation. Le meilleur catalyseur concernant la sélectivité en phénol est celui obtenu à partir d'Aerosil 380. Enfin, l'effet de l'ajout d'un second métal avec Ni (Co ou Fe) a été étudié en utilisant trois méthodes différentes, c'est-à-dire l'imprégnation de Co ou Fe sur le monolithe Ni@SBA-15, l'introduction directe des deux métaux par voie de synthèse one-pot ou la co-imprégnation des deux métaux Ni et Co ou Fe sur un monolithe de silice de structure hexagonale. La méthode d'incorporation des métaux s'est avérée être un paramètre critique pour l'activité catalytique. L'incorporation de Co ou Fe par la méthode des deux solvants sur le monolithe type Ni@SBA-15 a conduit à une meilleure sélectivité en du phénol. Dans ce travail,

l’hydrogénolyse du guaiacylglycérol-β-guaiacyl ether s’est avérée être plus difficile que celle du 2-phenoxy-1-phényléthanone et du 2-phenoxy-1-phényléthanol.

Mots-clefs : Nickel, Silice poreuse, Lignine, Hydrogénolyse, Phénol.

Table of Contents

General Introduction

Society currently depends mainly on fossil feedstocks for the production of energy, fuels and chemicals. However, concerns about the increasing energy and material demands, the depletion of fossil fuels, climate-change effects and today's turbulent geo-political situation stimulate the use of alternative and renewable resources [1]. Biomass offers a unique resource for the sustainable production of fuels and chemicals such as phenols [2]. Phenol itself, is used as an intermediate for the production of many chemicals (Figure GI.1). ***"The global phenol market size reached a value of around USD 19.44 billion in the year of 2021. The phenol market is further expected to grow at a Compound Annual Growth Rate (CAGR) of 4.2% between 2023 and 2028 to reach a value of about USD 24.07 billion by 2027"*** [3]. China has been the largest market for many years for production and consumption of phenols [4].

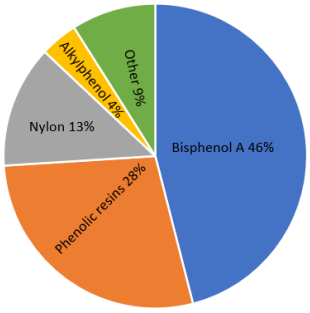

Figure GI.1: *Global worldwide demand for phenol [4].*

Alternately, phenols could be produced through the depolymerization of lignin [4,5] which is a highly branched phenolic polymer of high molecular weight, typically between 600 and 15 000 kDa, with an annual global production of around 50-70 million tons [6]. Lignin is present naturally in lignocellulosic plants accounting for approximately 300 billion tons globally with a CAGR of 7% (Figure GI.2). Its valorization has drawn a lot of attention from academia and industry worldwide [7], which can be measured by the number of patents involving its production, modification and application. Since 2008, *c.a.* 18 000 patents were registered in World Intellectual Property Organization [4].

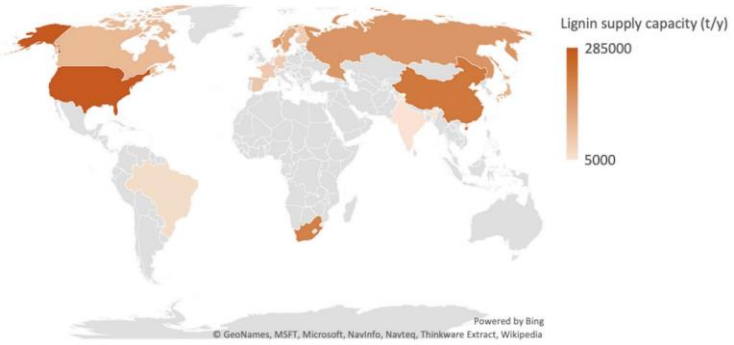

Figure GI.2: *Lignin's production capacity per country [4].*

Lignin (Figure GI.3) is mainly composed by radical polymerization of three monolignols (p-coumaryl, coniferyl, and sinapyl alcohols) [8]. It is the most recalcitrant component of the plant cell walls, due to the diversity of linkages between its monomeric units. Out of the β-O-4, β-5, β-1, 5-5, α-O-4, 4-O-5, β-β linkages, β-aryl ether (β-O-4) is the most dominant (constituting > 50% of lignin structure) (in red Figure GI.3). The structure and, hence, physicochemical properties of lignin vary with the biomass source. Recent study showed that it can be possible to tune the properties of a solubilized lignin in a solvent [9].

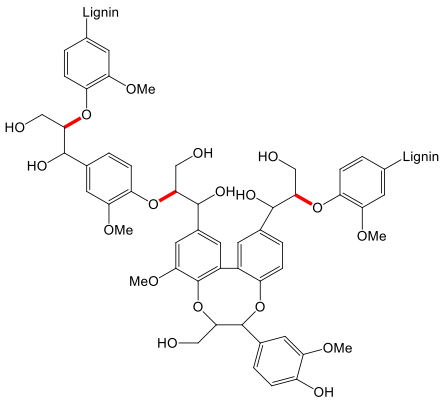

Figure GI.3: *Example of a lignin fragment.*

Many strategies have been developed to effectively degrade lignin into monomers, such as pyrolysis, gasification, liquid-phase reforming, solvolysis, chemical oxidation, hydrogenation, reduction, acidolysis, alkaline hydrolysis, alcoholysis, etc [10]. Oxidative cleavage of C-C and C-O-C bonds is performed to get vanillin, syringaldehyde and 4-hydroxybenzaldehyde [11]. However, oxidation may be accompanied by CO, CO_2, and H_2O formation, as well as a lot of side recondensation reactions related to the presence of free radicals. Reductive cleavage of C-O bonds

has proven to be more successful but drastic conditions are often used. Monomeric compounds, hence produced, are phenols, benzene, toluene, and/or xylene. The hydrogenolysis of aryl ether bonds usually requires high-pressure hydrogen as the hydrogen source, which increases the energy input and equipment investment, but also raises a series of potential safety issues. In this context, the use of organic solvents such as methanol, ethanol, and isopropanol as internal hydrogen donors for the transfer hydrogenolysis of C-O bonds is safer and easier to handle [12].

Many works are dealing with the reductive depolymerization of lignin or its models [13] into smaller phenolic molecules using homogeneous or heterogeneous catalysts [14]. Noble metals are the most commonly used heterogeneous catalysts. Very active phases include palladium, ruthenium and rhodium, as well as non-noble metals such as nickel, iron and copper are also used [15]. Nickel is one of the most preferred catalysts for lignin hydrogenolysis, due to its relatively low cost, its availability and activity [16]. The first use of a nickel-based catalyst can be dated back to the 1940s [17]. Besides, several bimetallic NiM (M=Ru, Rh, Pd, Ag, Au, Fe) materials were shown to catalyze the hydrogenolysis of lignin and of its model compounds [18–20]. Supports of various natures and compositions have been tested. Siliceous supports are very promising due to their inertia, easy preparation, high specific area that may be very important when the dispersion of metal particles has to be improved [21–23].

In this thesis, hydrogenolysis of lignin model compounds under relatively mild conditions using isopropanol as an H-donor solvent was carried out over mesoporous structured or non-structured materials made of silica supports bearing nickel or bimetallic type Ni-M (M: Rh, Co or Fe). Supported nanoparticles have been prepared by two different methods. The aims of this project were to obtain materials with high nickel dispersion, to study the effect of additional metals and to investigate the influence of the preparation methods on the catalytic activity as well as to study the influence of different mesoporous structures on the depolymerization reaction. A non-mesoporous silica (Aerosil 380) and mesoporous silica (monoliths) with different pore structures were synthesized and used as supports for Ni(0) nanoparticles and applied to the reductive depolymerization of lignin model compounds.

This manuscript is divided into three main chapters.

Chapter I is devoted to a general overview of lignin and its properties, and a bibliographic review providing a state of the art on the catalytic depolymerization of lignin and its model compounds under dihydrogen or H-donor molecules over Ni-based catalysts.

Chapter II, divided into three parts (A, B and C). Part A deals with materials made by impregnating silica (mainly Aerosil 380) with Ni^{2+} or Rh^{3+} or both in the presence of ammonia used for the hydrogenolysis of lignin model compounds. One of the main goals will be to understand the reason behind the good catalytic performance and the stability of nickel particles. Part B will describe the principle of innovative chemisorption and titration experiments used to perform a deeper study of the bimetallic Ni/Rh solids with the objective to quantify the amount of each metal available at the surface of the nanoparticles. Catalytic tests performed in Part C will be done with guaiacylglycerol-β-guaiacyl ether, *i.e.*, a molecule bearing a β-O-4 linkage. Hydrogenolysis conditions will be optimized by testing the effect of several parameters (substrate/metal molar ratio, reaction atmosphere as well as gas pressure) on the catalytic activity and product selectivity. ^{1}H NMR and 2D-NMR techniques will be used in order to identify the different products and propose the reaction pathways. Very preliminary tests dealing with the dissolution of Organosolv lignin in isopropanol and its reductive depolymerization will be presented.

Chapter III, divided into two parts (A and B), deals with structured mesoporous silica materials embedding Ni prepared by an original and relatively simple one-pot sol-gel method. In part A, Ni containing materials with a hexagonal pore organization and up to 5 wt.% of Ni will be synthesized and their physico-chemical properties compared to those of the materials of Chapter II. Then, a series of Ni@S with different mesopore structures (wormlike, hexagonal and cubic) will be synthesized using the one-pot strategy with the idea to emphasize some influence of the pore organization in the hydrogenolysis of a simple lignin model compound, the 2-phenoxy-1-phenylethanol. All these new catalysts will be compared to the Ni Aerosil 380-based one described in Chapter II - Part A. In part B, the effect of the addition of a second metal (Fe or Co), by using three incorporation strategies, will be probed. Then the metal-silica interaction and the reactivity of bimetallic nanoparticles will be evaluated under the same reaction conditions in the hydrogenolysis of 2-phenoxy-1-phenylethanol.

This manuscript ends with a general conclusion and proposals for future research.

Finally, an experimental part describing the instruments used for the characterization of the different materials as well as the analysis of the reaction mixtures after catalytic tests will be presented in appendix 1. The details for the chemicals used in this work as well as the synthesis and the calibration methods and curves will be presented in appendix 2 as chemicals and analyses protocols.

References

[1] W. Schutyser, T. Renders, G. Van den Bossche, S. Van den Bosch, S.-F. Koelewijn, T. Ennaert, B. F. Sels, *Nanotechnol. Catal.* **2017**, *23*, 537–584.

[2] A. Pineda, A. F. Lee, *Appl. Petrochemical Res.* **2016**, *6*, 243–256.

[3] "Phenol Market Size, Share Growth and Trends 2023-2028," can be found under https://www.expertmarketresearch.com/reports/phenol-market-report, **n.d.**

[4] L. Dessbesell, M. Paleologou, M. Leitch, R. Pulkki, C. (Charles) Xu, *Renew. Sustain. Energy Rev.* **2020**, *123*, 109768.

[5] S. Cheng, I. D'Cruz, Z. Yuan, M. Wang, M. Anderson, M. Leitch, C. (Charles) Xu, *J. Appl. Polym. Sci.* **2011**, *121*, 2743–2751.

[6] L. Yang, K. Seshan, Y. Li, *Catal. Today* **2017**, *298*, 276–297.

[7] C. Zhang, F. Wang, *Acc. Chem. Res.* **2020**, *53*, 470–484.

[8] S. Dutta, K. C. W. Wu, B. Saha, *Catal. Sci. Technol.* **2014**, *4*, 3785–3799.

[9] S. H. M. van Leuken, D. J. G. P. van Osch, P. D. Kouris, Y. Yao, M. A. Jedrzejczyk, G. J. W. Cremers, K. V. Bernaerts, R. A. T. M. van Benthem, R. Tuinier, M. D. Boot, E. J. M. Hensen, M. Vis, *Green Chem.* **2023**, 7534–7540.

[10] C. Zhang, X. Shen, Y. Jin, J. Cheng, C. Cai, F. Wang, *Chem. Rev.* **2023**, *123*, 4510–4601.

[11] L. Al-Hussaini, F. Launay, E. Galvez, *Materials (Basel).* **2020**, *13*, 812–845.

[12] Z. P. Fu, Y. P. Zhao, F. P. Wu, J. X. Xie, L. Le Qiu, J. Xiao, J. Liang, Y. H. Bai, F. J. Liu, J. P. Cao, *Mol. Catal.* **2023**, *547*, 113334.

[13] A. Shivhare, D. Jampaiah, S. K. Bhargava, A. F. Lee, R. Srivastava, K. Wilson, *ACS Sustain. Chem. Eng.* **2021**, *9*, 3379–3407.

[14] H. Ramzan, M. Usman, F. Nadeem, M. Shahzaib, M. Ur Rahman, R. R. Singhania, F. Jabeen, A. K. Patel, C. Qing, S. Liu, G. Piechota, N. Tahir, *Bioresour. Technol.* **2023**, *386*, 129492.

[15] M. Gale, C. M. Cai, K. L. Gilliard-Abdul-Aziz, *ChemSusChem* **2020**, *13*, 1947–1966.

[16] A. Agarwal, M. Rana, J. H. Park, *Fuel Process. Technol.* **2018**, *181*, 115–132.

[17] J. M. Pepper, H. Hibbert, *J. Am. Chem. Soc.* **1948**, *70*, 4275.

[18] J. Zhang, J. Teo, X. Chen, H. Asakura, T. Tanaka, K. Teramura, N. Yan, *ACS Catal.* **2014**, *4*, 1574–1583.

[19] J. Zhang, N. Yan, *Part. Part. Syst. Charact.* **2016**, *33*, 610–619.

[20] Y. Zhai, C. Li, G. Xu, Y. Ma, X. Liu, Y. Zhang, *Green Chem.* **2017**, *19*, 1895–1903.

[21] Y. Zheng, N. Zhao, J. Chen, *Appl. Catal. B Environ.* **2019**, *250*, 280–291.

[22] T. Klamrassamee, N. Laosiripojana, D. Cronin, L. Moghaddam, Z. Zhang, W. O. S. Doherty, *Bioresour. Technol.* **2015**, *180*, 222–229.

[23] P. Chen, Q. Zhang, R. Shu, Y. Xu, L. Ma, T. Wang, *Bioresour. Technol.* **2017**, *226*, 125–131.

Chapter I: Bibliographic review

Reductive depolymerization of lignin model compounds or lignin over heterogeneous Ni-based catalysts.

I.1. Introduction

Over the past few decades, the worldwide energy crisis and the environmental impact of a petroleum-based economy have led to extensive research on biomass conversion to chemical and fuels. In this context a global roadmap "REMAP 2030" has been launched by the International Renewable Energy Agency in order to help double the share of renewable energy by 2030. The U.S. Department of Energy also set an ambitious goal to generate 20% of the transportation fuel from biomass by 2030 [1]. The first-generation biomass feedstock (corn, starch, soy, sugarcane, *etc.*) cannot be envisaged as a sustainable option as it competes, directly or indirectly, with food production. On the other hand, with an annual production of around 170 billion metric tons worldwide, lignocellulose (second generation) is a much more promising alternative for fossil-based fuels and chemicals because it is the most abundant form of biomass and is inedible for human beings [2]. Recently, research on the production of value-added chemicals, alternative fuels, and platform compounds from lignin has grown rapidly. Lignin is used either directly or chemically modified, as a binder, dispersant agent for pesticides... [3,4]. Besides the above applications, biorefineries using lignocellulosic feedstock have been proposed [5]. Development of technical and cost-effective valorization strategies with catalysts has now attracted ever-increasing attention. Strategies can be classified into acid/ base catalyzed depolymerization/hydrolysis, pyrolysis, hydrotreating (hydrodeoxygenation, hydrogenation, hydrogenolysis), chemical oxidation, liquid-phase reforming as well as gasification (Figure I.1) [1].

Hydroprocessing of lignin produces simple aromatic compounds such as phenols, benzene, toluene, and xylene. It involves thermal reduction in the presence of a hydrogen source at temperatures typically ranging from 100 to 350^{o}C. Oxidation reaction takes place at lower temperatures (0-250^{o}C) and favors the production of aromatic alcohols, aldehydes, and acids that

are targets for fine chemicals. Pyrolysis of lignin (typically at 450-700°C) produces CO, CO_2, H_2O, gaseous hydrocarbons and a liquid product known as "bio-oil" containing volatile liquids such as benzene and monophenols. Depolymerization reactions catalyzed by both acid (typically at 0-200°C) and base (100-300°C) break the C-O or C-C linkages between lignin units leading to smaller fragments. Liquid-phase reforming, occurring generally at 250-400°C, produces hydrogen and light gases while gasification, typically carried out at 500-700°C, is the process that produces synthesis gas (CO and H_2) from a range of real lignin feedstocks and model compounds [1].

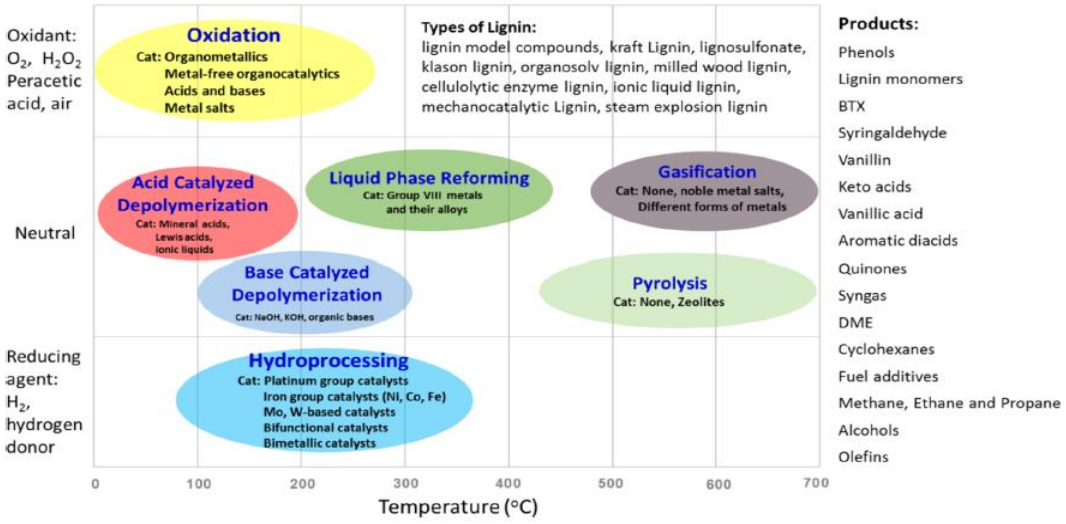

Figure I.1: *Summary of processes for conversion of lignin [1].*

Phenolic molecules are used as building blocks in phenol-formaldehyde resins or epoxy or polyurethane materials. For instance, 77% of the phenol demand goes to the formation of poly(Bisphenol A) carbonate. However, Bisphenol A (BPA) exhibits estrogen-mimicking, hormone-like properties which led several governments to investigate its safety and some retailers to withdraw BPA-based polycarbonate products. One solution would consist in using, instead of phenol, alternative molecules [6,7] such as 4-propylguaiacol and 4-propylsyringol issued from lignin depolymerization, through the cleavage of C-O bonds. Interestingly, the use of these bio-sourced phenols, instead of phenol itself, to get for example poly(Bisphenol A) carbonate analogs for food packaging, would lead to compounds with a reduced endocrine disruptor character [8].

Regarding reductive depolymerization, research works aim at optimizing the cleavage of C-O bonds connecting the aromatic rings (especially those involved in the β-O-4 linkage [9]), keeping the hydrogenation of the aromatic rings as low as possible. Compared to non-catalyzed reactions,

such processes are generally more environmentally friendly, economically viable and energy efficient [10]. Here, we will focus our attention on heterogeneous catalysts for the reductive depolymerization because they are preferred for industrial applications. Indeed, they are easier to recover and recycle and have multiple types of active sites on their surface. Noble metals such as Pd, Pt, Ru and Rh [11] possess good catalytic properties and catalyze not only the hydrogenolysis process but also other H-related reactions (hydrogenation) due to their high hydrogen transfer ability. In contrast, Ni catalysts bear higher intrinsic activity and, hence, have been widely used in direct hydrogenolysis of raw and pretreated lignins [1]. As exemplified by model compounds, under 50 bar of H_2 at 200°C and over Pd/C, the products consist mainly on dimers and cyclohexane, remarkably different from those over Ni/C, and this confirms that Pd/C hydrogenates the arenes concurrently with the hydrogenolysis of β-O-4 bonds [12]. Nickel is generally chosen as active phase due to its low cost [13,14] and is much more economically viable than precious metals [15]. It is reputed to have a great chemoselectivity and it has ferromagnetic properties interesting for the development of magnetism-assisted catalysis. In fact, it was reported that the selectivity of the C-O-C bond cleavage over Ni was higher [16] than the corresponding values in the case of Ru or Pd [17]. Bimetallic catalysts are booming development as a promising option since the "synergistic effects" can occur, leading to an improvement of the catalytic activity, a modification of the desired products selectivity and an increase of the catalyst stability [18–20]. Nickel-ruthenium [21], nickel-palladium [22] catalysts turned out to be more active than monometallic nickel. Thus, many efforts have been performed to lower the cost, including the use of cheap metal to replace the noble metal for synthesizing a non-precious alloy and improve these catalysts reusability [7,23,24]. According to literature, Ni/Rh bimetallic materials were very few in the reductive depolymerization of lignin, compared to carbon dioxide reforming of methane [25–27], hydrogen generation [28,29], hydrogenation of arenes [30], CO_2 methanation [31] or the oxidation of urea [32].

First, it is important to start by introducing lignin and the ways of its extraction. Then, this bibliographic survey will focus on the hydrocracking of lignin and its model compounds over Ni-based heterogeneous catalysts in order to produce phenolic monomers.

I.2. General properties of lignin and use of model compounds

Lignocellulosic biomass is constituted by lignin and two polymers made of C5 and C6 sugars *i.e.*, hemicellulose (20-30%) and cellulose (40-50%) [1]. Lignin provides rigidity and structural support to cell wall polysaccharides, makes the cell walls water-impermeable and offers protection against pests and pathogens. Lignin, which is derived from the Latin term *lignum*, meaning wood, is a random, complex, irregular, three-dimensional hetero biopolymer with hydrophobic properties. Lignin is well known for its low degree of order and high level of heterogeneity, it has variations in both chemical composition and structure depending on types of plants *i.e.*, hardwood, softwood or grass. Its structure is mainly based on aromatic rings linked to each other by C-O ether and C-C bonds. The degree of crosslinking of the chains that depends on the wood source may not be high [33]. The composition, molecular weight, and amount of lignin differ from plant to plant, with lignin abundance generally decreasing in the order of softwoods > hardwoods > grasses [34]. Lignin is composed of three main phenylpropane units, *i.e.*, *p*-coumaryl, coniferyl and sinapyl alcohols depicted in Figure I.2 (giving rise to *p*-hydroxyphenyl H, guaiacyl G and syringyl S type of lignins, respectively) [35].

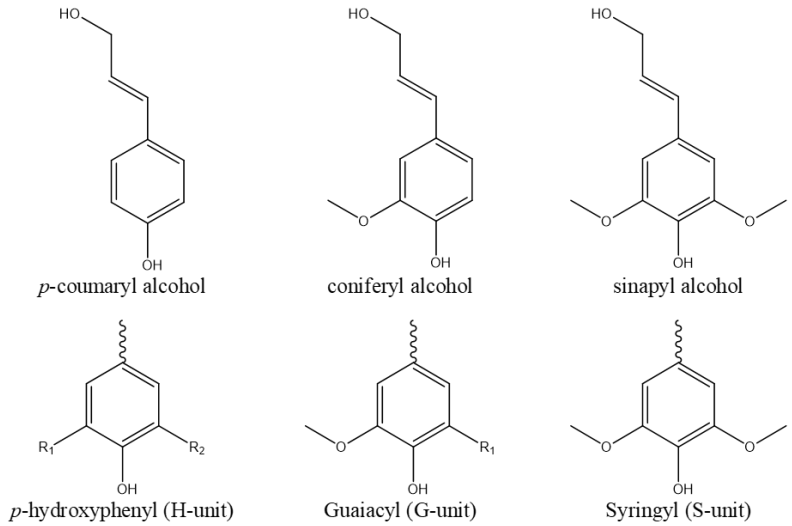

Figure I.2: *The three building blocks (monolignols) and their corresponding structures in lignin [35].*

The relative amount of the three monolignols depends on plant type and growth. However, hardwood lignins contain mostly G and S units and only traces of H units, whereas softwood lignins consist principally of G units and traces of H ones (Table I.1) [34].

Table I.1: *Lignocellulosic and lignin composition for softwoods, hardwoods and grasses.*

	Lignocellulose composition (wt.%)			Monolignol distribution in lignin (%)		
	Cellulose	Hemicellulose	Lignin	H	G	S
Softwoods	46-50	19-22	21-29	<5	>95	0
Hardwoods	40-46	17-23	18-25	0-8	25-50	45-75
Grasses	28-37	23-29	17-20	5-35	35-80	20-55

I.3. Extraction processes of lignin

The separation of lignin from cellulose and hemicellulose is a very challenging process. Moreover, it is well established that the way it is performed may have a strong effect on the bonds nature and, as such, on the recovered lignin reactivity [36]. Figure I.3 shows different extraction processes. Each one produces a distinct lignin fraction which may vary in overall composition, molecular weight, as well as type and abundance of different functional groups (Table I.2).

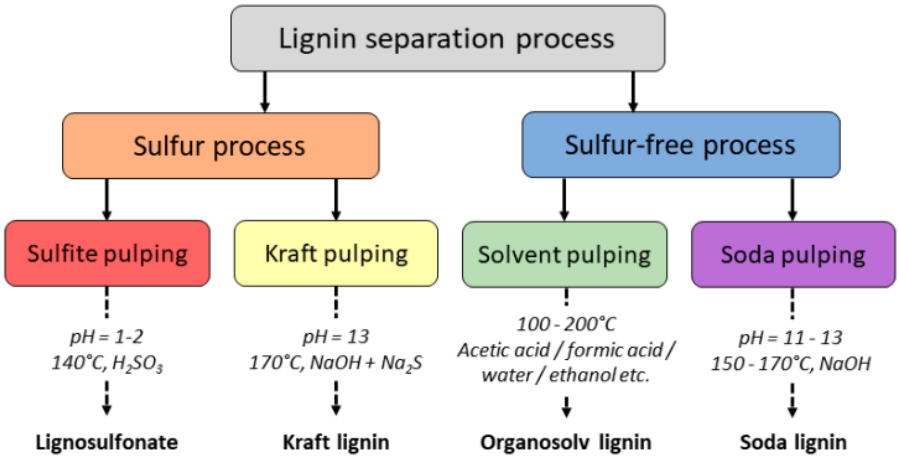

Figure I.3: *Lignin pulping processes and their dominant products [37].*

Kraft and Sulfite are the most common procedures. “Kraft lignin” (from the name of its extraction process) is obtained by the treatment of lignocellulosic biomass by sodium sulfide under alkaline conditions (Na_2S/NaOH) at 155-175^{o}C. Such procedure involves removal of lignin upon its dissolution, leaving cellulose as solid fraction [38]. Lignin issued from the Sulfite process, which

consists in the impregnation of the biomass with an aqueous solution of sulfur dioxide [36], is called lignosulfonate as the result of the presence of sulfonated groups.

Strong and dilute acid hydrolysis are also effective processes in the pretreatment of lignocellulosic biomass. Acids such as sulfuric can be used. However, during acid hydrolysis of biomass, lignin can undergo extensive structure change [39]. It has to be noted that hydrolysis process with the use of enzymes can be used. Here, cellulotic enzymes degrade the carbohydrate fraction and leave behind a cellulose-enzyme-lignin residue with only slight structural changes of the lignin part (less phenolic hydroxyl groups, more β-O-4 linkages) [40].

Other isolation methods were also developed by using organic solvents extraction, affording Organosolv lignin, which is often considered to be less altered and purer than the other extracted forms, is obtained from biomass in the presence of an organic solvent (*e.g.*, ethanol) with or without water at relatively high temperatures and pressures [41].

The soda process uses a sodium hydroxide solution as cooking liquor and provides chemical or semi-chemical pulp. The resulting pulp consists largely of readily bleached fibers [42].

Table I.2: *Different forms of lignin process extraction.*

Lignin type	Scale	Chemistry	Sulphur content	Purity
Kraft	Industrial	Alkaline	Low	High
Lignosulfonate	Industrial	Acidic	High	Low
Hydrolytic	Industrial/Pilot	Acidic	Low/Free	Moderate
Organosolv	Industrial/Pilot	Acidic	Free	High
Soda	Industrial/Pilot	Alkaline	Free	Moderate

As described above, lignin is very complex and a lot of compounds (either soluble molecules, or solids or gas) can be generated during its conversion. Moreover, these compounds may interact in a reaction network involving de-polymerization and re-polymerization reactions [35]. Working in milder conditions and using heterogeneous catalysts are helpful to minimize side reactions. Often studies are dealing with lignin models in order to simplify and explore the reaction mechanism [10]. Convenient lignin model compounds are aromatic compounds bearing linkages similar to those of lignin. Figure I.4 shows the most common types of linkages, *i.e.*, β-O-4, α-O-4, 4-O-5, 5-5, β-β, β-1 and β-5 with β-O-4, being the most dominating in several lignins.

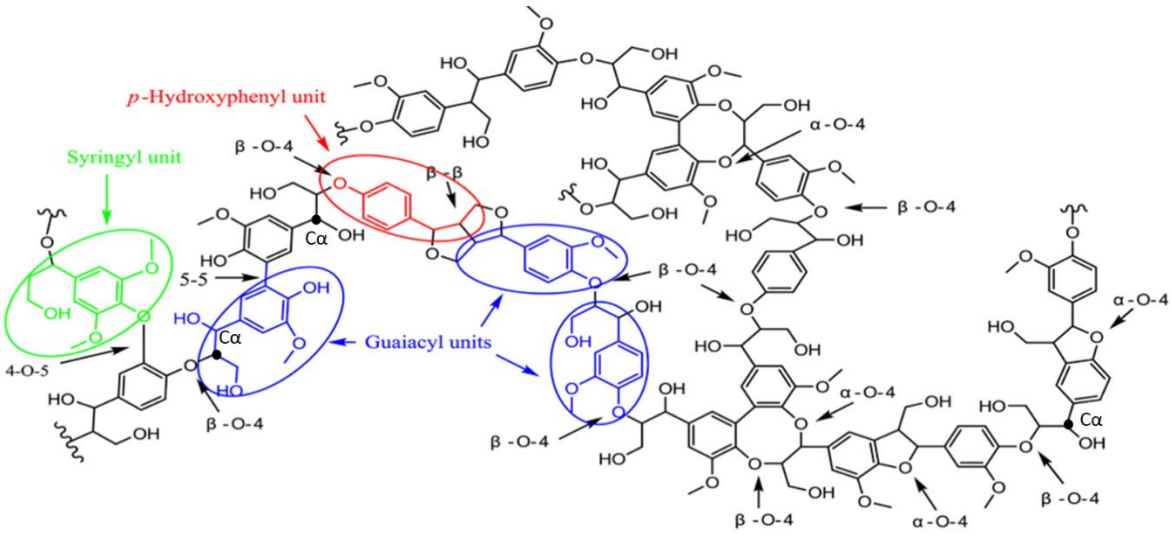

Figure I.4: *Representative structure models of lignin [1].*

In the literature, there are typically two sorts of lignin model compounds, *i.e.*, monomers and dimers. Monomers are aromatic compounds with hydroxyl, methoxyl and alkyl functional groups, *e.g.*, anisole, guaiacol and trans-anethole [43,44]. Dimers (Figure I.5) often tested are 2-phenethyl phenyl ether, 2-phenoxy-1-phenylethanol, benzyl phenyl ether, diphenyl ether and guaiacylglycerol-β-guaiacyl-ether [45–47] and others. An oxidized lignin model compound the 2-phenoxy-1-phenylethanone can also be used [48]. The advantage of performing lignin oxidation pretreatment before cleavage is related to the higher ability of those molecules to be cleaved especially in mild conditions [48]. In some studies, the oxidation and hydrogenolysis processes are coupled. Photocatalysis is an interesting reported strategy to oxidize Cα–OH of β-O-4 (Figure I.4) alcohols to Cα=O with light, and then cleave for example the C–O bonds close to the obtained Cα=O bonds through hydrogenolysis [49,50].

Hydrocracking of lignin gathers different chemical reactions such as hydrodeoxygenation (HDO), hydrogenation and hydrogenolysis. HDO refers to the removal of the oxygen present in the methoxyl and hydroxyl groups [51], hydrogenation refers to the saturation of the aromatic cycle, while hydrogenolysis is used to describe the cleavage of C-O ether bonds and C-C bonds between the aromatic rings. Hydrocracking of lignin or lignin model compounds usually involves noble or transition metal supported or not catalysts affording active hydrogen species either from H_2 or H-donors such as alcohols under an inert atmosphere Ar or N_2. Typical examples of hydrogen-donor

solvents used in lignin depolymerization include protic solvents such as water, alcohols and formic acid, and non-protic ones such as tetralin [13].

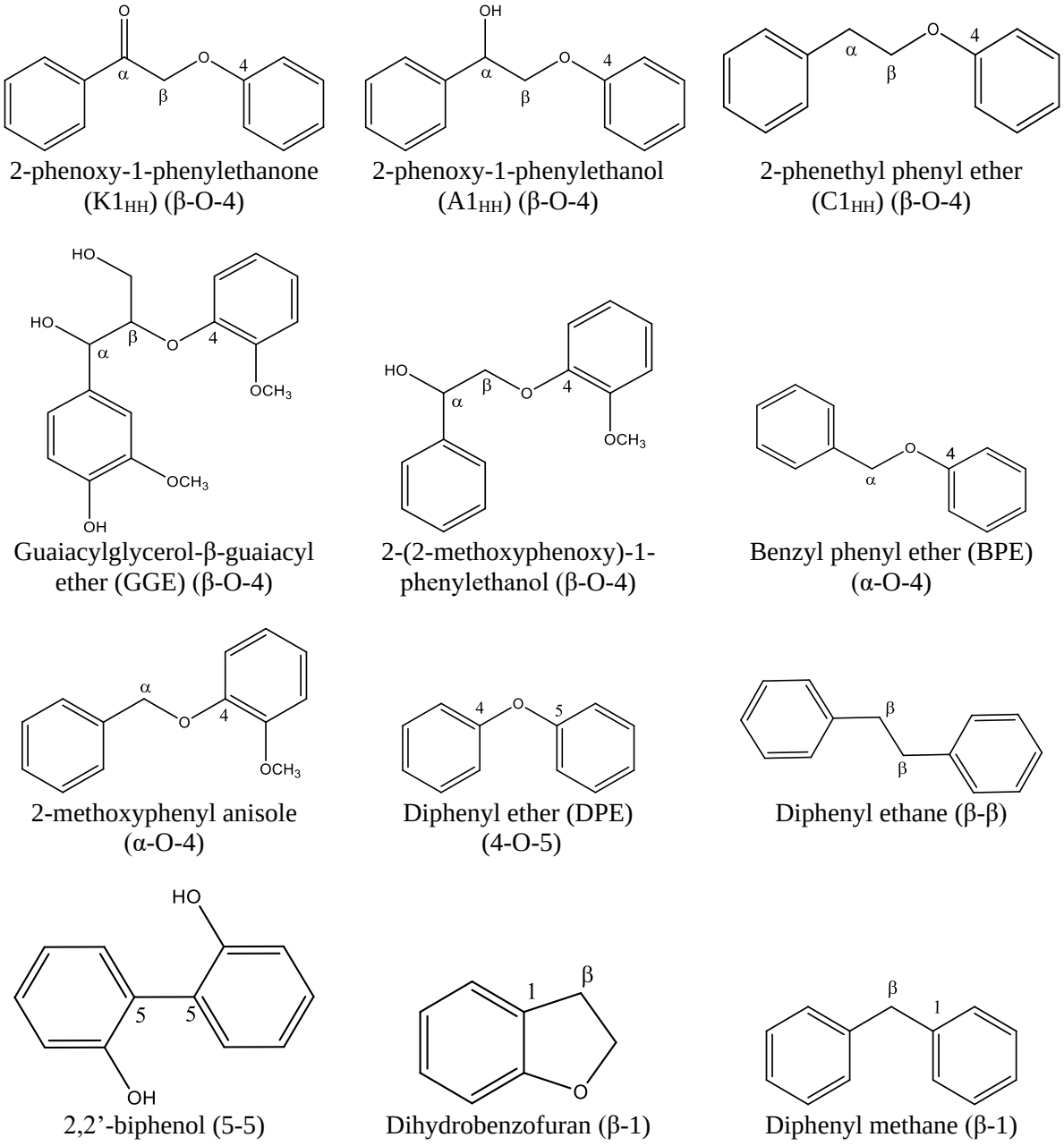

Figure I.5: *Dimeric lignin model compounds [36].*

I.4. Hydroprocessing of lignin model compounds and lignin over Ni supported catalysts

The fierce competition in lignin depolymerization is illustrated by the staggering increase in the number of publications in this topic over the past twenty years. Over 700 articles concerning nickel-based silica catalysts have been published between 2000 and 2022. Among them, around 60% were published between 2019 and 2022 (Figure I.6).

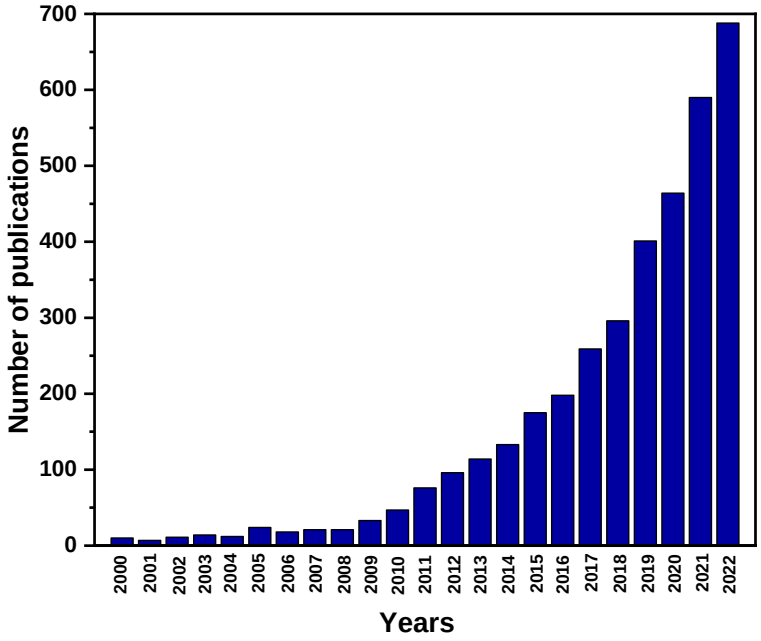

Figure I.6: *Number of articles/reviews published per year from 2000 to 2022 using nickel, silica, reductive catalytic lignin depolymerization as key words.*

This increase could be reflected by the effectiveness of the combination of siliceous supports and nickel as catalysts. A review solely treating heterogeneous nickel-based silica compared to other supports in the reductive depolymerization of lignin model compounds or a real lignin, does not exist which encouraged us to propose this bibliographic chapter.

I.4.1. Hydrogenolysis of lignin model compounds

The hydrogenolysis results of different lignin model compounds are listed in Table I.3. The supports used are zeolites, carbon, silica (porous SiO_2, SBA-15…), etc [6,52–54]. High 57% and low nickel 5% mass loadings were tested. Nickel nitrate and nickel chloride were mainly the two

nickel precursors and the methods to incorporate the nickel into the support were incipient wetness impregnation (IWI) and wet impregnation (WI). Most of the catalysts were thermally treated then reduced by H_2 in a temperature range between 400°C and 700°C. Hereafter, we will present works with lignin model compounds bearing α-O-4, β-O-4 and 4-O-5 type linkages.

I.4.1.a. Molecules bearing an α-O-4 type linkage

Benzyl phenyl ether (BPE) is widely used to represent the α-O-4 linkage in lignin. The α-O-4 is characterized by a low bond dissociation energy of the aliphatic C-O bond (BDE ~ 218 kJ mol^{-1}) compared to other type of C-O bonds [15]. Considering a typical hydrogenolysis reaction of BPE, two main products should be obtained *i.e.*, phenol and toluene. It is proposed that, during BPE cleavage, Ni-H species of the metal surface react with the oxygen atom of BPE, leading to the cleavage of the C-O bond with the dominant formation of benzyl and phenoxy radicals as intermediates [15,55].

Matsagar *et al.* (Table I.3, entry 1) [46] showed the efficiency of carbon black (CB) impregnated by 5 wt.% of Ni (5%Ni/CB) as a catalyst for the hydrogenolysis of BPE. The CB support used was a mesoporous material showing higher efficiency than conventional activated carbon. In such case, Ni nanoparticles with an average particle size of 8 nm were homogeneously distributed and the resulting catalyst led to more than 99% BPE conversion at mild conditions (80°C under 2 bar H_2) in the presence of ethanol/water (3/7 v/v) as co-solvent. The authors focused on using co-solvent systems because mixtures were better solvents. Zhu *et al.* chose activated carbon AC [15] and tested the resulting catalysts in more drastic conditions of temperature and pressure. For example, 10%Ni/AC, with uniformly distributed nickel spherical nanoparticles, was used under 20 bar H_2 for 2 h at 140°C with substrate/metal molar ratio of 16, in methanol showing a high selectivity in cleaving the C-O bond of BPE (Table I.3, entry 2) [15]. Zhu *et al.* (Table I.3, entry 3) [55] reported similar results under almost the same reaction conditions (160°C and 2 h) but while using 15 bar of H_2 pressure. Furthermore, Zhu *et al.* compared the catalytic activity of Ni/AC with Ni supported on ZSM-5 zeolite (Ni/H-ZSM-5). Ni/H-ZSM-5 needed higher temperature to totally convert BPE into its products (Table I.3, entry 4). According to the authors, the reason for such discrepancies would be linked to the size of the nanoparticles of nickel dispersed over the support. When Ni was incorporated into HZSM-5, the resulting catalyst obtained after thermal treatment under Ar at 450°C, exhibited bigger metal particles (average was about 41 nm) than Ni/AC which was

characterized by well-distributed nanoparticles with only a few of them displaying sizes larger than 12 nm. In contrast, no reaction occurred with the Ni/AC under super mild conditions (25°C, 2 h and 1 bar H_2). The weak ability of hydrogen adsorption on the Ni sites caused low conversion of BPE and yields of toluene and phenol (Table I.3, entry 5) [56]. It was found that temperature was a crucial parameter for BPE depolymerization, hydrogenolysis occurring at relatively high temperature of 60-150°C. Relatively high temperature would increase the concentrations of the activated hydrogen promoting the hydrogenation of aromatic rings. Therefore, it turned out to be crucial to choose an optimal temperature and relatively low H_2 pressure in order to produce less activated hydrogen, hence favoring hydrogenolysis process [55,56]. Guo *et al.* (Table I.3, entry 6) [57] prepared a novel Ni/CaO–H-ZSM-5 material (Si/Al = 60) by deposition-precipitation method to investigate the C-O bond cleavage in α-O-4 model compound. Metal oxides such CaO as catalyst have many drawbacks such as small surface area and easy aggregation during the reaction. In order to improve its catalytic activity, ZSM-5 zeolite was found to be suitable as catalytic support for the lignin conversion and has been studied. Under 10 bar H_2 and at 140°C in ethanol, the C-O bond of 2-methoxyphenyl anisole (α-O-4) (Figure I.5) could be almost cleaved in 15 min, producing 49% selectivity of toluene and 51% selectivity of guaiacol, and this reaction showed a total conversion. The difference of reactivities of the C-O bond cleavage in β-O-4 and the α-O-4 model compounds was also studied. Hence, the cleavage of the C-O bond in 2-(2-methoxyphenoxy)-1-phenylethanol, (a β-O-4 model compound, Figure I.5) was carried out strictly under the same reaction conditions. In that case, all the β-O-4 had been converted in 1 h, producing 31% selectivity of 1-phenylethanol, 47% selectivity of guaiacol and 20% selectivity of ethylbenzene. Consequently, the results meant that the α-O-4 linkage was quite unstable and could be more easily cleaved [57]. The search for materials with high active nickel catalysts which proceed with selective hydrogenolysis of C-O bridged bond but without hydrogenation of aromatic ring is still ongoing. This was seen with Ni/TiN catalyst operating at relatively harsh conditions (250°C, 10 bar H_2 for 3 h) (Table I.3, entry 7) [58].

In the works of He *et al.* (Table I.3, entry 8) [59] 57 wt.%. Ni supported on commercial silica SiO_2 via deposition-precipitation method and 70 wt.%. Ni on SiO_2 (Table I.3, entry 9) [60] were selected as catalysts to study the hydrogenolysis rate of BPE in water. The first experiment was conducted at 120°C with 6 bar H_2, while the second one at 250°C with 40 bar H_2. In these conditions, almost all BPE was converted into phenol and toluene. The authors also studied the same reaction in

apolar phase *i.e.*, undecane and concluded that Ni/SiO_2 leads to a higher rate of C-O bond cleavage in undecane than in water probably because of the much weaker adsorption of reactants onto active Ni sites in the aqueous phase [60].

An interesting approach for green and solvent-free biomass deconstruction and valorization is the use of mechano-catalysis. In fact, the hydrogenolysis of benzyl phenyl ether (BPE) via ball milling was demonstrated over supported $5\%Ni/SiO_2$ quartz at nominally room temperature and atmospheric hydrogen pressure under continuous H_2 flow with no solvent. It was shown that the production of undesirable side products was much higher on the high surface area catalysts (~ 500 $m^2\ g^{-1}$). Reactions with either 5 wt.% Ni on silica-alumina or silica gel resulted in carbon balances of just 30%, while the reaction with $5\%Ni/SiO_2$-quartz (6.7 $m^2\ g^{-1}$) had a carbon balance of 82% with only 30% conversion of BPE into toluene and phenol and hydrogenated ether (Table I.3, entry 10) [61].

Table I.3: *Hydrogenolysis examples of various lignin model compounds with α-O-4 linkage.*

Entry	Ref	Catalyst	Preparation method	Solvent	Substrate	Molar substrate /metal	T (ºC)	t (h)	Pressure (bar of H_2)	X (%)	Aromatic monomers (Yield %)
1	[46]	5%Ni/CB	WI	ethanol/ water	BPE	5	80	1	2	99	Phenol (45) Toluene (46)
2	[15]	10%Ni/AC	IWI	methanol	BPE	16	140	2	20	100	Phenol (40) Toluene (48)
3	[55]	10%Ni/AC	WI	methanol	BPE	6	160	2	15	100	Phenol (44) Toluene (52)
4	[55]	10%Ni/H-ZSM-5	WI	methanol	BPE	6	180	2	15	100	Phenol (45) Toluene (52)
5	[56]	10%Ni/AC	IWI	methanol	BPE	32	25 120	2	10	0 0.9	*n.d.*
6	[57]	45%Ni/5%CaO-H-ZSM-5	Deposition-Precipitation	ethanol	2-(2-methoxyphenoxy)-1-phenylethanol	3	140	1	10	100	Ethylbenzene (20) Guaiacol (47) 1-phenylethanol (31)
					2-methoxyphenyl anisole	8	140	0.2	10	100	Toluene (49) Guaiacol (50)
7	[58]	10%Ni/TiN	IWI	ethanol	BPE	6	250	3	10	100	Toluene (30) Phenol (30)
8	[59]	57%Ni/SiO_2	Deposition-Precipitation	water	BPE	34	120	2	6	100	Phenol (45) Toluene (50)
9	[60]	70%Ni/SiO_2	*commercial*	water	BPE	420	250	2	40	100	Phenol (50) Toluene (50)
10	[61]	5%Ni/SiO_2 quartz	IWI	H_2	BPE	1	27	3	1	30	Toluene (15) Phenol (10)

n.d.: not determined; CB: carbon black; AC: activated carbon; IWI: Incipient wetness impregnation; WI: wet impregnation.

I.4.1.b. Molecules with a β-O-4 linkage

The β-O-4 linkage is the most abundant type of C-O bonds, contributing to 45-62% of the ether bonds in lignin [59]. Therefore, the investigation of β-O-4 bond cleavage has received the greatest attention. Typically, in order to better understand the lignin depolymerization mechanism and to control it, lignin model compounds bearing the β-O-4 bond were used [62].

Under H_2, addition of a capping agent such as ethyl acetate in the case of oxidized lignin [63] or use of a small amount of Ni/SiO_2 catalyst, prepared by deposition-precipitation method, for the cleavage of $C1_{HH}$ [59] are possible strategies to enhance the cleavage of the ether bond at the expense of phenol hydrogenation operating in water at 120°C under 6 bar H_2. Other authors reported also that the incorporation of Rh into Ni colloids can help to reduce the conversion of aromatic to cyclohexyl rings for $K1_{HH}$, $A1_{HH}$ or $C1_{HH}$ in water at 1 bar H_2 at 95°C for 16 h (Table I.4, entry 1) [64]. Active metal-hydride species can also be produced from hydrogen donors, such as ethanol, formic acid, methanol, tetralin, isopropanol and glycerol, under inert atmosphere [52,65–68] preferred to high-pressure hydrogen for economic, safety, handling and selectivity issues [66,69]. Undesirable hydrogenation of the aromatic rings of $K1_{HH}$ was observed under H_2 in hexane, with Ni supported over $ZnO\text{-}Al_2O_3$ at 250°C under 20 bar H_2 for 2 h (Table I.4, entry 2) [70], while *in-situ* generation of H_2 limited it, even if a wide variety of products were obtained [71].

Similarly, in some works, with isopropanol as an H-donor solvent under an inert atmosphere, Ni@nitrogen-doped carbon (case of $A1_{HH}$ and $K1_{HH}$) under 10 bar of N_2 at 200°C (Table I.4, entry 3) [72] and Ni-Pd@SBA-15 (case of 2',6'-dimethoxyphenoxy)-1-phenylethanol) (Table I.4, entry 4) at high temperature (245°C) [22] exhibited high selectivity towards aromatic compounds. It was demonstrated that the high activity of the Ni-Pd bimetallic catalyst indicates the existence of the synergistic effect between the two metals [18]. However, a recent study conducted on $A1_{HH}$ with Ni unsupported catalyst at 180°C under 10 bar N_2, showed low selectivity towards phenol (Table I.4, entry 5) [73].

The combination of H_2 and alcohols as solvents was also frequently tested. It was ascribed that the common hydrogen supply of H_2 and alcohol could produce more active hydrogen [74] which could possibly lead to a non-desired hydrogenation of aromatics. However, it was reported in some

works, phenol yields higher than 95% in methanol combined with 10 bar of H_2 with a temperature range from 180°C to 220°C, with Ni-doped layered double hydroxides ($K1_{HH}$) (Table I.4, entry 6) [54], Ni-nitrogen doped carbon catalysts ($K1_{HH}$) (Table I.4, entry 7) [75] and NiMo sulfide ($K1_{HH}$ and $A1_{HH}$) [76]. Here, low conversion of $K1_{HH}$ and selectivity towards phenol were reported at 180°C for 1 h under 10 bar of H_2 (Table I.4, entry 8) [77].

He *et al.* (Table I.4, entry 9) [59] indicated a preferred interaction of the aliphatic C-O bond in 2-phenethyl phenyl ether (β-O-4) on the Ni surface. Hydrogenolysis is the dominant reaction pathway for cleavage of 2-phenethyl phenyl ether (β-O-4) with Ni/SiO_2 in water at 120°C and under 6 bar of H_2, affording ethylbenzene and phenol as primary products, then phenol was totally hydrogenated into cyclohexanol. This result also highlights the importance of the hydroxyl group of phenol for adsorption on Ni/SiO_2 under selected conditions [59]. In the hydrogenolysis of 2-phenoxy-1-phenethanol, Ni supported on SiO_2 led toward C-O bond cleavage with 26% monomers yield. However, when adding Ag thus forming NiAg bimetallic active phase by deposition-precipitation method, an enhanced selectivity toward C-O cleavage, achieving 95% conversion with 90% monomers yield (with three aromatic products: phenol, ethylbenzene and 1-phenylethanol) under optimized reaction conditions (130°C, 2 h and 10 bar H_2) (Table I.4, entry 10) [78]. A high yield of phenolic monomer (up to 79% of guaiacol and guaiacylpropanol) was reached too for the reaction of guaiacylglycerol-β-guaiacyl-ether (GGE) in the presence of mesoporous silica nanospheres bearing Ni NPs [47] at 180°C, under 20 bar of H_2 and for 2 h. The performance of the nickel-based catalyst was limited because of the aggregation of Ni^0 into large particles. Therefore, downsizing Ni particle size is highly desirable to improve the atom efficiency and catalytic activity. Anchoring metal sites to the support defects can help to control the dispersion and morphology of metal catalysts. A strategy consisting on the incorporation of aluminum into the framework of mesoporous silica to get monodispersed Ni (with a mean diameter of 1.2 nm) was reported [47]. The evenly distributed defects further acted as anchoring sites to immobilize Ni atoms and obtain the highly dispersed Ni clusters inside the channels as shown in Figure I.7. Therefore, the Ni clusters anchored to the defects in Ni/MSN-Al were more easily reduced.

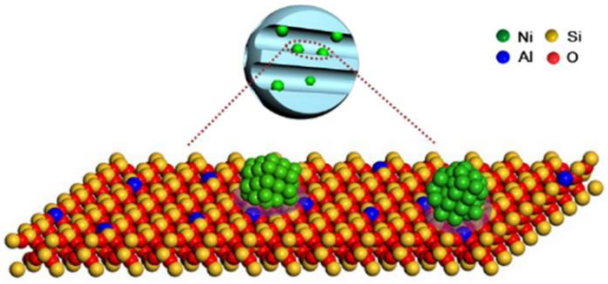

Figure I.7: *The schematic model of Ni/MSN-Al catalyst [47].*

As a result, the TEM of Ni/MSN-Al showed highly dispersed Ni clusters inside the channels without any significant formation of aggregates, and EDX mapping revealed that Si, Al and Ni were evenly distributed within the mesoporous silica nanospheres, as shown in Figure I.8.

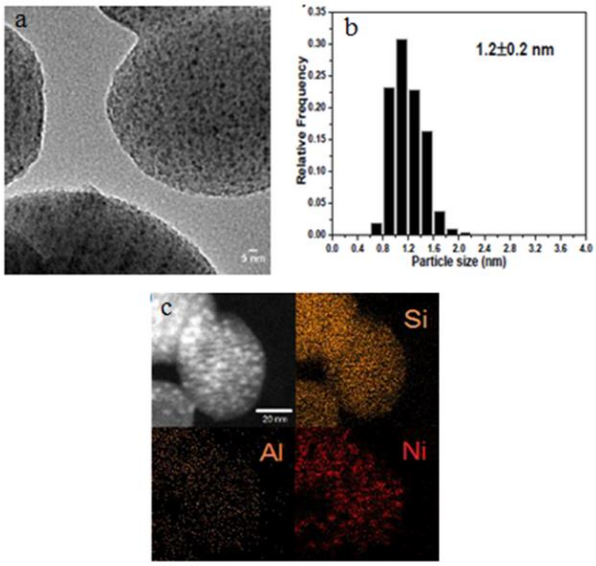

Figure I.8: *(a) HRTEM of Ni/MSN-Al, (b) Particle size distribution of Ni clusters (c) EDS elemental mapping of Ni/MSN-Al [47].*

Ni/MSN-Al achieved complete conversion of GGE on a high yield of phenolic monomers (79%). at 180°C under 20 bar H_2 after 2 h. For a better comparison, Ni/SiO_2 and Ni/MSN without Al were also used in the catalytic depolymerization of GGE. Ni/SiO_2 led to a yield of 70% with the conversion of 96% while Ni/MSN afforded 75% yield of phenolic monomers (Table I.4, entry 11) [47].

Table I.4: *Hydrogenolysis examples of various lignin model compounds with β-O-4 linkage.*

Entry	Ref	Catalyst	Preparation method	Solvent	Substrate	Molar substrate /metal	T (ºC)	t (h)	Pressure (bar of H_2)	X (%)	Aromatic monomers (Yield %)
1	[64]	2.5%Ni-0.8Rh	Deposition-Precipitation	water	$K1_{HH}$	20	95	16	1	100	1-phenylethanol (38) Phenol (35)
					$A1_{HH}$	20	95	16	1	100	1-phenylethanol (44) Phenol (43)
2	[70]	10%Ni/ZnO-Al_2O_3	IWI	n-hexane	$K1_{HH}$	11	250	2	20	100	Ethylbenzene (5) Trace of phenol
3	[72]	12%Ni/NC	IWI	isopropanol	$A1_{HH}$	3	200	4	10 (N_2)	100	1-phenylethanol (50) Phenol (50)
4	[22]	2%Ni-3.6%Pd/SBA-15	IWI	isopropanol/ water	2(2′,6′-dimethoxyphenoxy)-1-phenylethanol	5.3	245	8	5 (N_2)	*n.d.*	Syringol (55) Acetophene (43)
5	[73]	Ni	Co-precipitation	isopropanol	$A1_{HH}$	*n.d.*	180	8	10 (N_2)	93	1-phenylethanol (32) Phenol (6)
6	[54]	10%Ni/MgAl-oxide	IWI	methanol	$K1_{HH}$	0.03	200	6	10	100	Acetophenone (50) Phenol (50)
7	[75]	NiCN	One-pot	methanol	$K1_{HH}$	*n.d.*	220	8	10	99	1-phenylethanol (13) Ethylbenzene (9) Phenol (48)
8	[76]	1.7%Ni-1.9%Mo	*n.d.*	methanol	$K1_{HH}$	*n.d.*	180	4	10	100	Monomers (100)
	[77]				$A1_{HH}$	*n.d.*	180	4	10	100	Monomers (60)
9	[59]	57%Ni/SiO_2	Deposition-Precipitation	water	$C1_{HH}$	3.4	120	8	6	100	Ethylbenzene (50) Trace of phenol
10	[78]	$Ni_{0.8}$-$Ag_{0.2}$/SiO_2	Deposition-precipitation	water	$A1_{HH}$	1	130	2	10	95	Phenol Ethylbenzene 1-phenylethanol
11	[47]	10%Ni/MSN-Al	IWI	methanol	GGE	7.3	180	2	20	100	Guaiacol (33) Guaiacylpropanol (11) Methylguaiacylpropanol (8) Eugenol (4) Isoeugenol (1) Propylguaiacol (22)

n.d.: not determined; IWI: incipient wetness impregnation; MSN: mesoporous silica nanospheres.

I.4.1.c. Dimers with 4-O-5 type linkage

The 4-O-5 linkage contributes generally to 4-9% of ether bonds in lignin. Diphenyl ether (DPE) is usually selected as a model compound for this linkage in the exploration of C-O bond cleavage to form benzene and phenol [59]. In principle, the C-O bond of the 4-O-5 linkage should be the most difficult ether bond to cleave, as it has the highest BDE (~ 314 kJ mol^{-1}).

In the work of Xie *et al.* Ni-based catalysts supported on AC with different pore structures and hydrophilicities led to different reaction efficiencies and product distributions for the C−O bond cleavage of DPE. The yield of monomers increased gradually with the surface specific area enhancement of Ni/AC. At 140°C under 10 bar of H_2 and for 2 h in isopropanol, Ni/AC with the highest surface area (2399 m^2 g^{-1}) led to 90% conversion of DPE not into aromatic monomers but into cyclohexane and cyclohexanol (Table I.5, entry 1) [79]. Similarly, 15%Ni/Nb_2O_5 led to a total conversion of DPE in isopropanol at 220°C under 10 bar of H_2 for 2 h but with a low selectivity towards phenol (Table I.5, entry 2) [74].

Catalytic hydrogenolysis of diphenyl ether was also studied with 57%Ni/SiO_2 in water at 120°C under 6 bar H_2 (Table I.5, entry 3). Under selected conditions, the authors demonstrated different mechanism for the C-O cleavage of the model compounds. The C-O bond in β-O-4 or in α-O-4 was directly cleaved by Ni catalyzed hydrogenolysis while the C-O bond in 4-O-5 was cleaved by parallel hydrogenolysis and hydrolysis which produces two molecules of phenol. Phenol was identified as trace because it was hydrogenated into cyclohexanol due its high hydrogenation route under these conditions [59,80].

I.4.1.d. Molecules bearing C-C type linkage

C-C lignin linkages are much more difficult to cleave in comparison to C-O-C ether linkages. Güvenatam *et al.* [81] and Zhao *et al.* [82] studied the conversion of 5-5, β-1, and β-β lignin model compounds over noble metals Pt and Pd supported on carbon at 200°C under H_2 pressure in water using a batch reactor. They found out that the cleavage of C-C bonds in all the model compounds did not occur, hence they were converted into their corresponding saturated dimers in high yields.

Table I.5: *Hydrogenolysis examples of various lignin model compounds with 4-O-5 type linkages.*

Entry	Ref	Catalyst	Preparation method	Solvent	Substrate	Molar substrate /metal	T (ºC)	t (h)	Pressure (bar of H_2)	X (%)	Aromatic monomers (Yield %)
1	[79]	10%Ni/AC	IWI	isopropanol	DPE	7	140	2	10	90	Benzene (13) Cyclohexane (18) Phenol (20) Cyclohexanol (41)
2	[74]	15%Ni/Nb_2O_5	IWI	isopropanol	DPE	7.6	220	2	10	100	Benzene (40) Phenol (2)
3	[59]	57%Ni/SiO_2	Deposition-Precipitation	water	DPE	3.4	120	2	6	100	Benzene (30) Trace of phenol

AC: activated carbon; IWI: incipient wetness impregnation.

I.4.2. Catalytic lignin reductive depolymerization

Depolymerization strategies involving heterogeneous catalysts are promising deconstruction strategies in spite of the mass transfer limitations from the bulk lignin molecules to the catalyst surface. Such systems most frequently use metal catalysts for the cleavage of ether bonds in lignin and only a minority of the applied systems focus on the C-C bonds.

Noble-metal catalysts [83] show excellent activity in the hydrogenolysis but are expensive, as already mentioned. Interestingly, several reports have illustrated the utilization of supported transition metal catalysts (*e.g.*, Ni) in lignin depolymerization [84]. It has been found that the yields of products vary significantly across biomass type and origin, reaction conditions and catalyst formulation [66]. The two main concerns remain minimizing the repolymerization phenomena thus forming more condensed structure and suppressing char formation.

In this part, we present some examples of lignin depolymerization with the phenolic monomers (Table I.6) using nickel as active phase and carbon or zeolites as supports, then we focus on published works dealing with nickel silica and mesoporous silica-based catalysts.

Table I.6: *Main monophenols obtained from reductive lignin depolymerization, adapted from [22].*

Compounds					
H units	**Label**	**G units**	**Label**	**S units**	**Label**
phenol	H1	guaiacol	G1	syringol	S1
4-methylphenol	H2	4-methylguaiacol	G2	4-methylsyringol	S2
4-ethylphenol	H3	4-ethylguaiacol	G3	4-ethylsyringol	S3
4-vinylphenol	H4	4-vinylguaiacol	G4	4-propylsyringol	S4
		4-propylguaiacol	G5	4-propenylsyringol	S5
		4-propenylguaiacol	G6	syringylpropanol	S6
		guaiacylpropanol	G7	acetosyringone	S7
		vanillin	G8	syringylacetone	S8
		acetovanillone	G9	syringaldehyde	S9
		guaiacylacetone	G10	mesitol	S10

Incipient wetness impregnation and wet impregnation are mainly implemented for Ni incorporation one these supports. Most of the papers are dealing with weight percentages of Ni between 1% and 20%, and with nickel(II) nitrate or nickel(II) chloride as nickel precursors. The resulting catalysts were thermally treated and reduced in temperature ranges between 400°C and 500°C. There is a little variety in the nature of lignin used (*e.g.*, poplar, pine, birch, beech sawdust, etc.). Table I.7 shows some works of the depolymerization of lignin over Ni catalysts.

Table I.7: *Examples of reductive lignin depolymerization over Ni-based heterogeneous catalysts.*

Entry	Ref	Catalyst	Preparation method	Solvent	Lignin	Lignin extraction	T (ºC)	t (h)	Pressure (Bar of H_2)	X (%)	Aromatic monomers
1	[23]	5%Ni-5%Fe/C	Co-precipitation	methanol	Birch sawdust	Organosolv 1,4 dioxane	225	6	20	*n.d.*	Phenolic monomers: G1,G3,G5,S4
2	[85]	10%Ni/C	IWI	1,4 dioxane + THFA	Beech sawdust	Thermal treatement THFA/water	220	5	20	18	Phenolic monomers: G7,S4,S6
3	[86]	10%Ni5%Cu/C	IWI	ethanol/ isopropanol	Poplar lignin	Organosolv ethanol/toluene	270	4	10 (N_2)	*n.d.*	Phenolic monomers: G3,G5,G7,S2,S4, S6
4	[58]	10%Ni/TiN	IWI	ethanol	*n.d.*	Dealkylation	300	3	10	*n.d.*	Phenolic monomers: *n.d.*
5	[87]	10%Ni/LCNF	Electrospinning of lignin and Ni	ethanol/water	Poplar wood	Organosolv ethanol/water	300	5	10	91	Phenol: H1 Light fragments
6	[53]	32%Ni@NDC	IWI	ethanol	*n.d.*	Kraft	150	24	8	*n.d.*	Phenolic monomers: *n.d.*
7	[88]	10%Ni/HUSY	IWI	ethanol/water	Eucalyptus wood	Organosolv ethanol/water /formic acid	350	2	1	94	Phenolic monomers : *n.d.*
8	[89]	20%Ni/ZMS-5	IWI	ethanol (supercritical)	*n.d.*	Kraft	290	4	> 62	*n.d.*	Phenolic monomers : *n.d.*
9	[90]	15%Ni/C-SiO_2	WI	gas phase (H_2/ methanol)	Poplar wood	*n.d.*	190	3	60	*n.d.*	Phenolic monomers: *n.d.*
10	[7]	10%Ni/SBA-15	IWI	methanol	Birch sawdust	Organosolv ethanol/ benzene	200	6	1 (Ar)	27	Phenolic monomers: G5,S4

Table I.7: *Examples of reductive lignin depolymerization over Ni-based heterogeneous catalysts.*

11	[22]	2%Ni-3.6%Pd/SBA-15	IWI	isopropanol/ water	Birch	Sulfuric Acid extraction	245	8	5 (N_2)	*n.d.*	Phenolic monomers: S3,S4
12	[91]	19.5%Ni-20%Ru/SBA-15	IWI	ethanol	Wheat straw and sarkanda grass	Kraft	350	0.6	30	*n.d.*	Phenolic monomers: H1,G1,G3,S1
13	[6]	20%Ni/Al-SBA-15	WI	ethanol	Sorghum straw	Organosolv ethanol/water	300	4	10	90	Phenolic monomers: H1,G1,G2,G3
14	[67]	10%Ni/Al-SBA-15	Dry milling	formic acid	Olive tree pruning	Organosolv ethanol/water	140	0.5	*n.d.*	*n.d.*	Phenolic monomers: S1,S7,S9,G1, G8
15	[52]	10%Ni/Al-SBA-15	Dry milling	tetralin	Olive tree pruning	Organosolv ethanol/water	140	0.5	*n.d.*	*n.d.*	Phenolic monomers: S1,S7,S9,S10, G1, G8
16	[47]	10%Ni/MSN-Al	IWI	methanol	Beech sawdust	Organosolv ethanol/water	220	5	20	*n.d.*	Phenolic monomers: S1,S2,S3,S4, S5,S6,G1,G2,G3, G5,G6,G7
17	[92]	20%Ni/Al-SBA-15	IWI	ethanol	*n.d.*	Organosolv Ethanol/water	280	2	10	84.7	Phenolic monomers: *n.d.*

n.d.: not determined; LCNF: lignin-based carbon nanofiber, NDC: nitrogen doped carbon; IWI: incipient wetness impregnation; WI: wet impregnation; THFA: tetrahydrofuran.

Ni/C in methanol has been reported as an efficient catalyst for the conversion of wood lignin [93] and it has been reported that Fe can promote the hydrodeoxygenation without over-hydrogenation of aromatic rings. Inspired by this statement, Ni and Fe were co-precipitated by Zhai *et al.* to prepare non-precious bimetallic 5%Ni-5%Fe/AC catalyst. Such formulation achieved the highest total yield of monomers (23%) at 225°C, 20 bar H_2 and after 6 h (Table I.7, entry 1) in this study [23]. Si *et al.* (Table I.7, entry 2) [85] have treated a woody biomass with tetrahydrofurfuryl alcohol (THFA) and water to extract lignin. The latter was then converted into monomeric phenols (15% in yield) using 10%Ni/C at 220°C and 20 bar H_2 in a mixed solvent system THFA and 1,4-dioxane. In another work, 10%Ni-5%Cu/C was synthesized via incipient wetness impregnation and used as catalyst for the hydrogenolysis of poplar lignin in ethanol/isopropanol solvent. This bimetallic material compared to monometallic ones was found to be optimal for the conversion of lignin into phenolic monomers (yield of 63%) at 270°C for 4 h and without external H_2 (Table I.7, entry 3) [86]. 10%Ni/TiN, made from 20 nm Ni nanoparticles uniformly distributed and stable, was tested at 300°C under 10 bar of H_2 using ethanol, promoted the depolymerization of dealkaline lignin. In that case, aromatics with minimal cyclohexyl rings were produced giving rise to guaiacols (Table I.7, entry 4) [58].

Recently lignin-based carbon materials were also used as Ni supports for lignin depolymerization to produce aromatic platform chemicals. According to Du *et al.* Ni nanoparticles were inlaid in lignin-based carbon nanofibers (LCNF) to improve Ni stability and adjust its interaction with the support. The idea was to avoid Ni nanoparticles aggregation, sintering and loss during lignin depolymerization. After 5 h, about 91% of ethanol/water organosolv lignin from poplar wood were converted at 300°C and 10 bar H_2 with 10%Ni/LCNF catalyst and resulted in exceptionally high yields of light lignin fragments (87%) and phenols (7%) (Table I.7, entry 5) [87]. Nitrogen-doped carbons (NDC) can also be used as supports for the incorporation of Ni (32 wt.%) showing good activity for the degradation of lignin. Apparently, nitrogen would have a beneficial effect on the active Ni sites, enhancing catalytic activity and boosting the production of chemicals. Ni@NDC led to large quantities of aromatic molecules in ethanol under 8 bar of H_2 for 24 h at 150°C (Table I.7, entry 6) [53].

Zeolites are also reported to be efficient for depolymerization. The production of aromatics via the reductive organosolv lignin depolymerization process has been investigated over Ni/HUSY

catalysts using potassium formate/ethanol system (HCOOK/EtOH) under atmospheric pressure of H_2. It led to 17% yield of phenolic monomers with 94% conversion at 350°C after 1 h (Table I.7, entry 7). According to the authors, using HCOOK during the reaction not only produces *in-situ* hydrogen but also suppresses char formation and hinders fragmented species from condensation into heavier compounds [88]. Zhou *et al.* (Table I.7, entry 8) [89] have investigated the hydrogenolysis of alkali lignin in supercritical ethanol over Ni/ZSM-5. Lignin was converted into 39% phenolic monomers at 290°C under high H_2 pressure (>60 bar of H_2) after 4 h. The authors of this work also reported an improvement in the yield of products after adding phenol. They explained that phenol could promote the solubilization of both lignin and reaction products improving the depolymerization efficiency and suppressing the repolymerization of reactive intermediates formed in the depolymerization process.

Anderson *et al.* (Table I.7, entry 9) [90] have investigated the fractionation of lignin in a flowthrough reactor in gas phase while most reductive catalytic fractionation are conducted in a batch reactor in liquid phase. In their work, they added SiO_2 to 15%Ni/C prepared by wet impregnation method and tested the resulting solid as a catalyst at 190°C under 60 bar H_2 with a hydrogen flow rate of 50 mL min^{-1} and a methanol flow rate of 0.5 mL min^{-1}. Phenolic monomers were obtained with a 17% yield with the flow-based process which according to authors, enabled the acquisition of intrinsic kinetic and mechanistic data essential to better understand the lignin depolymerization process.

In the next part, some published works dealing with catalytic lignin valorization in liquid phase with Ni-based silica catalysts will be presented. Hence, it was demonstrated that 10%Ni/SBA-15, under 1 bar Ar and 200°C using methanol as an H-donor solvent, afforded 27% of lignin conversion into phenolic monomers (Table I.7, entry 10) [7]. A bimetallic catalyst 2%Ni-3.6%Pd/SBA-15 was efficient for the depolymerization of an acid-extracted birch lignin giving rise to 19% of monophenols 245 °C for 8 h, under 5 bar N_2 with isopropanol. According to the authors, the bimetallic catalysts which likely showed enhanced performances as compared with their parent metals because of the narrow distribution of Ni and Pd particles of small size (mean diameter of 2.7 nm) which would provide more contact opportunities between the active sites and substrates (Table I.7, entry 11) [22]. Kim *et al.* (Table I.7, entry 12) [91] also used a bimetallic catalyst 19.5%Ni-20%Ru/SBA-15 and supercritical ethanol with 30 bar of hydrogen gas at 350°C.

In that case, it was shown that this catalyst gave a high yield of phenol and monophenols (5% and 13% respectively) with a small char formation were obtained. According to the authors, this was consistent with the highest acidity and highest hydrogen desorption capacity of the bimetallic catalyst. Active hydrogen attacks the C-O or C-C bonds in lignin and suppresses recondensation reactions between lignin fragments, resulting in the increased yields of monomeric phenols. The addition of Al and Ni elements in SBA-15 could improve the lignin depolymerization performance, enhance the yield of phenolic monomers, and produce less char, this is why in the work of Chen *et al*. 20%Ni/Al-SBA-15 was synthesized and used for lignin depolymerization. In that work, the moderate acidity of the catalyst (Si/Al = 20) could promote the cleavage of main linkages (β-O-4, α-O-4 ether bonds) in lignin to monomeric units. Indeed, it has been reported that repolymerization of the phenolic dimer and oligomer could be promoted significantly over strong acid catalyst [6]. At 300ºC and under 10 bar of H_2, no char was generated and 22% of phenolic monomers were produced using 20%Ni/Al-SBA-15 in ethanol. The latter was found to be more effective in suppressing repolymerization than other solvents (Table I.7, entry 13). It is noteworthy that the degree of lignin depolymerization and the yield of phenolic monomers gradually declined with the increase of Al content. Lignin depolymerization to simple aromatics was investigated by using a mild microwave-assisted approach, and Ni nanoparticles supported on Al-SBA-15 (10 wt.%. Ni). In this study, the microwave power was set constant at 400 W over 30 min, and the reaction reached an average temperature of 140ºC. A high yield of phenolic monomers (17%) but also a high char yield (38%) were obtained using tetralin as hydrogen donor solvent. The advantage of tetralin is related to the formation of naphthalene as stable product which does not interfere in lignin hydrogenolysis. Formic acid which was also used as H-donor, led to an almost double product yield (30%) (Table I.7, entries 14 and 15) [52,67].

Ni/MSN-Al prepared by Si *et al*. (Table I.7, entry 16) [47] and used for the hydrogenolysis of GGE, was also used for the depolymerization of organosolv lignin from beech sawdust. Under 20 bar H_2, at 220ºC and after 5 h, all β-O-4 linkages were completely cleaved and the total yield of phenolic monomers reached 31%. According to the authors, Ni/MSN-Al catalyst exhibited excellent catalytic activity due to the presence of defects in the support as already mentioned in the depolymerization of the lignin model compound (GGE) (Table I.4, entry 11). In order to promote an efficient dispersion of Ni species over mesoporous supports, an addition of ethylene glycol (EG) has been done during the loading process. 20%Ni/Al-SBA-15 with Ni/EG molar ratio

of 1:1, where Ni species were evenly distributed exhibited excellent catalytic performance in lignin depolymerization in ethanol at 280ºC for 4 h. A monomer yield of 22% was achieved and no char was observed (Table I.7, entry 17) [92].

According to all aforementioned examples, results showed that the repolymerization was effectively suppressed over SBA-15 due to its well-ordered pore structure and large pore size. Pineda *et al.* wrote that the presence of larger NP sizes (~40 nm) may be convenient for depolymerization due to an improved interaction of the metal sites with lignin due to the bulky structure of lignin (with the possibility of the metal nanoparticles to target various hydrogenolytic neighboring sites of the complex lignin molecule) [94].

I.5. Repolymerization and char formation

Significant and serious char formation occurred in a big part of lignin depolymerization processes. The main reason is the repolymerizing and self-condensing ability of lignin that negatively affects the yields of lignin monomers [95–101]. Although side reactions are highly dependent on the reaction environment, the catalysts, and the quality of lignin, they are very difficult to avoid. Many strategies were applied for suppressing repolymerization of lignin such as adding capping agents, decreasing the reaction temperature and finally using mesoporous catalysts supports.

Condensation and repolymerization of lignins can be prevented by trapping reactive intermediates during its extraction or its depolymerization by chemically stabilizing the β-O-4 structure or physically removing lignin fragments from the reactor [102].

Stabilization of lignin with external agents by chemical reaction with aldehydes, ethylene glycol or 1,4 butanediol) during its extraction has shown to enhance the depolymerization efficiency. Furthermore, functionalization of lignin aromatic monomers is needed for some applications. As a major example, the amination of lignin depolymerization products stands as a hot research topic [95]. Figure I.9 shows the reactive sites in lignin structure and possible functionalization reactions at the aromatic ring, at the phenolic groups, and at aliphatic chains of lignin units.

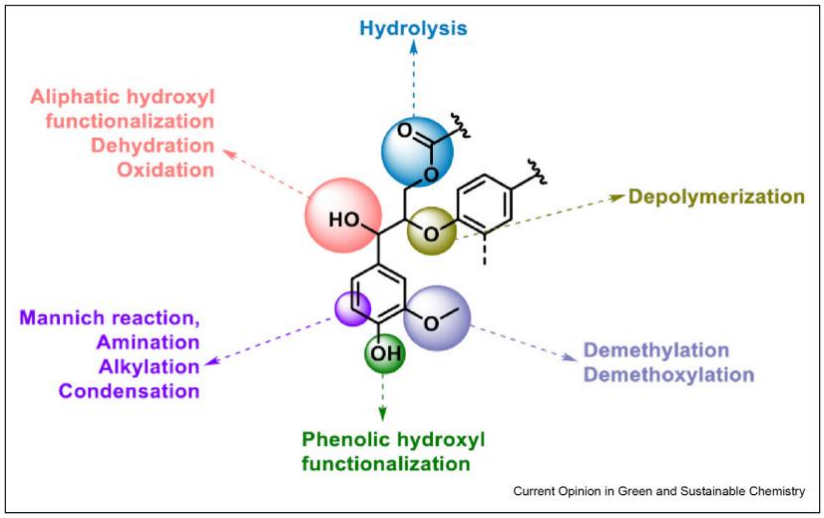

Figure I.9: *Reactive sites and possible functionalization reactions for lignin macromolecules or lignin aromatic products after depolymerization [95].*

Chemoselective blocking of the phenolic hydroxyl (Ar−OH) group by methylation (dimethyl sulfate) was found to suppress secondary repolymerization and charring during lignin depolymerization. Indeed, methylation of Ar−OH prevents formation of reactive quinone methide intermediates, which are partly responsible for undesirable secondary repolymerization reactions [103]. Boric acid also protects the Ar-OH groups by formation of boric ester, hence stabilizing the intermediates or reactive sites of lignin fragments [104,105]. A renewable capping agent derived from hemicellulose mainly composed of hydroxymethylfurfural and furfural was efficient not only in terms of increasing phenolic oil production but also in maximizing the monomeric phenolic compounds concentration and minimizing the undesired by-products yield [106].

Temperature plays a major role in maintaining the balance between depolymerization and repolymerizations reactions. At high temperatures, one of the main reactions responsible for lignin decomposition is homolytic cleavage resulting in free radical species which can either repolymerize or undergo hydrogen abstraction to form stable compounds. Products can become complex with carbon partitioning to coke [107].

Klamrassamee *et al.* claimed that the mesoporous catalysts would give less char in the depolymerization of lignin [108–110]. Based on steric constraints, well-ordered pore structure and large pore sizes could prevent the repolymerization of highly reactive intermediates. It appears that

the molecules produced during lignin depolymerization could be able to penetrate the interior of the support suppressing the char formation [6].

I.6. Conclusion

The depolymerization of lignin over Ni-based catalysts has been regarded as an efficient protocol to produce high-valued aromatic monomers. It has received extensive attention but comparisons are difficult due to the heterogeneity of lignin structures.

The use of different supports such as carbon, zeolite, silica, and mesoporous silica, in addition to many other parameters, including temperature, solvent, gas pressure can greatly affect the catalyst performance and its activity. Most of the works were carried out in liquid phase with alcohol as solvent in a hydrogen atmosphere at a reaction temperature range between 80°C and 250°C for lignin model compounds and from 140°C to 350°C for real lignin. Fewer hydrogenolysis processes were conducted under an inert atmosphere with hydrogen donor.

It was demonstrated for lignin model compounds bearing α-O-4 or β-O-4 linkages that a β-O-4 model compound is more difficult to cleave. The model bearing a 4-O-5 bond has the highest BDE, therefore its C-O bond cleavage has been reported to be usually challenging requiring severe conditions.

Among the interesting catalytic systems, we have noticed that described by Si *et al.* These authors developed immobilized Ni clusters highly dispersed inside the channel of mesoporous aluminosilica nanospheres (MSN-Al) which facilitated the hydrogenolysis of guaiacylglycerol-β-guaiacyl ether (GGE, β-O-4) at 180°C, with a molar substrate/metal ratio of 7.3, under 20 bar H_2 which only after 2 h led to a high yield of phenolic monomers (79%). In the same paper, it was also reported that all β-O-4 linkages of Organosolv lignin were completely depolymerized at 220°C and 20 bar H_2. Unfortunately, this work was not done with an H-donor.

Two main concerns should always be taken into consideration during lignin depolymerization *i.e.,* the char formation and the repolymerization of the monomers and of the lignin chains. Some results have shown that the repolymerization and the char formation were effectively suppressed over mesostructured silica supports due to its well-ordered pore structure and large pore size.

In this manuscript, two preparation methods to get well dispersed Ni over pure silica will be presented. The first one is based on the impregnation of a pre-formed Aerosil 380 with aqueous ammonia, easy to perform but without any control of porosity. The second one corresponds to a one pot incorporation of Ni in mesoporous silica where porosity can be easily controlled. Both type of materials were tested previously in our lab in Dry Reforming of Methane (DRM) reaction showing comparable high catalytic performance and stability at 650ºC [111,112]. However, DRM involves small molecules of reactants, therefore, lignin depolymerization is a better test to distinguish the two kinds of catalysts.

References

[1] C. Li, X. Zhao, A. Wang, G. W. Huber, T. Zhang, *Chem. Rev.* **2015**, *115*, 11559–11624.
[2] R. A. Sheldon, *Green Chem.* **2014**, *16*, 950–963.
[3] F. G. Calvo-flores, J. A. Dobado, *ChemSusChem* **2010**, *3*, 1227–1235.
[4] D. Stewart, *Ind. Crops Prod.* **2008**, *27*, 202–207.
[5] C. A. Gasser, G. Hommes, A. Schäffer, P. F.-X. Corvini, *Appl. Microbiol. Biotechnol.* **2012**, *95*, 1115–1134.
[6] P. Chen, Q. Zhang, R. Shu, Y. Xu, L. Ma, T. Wang, *Bioresour. Technol.* **2017**, *226*, 125–131.
[7] Q. Song, F. Wang, J. Cai, Y. Wang, J. Zhang, W. Yu, J. Xu, *Energy Environ. Sci.* **2013**, *6*, 994–1007.
[8] S. F. Koelewijn, S. Van Den Bosch, T. Renders, W. Schutyser, B. Lagrain, M. Smet, J. Thomas, W. Dehaen, P. Van Puyvelde, H. Witters, B. F. Sels, *Green Chem.* **2017**, *19*, 2561–2570.
[9] M. Wang, F. Wang, *Adv. Mater.* **2019**, *31*, 1–18.
[10] L. Yang, K. Seshan, Y. Li, *Catal. Today* **2017**, *298*, 276–297.
[11] I. Hita, P. J. Deuss, G. Bonura, F. Frusteri, H. J. Heeres, *Fuel Process. Technol.* **2018**, *179*, 143–153.
[12] Q. Song, F. Wang, J. Xu, *Chem. Commun.* **2012**, *48*, 7019–7021.
[13] D. Bourbiaux, J. Pu, F. Rataboul, L. Djakovitch, C. Geantet, D. Laurenti, *Catal. Today* **2021**, *373*, 24–37.
[14] S. Rautiainen, D. Di Francesco, S. N. Katea, G. Westin, D. N. Tungasmita, J. S. M. Samec, *ChemSusChem* **2019**, *12*, 404–408.
[15] C. Zhu, J. P. Cao, X. Y. Zhao, T. Xie, J. Ren, X. Y. Wei, *J. Energy Inst.* **2019**, *92*, 74–81.
[16] X. Chen, W. Guan, C. W. Tsang, H. Hu, C. Liang, *Catalysts* **2019**, *9*, 488–527.
[17] Q. Song, J. Cai, J. Zhang, W. Yu, F. Wang, J. Xu, *Chinese J. Catal.* **2013**, *34*, 651–658.
[18] J. Zhang, J. Teo, X. Chen, H. Asakura, T. Tanaka, K. Teramura, N. Yan, *ACS Catal.* **2014**, *4*, 1574–1583.
[19] J. W. Zhang, Y. Cai, G. P. Lu, C. Cai, *Green Chem.* **2016**, *18*, 6229–6235.
[20] J. Zhang, H. Asakura, J. Van Rijn, J. Yang, P. Duchesne, B. Zhang, X. Chen, P. Zhang, M. Saeys, N. Yan, *Green Chem.* **2014**, *16*, 2432–2437.
[21] C. Zhu, J. P. Cao, X. Y. Zhao, T. Xie, M. Zhao, X. Y. Wei, *Fuel Process. Technol.* **2019**, *194*, 106126.
[22] B. Jiang, J. Hu, Y. Qiao, X. Jiang, P. Lu, *Energy and Fuels* **2019**, *33*, 8786–8793.
[23] Y. Zhai, C. Li, G. Xu, Y. Ma, X. Liu, Y. Zhang, *Green Chem.* **2017**, *19*, 1895–1903.
[24] S. Qiu, M. Li, Y. Huang, Y. Fang, *Ind. Eng. Chem. Res.* **2018**, *57*, 2023–2030.
[25] M. Nowosielska, W. K. Jozwiak, J. Rynkowski, *Catal. Letters* **2009**, *128*, 83–93.
[26] W. K. Jóźwiak, M. Nowosielska, J. Rynkowski, *Appl. Catal. A Gen.* **2005**, *280*, 233–244.
[27] Y. Mao, L. Zhang, X. Zheng, W. Liu, Z. Cao, H. Peng, *Int. J. Hydrogen Energy* **2023**, *48*, 13890–13901.
[28] B. Xia, N. Cao, H. Dai, J. Su, X. Wu, W. Luo, G. Cheng, *ChemCatChem* **2014**, *6*, 2549–2552.
[29] J. Chen, Q. Yao, J. Zhu, X. Chen, Z. H. Lu, *Int. J. Hydrogen Energy* **2016**, *41*, 3946–3954.
[30] H. Duan, D. Wang, Y. Kou, Y. Li, *Chem. Commun.* **2013**, *49*, 303–305.
[31] Y. Wang, H. Arandiyan, S. A. Bartlett, A. Trunschke, H. Sun, J. Scott, A. F. Lee, K. Wilson, T. Maschmeyer, R. Schlögl, R. Amal, *Appl. Catal. B Environ.* **2020**, *277*, 1–23.
[32] P. Mirzaei, S. Bastide, A. Dassy, R. Bensimon, J. Bourgon, A. Aghajani, C. Zlotea, D. Muller-Bouvet, C. Cachet-Vivier, *Electrochim. Acta* **2019**, *297*, 715–724.
[33] K. E. Achyuthan, A. M. Achyuthan, P. D. Adams, S. M. Dirk, J. C. Harper, B. A. Simmons, A. K. Singh,

Molecules **2010**, *15*, 8641–8688.
[34] W. Schutyser, T. Renders, G. Van den Bossche, S. Van den Bosch, S.-F. Koelewijn, T. Ennaert, B. F. Sels, *Nanotechnol. Catal.* **2017**, *23*, 537–584.
[35] J. Zakzeski, P. C. A. Bruijnincx, A. L. Jongerius, B. M. Weckhuysen, *Chem. Rev.* **2010**, *110*, 3552–3599.
[36] M. Oregui-Bengoechea, I. Agirre, A. Iriondo, A. Lopez-Urionabarrenechea, J. M. Requies, I. Agirrezabal-Telleria, K. Bizkarra, V. L. Barrio, J. F. Cambra, *Lignin Chem.* **2019**, *377*, 197–271.
[37] J. Ruwoldt, *Surfaces* **2020**, *3*, 622–648.
[38] J. Gierer, *Wood Sci. Technol.* **1980**, *14*, 241–266.
[39] M. López, O. Huerta-Pujol, F. X. Martínez-Farré, M. Soliva, *Resour. Conserv. Recycl.* **2010**, *55*, 171–181.
[40] A. Abdulkhani, A. Karimi, A. Mirshokraie, Y. Hamzeh, N. Marlin, G. Mortha, *J. Appl. Polym. Sci.* **2010**, *118*, 469–479.
[41] X. Pan, N. Gilkes, J. Kadla, K. Pye, S. Saka, D. Gregg, K. Ehara, D. Xie, D. Lam, J. Saddler, *Biotechnol. Bioeng.* **2006**, *94*, 851–861.
[42] A. Rodríguez, R. Sánchez, A. Requejo, A. Ferrer, *J. Clean. Prod.* **2010**, *18*, 1084–1091.
[43] J. B. Binder, M. J. Gray, J. F. White, Z. C. Zhang, J. E. Holladay, *Biomass and Bioenergy* **2009**, *33*, 1122–1130.
[44] S. Kannan, P. Arumugam, G. Govindasamy, *J. Porous Mater.* **2023**, *30*, 639–653.
[45] H. W. Park, S. Park, D. R. Park, J. H. Choi, I. K. Song, *Catal. Commun.* **2010**, *12*, 1–4.
[46] B. M. Matsagar, T. C. Kang, Z. Y. Wang, T. Yoshikawa, Y. Nakasaka, T. Masuda, L. C. Chuang, K. C. W. Wu, *React. Chem. Eng.* **2019**, *4*, 618–626.
[47] X. Si, J. Chen, F. Lu, X. Liu, Y. Ren, R. Lu, H. Jiang, H. Liu, C. Miao, Y. Zhu, X. Luo, J. Xu, *ACS Sustain. Chem. Eng.* **2019**, *7*, 19034–19041.
[48] M. Wang, J. Lu, X. Zhang, L. Li, H. Li, N. Luo, F. Wang, *ACS Catal.* **2016**, *6*, 6086–6090.
[49] N. Luo, M. Wang, H. Li, J. Zhang, H. Liu, F. Wang, *ACS Catal.* **2016**, *6*, 7716–7721.
[50] X. Wu, N. Luo, S. Xie, H. Zhang, Q. Zhang, F. Wang, Y. Wang, *Chem. Soc. Rev.* **2020**, *49*, 6198–6223.
[51] K. Yang, X. Chen, G. Lafaye, C. Especel, F. Epron, C. Liang, *ChemistrySelect* **2018**, *3*, 11398–11405.
[52] A. Toledano, L. Serrano, A. Pineda, A. A. Romero, R. Luque, J. Labidi, *Appl. Catal. B Environ.* **2014**, *145*, 43–55.
[53] S. M. G. Lama, J. Pampel, T. P. Fellinger, V. P. Beškoski, L. Slavković-Beškoski, M. Antonietti, V. Molinari, *ACS Sustain. Chem. Eng.* **2017**, *5*, 2415–2420.
[54] M. Wang, X. Zhang, H. Li, J. Lu, M. Liu, F. Wang, *ACS Catal.* **2018**, *8*, 1614–1620.
[55] C. Zhu, J. P. Cao, T. Xie, X. Y. Zhao, X. Cui, Z. X. Guo, W. Z. Shen, J. Bai, X. Y. Wei, *Energy Technol.* **2019**, *7*, 1800694.
[56] T. Xie, J. P. Cao, C. Zhu, X. Y. Zhao, M. Zhao, Y. P. Zhao, X. Y. Wei, *Fuel Process. Technol.* **2019**, *188*, 190–196.
[57] J. Guo, Y. L. Ma, J. Y. Yu, Y. J. Gao, N. X. Ma, X. Y. Wu, *BMC Chem.* **2019**, *13*, 1–15.
[58] L. L. Bie, F. J. Liu, Z. M. Zong, G. H. Liu, J. P. Guo, Z. X. Li, Z. H. Ma, W. W. Yan, X. Y. Wei, *Fuel Process. Technol.* **2020**, *209*, 106523.
[59] J. He, C. Zhao, J. A. Lercher, *J. Am. Chem. Soc.* **2012**, *134*, 20768–20775.
[60] J. He, L. Lu, C. Zhao, D. Mei, J. A. Lercher, *J. Catal.* **2014**, *311*, 41–51.
[61] A. W. Tricker, S. Najmi, E. V. Phillips, K. L. Hebisch, J. X. Kang, C. Sievers, *RSC Sustain.* **2023**, *1*, 346–356.
[62] G. Zhu, X. Ouyang, L. Jiang, Y. Zhu, D. Jin, Y. Pang, X. Qiu, *Fuel Process. Technol.* **2016**, *154*, 132–138.
[63] S. Chen, Q. Lu, W. Han, P. Yan, H. Wang, W. Zhu, *Fuel* **2021**, *283*, 119333.
[64] S. Bulut, S. Siankevich, A. P. Van Muyden, D. T. L. Alexander, G. Savoglidis, J. Zhang, V. Hatzimanikatis, N. Yan, P. J. Dyson, *Chem. Sci.* **2018**, *9*, 5530–5535.
[65] G. Zhu, X. Qiu, Y. Zhao, Y. Qian, Y. Pang, X. Ouyang, *Bioresour. Technol.* **2016**, *218*, 718–722.
[66] J. Zakzeski, A. L. Jongerius, P. C. A. Bruijnincx, B. M. Weckhuysen, *ChemSusChem* **2012**, *5*, 1602–1609.
[67] A. Toledano, L. Serrano, J. Labidi, A. Pineda, A. M. Balu, R. Luque, *ChemCatChem* **2013**, *5*, 977–985.
[68] M. A. Hossain, T. Saelee, S. Tulaphol, M. S. Rahaman, T. K. Phung, T. Maihom, P. Praserthdam, S. Praserthdam, D. J. Yelle, N. Sathitsuksanoh, *ChemCatChem* **2022**, *14*, e202200549.
[69] X. Besse, Y. Schuurman, N. Guilhaume, *Appl. Catal. B Environ.* **2017**, *209*, 265–272.
[70] C. Xu, S. F. Tang, X. Sun, Y. Sun, G. Li, J. Qi, X. Li, X. Li, *Catal. Today* **2017**, *298*, 89–98.
[71] Y. Song, *Chem. Catal. Biomass Upgrad.* **2019**, 395–437.
[72] H. Tan, X. Li, H. Ma, X. Yang, T. Zhan, W. Xie, S. Wang, J. Zhu, *Sustain. Energy Fuels* **2022**, *6*, 2745–2754.
[73] Z. P. Fu, Y. P. Zhao, F. P. Wu, J. X. Xie, L. Le Qiu, J. Xiao, J. Liang, Y. H. Bai, F. J. Liu, J. P. Cao, *Mol.*

Catal. **2023**, *547*, 113334.
[74] W. Jiang, J. P. Cao, C. Zhu, T. Xie, X. Y. Zhao, M. Zhao, Y. P. Zhao, H. C. Bai, *Fuel* **2021**, *295*, 120635.
[75] W. Wu, H. Liu, H. Wu, B. Zheng, S. Han, K. Zhang, X. Mei, C. Xu, M. He, B. Han, *ACS Sustain. Chem. Eng.* **2021**, *9*, 11862–11871.
[76] C. Zhang, H. Li, J. Lu, X. Zhang, K. E. Macarthur, M. Heggen, F. Wang, *ACS Catal.* **2017**, *7*, 3419–3429.
[77] C. Zhang, J. Lu, X. Zhang, K. Macarthur, M. Heggen, H. Li, F. Wang, *Green Chem.* **2016**, *18*, 6545–6555.
[78] J. Zhang, N. Yan, *Part. Part. Syst. Charact.* **2016**, *33*, 610–619.
[79] J. X. Xie, J. P. Cao, X. Y. Zhao, W. Jiang, L. Zhao, M. Zhao, H. C. Bai, *Energy and Fuels* **2021**, *35*, 9599–9608.
[80] J. He, C. Zhao, D. Mei, J. A. Lercher, *J. Catal.* **2014**, *309*, 280–290.
[81] B. Güvenatam, O. Kurşun, E. H. J. Heeres, E. A. Pidko, E. J. M. Hensen, *Catal. Today* **2014**, *233*, 83–91.
[82] C. Zhao, J. A. Lercher, *ChemCatChem* **2012**, *4*, 64–68.
[83] B. Jacobs, I. Van Nieuwenhove, J. Lauwaert, T. De Saegher, J. Gracia-Vitoria, K. Vanbroekhoven, T. Renders, T. De Roo, J. De Clercq, A. Verberckmoes, *Waste and Biomass Valorization* **2023**, *14*, 1447–1460.
[84] A. Achour, D. Bernin, D. Creaser, L. Olsson, *Chem. Eng. J.* **2023**, *453*, 139829.
[85] X. Si, F. Lu, J. Chen, R. Lu, Q. Huang, H. Jiang, E. Taarning, J. Xu, *Green Chem.* **2017**, *19*, 4849–4857.
[86] C. Cheng, P. Li, W. Yu, D. Shen, X. Jiang, S. Gu, *ACS Sustain. Chem. Eng.* **2020**, *8*, 16217–16228.
[87] B. Du, C. Liu, X. Wang, Y. Han, Y. Guo, H. Li, J. Zhou, *Renew. Energy* **2020**, *147*, 1331–1339.
[88] W. Wanmolee, J. N. Beltramini, L. Atanda, J. P. Bartley, N. Laosiripojana, W. O. S. Doherty, *ACS Omega* **2019**, *4*, 16980–16993.
[89] M. Zhou, B. K. Sharma, P. Liu, J. Ye, J. Xu, J. C. Jiang, *ACS Sustain. Chem. Eng.* **2018**, *6*, 6867–6875.
[90] E. M. Anderson, M. L. Stone, R. Katahira, M. Reed, G. T. Beckham, Y. Román-Leshkov, *Joule* **2017**, *1*, 613–622.
[91] J. Y. Kim, S. Y. Park, I. G. Choi, J. W. Choi, *Chem. Eng. J.* **2018**, *336*, 640–648.
[92] Y. Xu, P. Chen, W. Lv, C. Wang, L. Ma, Q. Zhang, *Chinese J. Chem. Eng.* **2021**, *32*, 307–314.
[93] I. Klein, B. Saha, M. M. Abu-Omar, *Catal. Sci. Technol.* **2015**, *5*, 3242–3245.
[94] A. Pineda, A. F. Lee, *Appl. Petrochemical Res.* **2016**, *6*, 243–256.
[95] A. M. da Costa Lopes, A. J. D. Silvestre, J. A. P. Coutinho, *Curr. Opin. Green Sustain. Chem.* **2023**, *43*, 1–6.
[96] J. B. Binder, M. J. Gray, J. F. White, Z. C. Zhang, J. E. Holladay, *Biomass and Bioenergy* **2009**, *33*, 1122–1130.
[97] Z. Fang, T. Sato, R. L. Smith, H. Inomata, K. Arai, J. A. Kozinski, *Bioresour. Technol.* **2008**, *99*, 3424–3430.
[98] Wahyudiono, M. Sasaki, M. Goto, *Chem. Eng. Process. Process Intensif.* **2008**, *47*, 1609–1619.
[99] J. Long, Q. Zhang, T. Wang, X. Zhang, Y. Xu, L. Ma, *Bioresour. Technol.* **2014**, *154*, 10–17.
[100] J. M. Lavoie, W. Baré, M. Bilodeau, *Bioresour. Technol.* **2011**, *102*, 4917–4920.
[101] R. Shu, Q. Zhang, L. Ma, Y. Xu, P. Chen, C. Wang, T. Wang, *Bioresour. Technol.* **2016**, *221*, 568–575.
[102] W. Lan, J. S. Luterbacher, *Chimia (Aarau).* **2019**, *73*, 591–598.
[103] K. H. Kim, T. Dutta, E. D. Walter, N. G. Isern, J. R. Cort, B. A. Simmons, S. Singh, *ACS Sustain. Chem. Eng.* **2017**, *5*, 3913–3919.
[104] A. Toledano, L. Serrano, J. Labidi, *Fuel* **2014**, *116*, 617–624.
[105] K. H. Kim, C. S. Kim, *Front. Energy Res.* **2018**, *6*, 1–7.
[106] F. Hernández-Ramos, J. Fernández-Rodríguez, M. G. Alriols, J. Labidi, X. Erdocia, *Fuel* **2020**, *280*, 118524.
[107] V. Patil, S. Adhikari, P. Cross, H. Jahromi, *Renew. Sustain. Energy Rev.* **2020**, *133*, 1–66.
[108] T. Klamrassamee, N. Laosiripojana, D. Cronin, L. Moghaddam, Z. Zhang, W. O. S. Doherty, *Bioresour. Technol.* **2015**, *180*, 222–229.
[109] Y. Zhu, H. Li, J. Xu, H. Yuan, J. Wang, X. Li, *CrystEngComm* **2011**, *13*, 402–405.
[110] D. Gao, A. Duan, X. Zhang, Z. Zhao, H. E, J. Li, H. Wnag, *Appl. Catal. B Environ.* **2015**, *165*, 269–284.
[111] O. Daoura, G. Fornasieri, M. Boutros, N. El Hassan, P. Beaunier, C. Thomas, M. Selmane, A. Miche, C. Sassoye, O. Ersen, W. Baaziz, P. Massiani, A. Bleuzen, F. Launay, *Appl. Catal. B Environ.* **2021**, *280*, 119417.
[112] O. Daoura, N. El Hassan, M. Boutros, S. Casale, P. Massiani, F. Launay, *ACS Appl. Nano Mater.* **2022**, *5*, 18048–18059.

Chapter II

Study of the catalytic activity in hydrogenolysis of metal catalysts obtained by impregnation of Aerosil 380 in the presence of NH_3

II-1. Introduction

The part A of this chapter will focus on the hydrogenolysis of two compounds, *i.e.*, 2-phenoxy-1-phenylethanone and 2-phenoxy-1-phenylethanol in the presence of isopropanol as an H-donor solvent, at 180°C and under N_2 atmosphere, using Ni-, Rh- or Ni/Rh- based catalysts obtained by the impregnation of Aerosil 380 in the presence of NH_3. In this study, mainly the reaction time, the reduction temperature of Ni(II) and the molar substrate/metal ratio were the three parameters investigated. In this preparation method, Ni(II) forms phyllosilicates. The question that arises was: Is the formation of phyllosilicates related to the metal itself (Ni or Rh) or to the counterion used in the metal precursor during the synthesis? To answer, additional investigations were performed over monometallic Ni- and Rh-based Aerosil 380 using chloride or nitrate as precursors. In a last section, efforts have also been made to improve the phenol selectivity using Fe as doping agent.

Part B, will further investigate the surface composition of three bimetallic Ni/Rh-based samples used as catalysts in part A by an innovative methodology based on O_2 chemisorption and H_2-O_2 titration experiments.

Finally, in part C, a better mimic of β-O-4 linkage in lignin, *i.e.*, guaiacylglycerol-β-guaiacyl ether will be used for the hydrogenolysis reaction. Preliminary tests will also be conducted using an Organosolv lignin sample.

Chapter II – Part A1: Controlling C-OAryl hydrogenolysis vs aryl hydrogenation in lignin model depolymerization using Ni-, Rh- or Ni/Rh- based silica catalysts

This part focuses on the hydrogenolysis of 2-phenoxy-1-phenylethanone, modelling a pre-oxidized form of lignin using five catalysts of similar metal content, prepared by impregnation of Ni(II), Rh(III) and both metals onto Aerosil 380 in the presence of NH_3, followed by a reduction step. The materials were characterized in the dried *as-synthesized* state and after consecutive reductive and oxidative treatments, showing the great dispersion of the metal (oxide nanoparticles with sizes < 2 nm). Working with 1 mol% of the reduced metal (500°C) per substrate at 180°C with isopropanol as H-donor, the most active catalyst, but also the least selective towards phenol, was initially found to be the Ni-based one. Under similar conditions, the lower capacity of the Rh-based catalyst to induce H transfer from isopropanol favored phenol formation but resulted in much slower C-OAr cleavage. Despite a very high dispersion of the two metals in the bimetallic catalysts, no synergy was found, suggesting that Ni would be segregated at the surface. Finally, the best phenol productivity could be reached by reducing the Ni-based catalyst at 650°C, which led to a more efficient cleavage of C-OAr bonds. In this way, it was possible to produce 8 times more phenol per hour.

This part "A1" corresponds to a published article in ChemCatChem journal. Parts A2-1 and A2-2 correspond to additional studies.

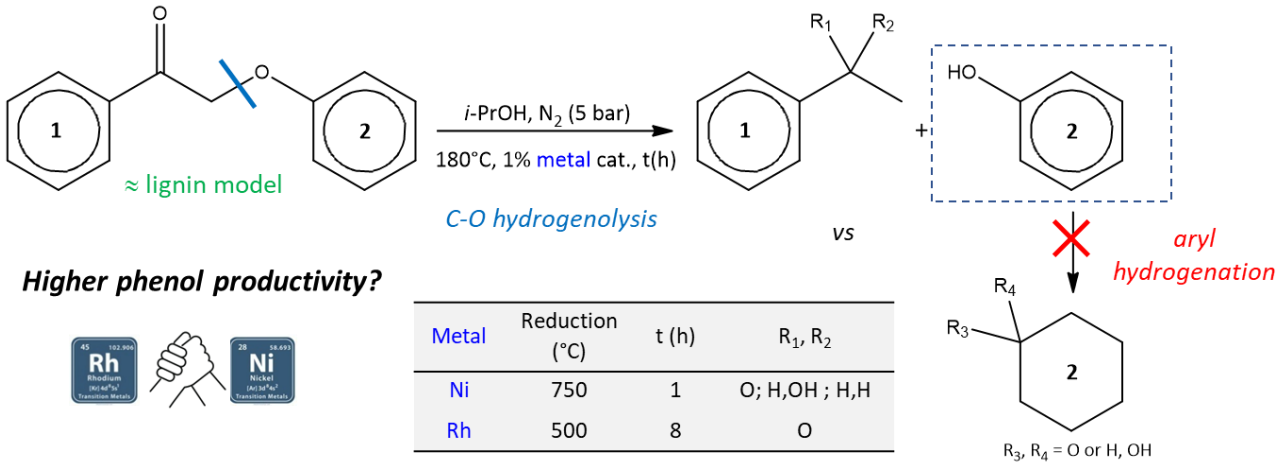

Metal	Reduction (°C)	t (h)	R_1, R_2
Ni	750	1	O; H,OH ; H,H
Rh	500	8	O

II-A1.1. Introduction

Due to the complexity and variability of lignin, most of the research on the design of catalysts for reductive depolymerization in the presence of H_2 or H-donor molecules [1] is carried out on model compounds, for example 2-phenoxy-1-phenylethanone ($K1_{HH}$) (Figure II-A.1) which mimics pre-oxidized lignin bearing C_β-O bonds with a lower dissociation energy than those of lignin [2–9]. Hydrogenolysis, hydrogenation and dehydrogenation are likely to occur (Figure II-A.1).

Hence $K1_{HH}$ can be cleaved directly into monomers (acetophenone and expected phenol) through C-O hydrogenolysis or can be transformed, by hydrogenation, to $A1_{HH}$, the latter being converted into $C1_{HH}$ through hydrogenolysis. Also, $A1_{HH}$ or $C1_{HH}$ can be cleaved into monomers through hydrogenolysis, affording 1-phenylethanol or ethylbenzene, and phenol in both cases. Last but not least, hydrogenation of the aromatic rings may occur, being responsible in particular for the conversion of phenol into cyclohexanone or cyclohexanol.

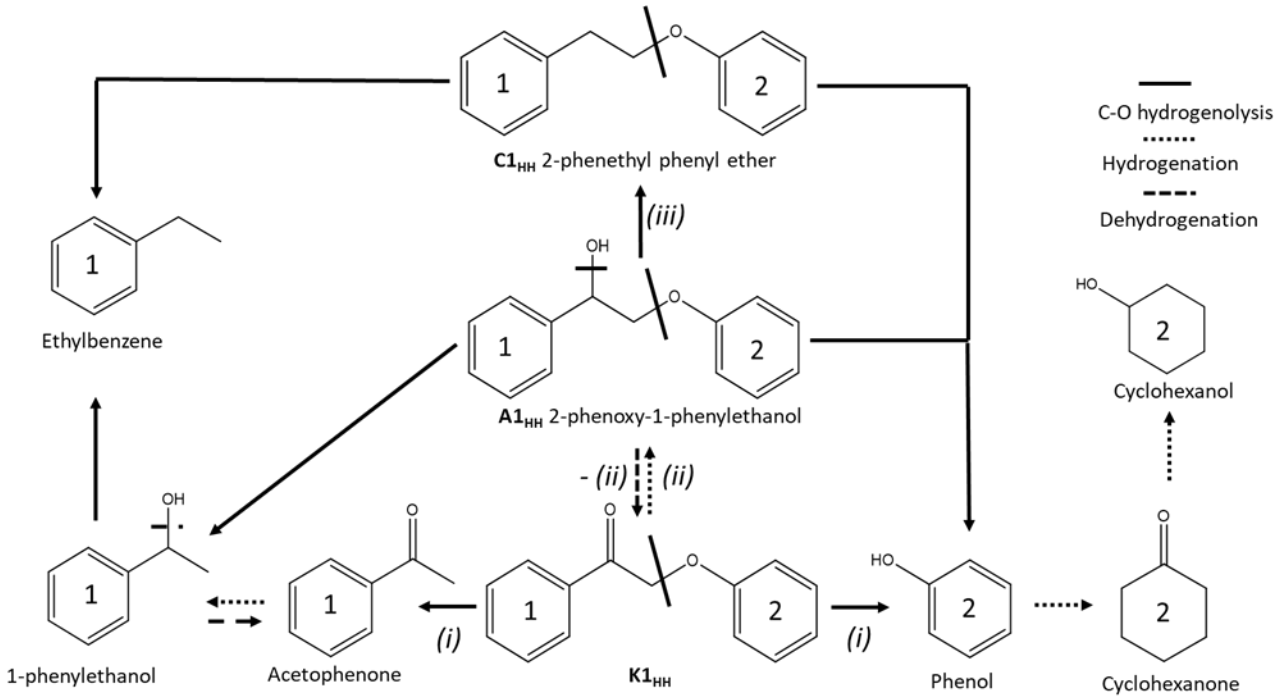

Figure II-A.1: *Main products expected from $K1_{HH}$ under reducing conditions.*

Reductive depolymerization of lignin and its models is often performed with heterogeneous catalysts based on noble metals which are often involved (Ru, Rh, Pt, Pd) [10], but other transition metals [11] are interesting too, *i.e.*, Ni [12]. With Ni, a lot of strategies have been adopted to enhance the cleavage of the ether bond at the expense of phenol hydrogenation. In the present chapter, we have retained the use of hydrogen donors instead of H_2 and Ni and/or Rh-based catalysts and have decided to use a simple and efficient method for catalyst preparation starting with a commercially available silica support [13–15].

In heterogeneous catalysis, materials with high specific area, and very often, catalysts preparation methods favoring metal dispersion despite rather high metal contents, with sometimes confinement effects are targeted. Considering the use of nickel for the hydrogenolysis of lignin and its model compounds, many preparation approaches have been developed. Low-cost and not time-consuming strategies such as, incipient wetness impregnation [13,16], deposition-precipitation [17,18], dry mechanochemical [19,20], *etc. ...* should be adopted but are not favoring systematically high Ni dispersion. Methodologies aiming at introducing the metal precursor in the synthesis gel of the support, especially used in the case of silica ("One-pot preparation"), *e.g.* SBA-15, were reported by some of us to be promising strategies in order to generate highly stable silica-based catalysts for dry reforming of methane (DRM), but could be considered difficult to perform at industrial scale [21]. Indeed, specific protocols using the less possible amount of water (formation of SBA-15 type monoliths [21]) or involving a pH adjustment step, by adding aqueous ammonia in the acidic synthesis gel of SBA-15, before the hydrothermal treatment [22,23] had to be implemented. More simply, our group has shown recently that it is possible to obtain silica-based catalysts with nickel dispersions as good (*c.a.* 40%) as those obtained using the one-pot method with a minimum of water [21], just by impregnating a commercial silica, such as Aerosil 380, which is characterized by a smaller specific surface area compared to SBA-15 silica, in the presence of NH_3[24]. In these conditions, Ni phyllosilicates were formed, ensuring strong interactions of Ni^{2+} cations with the support at the origin of the formation of small-sized Ni(0) nanoparticles upon reduction with a good resistance to aggregation and sintering in the harsh conditions implemented for DRM. The question here is "what about the activity of those nanoparticles in the liquid-solid hydrogenolysis of lignin model compounds under reducing atmosphere?".

A survey of the recent literature concerning the hydrogenolysis of $K1_{HH}$ in the presence of Ni shows that this reaction has been carried out in the presence of heterogeneous catalysts involving different supports (Al_2O_3-SiO_2 [25], ZnO-Al_2O_3 [26], nitrogen doped carbons [27–29], MgAl-oxide [30]) (Table II-A.1, entries 1, 2, 3, 4, 5 and 6) with Ni contents greater than or equal to 10 wt.%. Regarding the reaction conditions, there were of two types. Some tests were carried out in methanol, with dihydrogen pressures of *c.a.* 10 bar and temperatures between 180°C and 220°C, (Table II-A.1, entries 5, 6 and 7 [29–32]), while others were carried out in hexane (20 bar H_2 and 250°C, Table II-A.1, entry 2 [26]). Alternatively, reactions were also carried out in isopropanol under N_2 atmosphere, taking advantage of the well-known hydrogen donor ability of this solvent [28,33]. Such approach, which may be preferred for economic, safety and handling issues [19,20,34–36] will be used in the present work. On the basis of the results obtained, mainly in similar temperature and pressure ranges, it appears that the selective formation of phenol has often been claimed in methanol with H_2 (Table II-A.1, entry 5 (Ni-nitrogen doped carbon catalysts [29]), entry 6 (Ni-MgAl-oxide [30]), and entry 7 (NiMo sulphide [31,32]), but not in hexane (Table II-A.1, entry 3 [26]). Interestingly, using isopropanol under nitrogen atmosphere, Tan *et al*. reported differences in selectivity towards phenol or cyclohexanol related to the method of preparation of the Ni-based catalysts formed by deposition on doped carbon (12 wt.%). Tested under exactly the same operating conditions (10 bar N_2, 200°C, 4 h) (Table II-A.1, entries 3 and 4 [28]), the catalyst prepared by incipient wetness impregnation led mainly to cyclohexanol, while the other, resulting from a "one-pot" incorporation method, gave mainly phenol. It has also to be noted that reactions using nickel and rhodium-based bimetallic colloidal suspensions with Ni:Rh ratio 85:15, achieved very good phenol selectivity, even at high $K1_{HH}$ conversion rates (Table II-A.1, entry 8 [37]).

Table II-A.1: *Literature survey of Ni or Ni-M based catalysts tested for $K1_{HH}$ hydrogenolysis.*

Entry	Support	Active phase	Prep. method	SA (m^2 g^{-1}) D (%) d (nm)	Sub/M.	Reaction conditions	Conversion (%)	Products	Ref
1	Al_2O_3-SiO_2	65wt.%Ni	*n.d.*	*n.d.*	0.8	Water/-/120°C/1 h	84	Acetophenone (min) 1-phenylethanol (maj) Phenol (maj) Cyclohexanol (min)	**[25]**
2	ZnO-Al_2O_3	10wt.%Ni	IWI	53.0 *n.d.* 22.6	11	n-hexane/20 bar H_2/250°C/2 h	100	Ethylcyclohexane (maj) Ethylbenzene (min) Cyclohexanol	**[26]**
3	NC	12wt.%Ni	One-pot	398.9 *n.d.* 24.9	5	Isopropanol/10 bar N_2/200°C/4 h	100	1-phenylethanol Ethylbenzene Phenol	**[28]**
4	NC	12wt.%Ni	IWI	*n.d.* *n.d.* 13.4	5	Isopropanol/10 bar N_2/200°C/4 h	90	Ethylcyclohexane (maj) Ethylbenzene (min) Phenol (min) Cyclohexanol (maj)	**[28]**
5	NC	Ni	One pot	*n.d.*	*n.d.*	Methanol/10 bar H_2/220°C/8 h	99	1-phenylethanol (maj) Ethylbenzene (min) Phenol	**[29]**
6	MgAl-oxide	10wt.%Ni	One pot	*n.d.* *n.d.* 25	6	Methanol/10 bar H_2/200°C/6 h	100	Acetophenone Phenol	**[30]**
7	-	1.7wt.%Ni 1.9wt.%Mo	-	- - *n.d.*	0.5	Methanol/10 bar H_2/180°C/4 h	100	Monomers	**[31]** **[32]**
8	-	2.5wt.%Ni 0.8wt.%Rh	-	- - 2.7	20	Water/1 bar H_2/95°C/16 h	100	1-phenylethanol (maj) Ethylbenzene (min) Phenol (maj) Cyclohexanol (min)	**[37]**

SA: Specific area; D: Dispersion; d: particle diameter; IWI: Incipient wetness impregnation; NC: nitrogen doped carbon; maj: major product; min: minor product; n.d.: not determined.

In the end, various parameters appear to influence the selective formation of phenol rather than cyclohexanol from $K1_{HH}$ in the presence of nickel-based catalysts, and it is not easy to generalize, given the wide variety of materials used. In addition, our study of the literature showed that, on the one hand, the reported catalysts are characterized by a high nickel loading, which is not favorable to good metal dispersion and that, on the other hand, very often large quantities of active phase (low molar substrate/metal ratio) have to be used. It therefore seemed important to us to study the catalytic activity of less nickel-rich materials characterized by high dispersion. Although its use appears to be less widespread for lignin reductive depolymerization, silica was chosen because of the various possibilities for controlling its textural properties [13–15,38]. The aim of the present contribution was to prepare Ni-based catalysts with a lower metal loading (5 wt.%) and to test them at high molar substrate/metal ratio (ideally 100), under the mildest possible reaction temperature and pressure, targeting the optimization of phenol formation in the hydrogenolysis of $K1_{HH}$. Rhodium [39] was also introduced to reproduce on silica what was described by Bulut *et al.* [37] with colloidal suspensions of bimetallic NiRh particles. Here, high dispersion of nickel, rhodium and both was ensured by the impregnation of Aerosil 380 with an aqueous solution of the metal(s) salt(s) in the presence of aqueous ammonia [40,41], as previously shown, by our group, with Ni for the dry reforming of methane [41].

II-A1.2. Experimental section

II-A1.2.1. Materials synthesis

Metal insertion was performed by the impregnation of Aerosil 380 with aqueous Rh(III) and/or Ni(II) in the presence of ammonia affording Rh, Ni or $(Ni\text{-}Rh)_{NH_3}/SiO_2$ materials.

In the case of monometallic samples, 1.0 g of Aerosil 380 (DEGUSSA) was dispersed into 30 mL of distilled water for 30 min at room temperature, then 2.5 mL of aqueous NH_3 (25 wt.%, MERCK) were added. After 10 min, the required amount of $Ni(NO_3)_2.6H_2O$ (250 mg, SIGMA ALDRICH) or $RhCl_3.3H_2O$ (128 mg, STREM CHEMICALS) dissolved in 5 mL of distilled water was introduced. The resulting suspension was then heated at 60°C for 2 h. Finally, the solid was recovered by filtration (colorless filtrate), washed with distilled water (2 x 5 mL) and dried at 60°C

for 20 h. Reduction under H_2 flow (50 mL min^{-1}) at 500, 650 or 750°C was performed for 3 h, just before the catalytic test.

According to literature, Ni/Rh bimetallic materials were very few in the reductive depolymerization of lignin, compared to carbon dioxide reforming of methane [42–44], hydrogen generation [45,46], hydrogenation of arenes [47], CO_2 methanation [48] or the oxidation of urea [49]. Therefore, in the case of bimetallic samples, three materials, ($(Ni_xRh_{100-x})_{NH_3}/SiO_2$) with 75, 50 and 25 molar percent of Ni, respectively, were prepared using both $Ni(NO_3)_2.6H_2O$ and $RhCl_3.3H_2O$ as metal precursors (see details in Table II-A.2). Here, the resulting solids were reduced under H_2 at 500°C for 3 h, just before the catalytic test.

Table II-A.2: *Ni and Rh precursors quantities introduced for the preparation of the three bimetallic catalysts.*

	Weight (mg)	
Materials	**$Ni(NO_3)_2.6H_2O$**	**$RhCl_3.3H_2O$**
$(Ni^{II}_{25}$-$Rh^{III}_{75})_{NH_3}/SiO_2$	61	167
$(Ni^{II}_{50}$-$Rh^{III}_{50})_{NH_3}/SiO_2$	123	111
$(Ni^{II}_{75}$-$Rh^{III}_{25})_{NH_3}/SiO_2$	184	55

The characterization methods are detailed in the experimental part (Appendix 1).

II-A1.2.2. Catalytic test

The reductive treatment was conducted in a 120 mL high-pressure autoclave (Parr reactor 4560 with a 4848-reactor controller). Unless otherwise stated, the substrate/metal molar ratio was maintained at 100. In this case, a glass vessel was loaded with the catalyst, 15 mL of isopropanol and $[Substrate]_o \approx 0.06$ M. After stirring, the vessel was placed in the autoclave and, using N_2, the air was flushed out six times before pressurizing the reactor to 5 bar of N_2. During the test, the reaction mixture was stirred at 600 rpm and heated at 4°C min^{-1} up to 180°C and maintained at this temperature for a certain time. Then, the reactor was cooled, using an ice-water bath from 100°C to room temperature. An aliquot of 300 µL was withdrawn from the reaction mixture and combined with 300 µL of anisole (internal standard) and dichloromethane in a 10 mL flask. The resulting solution was analyzed by GC/MS.

The conversion of dimers and the yields of products (expressed as % of starting carbon) were defined as follows:

$$\text{Yield : } Y_j\,(\%_C) = \frac{mol\ of\ \text{"j" x number of carbons of "j"}}{initial\ mol\ of\ K1_{HH}\ (or\ A1_{HH})\ x\ number\ of\ carbons\ of\ K1_{HH}\ (or\ A1_{HH})} \text{ x } 100 \quad \text{(Eq. II-A1.1)}$$

$$\text{Conversion : } X_i\,(\%) = \frac{mol\ of\ reacted\ K1_{HH}\ (or\ A1_{HH})}{initial\ mol\ of\ K1_{HH}\ (or\ A1_{HH})} \text{ x } 100 \quad \text{(Eq. II-A1.2)}$$

During the hydrogenolysis of $K1_{HH}$ or $A1_{HH}$ molecules, which is supposed to lead to mono-aromatic compounds ("monomers"), determining the conversion of the substrate (X_i) is not enough because other molecules containing two aromatic rings ("dimers"), *i.e.*, with un-cleaved C-OAr bonds, can be produced. We have therefore introduced another conversion metric, X_{Di}, which, in fact, quantifies the overall rate of cleavage of the C-OAr bond. X_{Di} was calculated as follows:

$$X_{Di}\,(\%) = X_i - \sum_i Y_{Di} \quad \textit{where } Y_{Di} \textit{ corresponds to the yields of molecules keeping the C-OAr bond} \quad \text{(Eq. II-A1.3)}$$

$$\text{Phenol selectivity : } S(\%) = \frac{14}{6} \text{ x } \frac{Yphenol}{X_{Di}} \text{ x } 100 \quad \text{(Eq. II-A1.4)}$$

$$\text{Hourly formation rate : } HY_j\ (\text{mmol h}^{-1}) = \frac{\text{moles of "j"}}{\text{time of reaction (h)}} \text{ x } 10^3 \quad \text{(Eq. II-A1.5)}$$

II-A1.3. Results and discussion

Five silica-based heterogeneous catalysts were prepared by the impregnation of Aerosil 380 with either Rh(III), Ni(II) salts or both in the presence of aqueous ammonia. The targeted loadings were 5 wt.% Rh or Ni and a molar metal loading similar to 5 wt.% Ni for all bimetallic materials. The resulting solids were characterized in their dried *as-synthesized* form (*i.e.* $Rh^{III}_{NH_3}/SiO_2$, $Ni^{II}_{NH_3}/SiO_2$ and $(Ni^{II}_xRh^{III}_{100-x})_{NH_3}/SiO_2$), then after reduction by H_2 (*i.e.* $Rh^0_{NH_3}/SiO_2$, $Ni^0_{NH_3}/SiO_2$ and $(Ni_xRh_{100-x})^0_{NH_3}/SiO_2$) at 500, 650 or 750°C and calcination at 550°C. Their catalytic activity was evaluated in the hydrogenolysis of $K1_{HH}$ aiming at drawing relationships between phenol selectivity and the physico-chemical properties of the tested catalysts.

II-A1.3.1. Materials characterization

All dried *as*-synthesized samples (Figure II-A.2 A) were characterized by very similar N_2 sorption isotherms of type II, according to the IUPAC classification [50]. Pore size distributions

obtained by the BJH method applied to the desorption branch were very broad (from 5 to 40 nm) for all mono- and bimetallic materials (Figure II-A.2 B) and significantly different from that of Aerosil 380. As a result, significant changes in the textural parameters were observed when Rh, Ni or both were introduced (Table II-A.3). In fact, NH_3 was responsible for these changes, as shown by the comparison of the isotherms of Aerosil 380 (SiO_2) and of SiO_2-NH_3, a reference material obtained in a way similar to the metal-based samples, but without Ni or Rh (Figure II-A.2 A). Indeed, SiO_2-NH_3 was characterized by a pore volume (V_{Des}) of 1.23 instead of 0.56 $cm^3\ g^{-1}$ for Aerosil 380 (Table II-A.3), probably as the result of some dissolution of silica in alkaline conditions, while its specific surface area (S_{BET}) decreased by 20% (269 instead of 333 $m^2\ g^{-1}$).

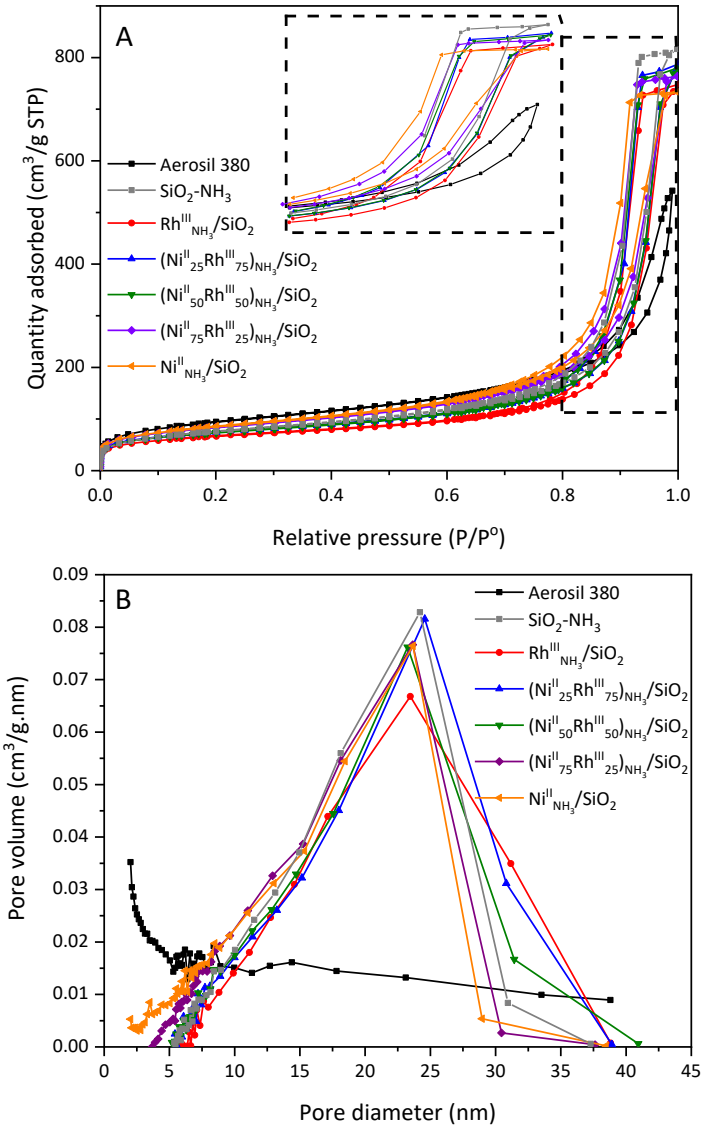

Figure II-A.2: *(A) N_2 adsorption-desorption isotherms (-196°C) and (B) pore size distribution of dried monometallic and bimetallic as-synthesized materials as well as references without metal.*

Interestingly, the decrease in specific surface area for $Rh^{III}_{NH_3}/SiO_2$ (231 $m^2\ g^{-1}$) was larger than that of SiO_2-NH_3 (269 $m^2\ g^{-1}$). For the Ni containing materials, intermediate S_{BET} values (between those of SiO_2 and $Rh^{III}_{NH_3}/SiO_2$) were generally obtained. Compared to SiO_2-NH_3, the addition of Ni^{2+}, Rh^{3+} or both led to pore volumes higher than that of Aerosil 380 (0.56 $cm^3\ g^{-1}$) and lower than that of SiO_2-NH_3 (1.23 $cm^3\ g^{-1}$). In fact, the pore volumes of the samples incorporating one or two metals were relatively similar throughout the series of five materials (1.00 to 1.17 $cm^3\ g^{-1}$) but their average pore diameter (D_{pores}) appeared to decrease monotonously from 19.8 nm (100% Rh) to 15.7 nm (100% Ni) revealing a shift of the pore size distribution. It should also be noted that all solids showed some microporosity, as evidenced by the shape of their isotherms at very low P/P^0.

Table II-A.3: *Physico-chemical properties of dried monometallic and bimetallic as-synthesized materials as well as references without metal.*

Material	S_{BET} ($m^2\ g^{-1}$)	V^a_{Des} ($cm^3\ g^{-1}$)	Average D^b_{pores} (nm)	Ni wt.% TPR [Theor.] *ICP*	Rh wt.% TPR [Theor.] *ICP*
Aerosil 380 (SiO_2)	333	0.56	10.7	-	-
SiO_2-NH_3	269	1.23	19.0	-	-
$Rh^{III}_{NH_3}/SiO_2$	231	1.12	19.8	-	3.8 [5] *4.25*
$(Ni^{II}_{25}Rh^{III}_{75})_{NH_3}/SiO_2$	260	1.15	19.6	1.11[c] [1.2] *0.97*	5.16[c] [5.3] *4.49*
$(Ni^{II}_{50}Rh^{III}_{50})_{NH_3}/SiO_2$	256	1.17	19.2	2.54[c] [2.5] *1.86*	4.67[c] [4.3] *3.42*
$(Ni^{II}_{75}Rh^{III}_{25})_{NH_3}/SiO_2$	293	1.15	17.6	3.82[c] [3.8] *3.24*	1.95[c] [2.2] *1.65*
$Ni^{II}_{NH_3}/SiO_2$	288	1.00	15.7	4.1 [5] *4.9*	-

[a] From BJH on the desorption branch (between 2 and 50 nm in diameter), [b] From the BJH desorption pore size distribution (see Figure II-A.2 B), [c] Using the nominal Ni:Rh ratio calculated from ICP-OES measurements.

Wide-angles XRD patterns for $Rh^{III}_{NH_3}/SiO_2$, $Ni^{II}_{NH_3}/SiO_2$ and $(Ni^{II}_xRh^{III}_{100-x})_{NH_3}/SiO_2$ (Figure II-A.3) exhibited a wide peak at $2\theta = 22°$ as the result of X-Ray diffusion by amorphous silica. Very small broad peaks around $2\theta = 35^o$ and 60^o (Figure II-A.3 d) were clearly evidenced in the case of $Ni^{II}_{NH_3}/SiO_2$. This could correspond to a nickel phyllosilicate phase ((200), (202) and (060) reticular planes at 2θ = 34.1, 36.4 and 60.5°) (PDF 00-049-1859) [51]. Despite similar metal loadings, no significant diffraction peak could be observed in the case of $Rh^{III}_{NH_3}/SiO_2$ and $(Ni^{II}_xRh^{III}_{100-x})_{NH_3}/SiO_2$ samples (Figure II-A.3 b and c).

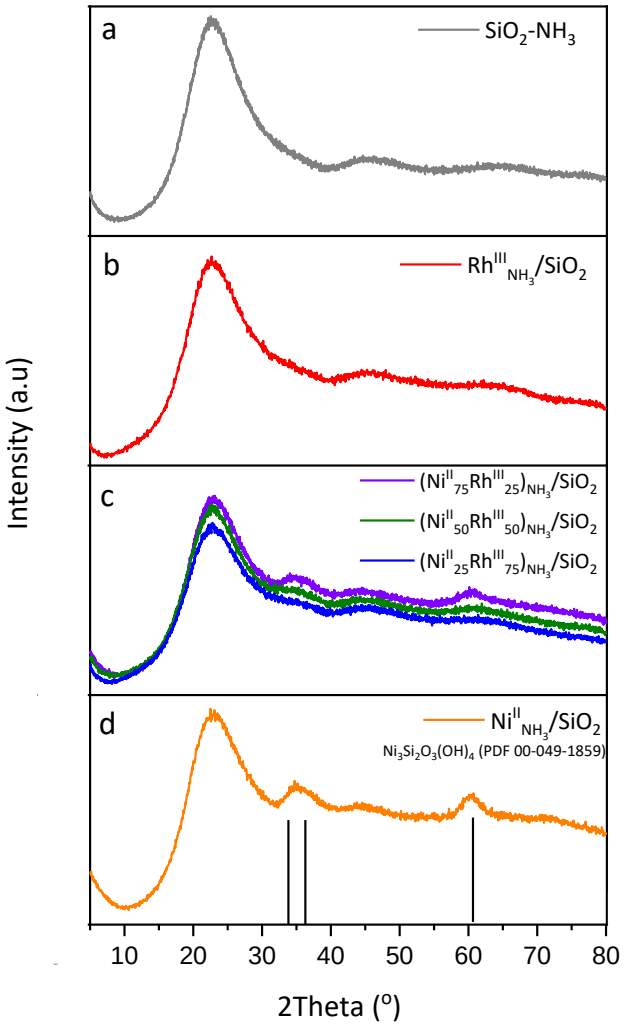

Figure II-A.3: *Wide angle XRD patterns of (a) SiO_2-NH_3, (b,d) dried monometallic and (c) bimetallic as-synthesized materials.*

PDF analyses of the dried *as-synthesized* $Rh^{III}_{NH_3}/SiO_2$ and $Ni^{II}_{NH_3}/SiO_2$ samples were carried out to provide details about the rhodium and nickel species formed after impregnation and drying [52]. Initially, experimental G(r) curves of SiO_2-NH_3, $Rh^{III}_{NH_3}/SiO_2$ and $Ni^{II}_{NH_3}/SiO_2$ looked similar (Figure II-A.4 a). It was then decided to subtract the G(r) signal of SiO_2-NH_3 from those of $Rh^{III}_{NH_3}/SiO_2$ and $Ni^{II}_{NH_3}/SiO_2$ for a better detection of impregnated species. This allowed to highlight completely different behaviors between Rh and Ni.

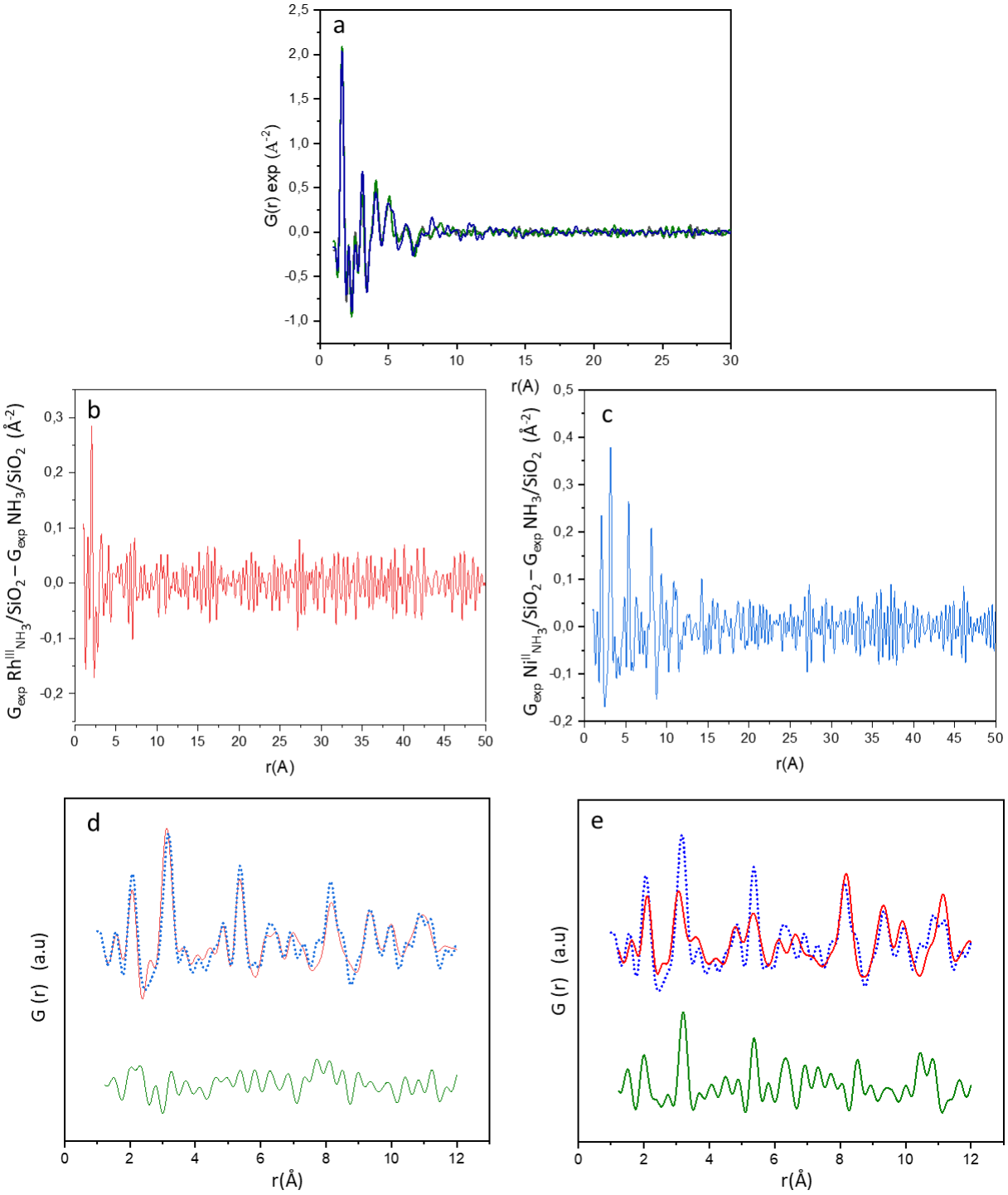

Figure II-A.4: *(a) Experimental PDF curve of SiO_2-NH_3 (black), $Rh^{III}_{NH_3}/SiO_2$ (green) and $Ni^{II}_{NH_3}/SiO_2$ (blue), PDF treatments for (b) $Rh^{III}_{NH_3}/SiO_2$ and (c) $Ni^{II}_{NH_3}/SiO_2$, Comparison of the experimental difference G(r) functions (material-support) of $Ni^{II}_{NH_3}/SiO_2$ with (d) the TOT talc model and (e) the TO serpentine model for Ni phyllosilicate. (Experimental and calculated curves are presented respectively in blue and red, the difference (G_{exp}-G_{cal}) below being in green.*

For rhodium (Figure II-A.4 b), only a single peak located at 2.0 Å attributed to a Rh---O distance was observed. No other peaks could be detected meaning no Rh---Rh, nor further Rh---O distances, which is consistent with Rh species isolated on the surface or within the silica matrix instead of oxide clusters. In the case of nickel (Figure II-A.4 c), coherent distances up to 20 Å were clearly observed revealing the formation of small ordered domains. As Ni phyllosilicates were suspected from XRD (Figure II-A.3 d), the difference experimental G(r) function of $Ni^{II}_{NH_3}/SiO_2$ was compared with two calculated G(r) functions corresponding to Talc (Figure II-A.4 e) or serpentine (Figure II-A.4 f) type structures. This, allowed us to propose the formation of nickel phyllosilicates with Talc type structures.

Since any published resolved structure for Ni based phyllosilicates could be found, for our calculations, we used two well-known Magnesium based phases: $Mg_3Si_4O_{10}(OH_2)_2$ (PDF 04-010-7170), presenting the TOT Talc structure and $Mg_3Si_2O_5(OH)_4$ (PDF 00-062-0394), presenting the TO Serpentine structure and replaced Mg^{2+} atoms by Ni^{2+}. We then compared the calculated G(r) (using a coherence length of 25 Å) with the experimental difference G(r), and allowed refinement: cell parameters, thermal displacements and peak shape. Atomic positions were blocked. As expected, for the talc TOT model, most Si---Ni and Si---Si calculated peaks presented higher intensities than for the TO Serpentine model. The Rw reliability factors clearly showed that the TOT talc structure can be considered as the best model for the Ni phyllosilicates clusters (Rw = 36% for TOT talc versus 60% for TO Serpentine).

The reducibility of $Rh^{III}_{NH_3}/SiO_2$, $Ni^{II}_{NH_3}/SiO_2$ and $(Ni^{II}_xRh^{III}_{100-x})_{NH_3}/SiO_2$ was investigated by H_2-TPR. As expected, H_2 consumption profiles of the monometallic samples, $Rh^{III}_{NH_3}/SiO_2$ and $Ni^{II}_{NH_3}/SiO_2$ (Figure II-A.5 a and b), showed that Rh is much more easily reduced than Ni (full reduction at T < 400°C for Rh and, at *ca.* 900°C for Ni). In fact, both were characterized by two reduction peaks: one minor (116ºC for Rh (7%) and 360°C for Ni (9%)) and one major (214ºC for Rh (93%) and 765°C for Ni (91%)). In both cases, the profiles should be attributed to the reduction of at least two different species, rather than considering a two-step reduction process of a single species [40]. It can therefore be assumed that the two signals observed for $Rh^{III}_{NH_3}/SiO_2$ and $Ni^{II}_{NH_3}/SiO_2$ correspond to Rh^{III} or Ni^{II} species located at different positions within the porous support and/or exhibiting different interactions with the silica surface [53]. Often, H_2 consumption

at the lowest temperature is assigned to large particles of oxides [54] while smaller particles, with a higher proportion of uncoordinated atoms at their periphery, are more strongly coordinated to the surface and more difficult to reduce. In the case of $Ni^{II}_{NH_3}/SiO_2$ (Figure II-A.5 b), the very high reduction temperature (765°C) agrees with the presence of Ni(II) phyllosilicates evidenced before using wide-angles XRD (Figure II-A.3 d) and PDF (Figure II-A.4 c and d). The experimental loading of Ni in $Ni^{II}_{NH_3}/SiO_2$ (4.1 wt.%) and of Rh in $Rh^{III}_{NH_3}/SiO_2$ (3.8 wt.%) (Table II-A.3) could be evaluated from these measurements (Figure II-A.5 a and b) considering that the reduction of one mole of Rh(III) (or Ni(II)) requires 3/2 mole of H_2 (or 1 H_2). In the case of the dried *as*-synthesized bimetallic $(Ni^{II}_xRh^{III}_{100-x})_{NH_3}/SiO_2$ samples (Figure II-A.5 c, d and e), no more H_2 consumption could be monitored beyond 400°C, for x = 25 and 50, or 650°C for x = 75, showing that the reducibility of Ni seems to be greatly improved. Clearly, the TPR profiles of these materials (Figure II-A.5 c, d and e) do not correspond to the weighted sum of the profiles of $Rh^{III}_{NH_3}/SiO_2$ and $Ni^{II}_{NH_3}/SiO_2$ shown in Figure II-A.5 a and b. H_2 consumption peaks were observed mainly in the range of 150 to 450°C, *i.e.* slightly shifted towards higher temperatures compared to Rh alone (Figure II-A.5 a). This observation might suggest that bimetallic species were formed upon impregnation of Aerosil 380 with aqueous mixtures of Ni(II) and Rh(III) in the presence of ammonia. For all three materials, ICP-OES analyses showed that, during silica impregnation, the experimental Ni/Rh molar ratio was very close to the nominal one (27.4 mol%, 48.8 mol% and 77.5 mol% of Ni to be compared with 25 mol%, 50 mol% and 75 mol%). Considering that, an estimation of the Rh and Ni weight loadings based on the total H_2 consumption and on the experimental Ni/Rh molar ratio, could be obtained (Table II-A.3).

In this protocol, ammonia not only provides an alkaline solution able to deprotonate and even attack the surface of silica but also, favors the formation of Rh(III) and Ni(II) cationic ammine complexes. It thus facilitates electrostatic interactions between the negatively charged surface and the metal precursors at the origin of an efficient grafting procedure. With Ni(II), phyllosilicates can be generated through Ni-O-Si heterocondensation-polymerization reactions [55]. During reducing treatment, such strong interaction is known to indirectly control the number of nuclei [56] and hence influence the particles size by preventing migration phenomena (aggregation) [41].

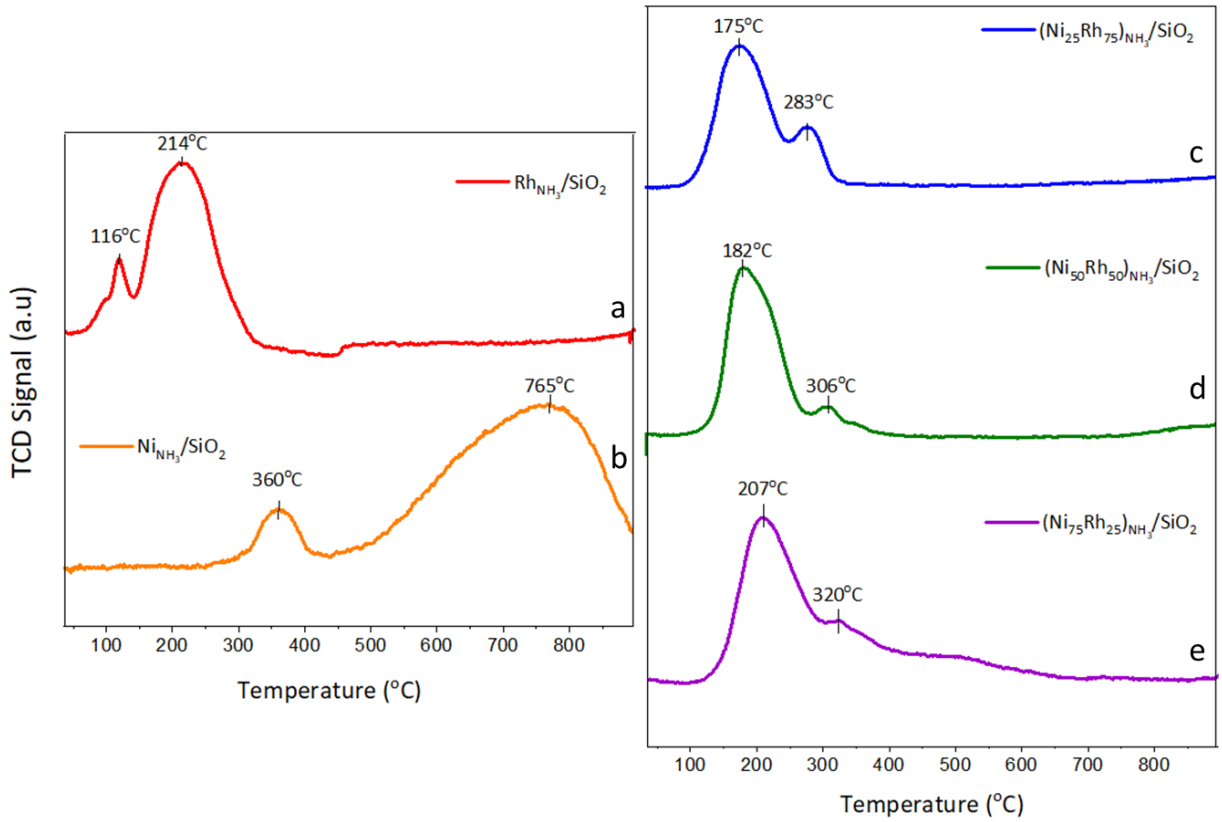

Figure II-A.5: *H_2-TPR profiles of monometallic and bimetallic dried as-synthesized materials (5 vol.% H_2 in Ar flow, 30 mL min^{-1}, 10°C min^{-1}).*

Transmission electron microscopy images of the dried *as*-synthesized forms of $Rh^{III}_{NH_3}/SiO_2$ and $Ni^{II}_{NH_3}/SiO_2$ samples emphasized very different features. In the case of $Rh^{III}_{NH_3}/SiO_2$, small and well-dispersed nanoparticles with an average size of *ca.* 1.5 ± 0.3 nm could be evidenced (Figure II-A.6 a and b). which, at first sight, is not in full agreement with PDF data (Figure II-A.4 b). In that case, there is however a great possibility of Rh(III) *in-situ* reduction under the electron beam of the microscope [57]. This was proved by additional TEM measurements. Indeed, new observations were conducted on the same area of the material either with a low value (190 pA/cm^2) or a high value (445 pA/cm^2) of current density. Clearly, no particles were observed at 190 pA/cm^2 (Figure II-A.7 a). However, at 445 pA/cm^2, with an exposition time of approximatively two minutes, small nanoparticles were revealed.

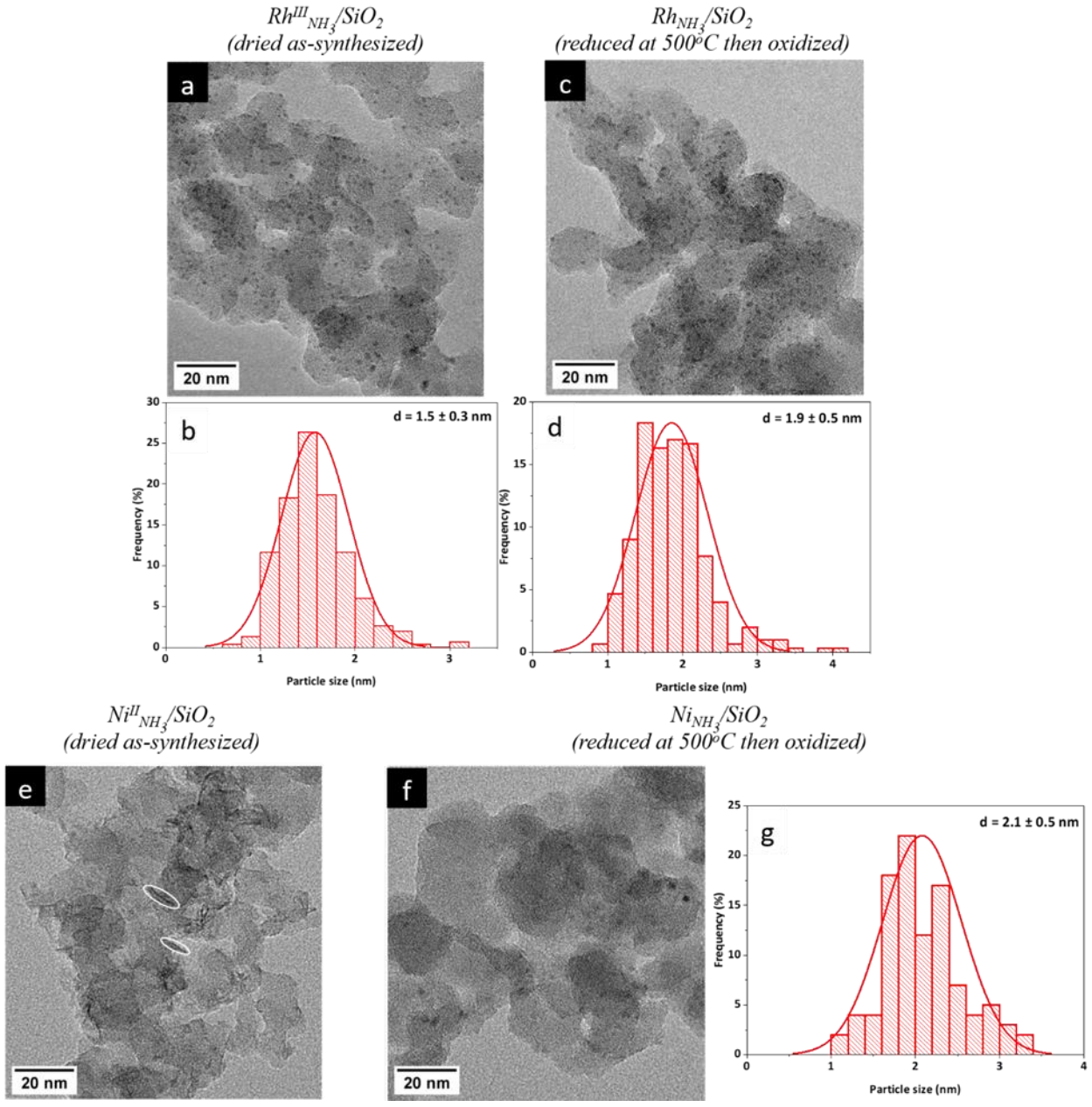

Figure II-A.6: *(a,c,e,f) TEM images and (b,d,g) particle sizes distribution of dried as-synthesized materials or after reduction at 500°C and calcination at 550°C.*

As expected for Ni phyllosilicates [58–60], nanosheets of up to 10 nm-length were evidenced in the case of $Ni^{II}_{NH_3}/SiO_2$ (Figure II-A.6 e). Since coherent distances of up to 2 nm were highlighted in the difference PDF analysis (Figure II-A.4 c), this would mean that the nanoplatelets observed in TEM (Figure II-A.6 e) are polycrystalline.

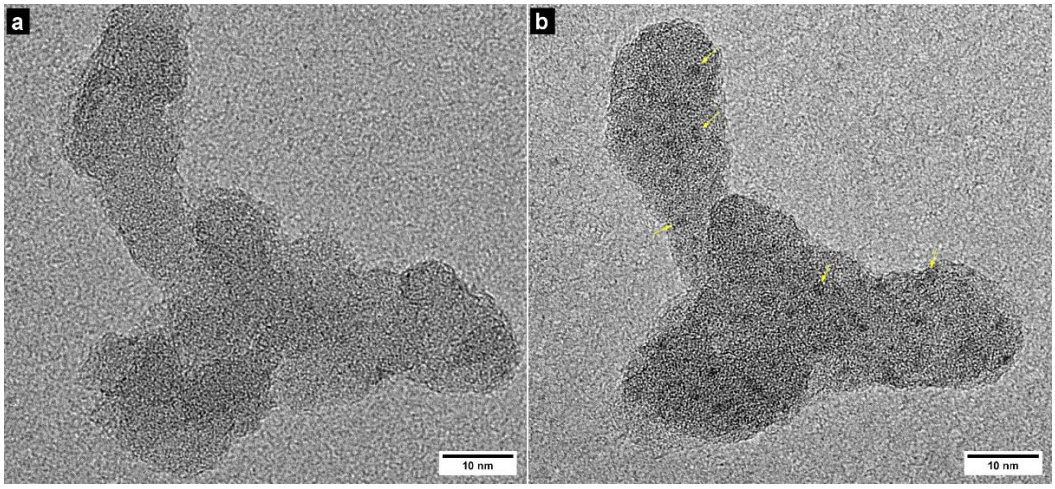

Figure II-A.7: *TEM images of dried $Rh^{III}_{NH_3}/SiO_2$ under (a) low current density (190 pA/cm^2) and (b) high current density (445 pA/cm^2).*

XPS measurements were performed on the dried *as-synthesized* $Rh^{III}_{NH_3}/SiO_2$ and $Ni^{II}_{NH_3}/SiO_2$ samples, as well as on their reduced counterparts, *i.e.*, $Rh^0_{NH_3}/SiO_2$ (500°C) and $Ni^0_{NH_3}/SiO_2$ (750°C). XPS analysis (Figure II-A.8 and Figure II-A.9) of dried *as-synthesized* $Rh^{III}_{NH_3}/SiO_2$ and $Ni^{II}_{NH_3}/SiO_2$ samples showed the presence of traces of chloride and nitrate from the nickel and rhodium salts used, respectively, as well as of some ammonia (Figure II-A.9). It is important to note that, after reduction under H_2, the XPS spectra of $Rh^0_{NH_3}/SiO_2$ and $Ni^0_{NH_3}/SiO_2$ revealed that those contaminations were eliminated. In addition, the reduced materials were found to be very unstable in air, especially in the case of nickel. For this reason, observations of the materials recovered after reductive treatments under H_2 at 500°C or more were made after a re-oxidation step performed under air at 550°C.

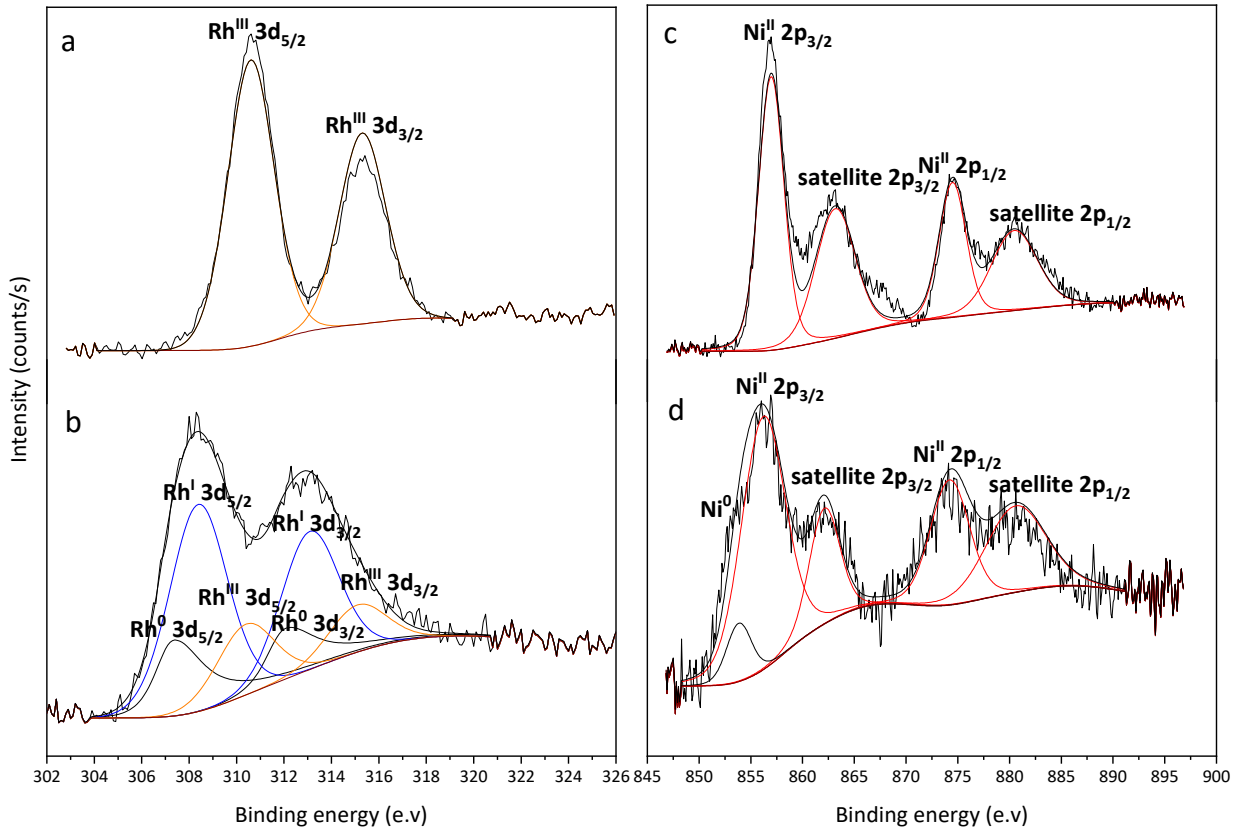

Figure II-A.8: *XPS spectra of the Rh 3d region in dried as-synthesized $Rh^{III}_{NH_3}/SiO_2$ (a) and $Rh^{0}_{NH_3}/SiO_2$ reduced at 500°C (b) or Ni 2p region in dried as-synthesized $Ni^{II}_{NH_3}/SiO_2$ (c) and $Ni^{0}_{NH_3}/SiO_2$ reduced at 750°C (d).*

XPS spectra of *as-synthesized* $Rh^{III}_{NH_3}/SiO_2$ and $Rh^{0}_{NH_3}/SiO_2$ (500°C) samples exhibited two main peaks corresponding to Rh $3d_{5/2}$ and Rh $3d_{3/2}$ in the Rh 3d region (Figure II-A.8 a and b). Deconvolution of the spectrum of *as-synthesized* $Rh^{III}_{NH_3}/SiO_2$ (Figure II-A.8 a) gave only one single component per peak, at 310.4 and 315.1 eV, which could be attributed to Rh(III) [61]. After reduction at 500°C, in addition to some Rh(III), the experimental spectrum could be fitted by introducing two Rh species. Those would be the expected zero-valent rhodium [62] (307.0 and 312.2 eV) and Rh^{I} species [63] (308.4 and 313.0) (Figure II-A.8 b). XPS spectra of $Rh^{III}_{NH_3}/SiO_2$ in the Cl 2p and N 1s regions were also analyzed (Figure II-A.9 a and c), respectively showing a peak at 199.3 eV and 401.0 eV, assigned to Cl^- [62] and probably protonated, rather neutral NH_3. It was checked that these peaks disappeared after reducing $Rh^{III}_{NH_3}/SiO_2$ (Figure II-A.9 b and d), meaning that both N and Cl were removed after the reduction step.

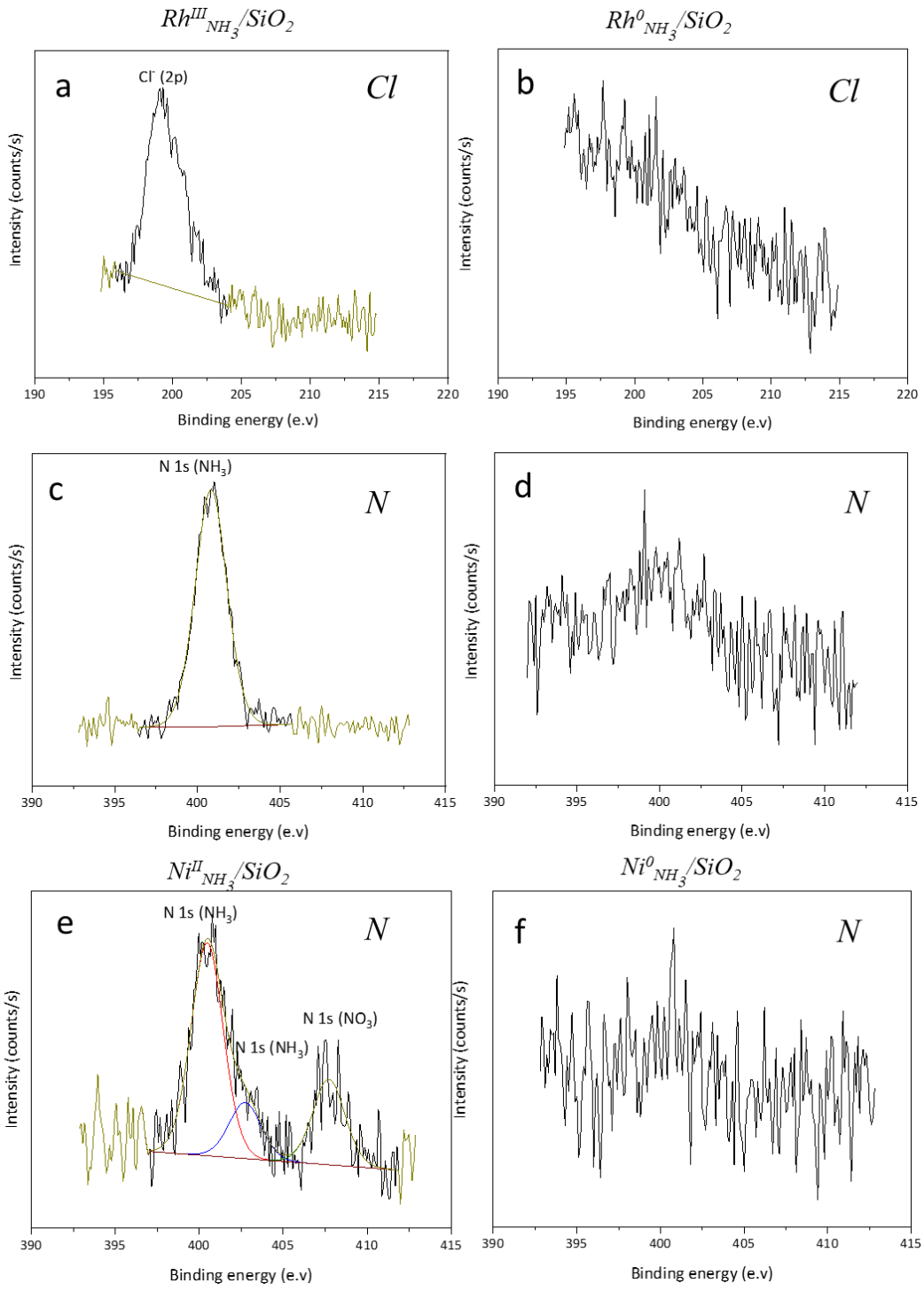

Figure II-A.9: *XPS spectra in N 1s and Cl 2p regions of $Rh^{III}_{NH_3}/SiO_2$ (a, c), $Rh^{0}_{NH_3}/SiO_2$ (b, d), $Ni^{II}_{NH_3}/SiO_2$ (e) $Ni^{0}_{NH_3}/SiO_2$ (f) materials.*

In the Ni 2p region, the XPS spectra of dried *as-synthesized* $Ni^{II}_{NH_3}/SiO_2$ and of $Ni^{0}_{NH_3}/SiO_2$ (reduced at 750°C) could be deconvoluted in two main peaks corresponding to Ni $2p_{3/2}$ and Ni

$2p_{1/2}$ with their satellites. In the case of $Ni^{II}_{NH_3}/SiO_2$ (Figure II-A.8 c) [64], these peaks were located at 874.5 eV ($2p_{1/2}$) and 856.9 eV ($2p_{3/2}$), with a spin-energy separation of 17.6 eV and satellites at 880.4 and 863.1 eV. The analysis of $Ni^{0}_{NH_3}/SiO_2$, showed, after deconvolution, the presence of Ni(0) highlighted by a small contribution at 853.8 eV [65,66] ($2p_{3/2}$). Other contributions, very similar to those found for $Ni^{II}_{NH_3}/SiO_2$, were revealed at 874.2 ($2p_{1/2}$), 856.2 ($2p_{3/2}$) with their satellites at 880.6 and 862.1 eV (Figure II-A.8 d), showing the great instability of Ni(0) under air. It should be noted that the shift in binding energy values observed for Ni(II) species in $Ni^{0}_{NH_3}/SiO_2$ compared to those in $Ni^{II}_{NH_3}/SiO_2$ would correspond to an enhanced interaction between Ni and the support upon the thermal reducing treatment carried out at 750°C [41,67]. The XPS spectrum of $Ni^{II}_{NH_3}/SiO_2$ in the N 1s region was also analyzed (Figure II-A.9 e), showing, after deconvolution, a peak at 400.7 eV [68] and a small shoulder at 402.6 eV, corresponding to coordinated NH_3 or NH_4^+, and finally a small peak at 407.6 eV [65,69] attributed to a higher oxidation state of N in NO_3^-. After the reduction treatment, no peak corresponding to N could be detected (Figure II-A.9 f), showing that all nitrogen, either derived from the nitrate precursor or from ammonia during the preparation process has disappeared. Binding energy of Rh, Ni, Cl and N species as well as atomic ratio are presented in Table II-A.4.

Table II-A.4: *XPS data for $Rh^{III}_{NH_3}/SiO_2$ and $Ni^{II}_{NH_3}/SiO_2$ as well as their reduced counterparts $Rh^{0}_{NH_3}/SiO_2$ (500°C) and $Ni^{0}_{NH_3}/SiO_2$ (750°C).*

	Binding energy (eV)								**Atomic ratio**			
Rh samples	**Rh^{III}**		**Rh^{I}**		**Rh^{0}**		**Cl**	**N**	**Cl/ Rh**	**N/ Rh**	**Cl/ Si**	**N/ Si**
	$3d_{5/2}$	**$3d_{3/2}$**	**$3d_{5/2}$**	**$3d_{3/2}$**	**$3d_{5/2}$**	**$3d_{3/2}$**						
$Rh^{III}_{NH_3}/SiO_2$	310.4	315.1	-	-	-	-	199.3	401.0	0.7	1.8	0.01	0.04
$Rh^{0}_{NH_3}/SiO_2$	310.4	315.1	308.4	313.0	307.0	312.2	-	-	-	-	-	-
Ni samples	**Ni^{II}**				**Ni^{0} 2p**		**Cl**	**N**	**Cl/ Ni**	**N/ Ni**	**Cl/ Si**	**N/Si**
	$2p_{3/2}$	**($2p_{3/2}$)**	**$2p_{1/2}$**	**($2p_{1/2}$)**								
$Ni^{II}_{NH_3}/SiO_2$	856.9	863.1	874.5	880.4	-		-	400.7	-	0.1	-	0.01
$Ni^{0}_{NH_3}/SiO_2$	856.2	862.1	874.2	880.6	853.8		-	-	-	-	-	-

($2p_{3/2}$) and ($2p_{1/2}$) satellites of $Ni2p_{3/2}$ and $Ni2p_{1/2}$, respectively.

According to Coenen [70], $\Delta E_{Ni\text{-}Si}$ (Ni $2p_{3/2}$ vs Si 2p) should be between 753.2 and 753.6 eV when nickel silicate is formed. In our case, the value of $\Delta E_{Ni\text{-}Si}$ (E_{Ni}-E_{Si} = 856.9 – 103.6 = 753.3 eV) for $Ni^{II}_{NH_3}/SiO_2$ (Figure II-A.8 c) would be in the good range confirming the formation of phyllosilicates as already anticipated from XRD, PDF, H_2-TPR and TEM data.

No significant variation in the particle sizes distribution (*ca.* 1.9 ± 0.5 nm) of Rh_{NH_3}/SiO_2 could be noted after those reduction-calcination treatments (Figure II-A.6 c and d). On the other hand, the lamellar structures observed for *as*-synthesized $Ni^{II}_{NH_3}/SiO_2$ were not detectable anymore after the reduction step at 500°C followed by calcination at 550°C. Instead, well-dispersed nanoparticles of *a priori* NiO (Figure II-A.6 f), with an average size of 2.1 ± 0.5 nm, could be detected. In both cases, reduction at 500°C, followed by re-oxidation at 550°C gave rise to particles with relatively small sizes, hence emphasizing the great stability of those samples under heating treatments. The nickel-based catalyst was also reduced at 650 and 750°C and TEM analyses performed after a calcination post-treatment carried out at 550°C (Figure II-A.10 a and b). In both cases, dispersed nanoparticles were still observed but, from 500 to 750°C, their average diameter increased from 2.1 (500°C, Figure II-A.6 g) to 2.5 (650°C, Figure II-A.10 c) and then to 3.7 nm (750°C, Figure II-A.10 d) which is quite reasonable for two consecutive heat treatments performed at relatively high temperatures.

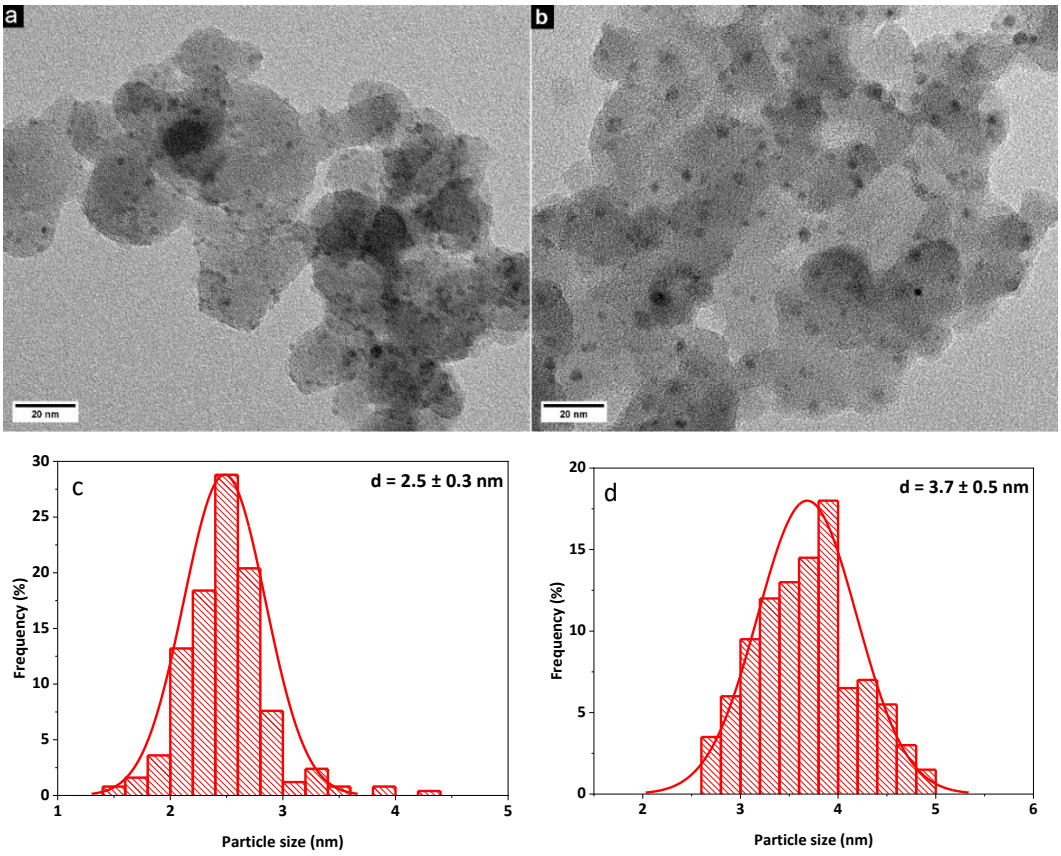

Figure II-A.10: *TEM images and corresponding particles sizes distributions of Ni NPs of* $Ni^0_{NH_3}/SiO_2$ *materials reduced at (a,c) 650°C and (b,d) 750°C. Both samples were calcined at 550°C before analysis.*

Like $Rh^{III}_{NH_3}/SiO_2$ (Figure II-A.6 a) and $Ni^{II}_{NH_3}/SiO_2$ (Figure II-A.6 e), dried as-synthesized bimetallic $(Ni^{II}_xRh^{III}_{100-x})_{NH_3}/SiO_2$ samples were also analyzed by TEM (Figure II-A.11 a, b and c), thus exhibiting small nanoparticles with average sizes of *ca.* 2 nm (Figure II-A.11 d, e and f), *i.e.*, very similar to $Rh^{III}_{NH_3}/SiO_2$ (Figure II-A.6 a). According to their binary solid-liquid phase diagram [71], zero-valent Ni and Rh are prone to form alloys for the different molar compositions tested (Rh/Ni: 25/75, 50/50 and 75/25).

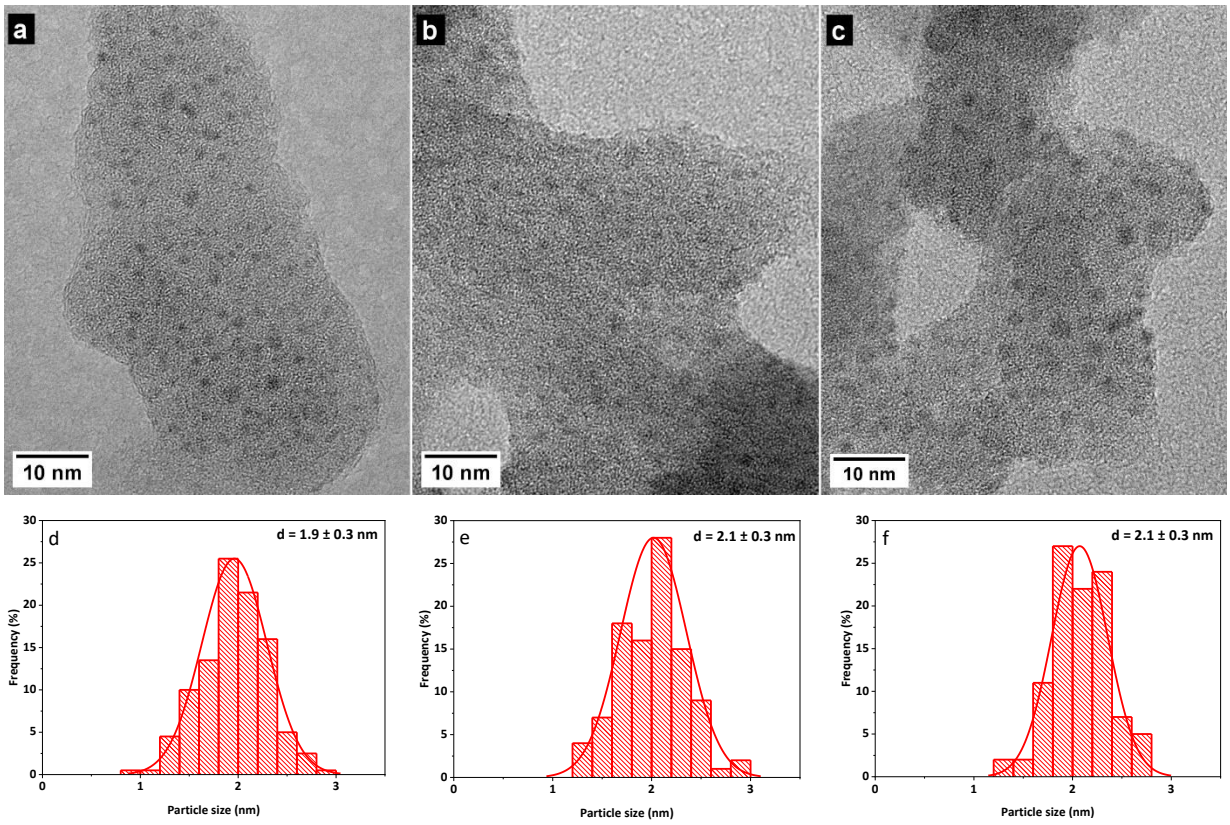

Figure II-A.11: *TEM images and corresponding particles sizes distributions of dried as-synthesized (a,d)* $(Ni^{II}_{25}Rh^{III}_{75})_{NH_3}/SiO_2$*, (b,e)* $(Ni^{II}_{50}Rh^{III}_{50})_{NH_3}/SiO_2$ *and (c,f)* $(Ni^{II}_{75}Rh^{III}_{25})_{NH_3}/SiO_2$ *samples.*

However, more information was needed for the validation of the preparation of bimetallic oxides, then metal nanoparticles, as suggested earlier by H_2-TPR. Complementary STEM/HAADF and TEM combined with EDX/mapping were carried out on bimetallic Ni-Rh-based silica in order to prove it (Figure II-A.12).

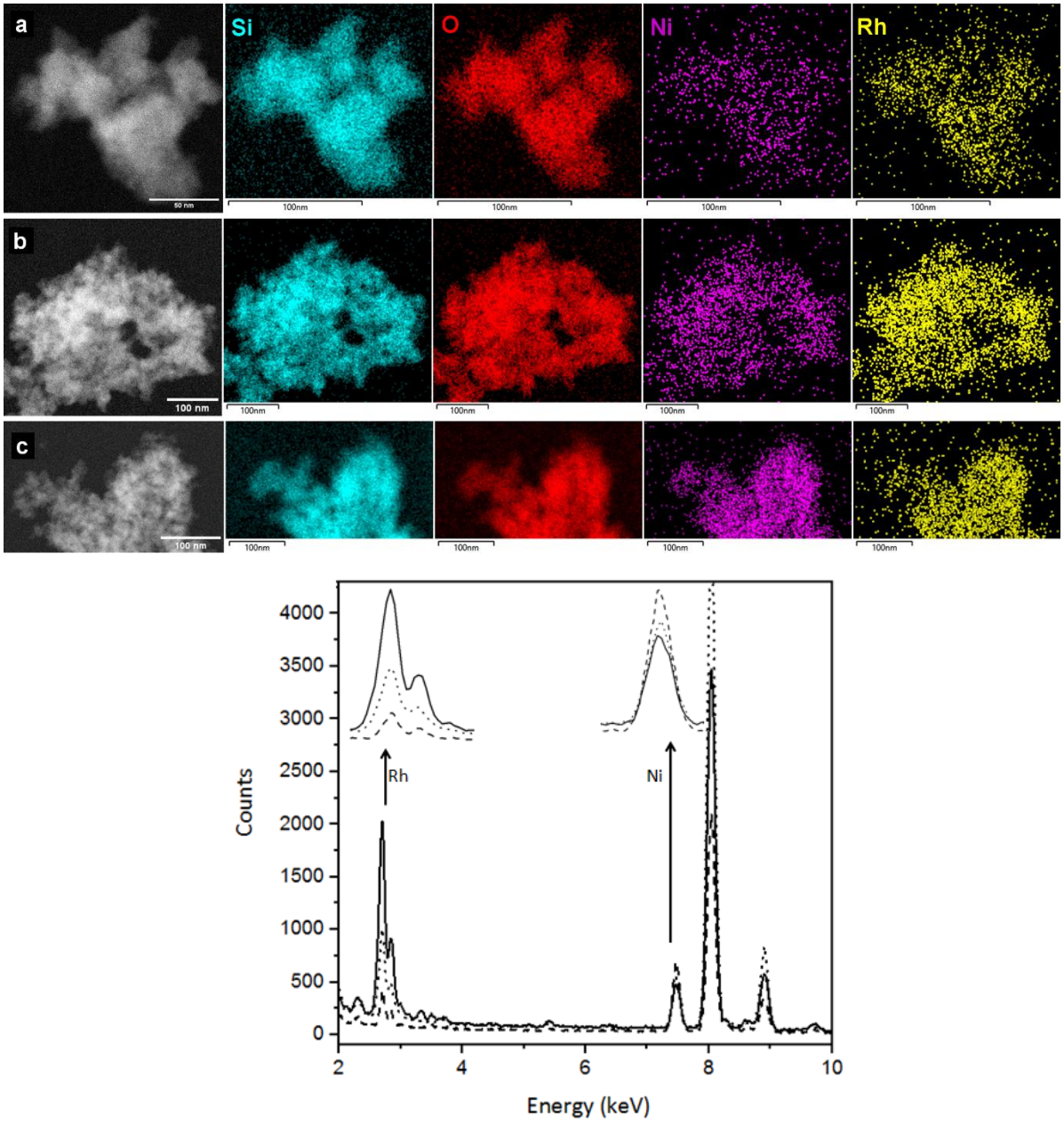

Figure II-A.12: *STEM/HAADF images, corresponding EDX elemental mapping and EDX spectra of dried bimetallic as-synthesized (a, continuous line) $(Ni^{II}_{25}Rh^{III}_{75})_{NH_3}/SiO_2$, (b, dotted line) $(Ni^{II}_{50}Rh^{III}_{50})_{NH_3}/SiO_2$ and (c, dashed line) $(Ni^{II}_{75}Rh^{III}_{25})_{NH_3}/SiO_2$ samples. (In the EDX spectra, peaks at 8 and 9 keV are attributed to copper from the grid used as sample holder).*

Indeed, the EDX mapping images of Ni, Rh, Si and O in Figure II-A.12 a, b and c confirmed that nickel and rhodium are present as highly dispersed. Clearly, these analyses emphasized that the use of NH_3 during the impregnation step, led to very good dispersion of Ni and Rh. EDX spectra were also realized, showing peaks corresponding to Ni, Rh, Si and O (Figure II-A.12). Comparing

the three spectra, the intensity of Rh peaks (at 2.8 keV) decreased with its theoretical content (from 75 to 25 mol%). On the other hand, the intensity of Ni peaks (at 7.5 keV) increased with its theoretical content (from 25 to 75 mol%). Resulting data indicate that the mean Ni mol% would be 23.7, 43.7 and 70% for $(Ni^{II}_{25}Rh^{III}_{75})_{NH_3}/SiO_2$, $(Ni^{II}_{50}Rh^{III}_{50})_{NH_3}/SiO_2$ and $(Ni^{II}_{75}Rh^{III}_{25})_{NH_3}/SiO_2$ samples (Table II-A.5).

The molar ratio of Ni/Rh calculated by EDX spectra was slightly low compared to the experimental one from ICP-OES (23.7 mol%, 43.7 mol% and 70.0 mol% of Ni to be compared with 27.4 mol%, 48.8 mol% and 77.5 mol%).

Table II-A.5: *Quantitative determination of Ni and Rh percentages for the as-synthesized bimetallic materials.*

Materials	Ni[a] (mol. %)	Rh[a] (mol. %)	Ni[b] (mol. %)	Rh[b] (mol. %)	Error[c] (%)
$(Ni^{II}_{25}Rh^{III}_{75})_{NH_3}/SiO_2$	25	75	23.7	76.3	0.85
$(Ni^{II}_{50}Rh^{III}_{50})_{NH_3}/SiO_2$	50	50	43.7	56.3	6.44
$(Ni^{II}_{75}Rh^{III}_{25})_{NH_3}/SiO_2$	75	25	70.0	30.0	0.26

[a] Theoretical value; [b] Experimental, as calculated from EDX (mean value obtained from 4 different regions of each sample); [c] Standard deviation.

II-A1.3.2. Catalysis tests

The above-prepared mono- and bimetallic materials, $Rh^0_{NH_3}/SiO_2$, $Ni^0_{NH_3}/SiO_2$ and $(Ni_xRh_{100-x})^0_{NH_3}/SiO_2$), were tested as catalysts for the reductive cleavage of $K1_{HH}$ under N_2 atmosphere at 180°C in isopropanol using, unless otherwise stated, a molar substrate/metal ratio of 100. Taking into account the total number of carbon atoms in $K1_{HH}$ (14), the expected maximum yield of phenol, Y_{phenol}, calculated in % of carbon, was 6/14 = 43%$_C$ (Eq. II-A1.1, see Exp. section). Phenol selectivity was 100% when neither cyclohexanol, nor cyclohexanone were formed, regardless the fate of the other aromatic ring in $K1_{HH}$.

Comparison of $Rh^0_{NH_3}/SiO_2$ and $Ni^0_{NH_3}/SiO_2$ reduced at 500°C

Using $Rh^0_{NH_3}/SiO_2$, $K1_{HH}$ conversion ($X_{K1_{HH}}$, Eq. II-A1.2, see Exp. section) was 85% after 5 h (Figure II-A.13). $A1_{HH}$ (Y = 25%$_C$) was formed. As a result, only 59% of C-OAr bonds (X_{Di}, Eq.

II-A1.3, see Exp. Section) were cleaved, affording acetophenone (Y = 32%C) and phenol (Y = 29%C) with a high selectivity.

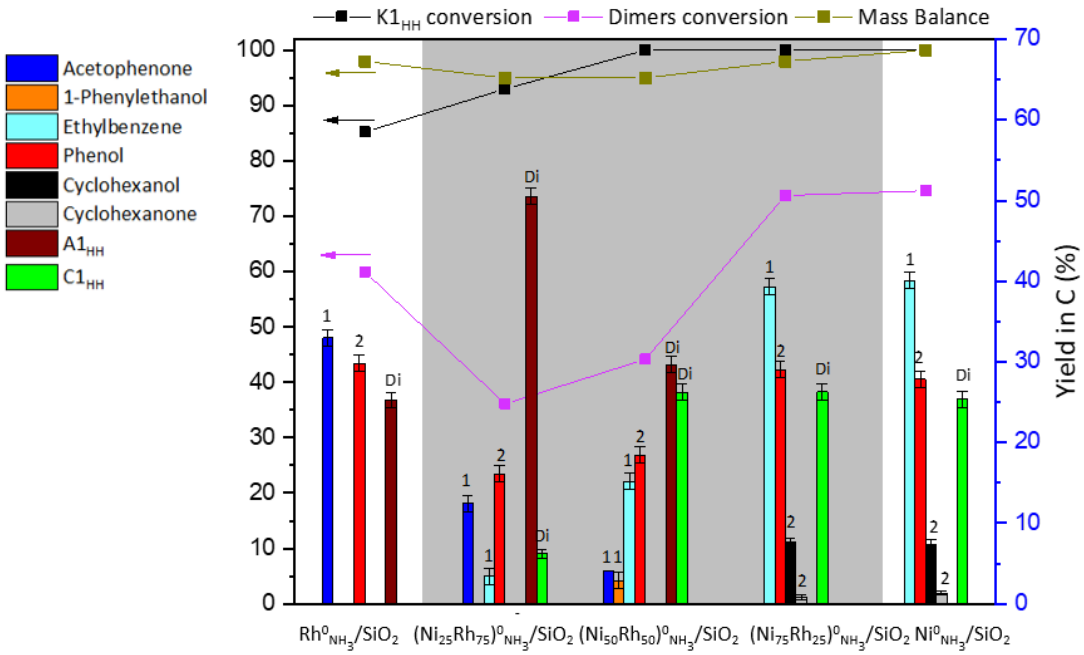

Figure II-A.13: *$K1_{HH}$/dimers conversion, mass balance and yields of the main products obtained with monometallic (Rh or Ni) (white background) and bimetallic Ni/Rh catalysts (grey background). Numbers 1 and 2 on the graph indicate from which aromatic ring of $K1_{HH}$ (Figure II-A.1) the monomers originate.*
Reaction conditions: $[K1_{HH}]_o$ = 0.06 M, $V_{i\text{-}PrOH}$ = 15 mL, molar subs./metal = 100, 180°C, 5 h, 5 bar of N_2.

After a longer reaction time (8 h), all $K1_{HH}$ molecules were converted (Table II-A.6, entry 1) and up to 90% of C-OAr bonds were cleaved ($Y_{A1_{HH}}$ = 10%C). Phenol (Y = 40%C) was formed very selectively. Besides acetophenone (Y = 40%C) remained the main co-product, but ethylbenzene and 1-phenylethanol were also formed.

In contrast, $Ni^0{}_{NH_3}/SiO_2$ was much more active and not selective towards phenol. After 8 h, $K1_{HH}$ was fully converted ($X_{K1_{HH}}$ = 100%) and 100% of the C-OAr bonds were cleaved, as evidenced by the absence of $A1_{HH}$ or $C1_{HH}$ (X_{Di} = 100%) (Table II-A.6, entry 2). The yield of phenol was very low (Y = 7%C). In this case, this result was explained by competitive phenol hydrogenation, leading to a selectivity of 16% (Eq. II-A1.4, see Exp. section). Already, after 5 h, $K1_{HH}$ was completely transformed, but only 75% of the C-OAr bonds were cleaved (presence of $C1_{HH}$) with the concomitant formation of ethylbenzene (Y = 41%C), phenol (Y = 27%C, S = 84%) as well as cyclohexanol (Y = 7%C) and cyclohexanone (Figure II-A.13).

Table II-A.6: *Additional tests on $K1_{HH}$ and $A1_{HH}$ with varying time, substrate/metal ratio.*

Entry	Substrate	Catalyst Pre-treatment	Reaction time	X_i [X_{Dimers}] (%)	Y Phenol (%C) [S_{Phenol}] (%)	Y C6_ol [C6_one] (%C)	Y Acetoph. (%C)	Y 1-phenylethanol (%C)	Y EB (%C)	Y $A1_{HH}$ (%C)	Y $C1_{HH}$ (%C)	MB[a] (%)
1	$K1_{HH}$	$Rh^0_{NH_3}/SiO_2$ reduced 500°C Subst/Rh = 100	**8 h**	100 [90]	40 [100]	0 [0]	40	4	2	10	0	96
2	$K1_{HH}$	$Ni^0_{NH_3}/SiO_2$ reduced 500°C Subst/Ni = 100	**8 h**	100 [100]	7 [16]	32 [3]	0	0	54	0	0	98
3	**$A1_{HH}$**	$Rh^0_{NH_3}/SiO_2$ reduced 500°C Subst/Rh = 100	**5 h**	77 [68]	29 [100]	0 [0]	27	0	9	-	9	97
4	**$A1_{HH}$**	$Rh^0_{NH_3}/SiO_2$ reduced 500°C Subst/Rh = **20**	**5 h**	100 [100]	42 [98]	0 [0]	0	0	55	-	0	97
5	**$A1_{HH}$**	$Ni^0_{NH_3}/SiO_2$ reduced 500°C Subst/Ni = 100	**5 h**	100 [100]	20 [47]	23 [1]	0	0	56	-	0	100
6	**$A1_{HH}$**	$Ni^0_{NH_3}/SiO_2$ reduced 500°C Subst/Ni = 100	**1 h**	100 [100]	33 [77]	10 [1]	0	0	56	-	0	100

C6_ol: Cyclohexanol; C6_one: Cyclohexanone; Acetoph: Acetophenone; EB: Ethylbenzene.

$[K1_{HH}$ or $A1_{HH}]_o$ = 0.06 M, $V_{i\text{-}PrOH}$ = 15 mL, 180°C, 5 bar of N_2. [a] Mass balance, MB = $\sum_i Y_i + (100 - X_{K1_{HH} \text{ or } A1_{HH}})$.

No acetophenone was obtained. So, clearly Ni promotes the formation of ethylbenzene instead of acetophenone and the hydrogenation of phenol. The latter observation was confirmed by blank experiments performed on phenol itself (Table II-A.7) in the same conditions and also under H_2 atmosphere (5 bar). From these results, it is clear that the reactivity of $Rh^0_{NH_3}/SiO_2$ was different depending on whether the hydrogen source was H_2 or isopropanol. Under H_2, phenol was hydrogenated very efficiently, affording cyclohexanol, whereas in the presence of isopropanol, the activity of $Rh^0_{NH_3}/SiO_2$ towards phenol was null, confirming the results of the present contribution. In the case of $Ni^0_{NH_3}/SiO_2$, hydrogenation of phenol occurred with H_2 as well as in the presence of isopropanol, but to a lesser extent in the presence of the latter. So, for both metals, the choice of isopropanol as the hydrogen donor in this study, aiming at maximizing phenol production, was justified. The inability of Rh(0) to hydrogenate phenol is a priori linked to the reduced capacity of $Rh^0_{NH_3}/SiO_2$ to dehydrogenate isopropanol. Hence, the lower activity of $Rh^0_{NH_3}/SiO_2$ could be the result either of some poisoning effect of *i*-PrOH or a competition between $K1_{HH}$ and *i*-PrOH adsorptions, that would be in favor of $K1_{HH}$.

Table II-A.7: *Phenol reduction with $Rh^0_{NH_3}/SiO_2$ or $Ni^0_{NH_3}/SiO_2$ reduced at 500°C under N_2 or H_2.*

	$Rh^0_{NH_3}/SiO_2$		**$Ni^0_{NH_3}/SiO_2$**	
Atmosphere	N_2	H_2	N_2	H_2
X_{PhOH} (%)	0	90	59	100
$Y_{Cyclohexanol}$ (%)	0	90	55	100
$Y_{Cyclohexanone}$ (%)	0	0	4	0

Reaction conditions: $[PhOH]_o$ = 0.06 M, $V_{i\text{-}PrOH}$ = 15 mL, molar subs./metal = 100, 180°C, 5 h, 5 bar of gas.

From this preliminary study, it is clear that $Rh^0_{NH_3}/SiO_2$ and $Ni^0_{NH_3}/SiO_2$ catalysts with very similar nanoparticle sizes (less than 2 nm, Figure II-A.6) behaved very differently. Rh was not very active, but it proved to be very selective for the C-O hydrogenolysis of $K1_{HH}$ and less for the hydrogenation reactions such as that of the C=O bond of $K1_{HH}$ and that of the aromatic rings. One hypothesis was that bimetallic materials, bearing both Ni and Rh, could be helpful in order to

enhance $K1_{HH}$ conversion into monomers, while increasing the phenol selectivity and lowering the price of the catalyst.

Use of bimetallic $(Ni_xRh_{100-x})^0_{NH_3}/SiO_2$ catalysts

After a reducing treatment performed at 500°C under H_2, $(Ni_xRh_{100-x})^0_{NH_3}/SiO_2$ solids led to $K1_{HH}$ conversion values higher than that of $Rh^0_{NH_3}/SiO_2$, but, after 5 h, the extent of C-OAr bonds cleavage with $(Ni_{25}Rh_{75})^0_{NH_3}/SiO_2$ and $(Ni_{50}Rh_{50})^0_{NH_3}/SiO_2$ was lower than that obtained with $Rh^0_{NH_3}/SiO_2$ and then $Ni^0_{NH_3}/SiO_2$ (Figure II-A.13). Concomitantly, no increase of the phenol production could be evidenced with the bimetallic catalysts. It is noteworthy that these materials behaved more or less as the main metal used in their formulation. Indeed, acetophenone and phenol (S = 100%) were favored as well as $A1_{HH}$ with $(Ni_{25}Rh_{75})^0_{NH_3}/SiO_2$ while $(Ni_{75}Rh_{25})^0_{NH_3}/SiO_2$ led mainly to ethylbenzene and products arising from the hydrogenation of phenol (S = 84%) as well as $C1_{HH}$ (Figure II-A.1 and Figure II-A.13). It clearly appears that $(Ni_{75}Rh_{25})^0_{NH_3}/SiO_2$ and $Ni^0_{NH_3}/SiO_2$ materials show exactly the same behavior in terms of conversions of $K1_{HH}$, dimers and selectivity towards all monomers produced and, in particular phenol. This could indicate that the active metal on the surface of the bimetallic nanoparticles in $(Ni_{75}Rh_{25})^0_{NH_3}/SiO_2$ is Ni, instead of a mixture of Ni (75%) and Rh (25%), as expected. Probably, $(Ni_{75}Rh_{25})^0_{NH_3}/SiO_2$ is composed of nanoparticles with highly Ni-enriched surfaces and even Rh@Ni core@shell structures, which is quite difficult to prove by TEM measurements due to their small size (*c.a.* 2 nm). Unlike other results published by J. Zhang *et al.* for bimetallic Ni-M (M = Rh, Pd and Ru) colloids [72], no synergistic effect could be emphasized here despite the bimetallic character of $(Ni_xRh_{100-x})^0_{NH_3}/SiO_2$ materials.

After catalysis, all the tested mono- and bimetallic materials were recovered by filtration, washed, dried, calcined at 550°C and analyzed by TEM (Figure II-A.14 and Figure II-A.15), showing different behaviors. Amongst the monometallic ones, observed after 8 h reaction, agglomeration of the Rh nanoparticles could be evidenced for Rh_{NH_3}/SiO_2 (Figure II-A.14 a) while Ni nanoparticles were still highly dispersed for Ni_{NH_3}/SiO_2 (Figure II-A.14 b, mean diameter of 2.3 nm Figure II-A.14 c). As mentioned previously, it should be remembered that the calcination post-

treatment performed on the used catalysts prior to TEM analysis cannot be held responsible for the agglomeration of Rh.

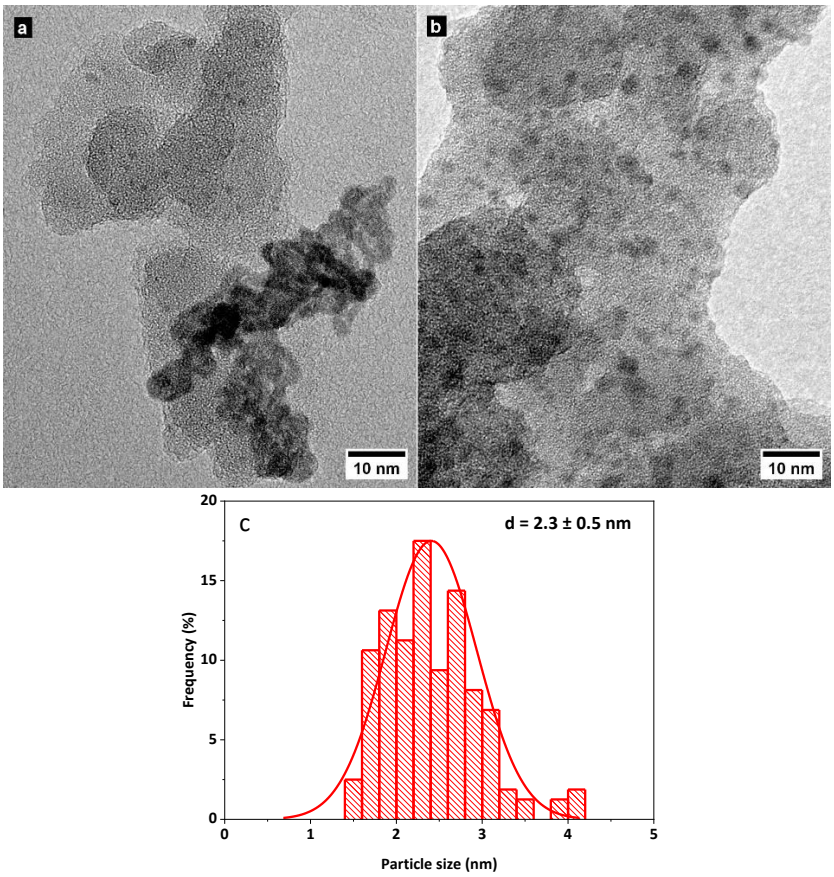

Figure II-A.14: *TEM images showing (a) the agglomeration of Rh NPs in used Rh_{NH_3}/SiO_2, (b) the well-dispersed Ni NPs and (c) the particle distribution of Ni NPs in used $Ni^0_{NH_3}/SiO_2$ after the catalytic test (8 h). All the samples were calcined at 550°C before analysis.*
Reaction conditions: $[K1_{HH}]_o$ = 0.06 M, $V_{i\text{-}PrOH}$ = 15 mL, molar subs./metal = 100, 180°C, 8 h, 5 bar of N_2.

Indeed, fresh Ni_{NH_3}/SiO_2 and Rh_{NH_3}/SiO_2 catalysts, also analyzed after reduction and calcination (Figure II-A.6 c and f for Rh and Ni, respectively) showed well-dispersed nanoparticles sizes distributions with 1.9 and 2.1 nm average diameters, respectively. Bimetallic catalysts behaved like Rh_{NH_3}/SiO_2 with the formation of bigger particles (Figure II-A.15) even after 5 h catalysis tests.

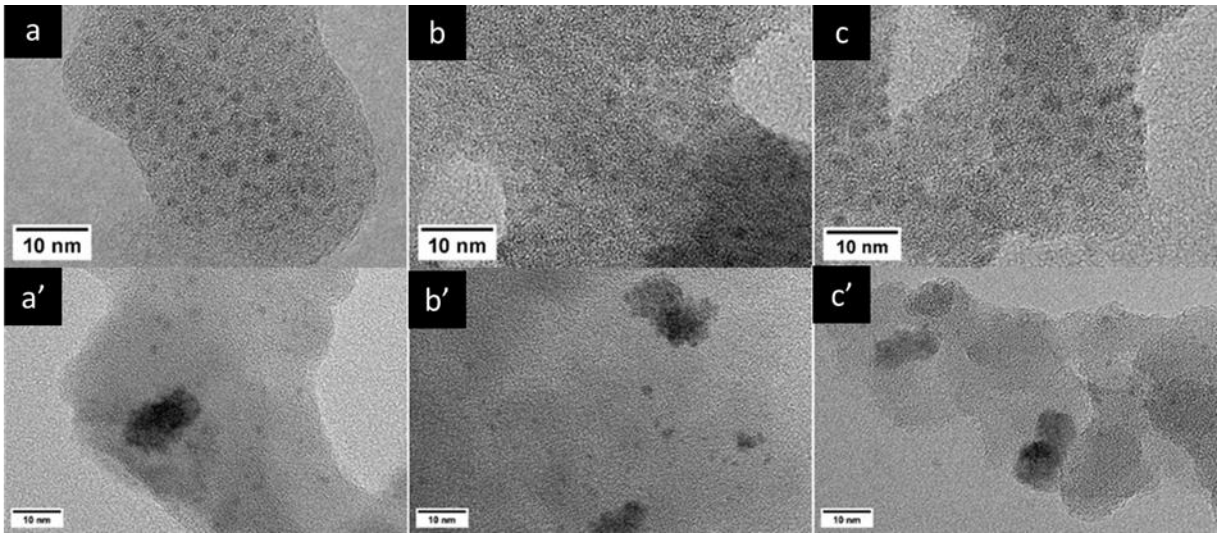

Figure II-A.15: *TEM images showing (a,b,c) the well-dispersed Ni-Rh bimetallic NPs in the dried as-synthesized state and (a',b',c') their agglomeration after the catalytic test (5 h). All the samples were calcined at 550°C before analysis.*
Reaction conditions: $[K1_{HH}]_o$ = 0.06 M, $V_{i\text{-}PrOH}$ = 15 mL, molar subs./metal = 100, 180°C, 5 h, 5 bar of N_2.

The reactor pressure was also monitored before and after the catalytic tests. Hence, it was observed that the latter, measured at room temperature, was not modified (5 bar) with $Rh^0_{NH_3}/SiO_2$ and $(Ni_{25}Rh_{75})^0_{NH_3}/SiO_2$ catalysts. However, for the materials with higher Ni loadings, *i.e.* $(Ni_{50}Rh_{50})^0_{NH_3}/SiO_2$, $(Ni_{75}Rh_{25})^0_{NH_3}/SiO_2$ and $Ni^0_{NH_3}/SiO_2$ itself, the reactor pressure increased up to 7 bar, meaning that some gas was released during the reaction. Dihydrogen could be identified by analyzing the composition of the gaseous phase in the reactor using a mass spectrometer. Figure II-A.16 displays the survey of selected m/z values *vs* time during the draining of the reactor at the end of the reaction. Expectedly, N_2 (m/z = 28) was the only gas detected with $Rh^0_{NH_3}/SiO_2$ and $(Ni_{25}Rh_{75})^0_{NH_3}/SiO_2$ catalysts (Figure II-A.16 a and b) while H_2 (m/z = 2, in black) was also evidenced with $(Ni_{50}Rh_{50})^0_{NH_3}/SiO_2$, $(Ni_{75}Rh_{25})^0_{NH_3}/SiO_2$ and $Ni^0_{NH_3}/SiO_2$ (Figure II-A.16 c, d and e). The transfer of hydrogen from isopropanol to the model substrates implies that chemisorbed hydrogen atoms are produced temporarily on the surface of the catalysts. Our pressure measurements confirm our previous hypothesis that the density of hydrides formed on the surface of nickel is greater than on rhodium, which favors their recombination to give dihydrogen [73].

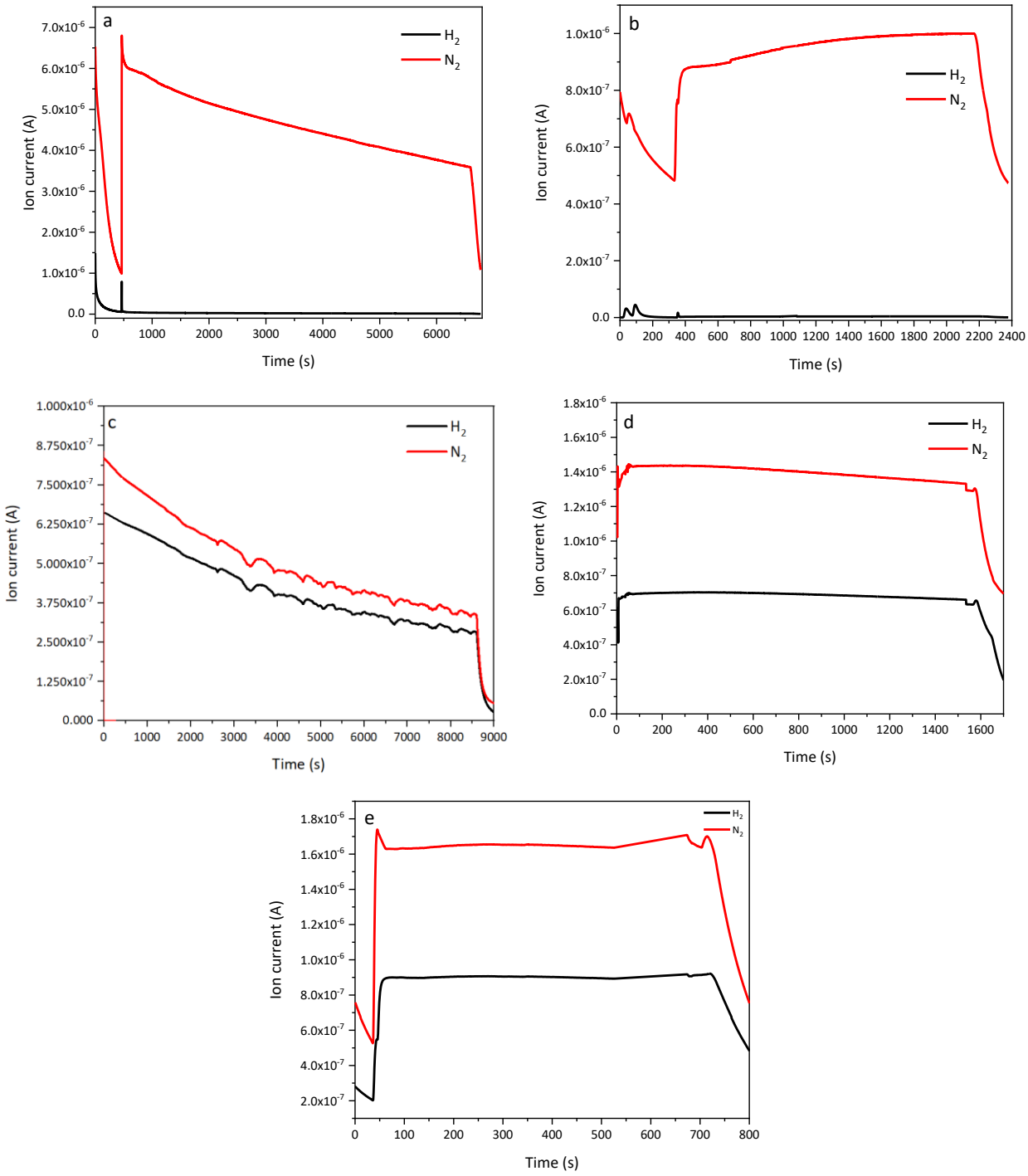

Figure II-A.16: *Monitoring of m/z = 2 and m/z = 28 by mass spectrometry for (a) $Rh^0_{NH_3}/SiO_2$, (b) $(Ni_{25}Rh_{75})^0_{NH_3}/SiO_2$, (c) $(Ni_{50}Rh_{50})^0_{NH_3}/SiO_2$, (d) $(Ni_{75}Rh_{25})^0_{NH_3}/SiO_2$ and (e) $Ni^0_{NH_3}/SiO_2$.*

Some insights on reaction pathways

Starting from $K1_{HH}$, 2-phenoxy-1-phenylethanol ($A1_{HH}$) clearly accumulated with time in the presence of $Rh^0_{NH_3}/SiO_2$ or of the bimetallic catalysts with the lowest amounts of Ni, *i.e.* $(Ni_{25}Rh_{75})^0_{NH_3}/SiO_2$ or $(Ni_{50}Rh_{50})^0_{NH_3}/SiO_2$ while $C1_{HH}$ was the predominant dimer with $(Ni_{75}Rh_{25})^0_{NH_3}/SiO_2$ and $Ni^0_{NH_3}/SiO_2$. So, it seemed that $A1_{HH}$ was less reactive than $K1_{HH}$ in the presence of the Rh rich catalysts. This led us to perform additional experiments using $A1_{HH}$ instead of $K1_{HH}$ under the same conditions. Indeed, with $Rh^0_{NH_3}/SiO_2$, reduced at 500°C and tested under 5 bar of N_2 at 180°C (Table II-A.6, entry 3), the transformation of $A1_{HH}$ and of all dimers was not complete within 5 h (X = 77% and X_{Di} = 68%) and inferior to those measured with $K1_{HH}$ (Figure II-A.13) (X = 85% and X_{Di} = 59%). Also, traces of $K1_{HH}$ were observed meaning that dehydrogenation of $A1_{HH}$ may occur during the test. In that case, *reactions(i)* and *(ii)* (Figure II-A.1) were clearly favored, and it was shown that the catalytic activity of $Rh^0_{NH_3}/SiO_2$ could be optimized by increasing the weight of the catalyst, *i.e.,* working with a lower molar substrate/metal ratio (20 instead of 100, before). After 5 h, under 5 bar of N_2 at 180°C (Table II-A.6, entry 4), only monomers were obtained with, a yield of phenol of *ca.* 42%$_C$ (S = 98%). We thus concluded that the metal surface needs to be increased to get higher amounts of Rh-H species available. With $Ni^0_{NH_3}/SiO_2$, reactions *(ii)* and *(iii)* were preferred (Figure II-A.1) as shown by Barton *et al.* [17]. Under 5 bar of N_2 at 180°C and a substrate/Ni molar ratio of 100, 100% of the C-OAr bonds were cleaved (no dimers remaining) after 5 h (Table II-A.6, entry 5) but the phenol yield and selectivity were low (Y = 20%$_C$, S = 47%) due to the rapid hydrogenation under these conditions. Working with a shorter time (1 h, Table II-A.6, entry 6), all dimers were also converted, and the phenol yield was, for a substrate/metal molar ratio of 100, among the highest of our work (Y = 33%$_C$) with fairly high selectivity (77%). It has to be noticed here that, for both $Rh^0_{NH_3}/SiO_2$ and $Ni^0_{NH_3}/SiO_2$ catalysts, phenol maximization could be achieved without the assistance of another metal such as Ag, which was tested for example with Ni [74].

At this stage, it seemed important to optimize the activity of Ni_{NH_3}/SiO_2. Indeed, all of the materials used that were reduced at 500°C, Ni_{NH_3}/SiO_2 was the only one capable of producing large quantities of phenol with a substrate/metal molar ratio of 100.

Reduction temperature effect on the Ni-based catalyst

Earlier, H_2-TPR analysis of the Ni-based catalyst showed that Ni(II) is much more difficult to reduce than Rh(III) (Figure II-A.5 b), particularly due to the formation of Ni(II) phyllosilicates precursors, upon silica impregnation in the presence of ammonia. For this reason, new $K1_{HH}$ hydrogenolysis tests were undertaken using Ni_{NH_3}/SiO_2 reduced at 650°C or 750°C. Under the conventional reaction conditions described previously (5 h and under 5 bar of N_2 at 180°C with a substrate/metal molar ratio of 100), $K1_{HH}$ conversion and also the cleavage C-OAr bond were clearly improved (100% each) by reducing Ni(II) at 650°C (Figure II-A.17). After only 1 h, $K1_{HH}$, as well as, all the potential dimers ($A1_{HH}$ or/and $C1_{HH}$) were converted into cleavage products giving rise to the highest phenol selectivity (S = 91%) and yield (39%$_C$) obtained starting from $K1_{HH}$ up to now, and a phenol hourly formation rate of 7.8 x 10^{-1} mmol h^{-1} (Eq. II-A1.5). This was 8 times more than with $Rh^0{}_{NH_3}/SiO_2$ reduced at 500°C, tested with $K1_{HH}$ for 8 h (40%$_C$, 9.59 x 10^{-2} mmol h^{-1}, S = 100%) (Table II-A.6, entry 1), and 4 times more than $Rh^0{}_{NH_3}/SiO_2$ reduced at 500°C, tested with $A1_{HH}$ for 5 h with a substrate/metal ratio 20 (42%$_C$, 1.87 x 10^{-1} mmol h^{-1}, S = 98%) (Table II-A.6, entry 4).

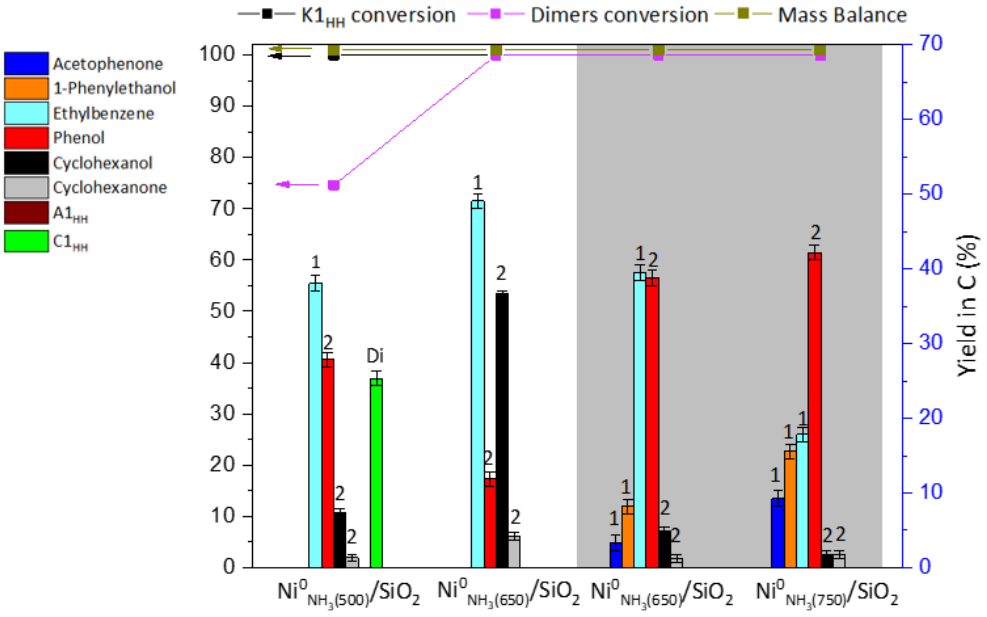

Figure II-A.17: *$K1_{HH}$/dimers conversion, mass balance and yields of the main products obtained with $Ni^0{}_{NH_3}/SiO_2$ reduced at different reduction temperatures (500, 650 or 750°C) and tested for 1 h (grey background) or 5 h (white background). Numbers 1 and 2 on the graph indicate from which aromatic ring of $K1_{HH}$ (Figure II-A.1) the monomers originate.*
Reaction conditions: $[K1_{HH}]_o$ = 0.06 M, $V_{i\text{-}PrOH}$ = 15 mL, molar subs./metal = 100, 180°C, 5 bar of N_2.

Similar results for phenol production (Y = 42%$_C$, 8.3 x 10^{-1} mmol h^{-1}) with a high selectivity (S = 98%) were obtained after reducing $Ni^{II}_{NH_3}/SiO_2$ at 750°C (Figure II-A.17). These results also confirm that $Ni^0_{NH_3}/SiO_2$ is very reactive towards the hydrogenation of aromatics, especially that of phenol [18]. Even after 1 h, cyclohexanone and cyclohexanol were observed when using $Ni^0_{NH_3(650)}/SiO_2$ and $Ni^0_{NH_3(750)}/SiO_2$ catalysts. These two catalysts also gave rise to 1-phenylethanol and acetophenone at the expense of ethylbenzene. The two, and especially acetophenone, which were never formed in the tests performed with $Ni^0_{NH_3(500)}/SiO_2$ (Figure II-A.13 and Table II-A.6) and which are disappearing with time (see after 5 h with $Ni^0_{NH_3(650)}/SiO_2$) would indicate that the reaction pathway *(i)* (Figure II-A.1) would be part of the global mechanism of $K1_{HH}$ reductive cleavage at least for the catalysts reduced at 650 and 750°C. As a result, the highest possible degree of Ni^{2+} reduction into metallic Ni appears to be necessary to optimize the cleavage of C-OAr bonds instead of the hydrogenation of the C=O bond of $K1_{HH}$.

Last but not least, it could be emphasized that $Ni^0_{NH_3(750)}/SiO_2$ was quite stable during the reaction (Figure II-A.18). Indeed, after the 1 h catalytic test, the particles sizes distribution was very similar to that of the fresh catalyst (Figure II-A.10 d), also analyzed after the same calcination post-treatment (average size of 3.7 nm in each case).

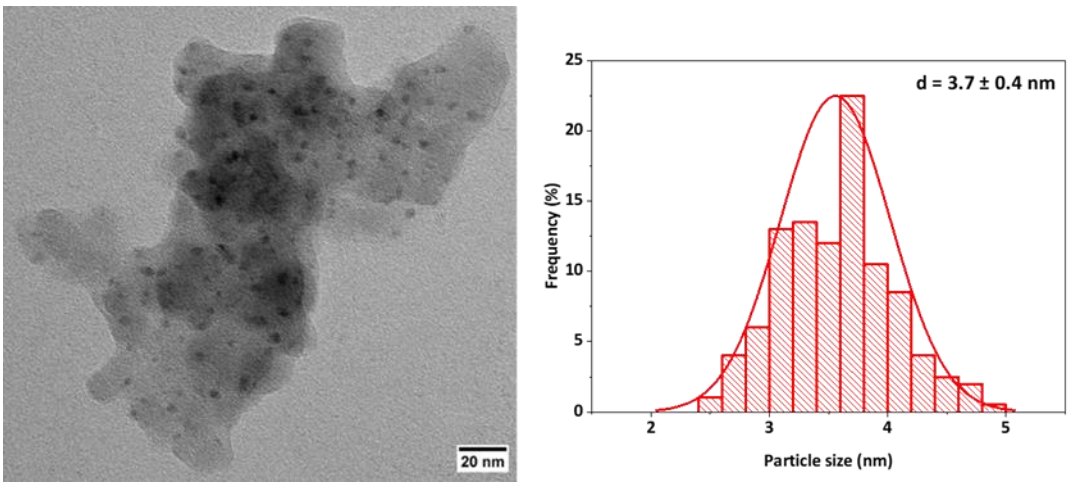

Figure II-A.18: *TEM image of used of $Ni^0_{NH_3(750)}/SiO_2$ after 1 h test (see Figure II-A.17) with $K1_{HH}$ and corresponding particle size distribution. The recovered catalyst was calcined at 550°C before analysis. Reaction conditions: $[K1_{HH}]_o$ = 0.06 M, $V_{i\text{-}PrOH}$ = 15 mL, molar subs./metal = 100, 180°C,1 h, 5 bar of N_2.*

The stability of the catalytic activity of $Ni^0_{NH_3(750)}/SiO_2$ during $K1_{HH}$ hydrogenolysis at 180°C for 1 h was also investigated (Figure II-A.19). Hence, a first test was carried out, affording 100% conversion of dimers and 42%$_C$ yield of phenol as already shown in Figure II-A.17. After cooling, $K1_{HH}$ was replenished and a second run was carried out immediately under the same conditions. It is noteworthy, that during this second run, $K1_{HH}$ was also totally converted but some decrease in dimers conversion and yield of phenol was observed (84% and 36%$_C$, respectively), probably as the result of a partial re-oxidation of Ni between the two tests. Again, acetophenone was detected in the two runs.

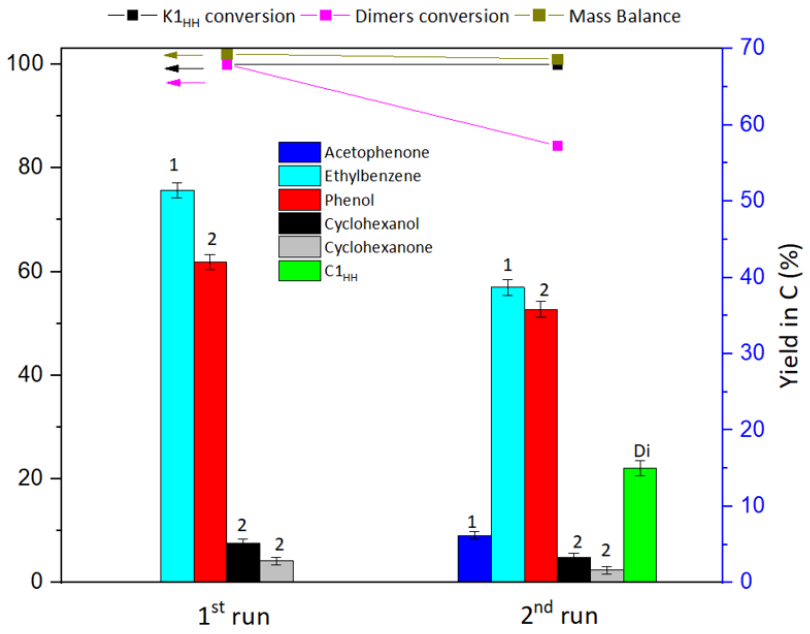

Figure II-A.19: *Stability test of $Ni^0_{NH_3(750)}/SiO_2$.*
Reaction conditions: $[K1_{HH}]_o$ = 0.06 M, $V_{i\text{-}PrOH}$ = 15 mL, molar subs./metal = 100, 180°C,1 h, 5 bar of N_2.

II-A1.4. Conclusion

Five materials based on Ni, Rh or Ni and Rh (in varying proportions) were prepared by the impregnation of a commercial silica (Aerosil 380) with aqueous solutions of the corresponding metal salts with added NH_3, targeting *c.a.* 5 wt.% of metal. After drying, a series of characterizations were carried out, showing a systematic increase in the pore volume associated with the use of NH_3. Concerning the deposited metal species, it could be stated that phyllosilicate-type nickel (II) species of the Talc type, difficult to reduce by H_2, were formed, whereas Rh(III) cations would tend to form isolated species, but easily reducible under the microscope electron

beam. In all cases, after reduction at 500°C and calcination at 550°C, nanoparticles, a priori consisting of Ni oxide, Rh oxide or mixed oxides of both, with an average diameter of around 2 nm, were observed under the microscope. In the case of bimetallic materials, the good dispersion of the two metals and the expected molar proportions (*i.e.*, 25/75, 50/50 and 75/25) were attested by STEM/HAADF, ICP-OES and H_2-TPR.

After reduction under H_2 at 500°C, these materials, which are fairly similar in terms of metallic dispersion and textural properties, were tested on a molecule modelling the β-O-4 bond of a pre-oxidized lignin in the presence of isopropanol as hydrogen donor. With such a substrate, eight compounds can be obtained, some by the desired hydrogenolysis (formation of phenol and acetophenone) and others by hydrogenation of the carbonyl group (formation a new dimeric molecule) or by the undesired hydrogenation of the aromatic rings or any combination of these reactions. After verification, dihydrogen was not selected as it is more effective in converting phenol to cyclohexanol and cyclohexanone for both metals, hence the decision to carry out catalytic tests at 180°C in isopropanol under N_2.

Clearly, the initial experiments carried out over a period of 5 h with a substrate/metal ratio equal to 100 highlighted the very high reactivity of the Ni-based catalyst and also its tendency to produce cyclohexanol before the final dimer ($C1_{HH}$) derived from the model molecule was completely cleaved by hydrogenolysis. The Rh-based catalyst was much less efficient at converting the model molecule but was more selective towards phenol, even though a dimer different from the previous one ($A1_{HH}$) had accumulated in the reaction medium. Unfortunately, the Rh- and Ni-based bimetallic materials prepared in this work did not increase the phenol yield in the time available. They seemed to behave like the dominant metal. Further studies confirmed the low reactivity of $A1_{HH}$ in the presence of the Rh-based catalyst and hence its accumulation. With Rh, more time is needed (8 h instead of 5 h) to compensate for the low reactivity of $A1_{HH}$ and, in the end phenol, is formed fairly selectively. On the other hand, an increase in time is not beneficial to the formation of phenol, but rather to its hydrogenation products. With the Ni-based catalyst, gas phase mass spectrometry studies have highlighted the presence of dihydrogen formed a priori from unstable Ni hydrides.

In the end, better phenol yields were obtained with the Ni-based catalyst provided the latter was reduced beyond 650°C. Under these conditions, still with a substrate/metal ratio equal to 100, the

maximum phenol yield was achieved in 1 h, instead of 8 h for Rh, which means that the Ni-based catalyst reduced to 750°C, for example, is 8 times more active than the Rh-based catalyst for hydrogenolysis of the bond between the two aromatic rings. Interestingly, microscopy images taken on the Ni-based catalyst reduced at 750°C and tested for 1 h showed the stability of the particles, even though some catalysts deactivation was observed. The present study has enabled a fairly perfect comparison to be made between materials prepared under very similar conditions and having textural and metallic dispersion properties that are potentially active for the valorization of lignin by reductive depolymerization. Admittedly, the molecule used is not the perfect model of the β-O-4 bond, which is why further work is being carried out with guaiacylglycerol-β-guaiacyl ether a more closely related molecule, but we believe that the main factors affecting selectivity have been identified.

Chapter II – Part A2: Additional studies

Part A2-1: Investigating the effect of the rhodium(III) and nickel(II) counter-anion (chloride or nitrate) on the corresponding silica-based supported catalysts

II-A2-1.1. Introduction

Phyllosilicates (PSs) are an important group of minerals constituted of tetrahedral and octahedral sheets. The tetrahedral one consists of Si^{4+} ions, each one bonded by 4 oxygen atoms and the octahedron involves another central cation, M^{n+} (such as Ni^{2+}, Mg^{2+}, Co^{2+}, Cu^{2+}, Zn^{2+} etc.…), coordinated with 6 anions, which can be O^{2-} or OH^{-}. For example, phyllosilicates can be obtained by impregnating silica supports with aqueous solutions of metal cations under alkaline conditions during the preparation of silica-based catalysts. In that case, it has been observed that superficial silica is partially dissolved, hence generating soluble silicates. The latter then react with metal cations, and hydroxide anions in the solution to form the phyllosilicate structure that is further deposited on silica [75] (this fact highlighted the reason behind the deposition of metal on the outer grains surface of porous supports). It is important to note that phyllosilicate-based materials have been developed and used in different areas, such as electrochemical water splitting, sensor, drug delivery [76].

The range of alkalinity provided by aqueous solutions of ammonia is able to induce a slight dissolution of the surface of silica grains. Meanwhile, when nickel nitrate was used as precursor [60,77,78], ammonia could contribute to the formation of a nickel ammonia complex, avoiding the generation of a $Ni(OH)_2$ precipitates. Then, soluble silicates can react with soluble nickel species in equilibrium with $[Ni(NH_3)_6]^{2+}$ [79,80] leading to Ni-O-Si hetero-condensation/polymerization affording PSs [55] (Figure II-A.20 [58]).

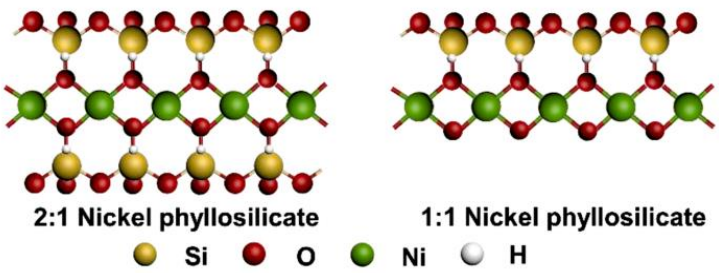

Figure II-A.20: *Schematic diagram of the layered structure of nickel phyllosilicate [58].*

The formation of PSs would help to minimize the size of the metal particles (and favor high dispersion) obtained by the reduction of the cations embedded in octahedra, since PSs provide an indirect way to control the number of nuclei [56] by preventing the migration (aggregation) to a large extent of nickel on the surface at high temperature. Another explanation for high metal dispersion at the end suggests that during the reduction step with H_2, Ni^{2+} species in phyllosilicate phase would not be fully reduced. Then, remaining nickel ions would act as strong anchoring sites of the Ni^0 nanoparticles onto silica leading to an enhanced metal dispersion and to a decreased metal sintering.

As reported, pH value of the mixed solution system between silica and nickel can significantly affect the crystal form and crystallization properties of nickel phyllosilicate. $Ni(OH)_2$ can be formed through the hydroxylation and polymerization reactions between Ni^{2+} ions and silanol groups on the surface of silica framework under neutral conditions. Ni–O–Si heterogeneous polycondensation reaction occurs between Ni^{2+}–$(OH)_2$ and silicic acid (denoted as Si–OH) on the SiO_2 framework to form 1:1 nickel phyllosilicate (Si–O–Ni−OH) under alkaline conditions. More silicic acid will be formed under acidic conditions, and 2:1 nickel phyllosilicate (Si–O–Ni–O–Si) can be obtained through the further reaction between 1:1 nickel phyllosilicate and silicic acid (Si–OH) [58,81].

Earlier in Part A1, phyllosilicates were formed with nickel nitrate as a precursor. This was demonstrated by TEM and H_2-TPR. No phyllosilicates were detected for rhodium chloride used as precursor. According to literature, no formation of rhodium-phyllosilicates was reported till now. The only occurrence dealing with “phyllosilicates” and “rhodium” is given by the work of Herrero *et al*. These authors reported the use of phyllosilicates as supports for rhodium catalysts but, in that case, these were prepared by reduction at room temperature of a cationic organometallic

rhodium norbornadiene compound anchored on palygorskite and montmorillonite supports [82,83]. Is this absence of rhodium phyllosilicates related to the counterion Cl^- or NO_3^-? The impact of the metal precursor on the textural properties as well as the rhodium and nickel characteristics will be analyzed in this part.

II-A2-1.2. Experimental section

Metal insertion was performed by the impregnation of Aerosil 380 with aqueous Rh(III) or Ni(II) using chloride or nitrate as precursors.

The detailed preparation of the solids was presented in Chapter II – Part A1, paragraph II-A1.2.1. The required amount of $RhCl_3.3H_2O$ or $Rh(NO_3)_3.xH_2O$ or $NiCl_2.6H_2O$ or $Ni(NO_3)_2.6H_2O$ (corresponding to 5 wt.% of Rh or Ni) was introduced. The resulting materials were denoted as **$Rh^{III}_{NH_3}/SiO_2$-Cl, $Rh^{III}_{NH_3}/SiO_2$-NO_3, $Ni^{II}_{NH_3}/SiO_2$-Cl and $Ni^{II}_{NH_3}/SiO_2$-NO_3**.

The characterization methods and the conditions for the catalytic test are detailed in experimental part (Appendix 1) and in Chapter II – Part A1, paragraph II-A1.2.2, respectively.

II-A2-1.3. Results and discussion

Figure II-A.21 A and B display the nitrogen adsorption-desorption isotherms of the solids in their dried *as-synthesized* form and, Table II-A.8, their textural parameters. As already shown for $Rh^{III}_{NH_3}/SiO_2$-Cl and $Ni^{II}_{NH_3}/SiO_2$-NO_3, all samples, were characterized by type II isotherms [50]. The specific area of $Rh^{III}_{NH_3}/SiO_2$-NO_3 was higher by 14% than that of $Rh^{III}_{NH_3}/SiO_2$-Cl, but their pore volume and mean pore diameter were almost the same. $Ni^{II}_{NH_3}/SiO_2$-Cl and $Ni^{II}_{NH_3}/SiO_2$-NO_3 samples showed similar textural parameters with a little decrease of the adsorbed N_2 volume for the sample obtained from the chloride precursor. To conclude, the pore volumes of the four samples were relatively similar between each other but the average pore diameter always appeared to be lower for the nickel samples.

Table II-A.8: *Physicochemical properties of dried as-synthesized Rh or Ni-Aerosil silica-based materials prepared with chloride and nitrate metal precursors.*

Materials	S_{BET} ($m^2\ g^{-1}$)	V_{Des}[a] ($cm^3\ g^{-1}$)	D_{pores}[b] (nm)	Ni (wt.%) TPR [Theo] *ICP*	Rh (wt.%) TPR [Theo] *ICP*
SiO_2	333	0.56	10.7	-	-
SiO_2-NH_3	269	1.23	19.0	-	-
$Rh^{III}{}_{NH_3}/SiO_2$-Cl	231	1.1	19.8	-	3.8[c] [5] *4.2*
$Rh^{III}{}_{NH_3}/SiO_2$-NO_3	264	1.2	19.8	-	11.5[c] [5] *4.0*
$Ni^{II}{}_{NH_3}/SiO_2$-Cl	291	1.0	15.7	4.2[c] [5] *4.6*	-
$Ni^{II}{}_{NH_3}/SiO_2$-NO_3	288	1.0	15.8	4.1[c] [5] *4.9*	-

[a] Estimated from BJH desorption (between 2 and 50 nm in diameter); [b] Deduced from the BJH desorption pore size distribution; [c] Ni and Rh loadings could be evaluated by considering the reduction of one mole of Rh(III) (or Ni(II)) requires 3/2 mole of H_2 (or 1 H_2). The large difference in Rh wt.% in the case of $Rh^{III}{}_{NH_3}/SiO_2$-NO_3 between the TPR and theoretical values may be due to the presence of nitrates not well eliminated during the washing process.

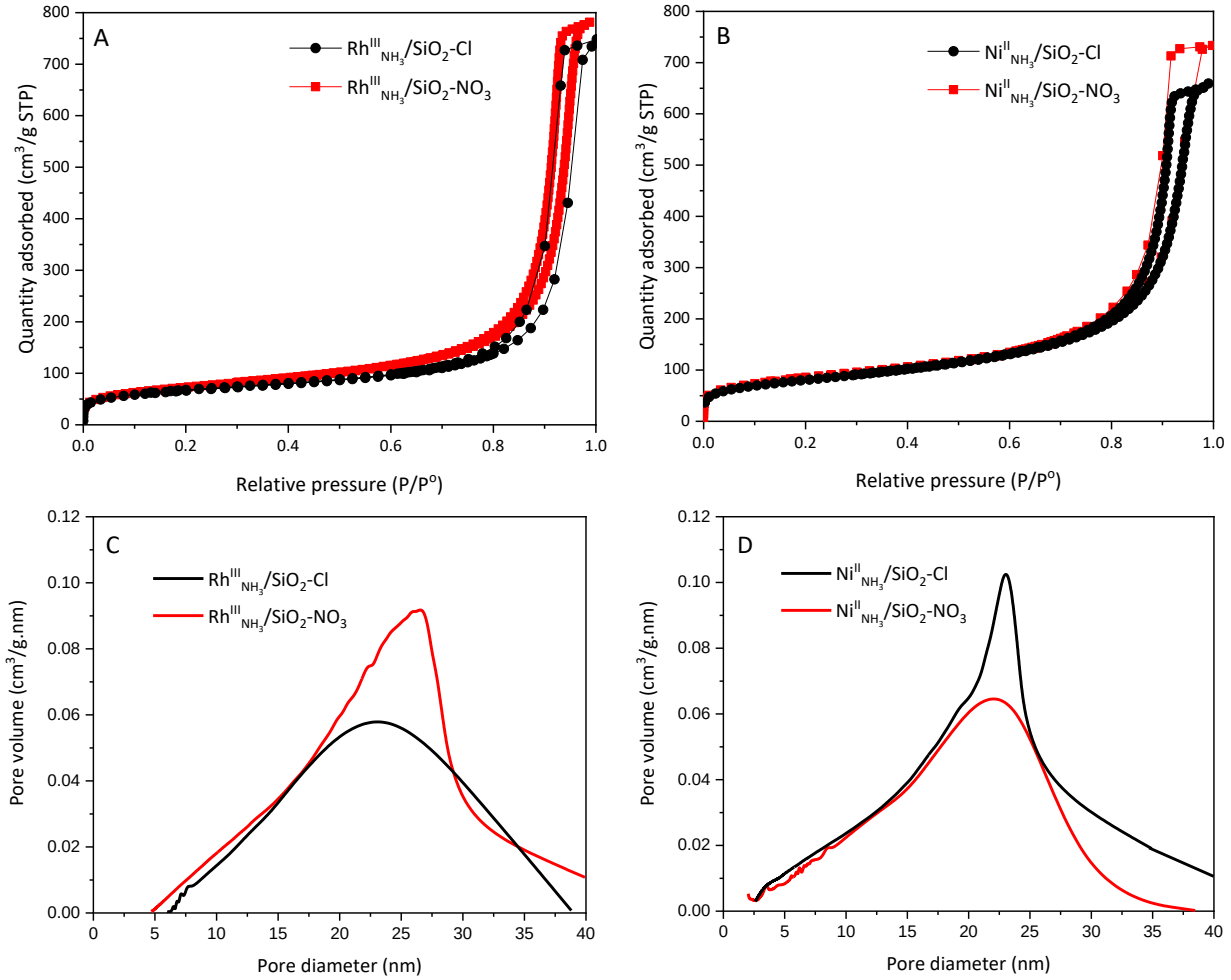

Figure II-A.21: *N_2 adsorption-desorption isotherms at -196°C of (A) Rh- and (B) Ni-Aerosil silica-based materials with their pore size distribution (C and D, respectively) prepared with chloride (black) or nitrate (red) precursors.*

According to ICP-OES measurements, it is important to note that the metal is well fixed on the support and more or less the same for the two Rh and the two Ni samples prepared with chloride or nitrate precursors. In fact, no effect of the counterion was seen on the quantity fixed.

In wide angle XRD, no clear peak could be evidenced for $Rh^{III}_{NH_3}/SiO_2$-Cl and for $Rh^{III}_{NH_3}/SiO_2$-NO_3 (Figure II-A.22 A). In contrast, $Ni^{II}_{NH_3}/SiO_2$-Cl showed small broad peaks, around $2\theta = 33.9^o$, 36.6^o and 60.5^o, corresponding to a nickel phyllosilicate phase, as observed previously in the case of $Ni^{II}_{NH_3}/SiO_2$-NO_3 (Figure II-A.22 B). It is noteworthy that those peaks would be less intense with the chloride counter-anion.

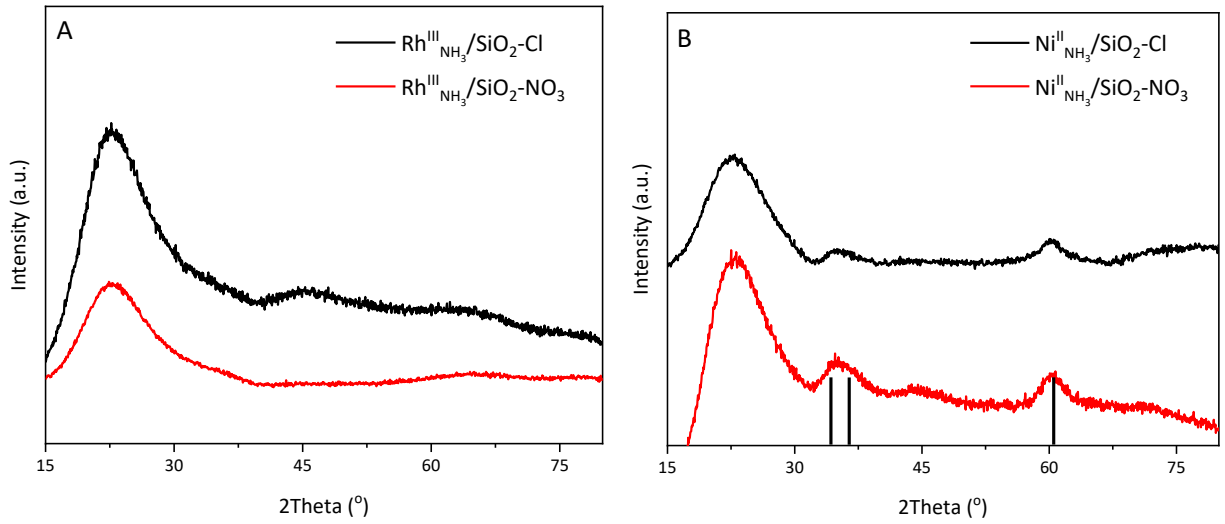

Figure II-A.22: *Wide angle XRD of dried Rh or Ni-Aerosil silica-based materials prepared from chloride and nitrate metal precursors.*

Earlier in this work, TPR analysis showed that the material prepared from Rh(III) chloride was much more readily reduced than that prepared from Ni(II) chloride. Here, it appears that changing from Rh(III) chloride to Rh(III) nitrate induces little modifications of the two reduction temperatures (with slightly lower reduction temperatures for chloride compared to nitrate) (Figure II-A.23 A). As mentioned before, the first, at 117°C (for $Rh^{III}_{NH_3}/SiO_2$-NO_3, 161°C for $Rh^{III}_{NH_3}/SiO_2$-Cl) could be attributed to the reduction of Rh^{3+} species with low interaction and/or big aggregates, the second at 215°C (for $Rh^{III}_{NH_3}/SiO_2$-NO_3, 254°C for $Rh^{III}_{NH_3}/SiO_2$-Cl) could be assigned to the reduction of Rh^{3+} ions strongly interacting with SiO_2. For $Rh^{III}_{NH_3}/SiO_2$-Cl, the first

peak was the minor contribution while it was the major one for $Rh^{III}_{NH_3}/SiO_2$-NO_3 meaning that Rh(III) would be less dispersed in that case.

For Ni samples, it appears that changing from Ni(II) nitrate to Ni(II) chloride induces stronger modifications of the reduction temperatures of the corresponding samples (Figure II-A.23 B). Indeed, earlier in this work, the TPR profile of $Ni^{II}_{NH_3}/SiO_2$-NO_3 was characterized by a major contribution at 765°C and a small one et 360°C while that of $Ni^{II}_{NH_3}/SiO_2$-Cl showed here a major peak of H_2 consumption at 400°C and a really small one at 719°C. Hence the use of chloride counter-ions for Ni(II) would have a negative effect on metal dispersion, since decreasing the amount of Ni-phyllosilicates evidenced for $Ni^{II}_{NH_3}/SiO_2$-NO_3 using TEM, PDF and XRD.

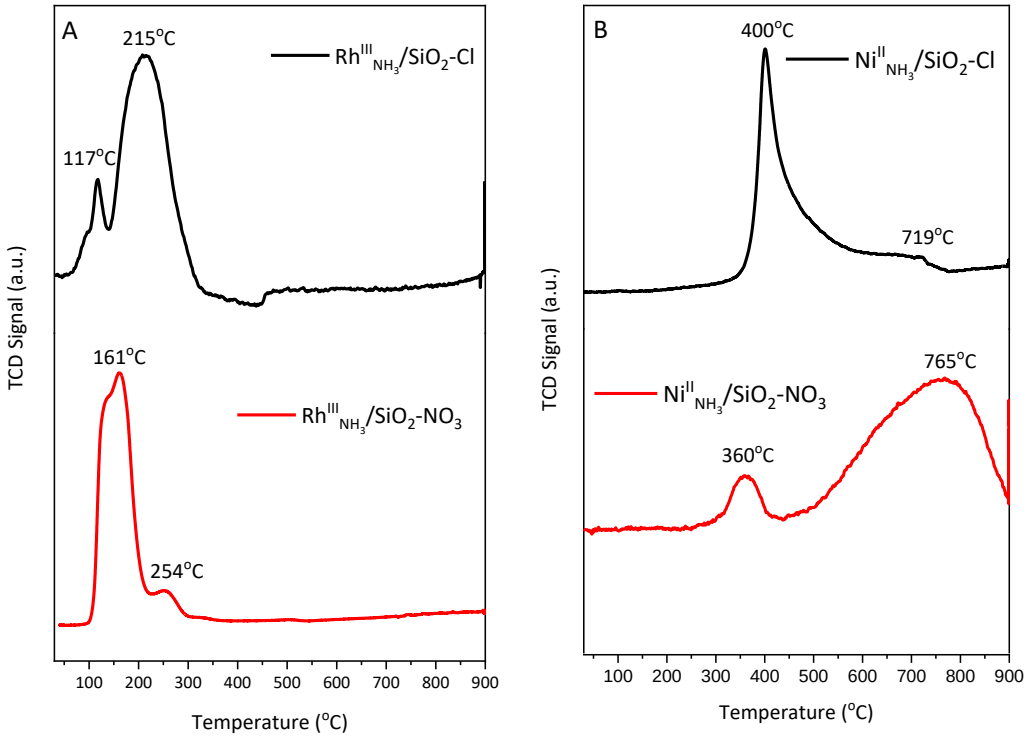

Figure II-A.23: *H_2-TPR profiles of dried as-synthesized Rh or Ni- Aerosil silica-based materials prepared either with chloride or nitrate metal salt precursors.*

The as-synthesized dried solids were also analyzed by transmission electron microscopy to complete the characterization of the Rh and Ni species. As shown before in Chapter II – Part A1, paragraph II-A1.3.1, $Rh^{III}_{NH_3}/SiO_2$-Cl showed small and well-dispersed nanoparticles (Figure II-A.24 A) probably obtained from the *in-situ* reduction of Rh(III) under the electron beam of the microscope [57]. Instead, the TEM images of $Rh^{III}_{NH_3}/SiO_2$-NO_3 revealed some heterogeneity with

large agglomerates of particles coexisting with more dispersed ones (Figure II-A.24 B). As shown before (Chapter II – Part A1, paragraph II-A1.3.1), $Ni^{II}_{NH_3}/SiO_2$-NO_3 TEM images (Figure II-A.24 D) showed branchlike structures that could correspond to Ni phyllosilicates [41]. Instead, those of $Ni^{II}_{NH_3}/SiO_2$-Cl emphasized the presence of small and well dispersed nanoparticles (Figure II-A.24 C)

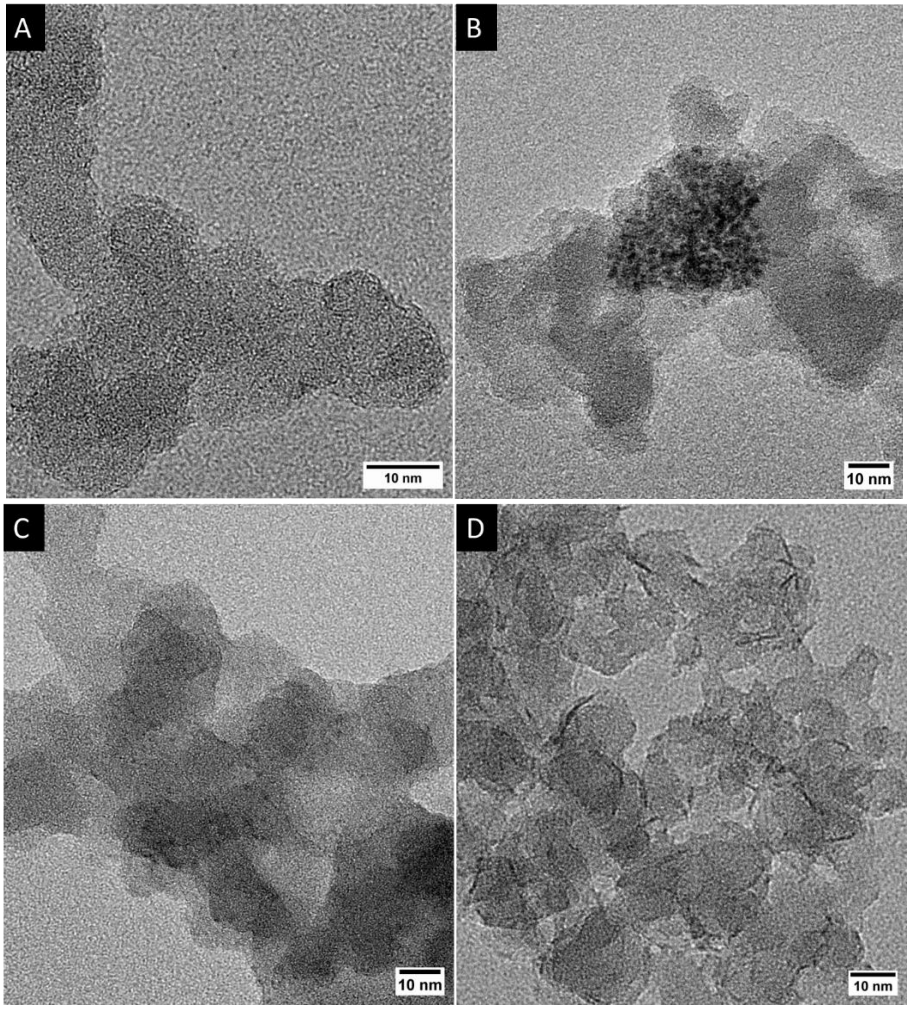

Figure II-A.24: *TEM images of dried as-synthesized (A) $Rh^{III}_{NH_3}/SiO_2$-Cl, (B) $Rh^{III}_{NH_3}/SiO_2$-NO_3, (C) $Ni^{II}_{NH_3}/SiO_2$-Cl and (D) $Ni^{II}_{NH_3}/SiO_2$-NO_3.*

The UV-Visible spectra (diffuse reflectance) of the four dried *as synthesized* materials were also recorded in order to identify some of the absorption bands that might be related to the soluble Rh(III) and Ni(II) species present in the aqueous ammonia during the impregnation procedure. Regarding rhodium, it is noteworthy that $[Rh(NH_3)_6]^{3+}$ or $[Rh(NH_3)_5X]^{3+}$ (X = Cl) complexes or

rhodium hydroxides are expected. According to literature, $[Rh(NH_3)_6]^{3+}$ complex shows maximum absorption at 255 nm and 305 nm attributed to $^1A_{1g}$ to $^1T_{2g}$ and $^1A_{1g}$ to $^1T_{1g}$ transitions, respectively [84]. $[Rh(NH_3)_5X]^{3+}$ exhibited absorption peaks at 188, 275 and 345 nm [85]. Regarding $Rh^{III}_{NH_3}/SiO_2$-NO_3 and $Rh^{III}_{NH_3}/SiO_2$-Cl solids (Figure II-A.25 A), both exhibited absorption bands at 265 and 440 nm. Another one at a maximum wavelength higher than 800 nm was also observed for $Rh^{III}_{NH_3}/SiO_2$-NO_3. The band at 265 nm could be attributed to one of both complexes, $[Rh(NH_3)_6]^{3+}$ or $[Rh(NH_3)_5X]^{3+}$. However, the band at 440 nm did not correspond to either complex.

$Ni^{II}_{NH_3}/SiO_2$-Cl and $Ni^{II}_{NH_3}/SiO_2$-NO_3 solids were characterized by at least two absorption bands corresponding to i) the intense $^3A_{2g}$ to $^3T_{1g}$(P) transition in the 500-350 nm range and ii) the $^3A_{2g}$ to $^3T_{1g}$ transition in the 800-550 nm range which is itself divided into a peak at 740 nm and a shoulder at 660 nm (Figure II-A.25 B) observed for Ni^{2+} in octahedral or pseudo-octahedral geometry [86,87]. This absorption band system arises from coupling between two excited states at different multiplicity close in energy, leading to an interference between two transitions [88], it is due to spin–orbit coupling that mixes the $^3T_{1g}$(F) and ^1E_g states [89]. This absorption spectra is typical of UV-Vis spectra of $[Ni(H_2O)_6]^{2+}$ complex in aqueous solution [88]. In our case, no bands or peaks could be attributed to $[Ni(NH_3)_6]^{2+}$ at 357, 588 and 952 nm [88]. This can be explained by the fact that this complex formed during the impregnation step, has entirely disappeared after washing and drying.

It should be noted that for both metals, the spectra of the materials prepared with salts involving nitrate as a counter ion, in red, were apparently more intense, whereas the metals were deposited in equivalent quantities for Rh and Ni, respectively.

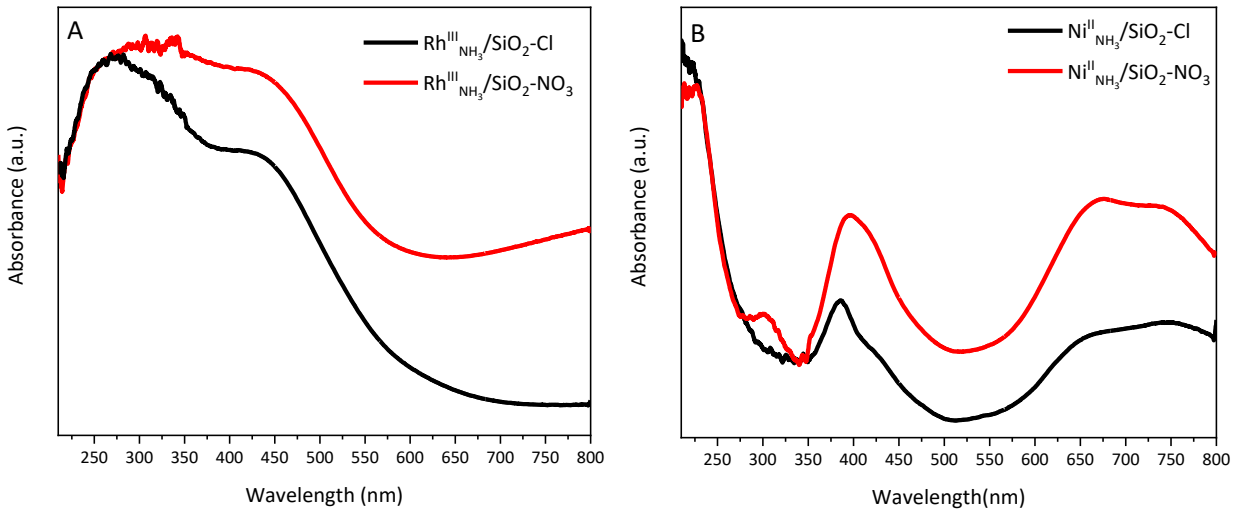

Figure II-A.25: *UV-Visible diffuse reflectance spectra of dried as-synthesized (A) Rh and (B) Ni-Aerosil based silica materials prepared with chloride (black) or nitrate (red) precursors.*

Another suitable way of monitoring the surface species of Rh and Ni is to use XPS. Measurements were made on dried *as-synthesized* $Rh^{III}_{NH_3}/SiO_2$-Cl, $Rh^{III}_{NH_3}/SiO_2$-NO_3, $Ni^{II}_{NH_3}/SiO_2$-Cl and $Ni^{II}_{NH_3}/SiO_2$-NO_3 (Figure II-A.26).

Both solids with Rh, prepared with chloride or nitrate precursors, exhibited exactly the same XPS spectra as shown in Figure II-A.26 A and B. After deconvolution, two main peaks, corresponding to Rh $3d_{5/2}$ and Rh $3d_{3/2}$, were evidenced. In the case of nickel samples, both solids showed also similar XPS spectra (Figure II-A.26 C and D), exhibiting two main peaks attributed to Ni $2p_{3/2}$ and Ni $2p_{1/2}$ core levels with their shake up satellites. XPS data were useful to reinforce the idea of the presence of phyllosilicates in $Ni^{II}_{NH_3}/SiO_2$-NO_3 [90]. Indeed, according to Coenen [70], $\Delta E_{Ni\text{-}Si}$ (Ni $2p_{3/2}$ *vs* Si 2p) should be between 753.2 and 753.6 eV when nickel silicate is formed. In our case, the value of $\Delta E_{Ni\text{-}Si}$ (753.3 eV) for $Ni^{II}_{NH_3}/SiO_2$-NO_3 was in the good range confirming the formation of phyllosilicates as already anticipated from XRD and TEM data while $\Delta E_{Ni\text{-}Si}$ (753.0 eV) for $Ni^{II}_{NH_3}/SiO_2$-Cl was a little bit out of the range expected.

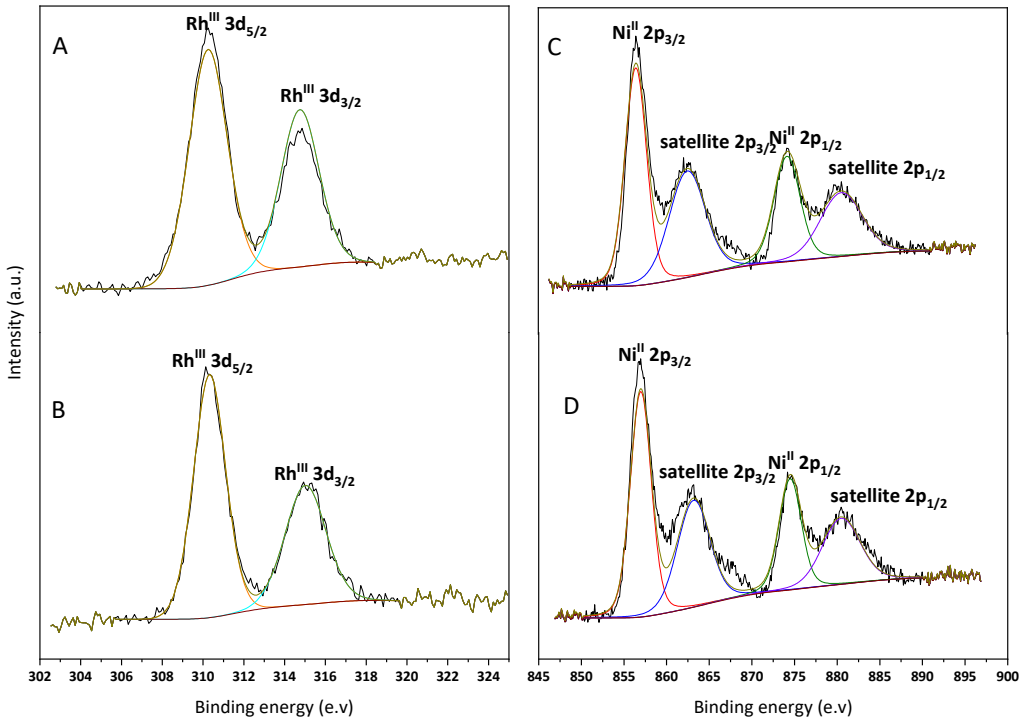

Figure II-A.26: *XPS spectra of the dried (A) $Rh^{III}_{NH_3}/SiO_2$-Cl, (B) $Rh^{III}_{NH_3}/SiO_2$-NO_3, (C) $Ni^{II}_{NH_3}/SiO_2$-Cl and (D) $Ni^{II}_{NH_3}/SiO_2$-NO_3.*

XPS spectra of chlorine and nitrogen were also performed (Figure II-A.27), chlorine being from rhodium or nickel chloride used as precursors in the preparation of $Rh^{III}_{NH_3}/SiO_2$-Cl or $Ni^{II}_{NH_3}/SiO_2$-Cl, nitrogen from ammonia and rhodium or nickel nitrate used as precursors in the synthesis of $Rh^{III}_{NH_3}/SiO_2$-NO_3 or $Ni^{II}_{NH_3}/SiO_2$-NO_3. As mentioned earlier (Chapter II – Part A1, paragraph II-A1.3.1), for $Rh^{III}_{NH_3}/SiO_2$-Cl and $Ni^{II}_{NH_3}/SiO_2$-Cl samples, one peak rather at low intensity at 199.3 eV was evidenced corresponding to Cl^- (Figure II-A.27 A and D). Figure II-A.27 B, C, E and F show a peak at 400.3 eV corresponding to N 1s (NH_3) for all samples, with a small shoulder at 402.6 eV for $Ni^{II}_{NH_3}/SiO_2$-NO_3. It can be noticed that the peak at 400.3 eV seemed to be more intense with $Rh^{III}_{NH_3}/SiO_2$ samples. For samples prepared with nitrate precursors, a peak at 407.6 eV was evidenced and could be attributed to a higher oxidation state of N corresponding to N 1s (NO_3) (Figure II-A.27 C and F).

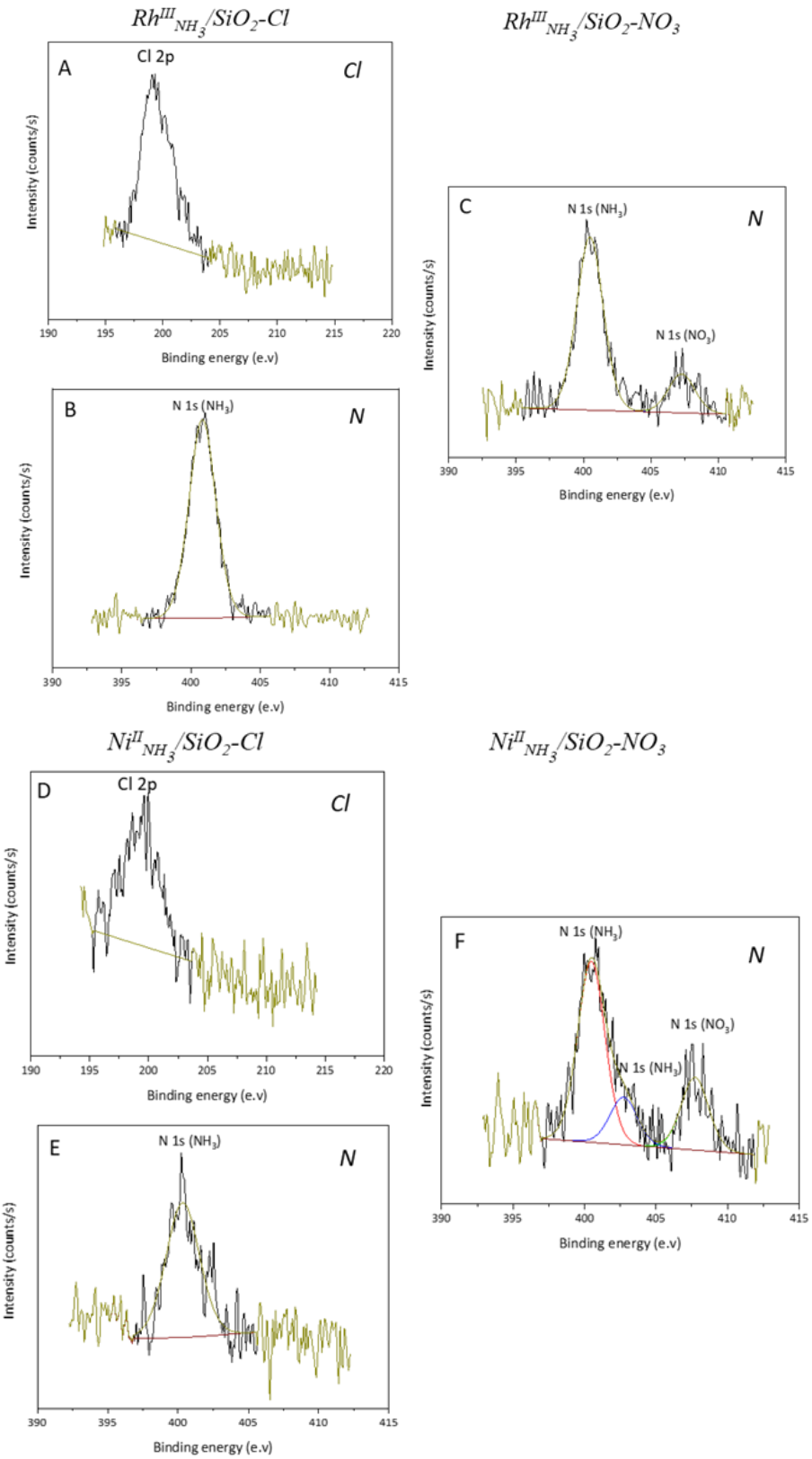

Figure II-A.27: *XPS spectra in N 1s and Cl 2p regions of (A,B) $Rh^{III}_{NH_3}/SiO_2$-Cl, (C) $Rh^{III}_{NH_3}/SiO_2$-NO_3, (D,E) $Ni^{II}_{NH_3}/SiO_2$-Cl and (F) $NI^{II}_{NH_3}/SiO_2$-NO_3.*

In parallel, pH measurements were performed at the different steps of the catalyst preparation, *i.e.*, on all four metal precursors dissolved in water then after adding NH_3 and silica, and finally after heating at 60°C for 2 h (Table II-A.9, entries 2, 3, 4 and 5). A blank experiment with no metal salt (Table II-A.9, entry 1) was also carried out. As Table II-A.9, entries 2 and 3 show, the pH value of aqueous nickel nitrate evidenced the influence of the counter-anion. Hence, the pH was lower with nitrate than that measured with nickel chloride in agreement with a higher acidity of Ni^{2+} in that case. After adding NH_3, the pH reached almost the same value (11.43-11.44) showing no more influence of the counter-anion. No precipitation was observed, but a blue color indicating the formation of $[Ni(H_2O)_{6-x}(NH_3)_x]^{2+}$ complexes at least in solution. The color of the silica changed from blue to green with time. The pH decreased sharply by 10% after adding silica (10.39) and, after heating the mixture at 60°C for 2 h, the pH values turned out to be the same (10.24 and 10.25).

As expected, both rhodium(III) precursors, nitrate and chloride, dissolved in water led to more acidic solutions than those with nickel at the same concentration (2.31 and 2.03 *vs.* 4.25 and 5.38, respectively). After adding NH_3, the pH increased to reach 10.55 and 10.65. In that case, precipitation occurred indicating the formation of yellowish rhodium hydroxide (instead of $[Rh(NH_3)_6]^{3+}$). The pH decreased slightly to 10.28 for both after adding silica (Table II-A.9 entries 4 and 5). Still, no significant influence of the counter-anion could be evidenced showing the small influence of the counter-anion after adding NH_3 and silica.

These results would indicate, in agreement with the UV-Vis spectra (Figure II-A.25), that similar species are obtained with the nitrate or chloride precursors used for each metal after contacting them with ammonia and silica.

Table II-A.9: *pH measurements of nickel and rhodium salts dissolved in water, after adding NH_3 and silica and after heating at 60°C for 2 h.*

Entry	Salt	pH			
		In water	**After NH_3 25 % addition**	**After SiO_2 introduction**	**After 60°C, 2 h**
1	-	6.12	11.58	10.76	10.74
2	$NiCl_2,6H_2O$	5.38	11.43	10.39	10.24
3	$Ni(NO_3)_2,6H_2O$	4.25	11.44	10.40	10.25
4	$RhCl_3,3H_2O$	2.03	10.55	10.28	10.15
5	$Rh(NO_3)_2,2H_2O$	2.31	10.65	10.28	10.33

After an *ex-situ* reduction treatment performed under H_2 (flow: 50 mL min^{-1}) at 500°C during 3 h, the four materials were tested as catalysts in the hydrogenolysis of $A1_{HH}$, looking at the influence of the metal precursor on the conversion of $A1_{HH}$ and of the dimers as well as on phenol selectivity. Earlier, it was shown that $Rh^0_{NH_3}/SiO_2$-Cl led to a slow reaction and reaction times up to 5 h were needed when using 1% mol of Rh (*vs.* $A1_{HH}$). Therefore, both Rh-based Aerosil silica materials were tested here for 5 h (Figure II-A.28 A), whereas, $Ni^{II}_{NH_3}/SiO_2$-Cl and $Ni^{II}_{NH_3}/SiO_2$-NO_3 were studied as catalysts for only 1 h (Figure II-A.28 B).

Regarding the rhodium catalysts, both showed relatively similar behaviors given the accuracy of our data. The conversion of $A1_{HH}$ was 85% with $Rh^0_{NH_3}/SiO_2$-NO_3 and 80% with $Rh^0_{NH_3}/SiO_2$-Cl. Dimers conversion values were 67% and 65%, respectively. Acetophenone and phenol were the two main products of $A1_{HH}$ cleavage, meaning that the two rhodium catalysts led to the dehydrogenation of the alcohol function of either $A1_{HH}$ or 1-phenylethanol. In this respect, it should be noted that, after 5 h, a significant amount of $K1_{HH}$ was formed with $Rh^0_{NH_3}/SiO_2$-NO_3 (Figure II-A.28 A).

Regarding the nickel catalysts, earlier in this chapter, it was shown that nickel nitrate, as a precursor, led only to monomers within 1 h with a phenol yield of *c.a.* $33\%_C$ (100% conversion of $A1_{HH}$ and all dimers) and some unwanted cyclohexanol and cyclohexanone. $Ni^0_{NH_3}/SiO_2$-Cl led also to 100% conversion of $A1_{HH}$, but lots of $C1_{HH}$ accumulated (only 34% of dimer conversion), resulting in 100% selectivity towards phenol, but a rather low yield ($18\%_C$) compared to $Ni^0_{NH_3}/SiO_2$-NO_3 (Figure II-A.28 B). These results highlight that the use of nitrate as a nickel precursor offers certain advantages in terms of activity. As phyllosilicates appeared to be the main species in the corresponding dried *as-synthesized* catalyst (see reducibility by TPR (Figure II-A.23 B), TEM (Figure II-A.24 D)), these new results appear to support our initial conclusions that Ni phyllosilicates play a crucial role in improving the catalytic behavior of the corresponding reduced Ni-based materials.

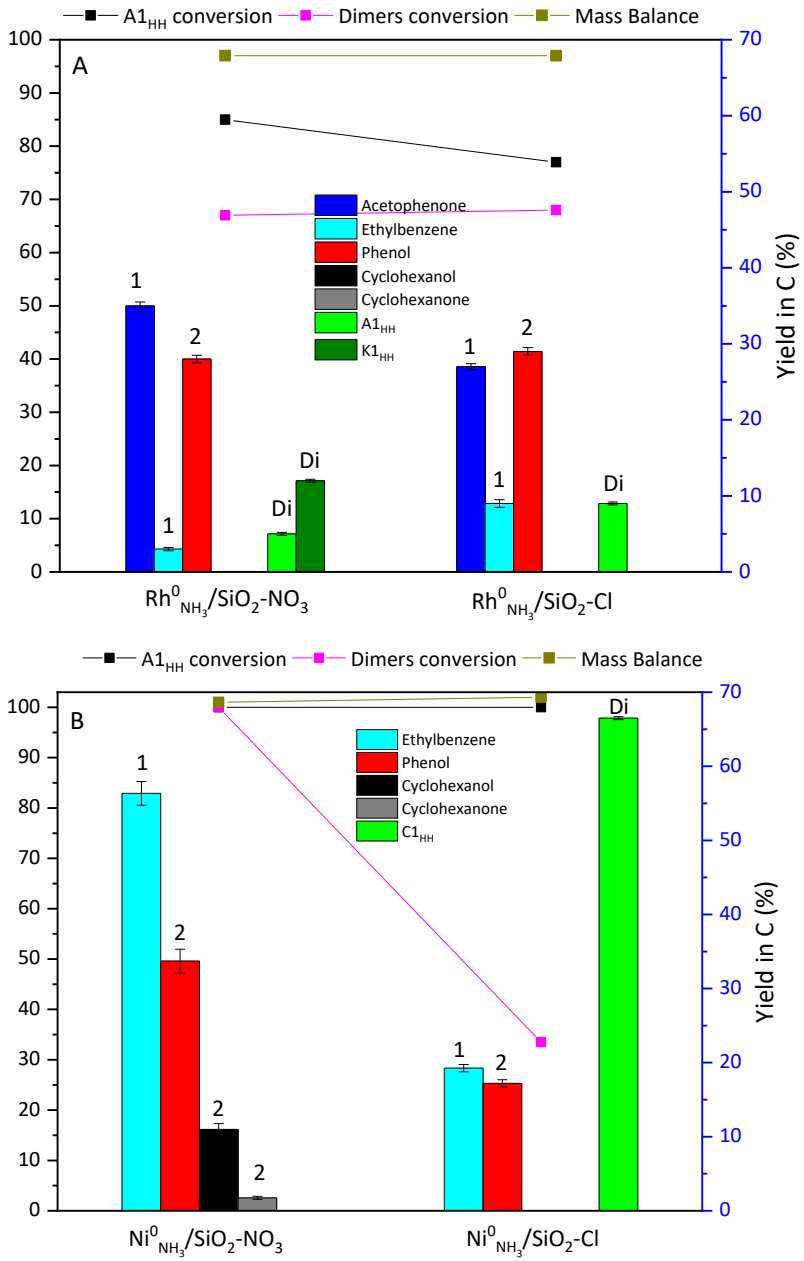

Figure II-A.28: *$A1_{HH}$/dimers conversion, mass balance and yield of the main products obtained with (A) Rh- and (B) Ni-Aerosil silica-based materials prepared with nitrate or chloride precursors.*
Reaction conditions: $[A1_{HH}]_o$ = 0.06 M, $V_{i\text{-}PrOH}$ = 15 mL, molar subs./metal = 100, 180°C, (A) 5 h, (B) 1 h, 5 bars of N_2.

II-A2-1.4. Conclusion

Using either nitrate or chloride metal salts precursors, two Rh(III) and two Ni(II)-Aerosil 380 based materials were prepared in the presence of aqueous ammonia and deeply characterized by TEM, H_2-TPR, XRD, N_2 physisorption, UV-Vis. spectroscopy and XPS. This confirmed that

nickel tends to form phyllosilicates under these conditions, whereas this does not seem to be the case with rhodium, for which we have found no traces of such compounds in the literature. Differences in reduction behavior were established by TPR measurements. Rhodium is reduced more easily than nickel, with slight differences between the use of rhodium (III) chloride and nitrate. With nickel, the differences in reduction behavior were much greater. Using nickel chloride leads to supported nickel(II) species that are much easier to reduce than using nickel(II) nitrate. The UV-Visible and XPS spectra of the materials before reduction did not appear so different to us, but more nano-sheets, also identifiable by XRD, were observed by TEM, suggesting that the use of nickel nitrate appears to be much more favorable to the formation of phyllosilicates than that of nickel chloride, as the result of the higher acidity of Ni^{2+} in that case. From the point of view of catalytic activity, the same strong differences between the use of nitrate or chloride were demonstrated for nickel-based materials, whereas they were less marked for rhodium. These new results provide further evidence in favor of the important role played by nickel phyllosilicates in obtaining more active Ni(0) particles, a priori because they are smaller than in the absence of these compounds, due to stronger interactions between Ni^{2+} and the support. TEM studies of the reduced materials should confirm this.

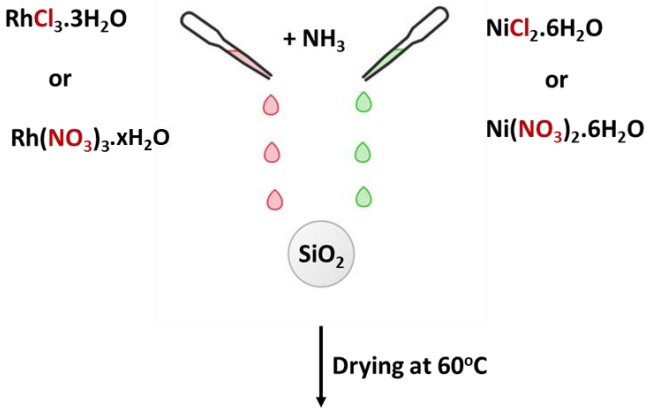

Materials	Formation of M-Phyllosilicates
$Rh^{III}_{NH_3}/SiO_2$-Cl	No
$Rh^{III}_{NH_3}/SiO_2$-NO_3	No
$Ni^{II}_{NH_3}/SiO_2$-Cl	No
$Ni^{II}_{NH_3}/SiO_2$-NO_3	Yes

Part A2-2: Impact of doping nickel by iron

II-A2-2.1. Introduction

To investigate the effect of iron on the catalytic activity, hydrogenolysis catalysts were prepared by supporting Ni and Fe nanoparticles on Aerosil 380. Interestingly, literature reported nickel-based bimetallic catalysts such as Ni-Fe for efficient hydrogenolysis of lignin [91–93]. This was interpreted by a synergistic effect between metal Ni and Fe which is thought not only to show high efficiency for cleaving ether bonds, but also to help prevent the hydrogenation of aromatic rings. Indeed, Fe-containing catalysts would exhibit a higher activity for the selective cleavage of C−O and C−OH bonds due to strong interactions between Fe sites and methoxy or hydroxyl groups, and low activity in ring hydrogenation [94,95].

Two silica-based heterogeneous catalysts were prepared by the impregnation of Aerosil 380 with Ni(II) and Fe(III) salts in the presence of aqueous ammonia. Targeted loadings were 5 wt.% for Ni and 0.5 or 1.2 wt.% of Fe. The prepared solids were characterized in their dried *as-synthesized* form $(Ni^{II}_{5\%}Fe^{III}_{0.5\%})_{NH_3}/SiO_2$ and $(Ni^{II}_{5\%}Fe^{III}_{1.2\%})_{NH_3}/SiO_2$ then their reactivity, after reduction, was evaluated and compared to that of non-doped $Ni^{II}_{NH_3}/SiO_2$ toward the hydrogenolysis of $A1_{HH}$.

II-A2-2.2. Materials preparation

Nickel-iron bimetallic catalysts were prepared according to Chapter II – Part A1, paragraph II-A1.2.1. where the required amount of $Ni(NO_3)_2.6H_2O$ (250 mg) and $Fe(NO_3)_3.9H_2O$ (35 mg or 86 mg) (corresponding to 5 wt.% of Ni and 0.5 wt.% or 1.2 wt.% of Fe, i.e. Fe/Ni molar percentage of 10 mol% and 25 mol%, respectively) dissolved in 5 mL of distilled water was introduced. Resulting solids were denoted $(Ni^{II}_{5\%}Fe^{III}_{0.5\%})_{NH_3}/SiO_2$ and $(Ni^{II}_{5\%}Fe^{III}_{1.2\%})_{NH_3}/SiO_2$. These solids will be compared to $Ni^{II}_{NH_3}/SiO_2$ containing also 5 wt.% of Ni.

The characterization methods and the conditions for the catalytic test are detailed in the experimental part (Appendix 1) and in Chapter II – Part A1, paragraph II-A1.2.2, respectively.

II-A2-2.3. Results and discussion

Herein, the difference between non-doped and doped $Ni^{II}_{NH_3}/SiO_2$ with 0.5 and 1.2 wt.% of Fe will be discussed. As shown in Figure II-A.29 A, the dried *as-synthesized* $Ni^{II}_{NH_3}/SiO_2$, $(Ni^{II}_{5\%}Fe^{III}_{0.5\%})_{NH_3}/SiO_2$ and $(Ni^{II}_{5\%}Fe^{III}_{1.2\%})_{NH_3}/SiO_2$ samples present type II isotherms [50]. Pore size distributions obtained by the BJH method applied to the desorption branch are very broad (from 5 to 40 nm) for all the materials (Figure II-A.29 B).

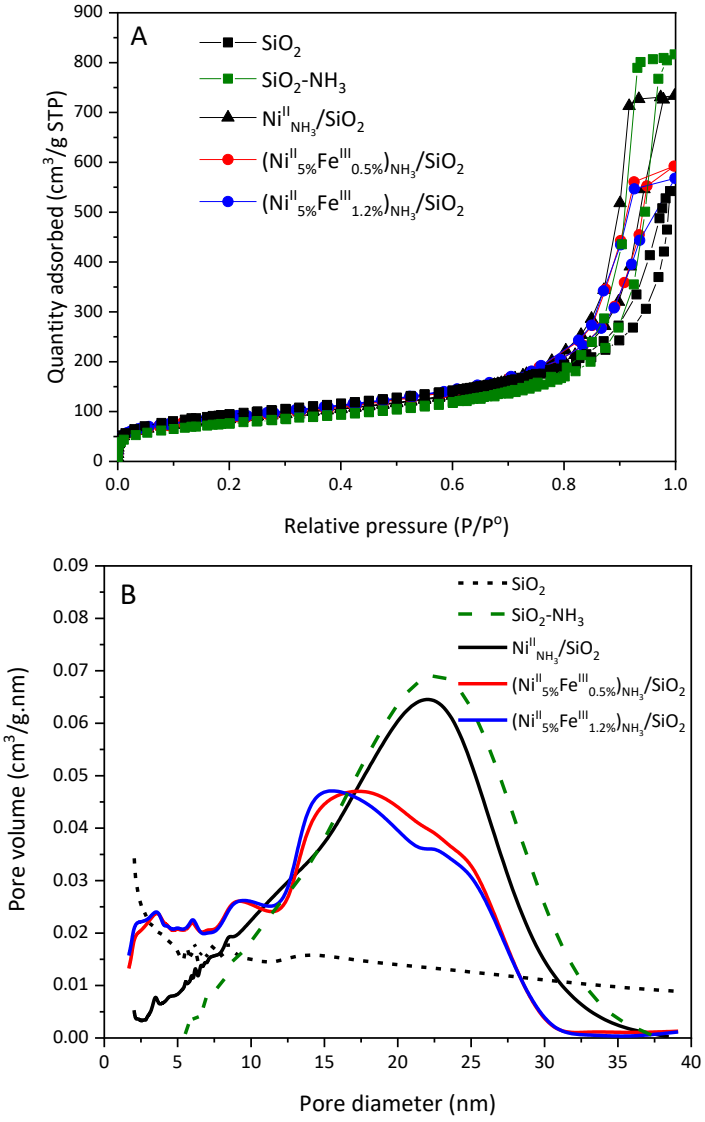

Figure II-A.29: *(A) N_2 adsorption-desorption isotherms at -196°C and (B) pore size distribution of $Ni^{II}_{NH_3}/SiO_2$, $(Ni^{II}_{5\%}Fe^{III}_{0.5\%})_{NH_3}/SiO_2$ and $(Ni^{II}_{5\%}Fe^{III}_{1.2\%})_{NH_3}/SiO_2$ samples.*

As seen in Table II-A.10, the specific area of both doped nickel with 0.5 or 1.2 wt.% iron samples exhibited a small increase of 9% compared to $Ni^{II}_{NH_3}/SiO_2$. However, doping nickel with iron resulted in a small decrease of the pore volume by 10% and 14% and the mean pore diameter value by 28% and 36% for $(Ni^{II}_{5\%}Fe^{III}_{0.5\%})_{NH_3}/SiO_2$ and $(Ni^{II}_{5\%}Fe^{III}_{1.2\%})_{NH_3}/SiO_2$, respectively. Such observations tend to confirm that nickel and iron species have been incorporated into the support.

Table II-A.10: *Physico-chemical properties of dried bimetallic Ni-Fe materials.*

Materials	S_{BET} ($m^2\ g^{-1}$)	V_{Des}[a] ($cm^3\ g^{-1}$)	D_{pores}[b] (nm)	Ni (wt.%) TPR [Theor] *ICP*	Fe (wt.%) TPR [Theor] *ICP*
$Ni^{II}_{NH_3}/SiO_2$	288	1.00	15.8	4.1 [5] *4.9*	-
$(Ni^{II}_{5\%}\text{-}Fe^{III}_{0.5\%})_{NH_3}/SiO_2$	315	0.90	11.3	5.65[c] [5] 4.91	0.57[c] [0.5] *0.50*
$(Ni^{II}_{5\%}\text{-}Fe^{III}_{1.2\%})_{NH_3}/SiO_2$	323	0.86	10.0	4.46[c] [5] *5.03*	1.00[c] [1.2] *1.12*

[a] From BJH desorption (between 2 and 50 nm in diameter); [b] From the BJH desorption pore size distribution; [c] Assuming that the nominal Ni:Fe ratio is not modified upon impregnation.

For the two Ni-Fe materials, ICP-OES analyses showed that, during silica impregnation, the experimental molar ratio of Fe/Ni was very similar to the nominal one (10.6 mol% and 23.6 mol% to be compared with 10 mol% and 25 mol%).

Previously, the broad signals of low intensity observed at 2θ = 34.1, 36.4 and 60.5° in the wide-angle X-ray diffractograms of $Ni^{II}_{NH_3}/SiO_2$ were assigned to nickel phyllosilicates (Figure II-A.30 a, (PDF 00-049-1859)) [51]. Adding iron(III) led to a continuous decrease of the intensity of these peaks (Figure II-A.30 b and c). This, possibly, could be explained by the inhibition of the formation of nickel phyllosilicates while adding iron.

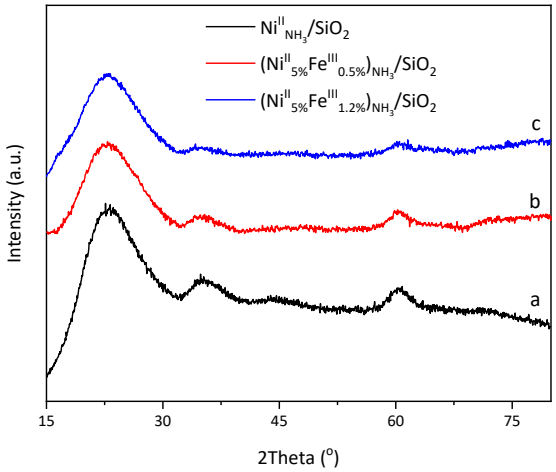

Figure II-A.30: *XRD patterns of (a) $Ni^{II}_{NH_3}/SiO_2$, (b) $(Ni^{II}_{5\%}Fe^{III}_{0.5\%})_{NH_3}/SiO_2$ and (c) $(Ni^{II}_{5\%}Fe^{III}_{1.2\%})_{NH_3}/SiO_2$ samples.*

To get some information on the interaction of nickel and iron with silica, the reducibility of the various dried *as-synthesized* materials was investigated by H_2-TPR. As mentioned before, $Ni^{II}_{NH_3}/SiO_2$ exhibited a two-step reduction as shown in Figure II-A.31 A. Our interpretation was that the first peak with the smallest area (meaning the smallest H_2 consumption) detected at 360°C was due to large Ni^{2+} species, possibly NiO, hardly interacting with the silica support. The other peak, with the highest reduction temperature (765°C), was assigned to Ni^{2+} in strong interaction with silica, possibly owing to the formation of Ni-phyllosilicates. $(Ni^{II}_{5\%}Fe^{III}_{0.5\%})_{NH_3}/SiO_2$ and $(Ni^{II}_{5\%}Fe^{III}_{1.2\%})_{NH_3}/SiO_2$ exhibited the same behavior towards H_2 consumption. Compared to $Ni^{II}_{NH_3}/SiO_2$, their reduction peaks were shifted to lower temperatures, 290°C instead of 350°C and 600°C instead of 765°C (Figure II-A.31 A, B and C). The appearance of H_2-TPR profiles of Ni-Fe samples were relatively comparable to Ni-Fe materials supported over activated carbon [91] or zeolite [95] or carbon nanotubes [96] where a broad peak was detected in a range between 350°C and 380°C, and a shoulder at a range between 500°C and 550°C. In both iron-doped samples, the first peak (at low temperature) has intensified which could be explained by an increasing amount of Ni^{2+} species weakly attached to the silica support compared to $Ni^{II}_{NH_3}/SiO_2$. It is clear that the TPR profiles of Ni-Fe samples do not show any additional peak [97]. However, the peaks are more complex with shoulders and it is difficult to conclude about the nature of the Fe^{3+} and Ni^{2+} species involved. It can just be stated that Ni species or Ni/Fe species are reduced more easily in $(Ni^{II}_{5\%}Fe^{III}_{0.5\%})_{NH_3}/SiO_2$ and $(Ni^{II}_{5\%}Fe^{III}_{1.2\%})_{NH_3}/SiO_2$ samples than in $Ni^{II}_{NH_3}/SiO_2$. The question that also arises is: "Do nickel phyllosilicates still form in iron-doped samples?

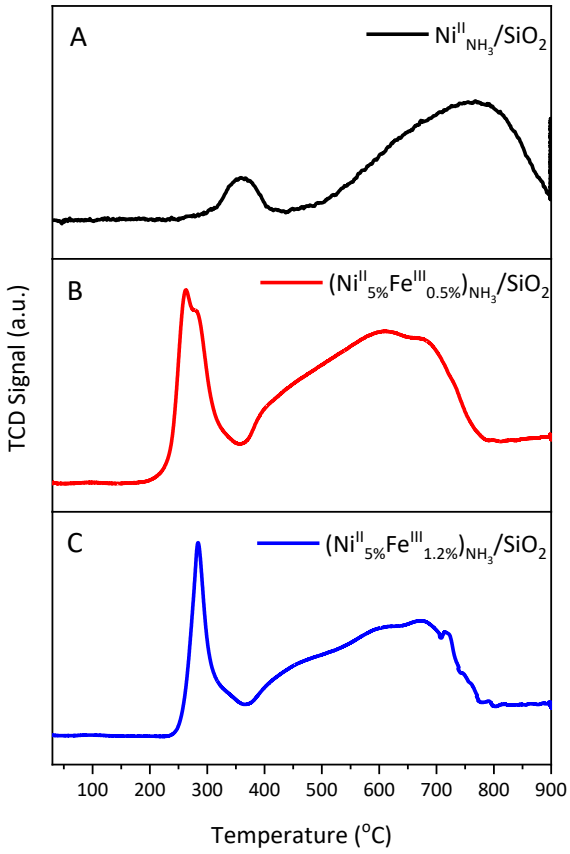

Figure II-A.31: *H_2-TPR results of dried as-synthesized $Ni^{II}_{NH_3}/SiO_2$, $(Ni^{II}_{5\%}Fe^{III}_{0.5\%})_{NH_3}/SiO_2$ and $(Ni^{II}_{5\%}Fe^{III}_{1.2\%})_{NH_3}/SiO_2$ samples recorded with a H_2 vol.%/Ar flow of 30 mL min^{-1} and a heating rate of 10°C min^{-1}.*

Indeed, TEM images of dried *as-synthesized* $Ni^{II}_{NH_3}/SiO_2$ and iron-doped nickel samples are different, as shown in Figure II-A.32. As mentioned earlier in Chapter II – Part A1, paragraph II-A1.3.1, nanosheets structures could be observed for $Ni^{II}_{NH_3}/SiO_2$ (Figure II-A.32 A). But, after doping nickel with iron, more classical rather well-dispersed and tiny nanoparticles of, normally, Ni^{2+} and Fe^{3+} species (probably hydroxides or oxides) could be detected on the grains surface (Figure II-A.32 B and C). Their mean diameter turned out to decrease from 2.4 nm (for $(Ni^{II}_{5\%}Fe^{III}_{0.5\%})_{NH_3}/SiO_2$, Figure II-A.32 D) to 2.0 nm (for $(Ni^{II}_{5\%}Fe^{III}_{1.2\%})_{NH_3}/SiO_2$, Figure II-A.32 E). However, it is worth to note that samples with Fe showed not only nanoparticles, but few branch-like structures emphasized with yellow arrows (Figure II-A.32 B' and C') that could correspond to phyllosilicates, in good agreement with XRD patterns (Figure II-A.30 b and c).

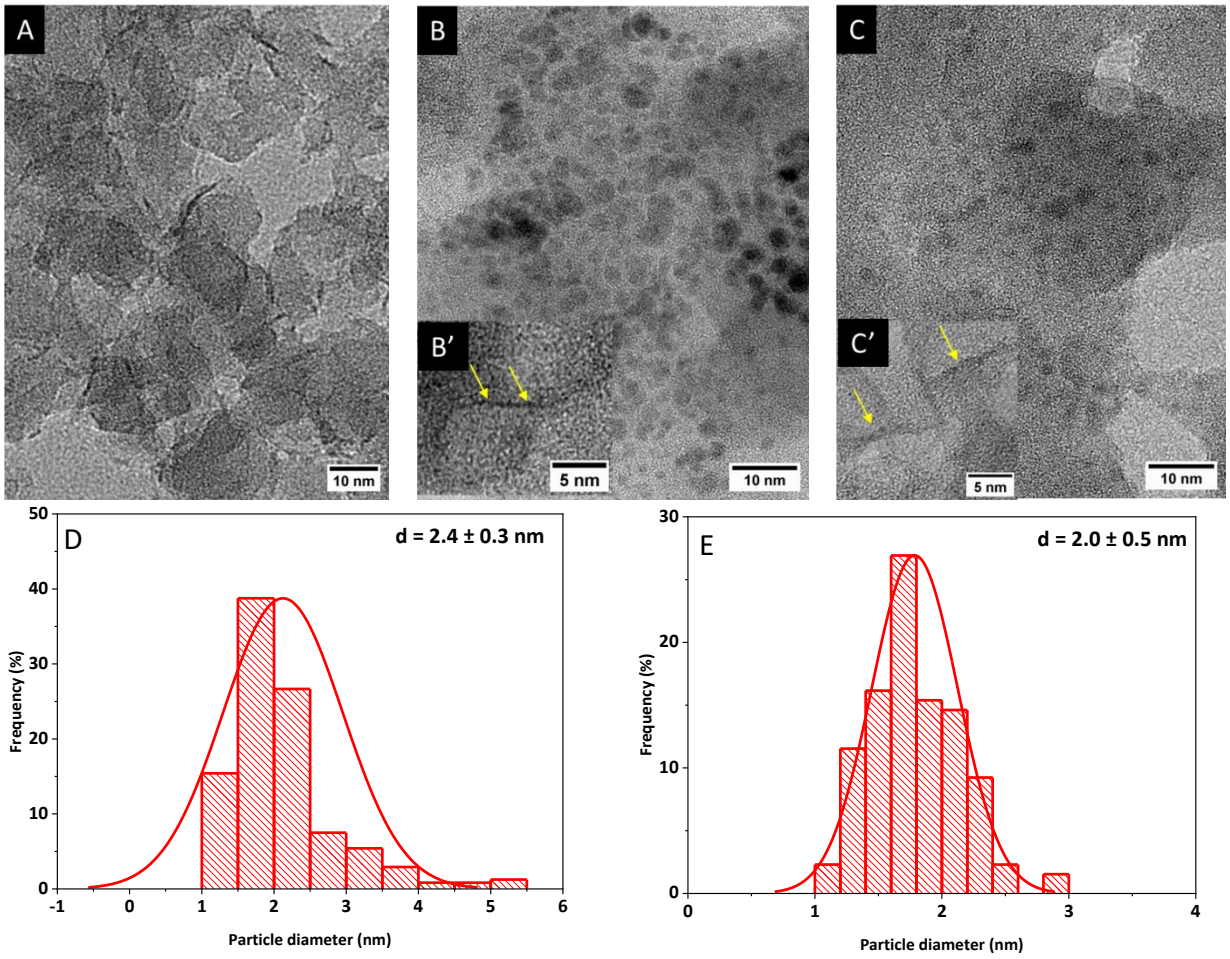

Figure II-A.32: *TEM images and particles size distribution of (A) $Ni^{II}_{NH_3}/SiO_2$, (B,B',D) $(Ni^{II}_{5\%}Fe^{III}_{0.5\%})_{NH_3}/SiO_2$ and (C,C',E) $(Ni^{II}_{5\%}Fe^{III}_{1.2\%})_{NH_3}/SiO_2$.*

Before testing them in the hydrogenolysis of $A1_{HH}$ in *i*-PrOH, all dried *as-synthesized* non-doped and iron-doped samples were *ex-situ* reduced at 500°C using H_2 (50 mL min^{-1}) for 3 h. These pre-treatments conditions were established in accordance with the good results obtained with $Ni^{II}_{NH_3}/SiO_2$ reduced at 500°C and tested only for 1 h at 180°C. Therefore, a comparison of the catalytic performances of $(Ni^{II}_{5\%}Fe^{III}_{0.5\%})_{NH_3}/SiO_2$, $(Ni^{II}_{5\%}Fe^{III}_{1.2\%})_{NH_3}/SiO_2$ and $Ni^{II}_{NH_3}/SiO_2$ is presented in Figure II-A.33 in order to evaluate the impact of the iron-doping on the activity and the selectivity.

$Ni^{0}_{NH_3}/SiO_2$ and $(Ni_{5\%}Fe_{0.5\%})^{0}_{NH_3}/SiO_2$ turned out to be the most active catalysts with a total $A1_{HH}$ and $C1_{HH}$ conversions for both samples, but the selectivity toward phenol was better without Fe doping. In fact, $(Ni_{5\%}Fe_{0.5\%})^{0}_{NH_3}/SiO_2$, the material with the smallest iron content, led to more

phenol hydrogenation into cyclohexanol. Such catalyst should have been tested on a shorter duration of time. By increasing the Fe weight loading to 1.2 wt.%, the solid obtained, $(Ni_{5\%}Fe_{1.2\%})^0_{NH_3}/SiO_2$, allowed to reach a total conversion of $A1_{HH}$, but only 90% conversion of $C1_{HH}$. In addition, the yield of phenol was close to that of $Ni^0_{NH_3}/SiO_2$ (Y = 33%$_C$). In fact, the selectivity in phenol was also very similar. In this case, a longer duration should have been tested, but more phenol would have been hydrogenated at the end, showing no improvement over $Ni^0_{NH_3}/SiO_2$.

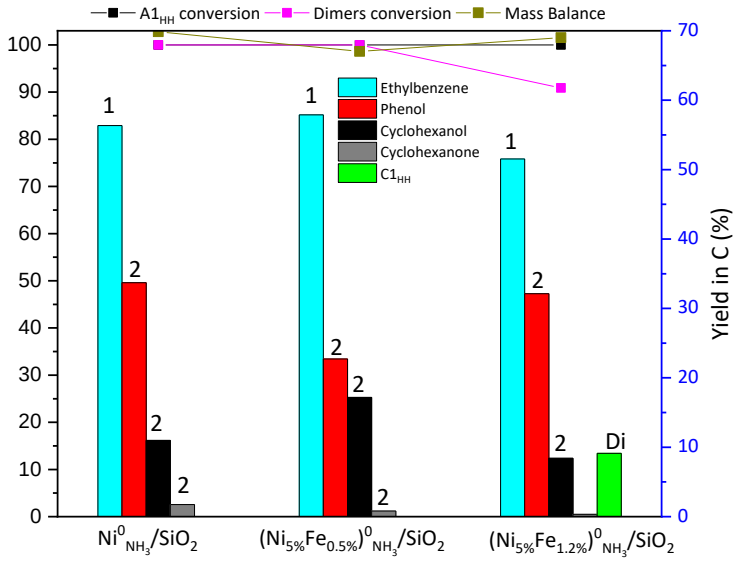

Figure II-A.33: *$A1_{HH}$/dimers conversion, mass balance and yields of the main products obtained with $Ni^0_{NH_3}/SiO_2$ and the two iron-doped nickel samples.*
Reaction conditions: $[A1_{HH}]_o$ = 0.06 M, $V_{i\text{-}PrOH}$ = 15 mL, molar subs./metal = 100, 180°C, 1 h, 5 bar of N_2.

II-A2-2.4. Conclusion

Aerosil 380 was impregnated in aqueous ammonia in the presence of nickel(II) (5 wt.% expected) and iron(III) nitrate, used here as a doping element (0.5 wt.% and 1.2 wt.% expected). Iron addition led to the decrease of the pore volume and of the mean pore diameter as well as a little bit improved reducibility shown by H_2-TPR. Much less phyllosilicates were formed as shown by XRD and TEM, probably explaining the easier reduction of the metal. Neither the small (0.5 wt.%), nor the high iron weight loading (1.2 wt.%), led to a significant improvement of the results of $A1_{HH}$ hydrogenolysis in *i*-PrOH at 180°C within 1 h. It is clear that the addition of 1.2 wt.% led to a decrease in activity and a priori phenolic selectivity at 100% C-OAr bonds conversion, of the

resulting solid compared to $Ni^0_{NH_3}/SiO_2$. Decreasing the amount of Fe to 0.5 wt.% led to higher catalyst activity and a non-negligible amount of cyclohexanol, but the resulting solid should be tested for a shorter period.

However, it was reported in the literature that a β-O-4 lignin model compound was totally depolymerized by Ni5%-Fe5% prepared by co-precipitation and supported on activated carbon, to monomers with the aromatic ring completely retained, in methanol with molar substrate/total metal ratio of 328, under 20 bar of H_2 at 200ºC for 6 h. Interestingly, only phenolic monomers were obtained with no traces of hydrogenated cycles, unlike with 10%Ni where the selectivity towards phenol monomers was lower [91]. The selectivity performance of Ni-Fe catalyst may be due to the synergism between Ni domains, where H_2 could be easily activated, and Fe domains, which exhibited strong oxophilicity [96]. NiFe, as well as Ni-Co catalysts with similar Ni and iron (or cobalt) contents, will be explored in Chapter III – Part B.

Chapter II – Part B: Oxygen chemisorption followed by hydrogen-oxygen titrations as a tool to estimate the surface composition of silica-supported rhodium-nickel bimetallic nanoparticles

In this work, O_2 chemisorption and H_2-O_2 titration experiments were carried out in order to provide a tool to estimate the surface composition of highly dispersed silica-supported rhodium-nickel bimetallic nanoparticles in three materials with different Ni/Rh atomic ratios. A 3-step method, based on O_2 chemisorption (O_C), followed by titration of the oxygen adsorbed species by hydrogen (H_T), and titration of the hydrogen adsorbed species by oxygen (O_T), is proposed and first applied to Rh and Ni monometallic catalysts, highlighting the different behavior of the two metals, in particular the higher sensitivity of the Ni metallic nanoparticles to bulk re-oxidation. These chemisorption data, coupled with TEM measurements, provide insights into the surface composition of the bimetallic nanoparticles, which appeared to be enriched in Ni compared to their bulk nominal composition, leading to the formation of Rh@Ni core@shell nanoparticles for the sample exhibiting the lowest content of rhodium investigated in the present work.

II-B.1. Introduction

Surface composition of bimetallic nanoparticle is of the utmost interest in establishing structure-activity relationships in catalysis. While electronic microscopies are straightforward tools in determining the size of the nanoparticles, such techniques remain of little interest in estimating the surface composition of bimetallic nanoparticles quantitatively. Very few techniques have been developed to quantify the amount of metal atoms available on the surface of supported metal nanoparticles [98]. The chemisorption of probe molecules has been used for decades in estimating the metal dispersion D, defined as the fraction of the total number of metal atoms located on the surface of the metal particles, *i.e.*, the percentage of metal atoms available for catalysis applications [99] in the case of monometallic samples. In the case of bimetallics, such a

technique has been scarcely applied as both metals may chemisorb the probes, making the analysis of the chemisorption data more complex. To our knowledge, the oxygen-hydrogen titrations have been reported to be extremely useful in characterizing the well-known reforming catalysts made of PtSn bimetallic nanoparticles supported on Al_2O_3 [100]. For such a particular system, the hydrogen species chemisorbed onto the reduced surface atoms of Pt and Sn from the bimetallic nanoparticles are first titrated with oxygen, producing water when reacting with the chemisorbed hydrogen species and replacing them by oxygen chemisorbed species, of which only those chemisorbed onto the Pt surface sites can be subsequently titrated with hydrogen. Such a methodology allows to quantify both the total number of Pt and Sn surface atoms and the amount of Pt surface atoms of the PtSn bimetallic nanoparticles, based upon the lack of reactivity of the Sn-O species with hydrogen.

While supported RhNi bimetallic nanoparticles have been shown to be promising for various catalytic reactions such as dry and/or wet reforming of methane [4–6], hydrazine decomposition [7,8], hydrogen and syngas production by biogas reforming processes [104] and CO_2 methanation [10,11], only the work of Wang *et al.* [48] reported on the surface composition of the RhNi nanoparticles. In the latter work, the surface composition of the RhNi nanoparticles was estimated on the basis of XPS measurements, although XPS not only strictly probes surface metal atoms but also metal atoms in the first layers of the nanoparticles. Yet these authors did not report on the use of chemisorption techniques to characterize the RhNi bimetallic nanoparticles, while O_2 chemisorption has been elegantly reported to be a method of choice in characterizing supported monometallic Ni nanoparticles [98].

Differences in O/Metal stoichiometry for Rh [106] and Ni [98], in the reactivity of $Rh\text{-}O_{3/2}$ [106] and Ni-O [107] species at RT towards H_2, which is assumed to be much lower for Ni-O compared to $Rh\text{-}O_{3/2}$, led us to consider $H_2\text{-}O_2$ titrations as a means to quantify the surface composition of supported RhNi bimetallic nanoparticles, by analogy of what was done earlier for the PtSn system [100]. As very few laboratories, unless none, should be equipped with the pulse system coupled to the TGA device described by Millet *et al.* [98] and our lab was not equipped with a pulse chemisorption device when the RhNi materials needed to be characterized, it was decided to try to extrapolate the $H_2\text{-}O_2$ titration method in a volumetric adsorption system, which most of the catalysis laboratories should be equipped with. As will be shown in the present work, the use of

such an approach was found to be much more complicated compared to the earlier PtSn system mainly because of overoxidation of Ni [98] and the reactivity of Ni-O surface species towards hydrogen could not be neglected. The present work thus describes an original chemisorption approach that can help determine the surface composition of Rh-Ni bimetallic nanoparticles that could not be obtained, to our knowledge, by any other means.

The proposed three-step chemisorption method relies on (i) O_2 chemisorption (O_C step), followed by (ii) titration of the M_s-O adsorbed species by hydrogen (H_T step) and finally by (iii) titration of the M_s-H hydrogen adsorbed species by oxygen (O_T step), as described in the following equations where Rh_s (Eqs. II-B.1-3) and Ni_s (Eqs. II-B.4-6) denote surface Rh and Ni atoms, respectively, and the chemisorption stoichiometries are issued from earlier studies for Rh [106] and Ni [1,13–15]:

$O_{C, Rh}$	$Rh_S + ¾\ O_2 = Rh_S\text{-}O_{3/2}$	**Eq. II-B.1**
$H_{T, Rh}$	$Rh_S\text{-}O_{3/2} + 2\ H_2 = Rh_S\text{-}H + 3/2\ H_2O$	**Eq. II-B.2**
$O_{T, Rh}$	$Rh_S\text{-}H + 1\ O_2 = Rh_S\text{-}O_{3/2} + ½\ H_2O$	**Eq. II-B.3**
$O_{C, Ni}$	$Ni_S + ½\ O_2 = Ni_S\text{-}O$	**Eq. II-B.4**
$H_{T, Ni}$	$Ni_S\text{-}O + 3/2\ H_2 = Ni_S\text{-}H + H_2O$	**Eq. II-B.5**
$O_{T, Ni}$	$Ni_S\text{-}H + ¾\ O_2 = Ni_S\text{-}O + ½\ H_2O$	**Eq. II-B.6**

As the surface composition of the bimetallic nanoparticles could not be estimated on the basis of a single chemisorption experiment because of the existence of two unknowns (Rh_s and Ni_s), at least two chemisorption experiments were needed and it was decided to perform an additional chemisorption experiment to test the robustness of the proposed method. This method was first applied to the Rh and Ni monometallic samples before being carried out on three bimetallic materials to estimate their surface composition in terms of Rh and Ni surface atoms (Rh_s and Ni_s) and the metal (Rh_s + Ni_s) dispersion in the bimetallics was compared to the size of the bimetallic nanoparticles determined by TEM.

II-B.2. Experimental section

The experimental protocol for the preparation of monometallic Ni and Rh and bimetallic Ni/Rh solids is described elsewhere in details in Chapter II – Part A1, paragraph II-A1.2.1.

In agreement with the H_2-TPR profiles recorded on such samples (Chapter II – Part A1, paragraph II-A1.3.1), the monometallic Rh and the three bimetallic Ni-Rh catalysts were reduced *ex-situ* under a flow of H_2 (50 mL min^{-1}) for 3 h at 500°C, whereas the monometallic Ni catalyst was reduced at 750°C for 3 h.

Adsorption measurements were performed on the *ex-situ* reduced materials in a static mode using a conventional volumetric apparatus (Belsorp max, Bel Japan). Before analysis, all samples (~ 100-160 mg) were pretreated *in-situ* under H_2 (10 mL min^{-1}) at 400°C for 30 min, then evacuated for 2 h at 400°C, and before each titration step (hydrogen or oxygen titration), samples were evacuated for 2 h at 25°C. O_C was carried out at 40°C, whereas H_T and O_T were carried out at 25°C. In each step, the back-sorption method [99] was used and consisted in the measurement of two successive isotherms with an intermediate evacuation at room temperature for 2 h allowing the determination of the amount of probe molecule irreversibly chemisorbed on the metals by difference of the two isotherms (the second isotherm being due to a reversible weak interaction of the probe molecule with the support).

II-B.3. Results and discussion

The TEM micrographs and particle size distributions measured on the five post-chemisorption samples are shown in Figure II-B.1. It must be emphasized that the solids did not evolve after chemisorption since TEM analyses carried out on samples before (Figure II-B.1 A, B, C, D and E) and after chemisorption studies (Figure II-B.1 a, b, c, d and e) showed that the mean particle diameter remained essentially the same. It can be seen that the mean particle size ($d = \Sigma n_i d_i^3 / \Sigma n_i d_i^2$ [17]) is the greatest for the monometallic samples (3.3 and 2.9 nm for Rh_{NH_3}/SiO_2 and Ni_{NH_3}/SiO_2, respectively, Figure II-B.1 a' and b') and decreases to a significant extent for the bimetallic samples (1.8 ± 0.1 nm, Figure II-B.1 c'-e').

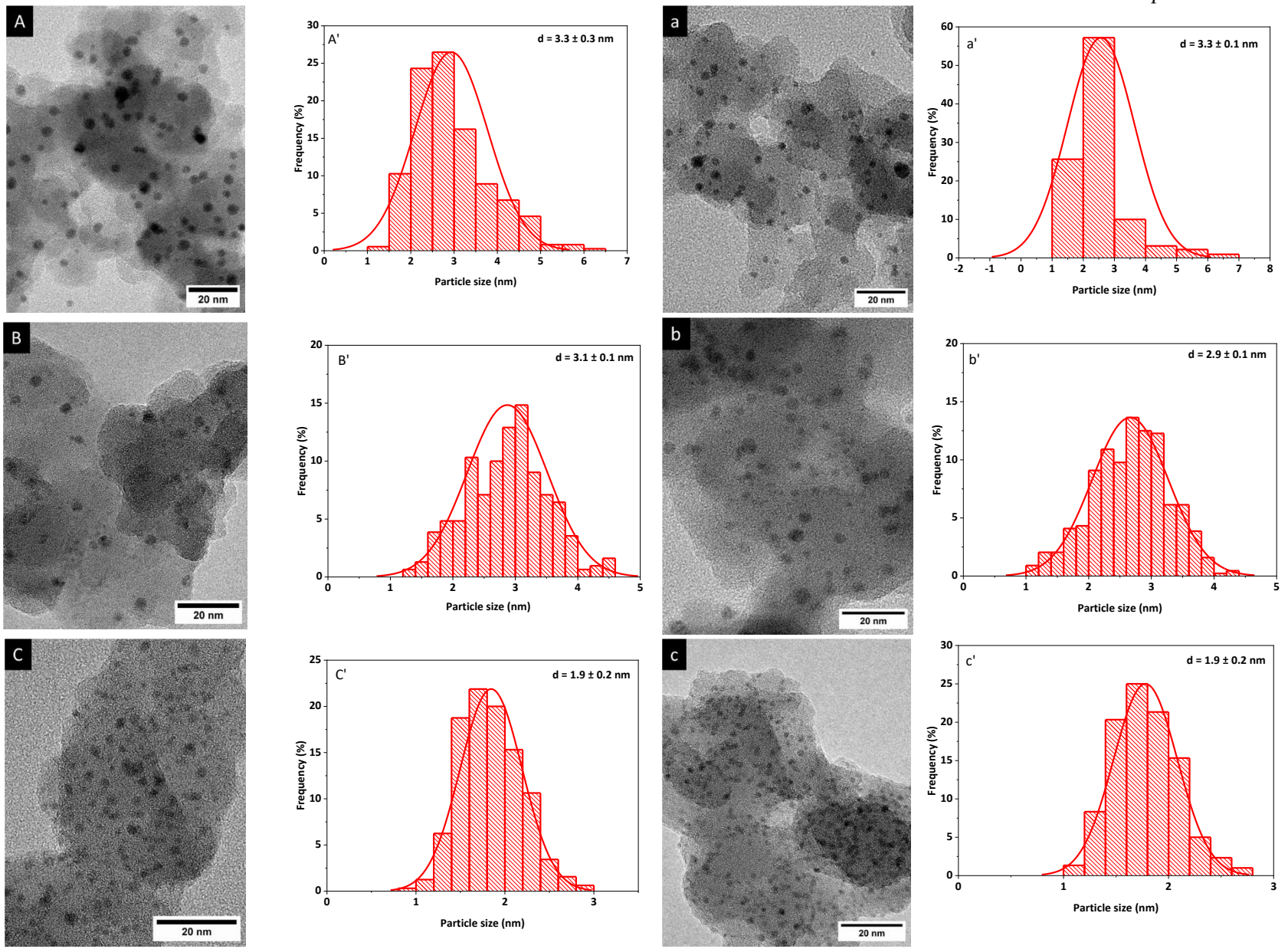
A
20 nm
A'
d = 3.3 ± 0.3 nm
Frequency (%)
Particle size (nm)
a
20 nm
a'
d = 3.3 ± 0.1 nm
Frequency (%)
Particle size (nm)
B
20 nm
B'
d = 3.1 ± 0.1 nm
Frequency (%)
Particle size (nm)
b
20 nm
b'
d = 2.9 ± 0.1 nm
Frequency (%)
Particle size (nm)
C
20 nm
C'
d = 1.9 ± 0.2 nm
Frequency (%)
Particle size (nm)
c
20 nm
c'
d = 1.9 ± 0.2 nm
Frequency (%)
Particle size (nm)

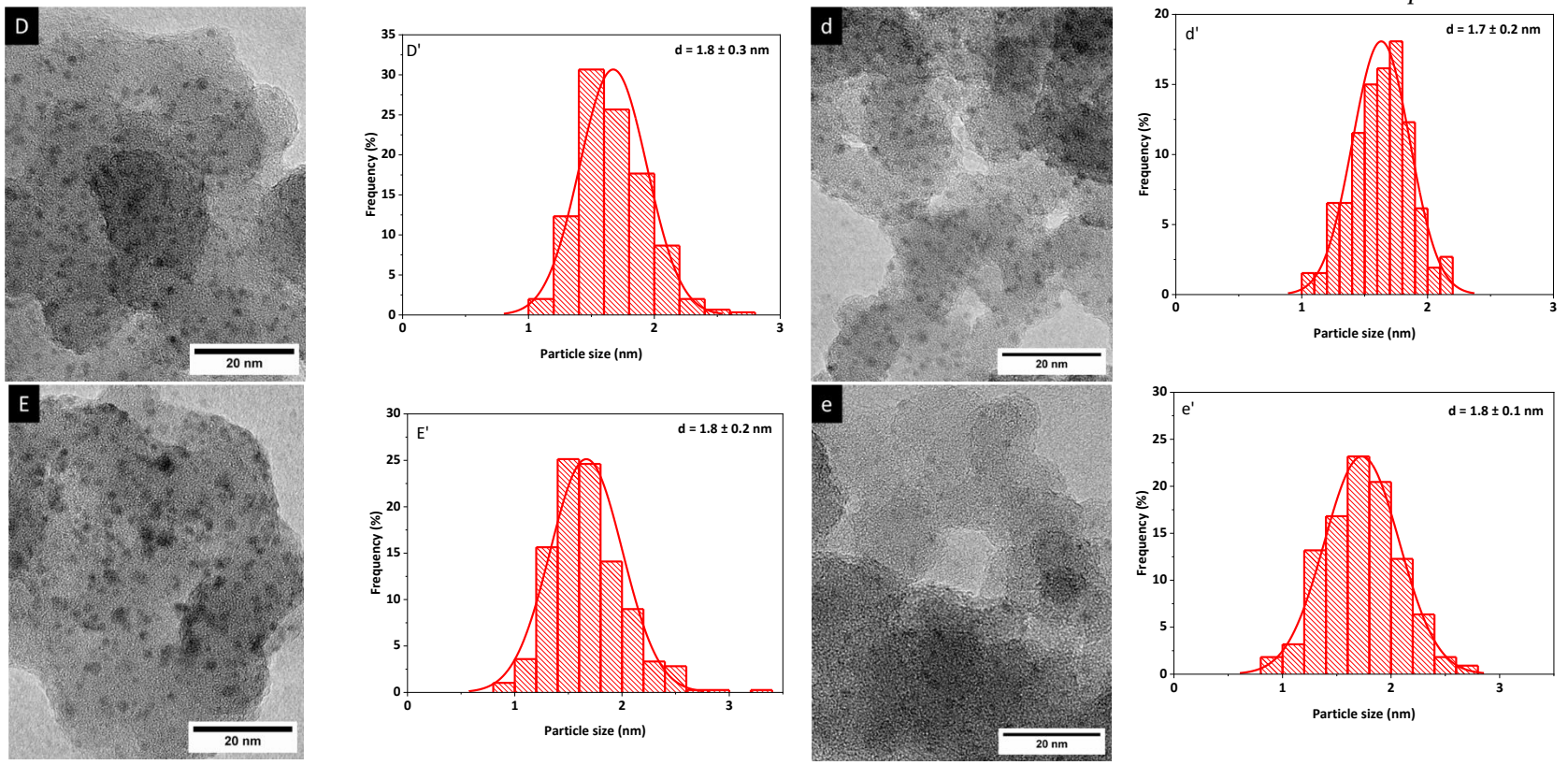

Figure II-B.1: *TEM images and particle sizes distribution of (A,A',a,a') Rh_{NH_3}/SiO_2, (B,B',b,b') Ni_{NH_3}/SiO_2, (C,C',c,c') $(Ni_{25}Rh_{75})_{NH_3}/SiO_2$, (D,D',d,d') $(Ni_{50}Rh_{50})_{NH_3}/SiO_2$ and (E,E',e,e') $(Ni_{75}Rh_{25})_{NH_3}/SiO_2$ samples recovered after reduction (uppercase letters) and after chemisorption experiments (lowercase letters).*

The five SiO_2-supported samples were subjected to measurements of the consumed quantities of probe molecules for the O_2 chemisorption step at 40°C, the titration of surface oxygen adsorbed species by H_2, and the titration of hydrogen adsorbed species by O_2 at 25°C. At each step, these quantities were deduced from the difference between the measurement of a first isotherm carried out on the sample previously evacuated under vacuum (strongly and weakly held species), then a second isotherm carried out after evacuation at room temperature (weakly held species). It was subsequently shown that the adsorption of O_2 or H_2 during the O_C and O_T or H_T stages followed a Langmuir model (see Figure II-B.2 for the case of Rh_{NH_3}/SiO_2, Figure II-B.3 for Ni_{NH_3}/SiO_2, Figure II-B.4 for $(Ni_{25}Rh_{75})_{NH_3}/SiO_2$, Figure II-B.5 for $(Ni_{50}Rh_{50})_{NH_3}/SiO_2$ and Figure II-B.6 for $(Ni_{75}Rh_{25})_{NH_3}/SiO_2$).

The irreversible consumed volumes of the O_2 and H_2 probes recorded for each sample during the chemisorption of O_2, and the hydrogen and oxygen titrations are listed in Table II-B.1. For each material, the total metal content (M_T: Rh_T or Ni_T for the monometallic samples and the sum of those as TMC in the bimetallic samples as μmol/g) were calculated from the metal weight loadings determined by ICP-OES (Chapter II – Part A1, paragraph II-A1.3.1). Overall, it can be seen that the volumes of irreversibly adsorbed O_2 in the O_C experiments increase to a significant extent in the bimetallic samples compared to the monometallic ones. The volumes of H_2 and O_2 consumed in the H_T and O_T experiments also increase in the bimetallic samples with the higher amounts of Rh ($(Ni_{25}Rh_{75})_{NH_3}/SiO_2$ and $(Ni_{50}Rh_{50})_{NH_3}/SiO_2$) compared to the monometallic ones, whereas such volumes recorded on $(Ni_{75}Rh_{25})_{NH_3}/SiO_2$ were found to be intermediate to those of Rh_{NH_3}/SiO_2 and Ni_{NH_3}/SiO_2.

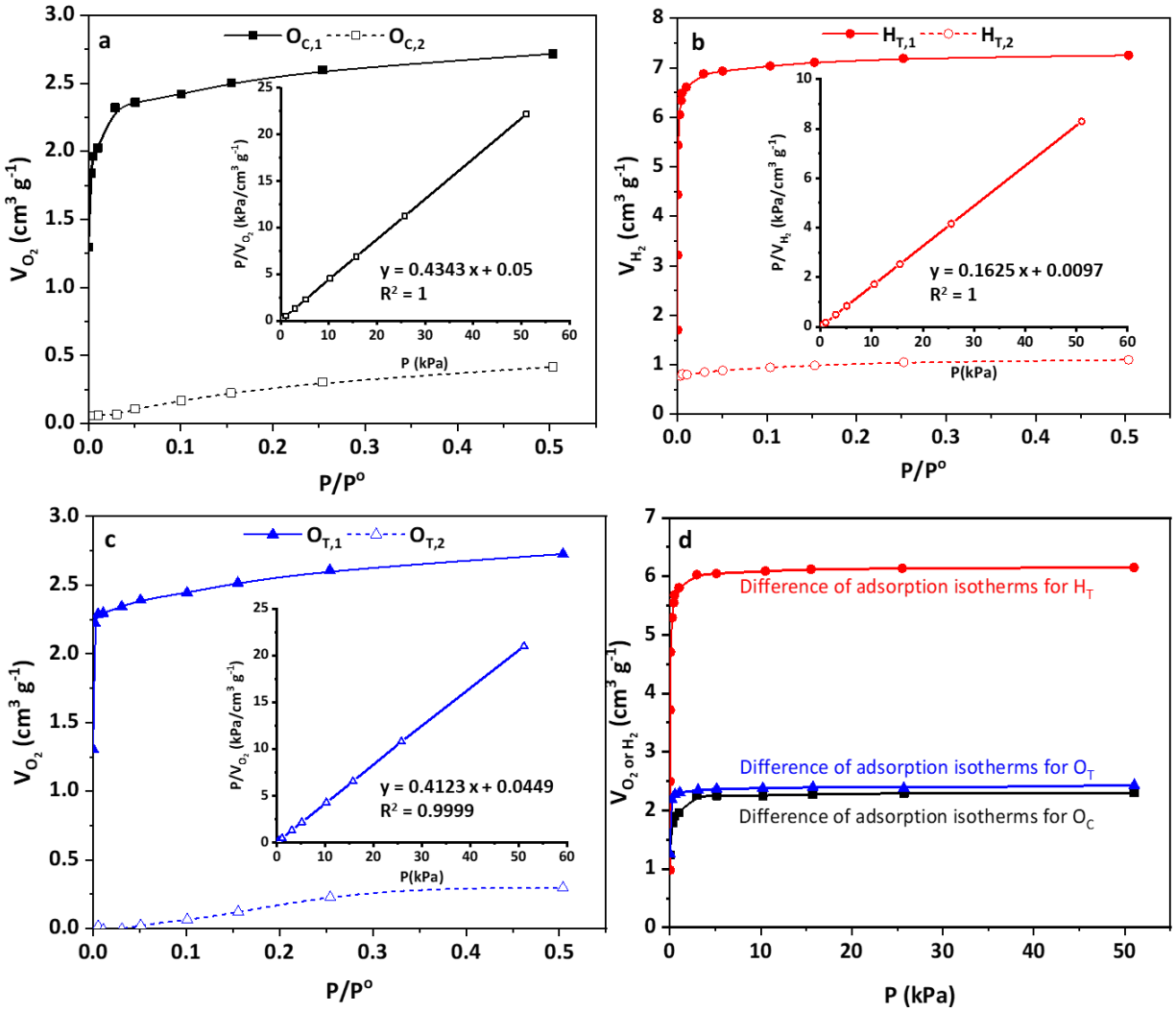

Figure II-B.2: *First and second isotherm recorded, after evacuation, for oxygen chemisorption at 40°C (A) followed by hydrogen titration (B) and oxygen titration (C) at 25°C and difference of adsorption isotherms for each step (D) in the case of* Rh_{NH_3}/SiO_2*. Langmuir modelling of the difference isotherms for* O_C*,* H_T *and* O_T *are provided in the insets of figures (A), (B) and (C), respectively.*

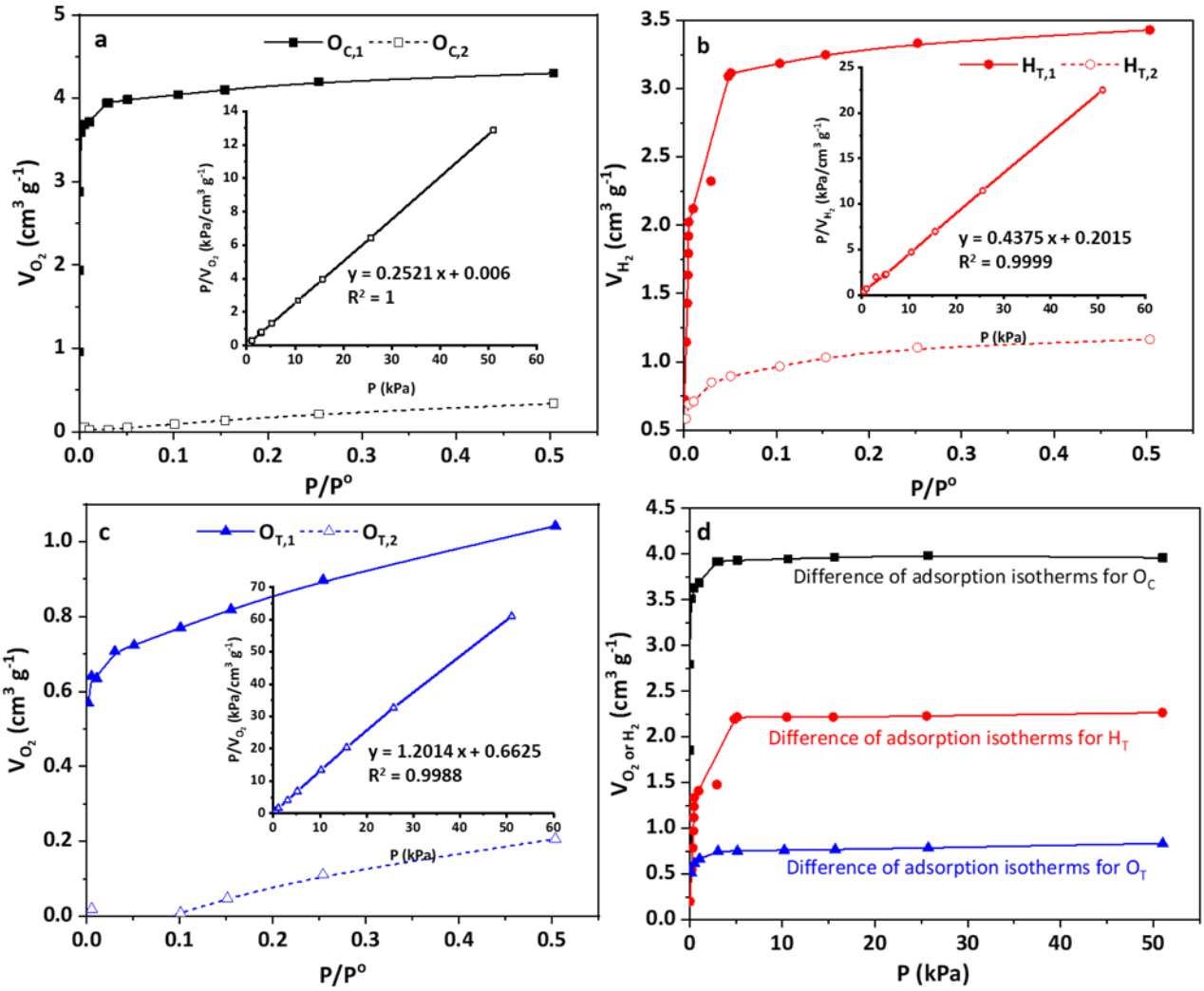

Figure II-B.3: *First and second isotherm recorded, after evacuation, for oxygen chemisorption at 40°C (A) followed by hydrogen titration (B) and oxygen titration (C) at 25°C and difference of adsorption isotherms for each step (D) in the case of* Ni_{NH_3}/SiO_2*. Langmuir modelling of the difference isotherms for* O_C*,* H_T *and* O_T *are provided in the insets of figures (A), (B) and (C), respectively.*

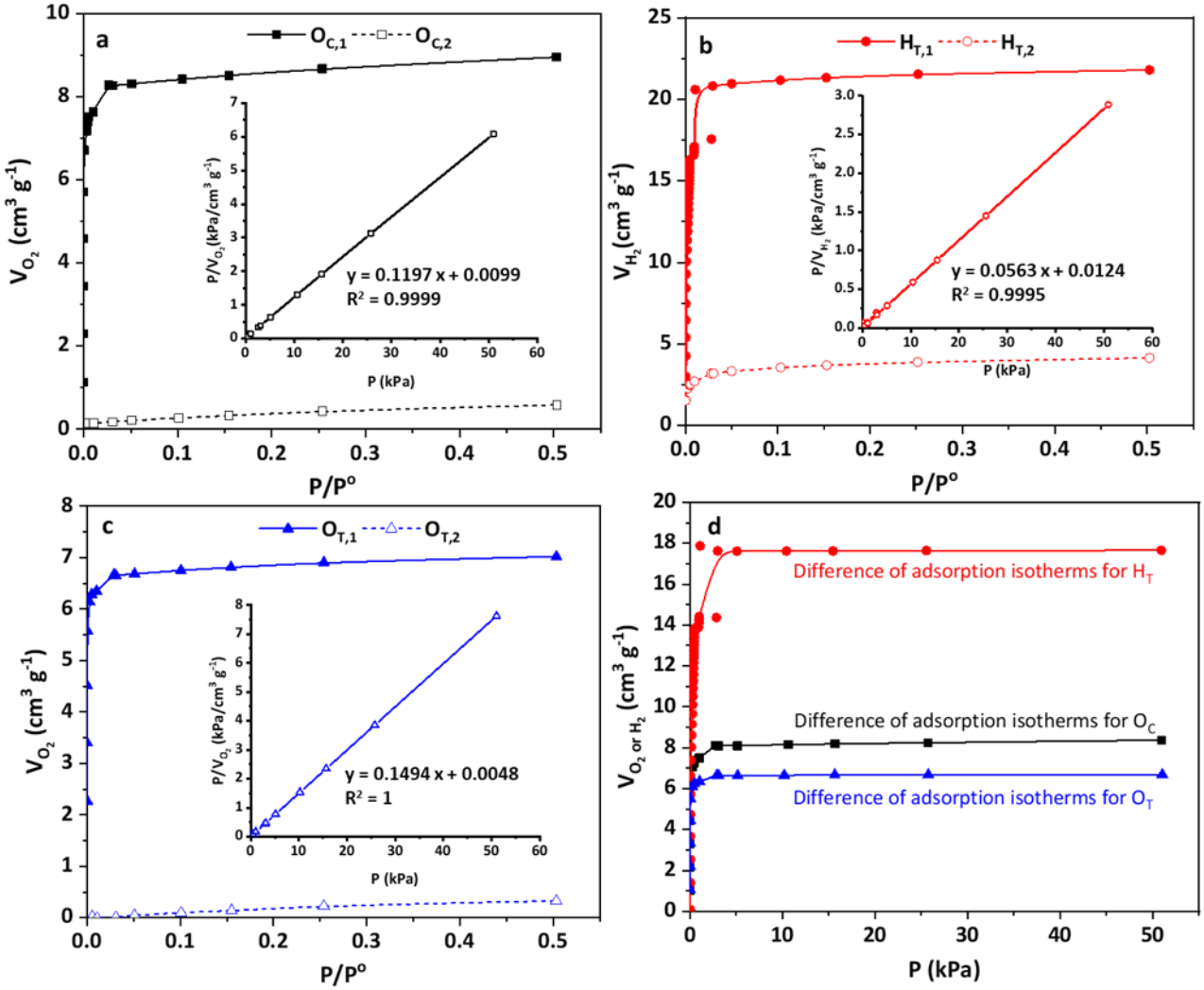

Figure II-B.4: *First and second isotherm recorded, after evacuation, for oxygen chemisorption at 40°C (a) followed by hydrogen titration (b) and oxygen titration (c) at 25°C and difference of adsorption isotherms for each step (d) in the case of* $(Ni_{25}Rh_{75})_{NH_3}/SiO_2$. *Langmuir modelling of the difference isotherms for* O_C, H_T *and* O_T *are provided in the insets of figures (a), (b) and (c), respectively.*

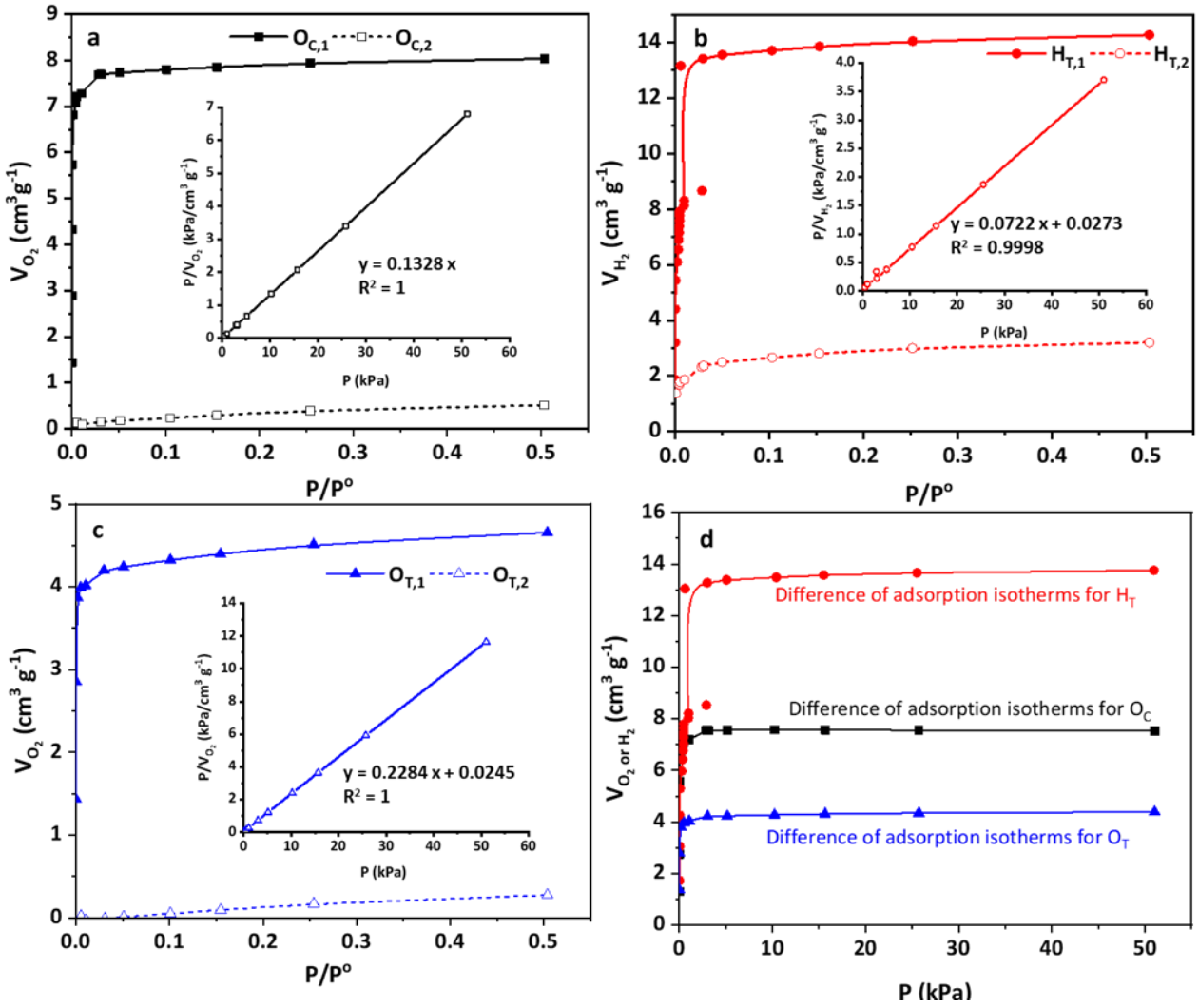

Figure II-B.5: *First and second isotherm recorded, after evacuation, for oxygen chemisorption at 40°C (a) followed by hydrogen titration (b) and oxygen titration (c) at 25°C and difference of adsorption isotherms for each step (d) in the case of* $(Ni_{50}Rh_{50})_{NH_3}/SiO_2$*. Langmuir modelling of the difference isotherms for* O_C*,* H_T *and* O_T *are provided in the insets of figures (a), (b) and (c), respectively.*

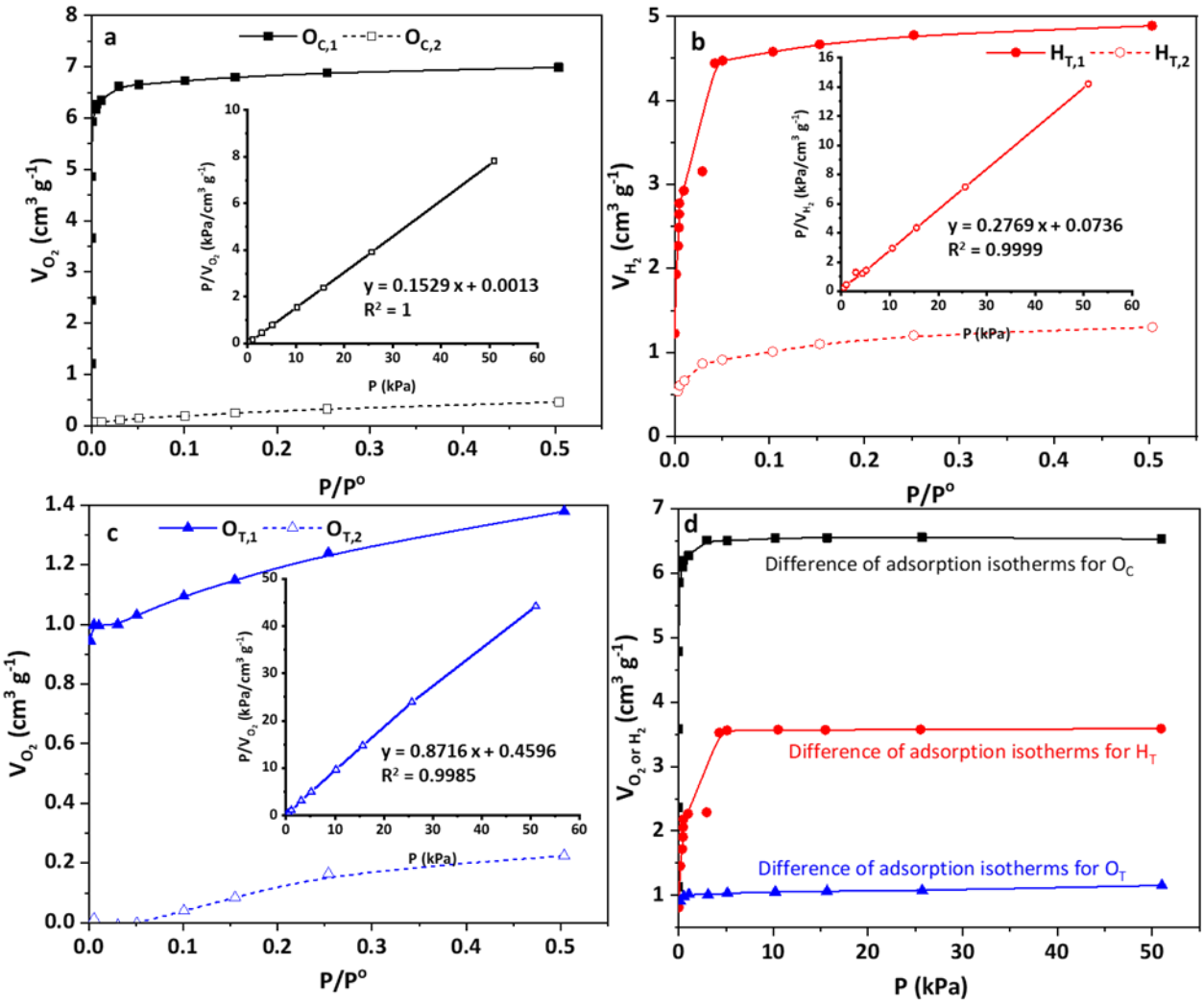

Figure II-B.6: *First and second isotherm recorded, after evacuation, for oxygen chemisorption at 40°C (a) followed by hydrogen titration (b) and oxygen titration (c) at 25°C and difference of adsorption isotherms for each step (d) in the case of* $(Ni_{75}Rh_{25})_{NH_3}/SiO_2$. *Langmuir modelling of the difference isotherms for* O_C, H_T *and* O_T *are provided in the insets of figures (a), (b) and (c), respectively.*

Table II-B.1: *Irreversible consumed volumes of* O_2, H_2 *and* O_2 *collected from the* O_C, H_T *and* O_T *experiments performed on* SiO_2*-supported Ni, Rh and Ni-Rh nanoparticles.*

Sample	Exp	Pretreatments[a]	M_T/TMC[b] (µmol/g)	V ($mL_{0\,°C,\,1\,atm}$/g)		
				O_C[c]	H_T[d]	O_T[c]
Rh_{NH_3}/SiO_2	**1A**	❶	Rh_T: 413.0	**2.3026**		
	1B	❷			6.1548	
	1C	❷				2.4257
Ni_{NH_3}/SiO_2	**2A**	❶	Ni_T: 834.9	**3.9664**		
	2B	❷			2.2906	
	2C	❷				0.8324
$(Ni_{25}Rh_{75})_{NH_3}/SiO_2$	**3A**	❶	Rh_T: 436.3 Ni_T: 165.3	**8.3518**		

	3B	❷	TMC: 601.6		17.761	
	3C	❷				6.6926
$(Ni_{50}Rh_{50})_{NH_3}/SiO_2$	**4A**	❶	Rh_T: 332.4 Ni_T: 316.9	**7.5321**		
	4B	❷	TMC: 649.3		11.060	
	4C	❷				4.3786
$(Ni_{75}Rh_{25})_{NH_3}/SiO_2$	**5A**	❶	Rh_T: 160.3 Ni_T: 552.1	**6.5386**		
	5B	❷	TMC: 712.4		3.6224	
	5C	❷				1.1473

[a] ❶ *in-situ* H_2 reduction (10 mL min^{-1}) at 400 °C for 30 min, evacuation 2 h at 400°C, ❷ Evacuation for 2 h at 25°C; [b] Amount of metal (M_T: Rh_T or Ni_T); Total amount of metal (sum of Rh_T and Ni_T as TMC); [c] Volume of O_2; [d] Volume of H_2. See calculation details.

For the monometallic samples, the amount of metal surface atoms (M_s) can be deduced from the irreversible volumes of consumed probes recorded during O_C, H_T and O_T (Table II-B.1) and Eqs. II-B.1-6, and the corresponding dispersions estimated from the ratio of M_s (Table II-B.3) to M_T (Table II-B.1) respectively. The mean particle diameter of the nanoparticles, d, could be estimated from Eq. II-B.7 [17]:

$$d = \left(6 \frac{v_m / a_m}{D}\right) \qquad \textbf{Eq. II-B.7}$$

where v_m is the volume occupied by an atom m in the bulk metal (for rhodium v_m = 13.78 Å^3 and for nickel v_m = 10.95 Å^3) and a_m is the surface area occupied by an atom m on a polycrystalline surface (for rhodium a_m = 7.58 Å^2 and for nickel a_m = 6.51 Å^2), and D (M_s/M_T) is the dispersion of the metal.

For the bimetallic samples, the estimation of such data remains much more challenging and will be described in details in section II-B.3.2.

II-B.3.1. Calculation of M and Ms (µmol/g) in Tables II-B.1 and II-B.2:

Total metal contents are determined from the metal weight loadings obtained by ICP-OES, whereas the amounts of Rh and Ni surface atoms (Rh_S and Ni_S) are estimated from Oc, H_T and O_T

data and Eqs. II-B.1-3 and Eqs. II-B.4-6, respectively. Calculations are detailed for the Rh_{NH_3}/SiO_2, Ni_{NH_3}/SiO_2 and $(Ni_{25}Rh_{75})_{NH_3}/SiO_2$ samples.

Rh_{NH_3}/SiO_2

Total metal content in Rh_{NH_3}/SiO_2: 4.25 wt.% Rh ➔ Rh_T = 4.25/(100 x 102.9) = 413.0 µmol/g.

For Rh_S:

V_{Oc} = 2.3026 mL O_2/g ➔ $n_{Oc} = V_{Oc}/V_{molar}$ = 2.3026/22414 = 102.73 µmol O_2/g.

From Eq. II-B.1: $n_{Rhs} = 4/3 \times n_{Oc}$ = (4 x 102.73)/3 = 137.0 µmol/g.

D = 137.0/413.0 = 33.2%

V_{H_T} = 6.1548 mL H_2/g ➔ $n_{H_T} = V_{H_T}/V_{molar}$ = 6.1548/22414 = 274.59 mol H_2/g.

From Eq. II-B.2: $n_{Rhs\text{-}O_{3/2}} = n_{Rhs} = n_{H_T}/2$ = 274.59 /2 = 137.3 µmol/g.

D = 137.3/413.0 = 33.2%

V_{O_T} = 2.4257 mL O_2/g ➔ $n_{O_T} = V_{O_T}/V_{molar}$ = 2.4257/22414 = 108.22 µmol O_2/g.

From Eq. II-B.3: $n_{Rhs\text{-}H} = n_{Rhs} = n_{O_T}$ = 108.2 µmol/g.

D = 108.22/413 = 26.2%

Ni_{NH_3}/SiO_2

Total metal content in Ni_{NH_3}/SiO_2: 4.90 wt.% Ni ➔ Ni_T = 4.90/(100 x 58.7) = 834.9 µmol/g.

For Ni_S:

V_{Oc} = 3.9664 mLO_2/g ➔ $n_{Oc} = V_{Oc}/V_{molar}$ = 3.9664/22414 = 176.96 µmol O_2/g.

Without any oxidation of bulk Ni atoms (Ni_B), n_{Nis} should be obtained from Eq. II-B.4, as follows:

$n_{Nis} = n_{Oc}/0.5$ = 353.9 µmol/g

D = 353.9/834.9 = 42.4%

Considering that part of the bulk Ni atoms are oxidized at the O_c stage, the corrected number for Ni_S should be lower. The corrected value of n_{Nis} and the value of bulk Ni atoms involved in the oxidation, n_{Ni_B}, were obtained using the average size of Ni nanoparticles determined by TEM, as follows:

From Eq. II-B.7: $D = (6\frac{v_m/a_m}{d}) = \frac{n_{Nis}}{n_{NiT}} \Rightarrow n_{Nis} = n_{NiT}\ x\ 6\frac{v_m/a_m}{d} = 834.9\ x\ 6\frac{10.95/6.51}{29}$ =290.1 µmol/g

D = 290.1/834.9 = 34.7%

And n_{Ni_B} = 353.9 - 290.1 = 63.8 µmol/g

As a result, in the case of partial bulk Ni atoms oxidation, $n_{Nis} = n_{Oc}/0.61$ = 290.1 µmol/g and n_{Ni_B} / n_{Nis} = 0.22.

V_{H_T} = 2.2906 mL H_2/g ➔ $n_{H_T} = V_{H_T}/V_{molar}$ = 2.2906/22414 = 102.19 µmol H_2/g.

From Eq. II-B.5: $n_{Nis-O} = n_{Nis} = (2 \times n_{H_T})/3 = (2 \times 102.19)/3$ = 68.1 µmol/g.

D = 68.1/834.9 = 8.2%

V_{O_T} = 0.8324 mL O_2/g ➔ $n_{O_T} = V_{O_T}/V_{molar}$ = 0.8324/22414 = 37.13 µmol O_2/g.

From Eq. II-B.6: $n_{Nis-H} = n_{Nis} = (4 \times n_{O_T})/3 = (4 \times 37.13)/3$ = 49.5 µmol/g.

D = 49.5/834.9 = 5.9%

$(Ni_{25}Rh_{75})_{NH_3}/SiO_2$

Total metal content in $(Ni_{25}Rh_{75})_{NH_3}/SiO_2$:

Rh: 4.49 wt.% ➔ Rh = 4.49/(100 x 102.9) = 436.3 µmol/g.

Ni: 0.97 wt.% ➔ Ni = 0.97/(100 x 58.7) = 165.3 µmol/g.

Therefore, the total metal content (TMC) in $(Ni_{25}Rh_{75})_{NH_3}/SiO_2$ = Rh + Ni = 463.3 + 165.3 = 601.6 µmol/g.

The same methodology can be applied to the other bimetallic samples and TMCs in in $(Ni_{50}Rh_{50})_{NH_3}/SiO_2$ and in $(Ni_{75}Rh_{25})_{NH_3}/SiO_2$ are found to be 649.3 and 712.4 µmol/g, respectively.

II-B.3.2. Monometallic samples

II-B.3.2.a. Rhodium sample (Rh_{NH_3}/SiO_2)

The amount of Rh surface atoms (Rh_s) can be deduced from the irreversible volumes of consumed probes recorded during O_C, H_T and O_T (Table II-B.2) in Exps. 1A-C and by using Eqs. II-B.1-3, and the corresponding dispersions estimated from the ratio of the number of Rh_s (Table

II-B.3) to the number of Rh_T (Table II-B.1), respectively. An excellent agreement was found between O_C (Exp-1A) and H_T (Exp-1B) that both led to a Rh dispersion of 33.2% corresponding to a Rh nanoparticle average size of 3.3 nm, which is in excellent agreement with the average size measured by TEM (Figure II-B.1 A', Table II-B.2). The O_T experiment (Exp-1C, Table II-B.2) led to a slightly lower Rh dispersion (26.2%), which may be attributed to a competition of the water molecules formed in the previous H_T experiment (Exp-1B) for surface Rh sites, therefore decreasing the amount of H chemisorbed species in this latter experiment. In the case of Rh, it can be concluded that 100% (137.3/137.0) and about 79% (108.2/137.0) of the Rh_S sites were titrated by H_T following O_C and O_T following H_T, respectively.

Table II-B.2: *Amounts of surface metals estimated from O_2 chemisorption, H_2 and O_2 titrations for SiO_2-supported Ni, Rh and Ni-Rh nanoparticles - Dispersion (D) and estimated mean particle diameters.*

Sample	Exp	M_S (µmol/g)[a]			D (%)	Size, d (nm)[b]	TEM (nm)
		O_C	H_T	O_T			
Rh_{NH_3}/SiO_2	**1A**	Rh_s: 137.0			33.2		
	1B		Rh_s: 137.3		33.2	3.3	3.3
	1C			Rh_s: 108.2	26.2		
Ni_{NH_3}/SiO_2	**2A**	Ni_s: 353.9 (290.1)[c] Ni_B: - (63.8)[c] Ni_s+Ni_B: - (353.9)[c]			42.4 (34.7)[c]	2.4 (2.9)[c]	2.9
	2B		Ni_s: 68.1		8.2		
	2C			Ni_s: 49.5	5.9		

[a] Amounts of surface metal atoms (M_s) derived from Eqs. II-B.1-6; [b] Calculated from D using Eq. II-B.7; [c] Assuming that part of bulk Ni is oxidized during Exp. 2A. Detailed calculation II-B.3.1

II-B.3.2.b. Nickel sample (Ni_{NH_3}/SiO_2)

The amount of Ni surface atoms (Ni_s) should be deduced from the irreversible volumes of consumed probes recorded during O_C, H_T and O_T (Table II-B.1) in Exps. 2A-C and by using Eqs. II-B.4-6, and the corresponding dispersions estimated from the ratio of the number of Ni_s (Table II-B.2) to the number of Ni_T (Table II-B.1), respectively. The total amount of O_2 irreversibly chemisorbed in the O_C experiment performed on Ni_{NH_3}/SiO_2 (Exp-2A, 353.9 µmol O_2/g_{sample}, Table II-B.2) suggested that Ni dispersion would be 42.4%, corresponding to a Ni nanoparticle average size of 2.4 nm, whereas TEM showed that the average particle size should rather be 2.9 nm (Figure II-B.1 b', Table II-B.2). Contrary to what was observed for $Rh^0{}_{NH_3}/SiO_2$, the average size of the Ni nanoparticles appeared to be underestimated by O_C compared to that estimated by

TEM. Such an underestimation of the Ni average size may be attributed to an overoxidation of Ni nanoparticles, namely oxidation of Ni atoms located in the bulk of the nanoparticle (Ni_B) beneath the surface Ni atoms (Ni_s), at high partial pressure of O_2 [98] in the O_C experiment. By considering the average size of the Ni particles determined by TEM (2.9 nm) and the total amount of Ni atoms probed by oxygen in the O_C experiment (Exp-2A, 353.9 µmol O_2/g_{sample}, Table II-B.2), the amount of surface and bulk Ni atoms probed by oxygen may be estimated to 290.1 (Ni_s) and 63.8 (Ni_B) µmol/g (Table II-B.2), corresponding to a dispersion of 34.7%. Contrary to what was found in the case of Rh, H_T obviously underestimated Ni dispersion to a significant extent (about 8 % in Exp-2B, Table II-B.2). Finally, O_T also provided a poor estimation of the Ni dispersion (5.9 %, Exp-2C, Table II-B.2). This could be assigned to the lower interaction of hydrogen with Ni^0 sites [109] and/or to the greater affinity of the previously formed H_2O molecules in the H_T experiment with Ni^0 compared to Rh^0. Overall, the Ni_S atoms titrated by H_T and O_T amounted to 23.5% (68.1/290.1) and 17.1% (49.5/290.1) of those determined by O_C, showing a significantly different behavior for Rh and Ni-based catalysts, as could be expected from earlier investigations [12,13].

II-B.3.3. Rhodium and nickel bimetallic samples

The determination of the surface composition and the dispersion of the bimetallic samples $(Ni_{25}Rh_{75})_{NH_3}/SiO_2$, $(Ni_{50}Rh_{50})_{NH_3}/SiO_2$ and $(Ni_{75}Rh_{25})_{NH_3}/SiO_2$) by chemisorption techniques remains challenging but the substantial different affinity of both metals for oxygen and hydrogen, as illustrated above in the case of the monometallic samples, should help unravel such data. The comparison of the irreversibly consumed quantities of O_2 in O_C and O_T listed in Table II-B.1 for $(Ni_{25}Rh_{75})_{NH_3}/SiO_2$, $(Ni_{50}Rh_{50})_{NH_3}/SiO_2$ and $(Ni_{75}Rh_{25})_{NH_3}/SiO_2$ with those of the monometallic samples may indicate that the most Rh-rich and Ni-rich bimetallic samples ($(Ni_{25}Rh_{75})_{NH_3}/SiO_2$, and $(Ni_{75}Rh_{25})_{NH_3}/SiO_2$), respectively) would be mainly exposing Rh and Ni atoms, consistently with the greater proportions of Rh and Ni in these samples, respectively, whereas the second sample $(Ni_{50}Rh_{50})_{NH_3}/SiO_2$ would display an intermediate behavior. By assuming that Ni and Rh would exhibit similar chemisorptive properties in both non-alloyed (monometallic) and alloyed (bimetallic) nanoparticles, mathematical equations derived from Eqs. II-B.1-6 with two unknown variables, *i.e.*, *x* (number of Rh surface atoms: Rh_s) and *y* (number of Ni surface atoms: Ni_s) could

be written to take into account the chemisorption of both probe molecules on both metals for the O_C (Eq. II-B.8), H_T (Eq. II-B.9) and O_T (Eq. II-B.10) steps, as follows:

O_C (Hypothesis from the monometallic samples: 100% of Rh_S and Ni_S interacts with O_2, and part of O_2 is also consumed by subsurface oxidation of Ni_B as Ni_B-O)

$$\boldsymbol{x\ Rh_S + y\ Ni_S + 0.22\ y\ Ni_B + (¾\ x + 0.61\ y)\ O_2 = x\ Rh_S\text{-}O_{3/2} + y\ Ni_S\text{-}O + 0.22\ y\ Ni_B\text{-}O} \quad \textbf{Eq. II-B.8}$$

where Eq. II-B.8 is obtained by summing Eqs. II-B.S1 and II-B.S2, corresponding to Rh and Ni, respectively. The factor of 0.61 in this equation was preferred to that of ½ in Eq. II-B.1, to take the subsurface oxidation of Ni into account in the O_C experiment.

$x\ Rh_S + ¾\ x\ O_2 = x\ Rh_S\text{-}O_{3/2}$ **Eq. II-B.S1** (derived from Eq. II-B.1)

$y\ Ni_S + 0.22\ y\ Ni_B + 0.61\ y\ O_2 = y\ Ni_S\text{-}O + 0.22\ y\ Ni_B\text{-}O$ **Eq. II-B.S2** (derived from Eq. II-B.4)

H_T (Hypothesis from the monometallic samples: 100% of Rh_S-$O_{3/2}$ and of 23.5% of Ni_S-O are titrated by H_2)

$$\boldsymbol{x\ Rh_S\text{-}O_{3/2} + 0.235\ y\ Ni_S\text{-}O + (2\ x + 3/2 * 0.235\ y)\ H_2 = x\ Rh_S\text{-}H + 0.235\ y\ Ni_S\text{-}H + (3/2\ x + 0.235\ y)\ H_2O} \quad \textbf{Eq. II-B.9}$$

where Eq. II-B.9 is obtained by summing Eqs. II-B.S3 and II-B.S4, corresponding to Rh and Ni, respectively.

$x\ Rh_S\text{-}O_{3/2} + 2\ x\ H_2 = x\ Rh_S\text{-}H + 3/2\ x\ H_2O$ **Eq. II-B.S3** (derived from Eq. II-B.2)

$0.235\ y\ Ni_S\text{-}O + 3/2\ 0.235\ y\ H_2 = 0.235\ y\ Ni_S\text{-}H + 0.235\ y\ H_2O$ **Eq. II-B.S4** (derived from Eq. II-B.5)

O_T (Hypothesis from the monometallic samples: 79% of Rh_S-H and of 17.1% of Ni_S-H are titrated by O_2)

$$\boldsymbol{0.79\ x\ Rh_S\text{-}H + 0.171\ y\ Ni_S\text{-}H + (0.79\ x + ¾\ 0.171\ y)\ O_2 = 0.79\ x\ Rh_S\text{-}O_{3/2} + 0.171\ y\ Ni_S\text{-}O + (½\ 0.79\ x + ½\ 0.171\ y)\ H_2O} \quad \textbf{Eq. II-B.10}$$

where Eq. II-B.10 is obtained by summing Eqs. II-B.S5 and II-B.S6, corresponding to Rh and Ni, respectively.

$0.79\ x\ Rh_S\text{-}H + 0.79\ x\ O_2 = 0.79\ x\ Rh_S\text{-}O_{3/2} + ½\ 0.79\ x\ H_2O$ **Eq. II-B.S5** (derived from Eq. II-B.3)

$0.171\ y\ Ni_S\text{-}H + ¾\ 0.171\ y\ O_2 = 0.171\ y\ Ni_S\text{-}O + ½\ 0.171\ y\ H_2O$ **Eq. II-B.S6** (derived from Eq. II-B.6)

Hence, the surface composition in Rh_S (x) and Ni_S (y) of the bimetallic nanoparticles could be estimated (Table II-B.2 and Table II-B.3) by solving two different mathematical systems of equations (one for O_C-H_T, the other one for O_C-O_T data, note that the H_T-O_T equation system could have also been used), namely:

For the **O_C-H_T** system, Eqs. II-B.8 and II-B.9 give:	For the **O_C-O_T** system, Eq. II-B.8 and II-B.10 give:
(¾ x + 0.61 y) = n O_{2,O_C}	(¾ x + 0.61 y) = n O_{2,O_C} **Eq. II-B.11**
(2 x + 3/2 0.235 y) = n H_{2,H_T} **Eq. II-B.12**	(0.79 x + ¾ 0.171 y) = n O_{2,O_T} **Eq. II-B.13**

Where n O_{2,O_C}, n H_{2,H_T} and n O_{2,O_T} are the number of moles of O_2, H_2 and O_2 consumed per g of sample in the O_C, H_T and O_T experiments, respectively.

for $(Ni_{25}Rh_{75})_{NH_3}/SiO_2$, n O_{2,O_C} = 8.3518/22414 = 372.6 µmol O_2/g

n H_{2,H_T} = 17.761/22414 = 792.4 µmol H_2/g

n O_{2,O_T} = 6.6926/22414 = 298.6 µmol O_2/g

for $(Ni_{50}Rh_{50})_{NH_3}/SiO_2$, n O_{2,O_C} = 7.5321/22414 = 336.0 µmol O_2/g

n H_{2,H_T} = 11.060/22414 = 493.4 µmol H_2/g

n O_{2,O_T} = 4.3786/22414 = 195.4 µmol O_2/g

for $(Ni_{75}Rh_{25})_{NH_3}/SiO_2$, n O_{2,O_C} = 6.5386/22414 = 291.7 µmol O_2/g

n H_{2,H_T} = 3.6224/22414 = 161.6 µmol H_2/g

n O_{2,O_T} = 1.1473/22414 = 51.2 µmol O_2/g

Table II-B.3: *Dispersion and surface composition of the bimetallic Ni-Rh nanoparticles determined by O_C-H_T and O_C-O_T methods.*

Sample	Method	Rh_S (µmol/g)	Ni_S (µmol/g)	$Rh_S/(Rh_S+Ni_S)$ %	TMC[b] (µmol/g)	D (%)	Mean D (%)	Particle size (d, nm) from D[c]	Particle size (d, nm) from TEM
$(Ni_{25}Rh_{75})_{NH_3}/SiO_2$	O_C-H_T	368.4	157.9	70	601.6	87.5	87.9	1.2	1.9
	O_C-O_T	348.3	182.5	66	601.6	88.2			
$(Ni_{50}Rh_{50})_{NH_3}/SiO_2$	O_C-H_T	191.0	316.0	38	649.3	78.1	78.0	1.4	1.7
	O_C-O_T	197.3	308.2	39	649.3	77.9			
$(Ni_{75}Rh_{25})_{NH_3}/SiO_2$	O_C-H_T	- 4.4[a]	483.7	0	712.4	64.1	65.9	1.6	1.8
	O_C-O_T	-16.0[a]	497.9	0	712.4	67.6			

[a] The negative values close to 0 are likely due to the accuracy with which the consumed volumes of probe molecules were recorded (a change in the O_2 uptake of 10 µmol O_2/g on the O_T measurement on $(Ni_{75}Rh_{25})_{NH_3}/SiO_2$ (Exp-5C), namely 61.2 µmol O_2/g instead of 51.2 µmol O_2/g as reported in Table II-B.2, to which would correspond to an increase in the O_2 uptake of 0.22 mL O_2/g (0.026 mL O_2/0.1179 g), would lead to Rh_S values closer from 0); [b] Total metal content (Table II-B.1); [c] Calculated from D and using Eq. II-B.7 by assuming either 100% of Rh or 100% of Ni in the nanoparticles, which does not influence the obtained particle size to a significant extent.

Remarkably, Table II-B.2 shows that similar values of the number of Rh_S and Ni_S can be determined by using either the O_C-H_T or the O_C-O_T systems of equations for the three bimetallic materials. The average value of the fraction of Rh on the surface of these samples would be about 68, 38 and 0% in $(Ni_{25}Rh_{75})_{NH_3}/SiO_2$, $(Ni_{50}Rh_{50})_{NH_3}/SiO_2$ and $(Ni_{75}Rh_{25})_{NH_3}/SiO_2$, respectively, which is always lower than that in the bulk (72, 51 and 22%, respectively), indicating that Ni surface-enriched bimetallic nanoparticles were formed. The dispersion calculated on the basis of the total metal content would be about 87.9, 78.0 and 65.9% for $(Ni_{25}Rh_{75})_{NH_3}/SiO_2$, $(Ni_{50}Rh_{50})_{NH_3}/SiO_2$ and $(Ni_{75}Rh_{25})_{NH_3}/SiO_2$, respectively. By considering such dispersions, the size of the bimetallic nanoparticles may be estimated to be about 1.2, 1.4 and 1.6 nm, respectively, with the use of Eq. II-B.7 and by assuming either 100% of Rh or 100% of Ni in the nanoparticles, which does not influence the obtained particle size to a significant extent. Overall, the size of the bimetallic particles of estimated from the chemisorption measurements is found to be in reasonably good agreement with those determined by TEM (Table II-B.3), albeit one may argue that this agreement appears to be better for the samples containing Ni contents greater than or equal to 1.86 wt.% (in other words samples for which the bulk molar fraction of Ni in the bimetallic nanoparticles is greater than or equal to 50%) rather than for the Rh-rich sample ($(Ni_{25}Rh_{75})_{NH_3}/SiO_2$ sample). The greater discrepancy between the particle size estimated by the chemisorption measurements compared to that determined by TEM remains difficult to explain at this stage of the study and may be attributed to a greater susceptibility of Ni to bulk oxidation that would be favored by the lower size and/or the easier oxygen diffusion in the bimetallic nanoparticles during the O_C experiment. Finally, the fact that the most Ni-rich bimetallic nanoparticles ($(Ni_{75}Rh_{25})_{NH_3}/SiO_2$) shows only Ni surface atoms indicates that such sample should mainly exhibit Rh@Ni core@shell nanoparticles, which could not be revealed by any other means.

II-B.4. Conclusion

The metal dispersion and the mean particle diameter of monometallic (Rh or Ni) nanoparticles supported on silica, prepared by impregnation of SiO_2 by the corresponding metal precursor salts in aqueous ammonia solutions, could be ascertained by using a three-step chemisorption method involving O_2 chemisorption (O_C), followed by surface O titration by H_2 (H_T) and surface H titration by O_2 (O_T). Assuming that the two metals (Ni and Rh) exhibited similar

chemisorptive properties in both monometallic and bimetallic nanoparticles, the surface composition of the bimetallic samples could be estimated for the first time, on the basis of the resolution of systems of equations related to either O_C-H_T or O_C-O_T data providing remarkably similar estimation of surface compositions. Hence, it was shown that, for all the bimetallic samples, the Rh content on the surface of the bimetallic nanoparticles was systematically lower than that of the bulk measured by ICP-OES. For a bulk atomic composition of the bimetallic nanoparticles of 72% of Ni, the Ni-Rh bimetallic nanoparticles are present as Rh@Ni core@shell structure, which could not be revealed by any other means and in particular by TEM as a result of their small size. The average size of the bimetallic nanoparticles could also be estimated from the chemisorption measurements and associated dispersions, and were found to compare reasonably well with those measured by TEM, in particular for the samples containing Ni contents greater than or equal to 50% on an atomic basis. Further investigation of the same samples using EXAFS are currently under progress to validate such findings.

Chapter II – Part C: Hydrogenolysis of guaiacylglycerol-β-guaiacyl ether and an Organosolv lignin with nickel-based Aerosil 380

In this chapter, the catalytic tests were conducted on guaiacylglycerol-β-guaiacyl ether which is a better lignin model than $K1_{HH}$ and $A1_{HH}$ presented in Chapter II – Part A. Using Aerosil 380 impregnated with Ni in aqueous ammonia and reduced at 650°C, ($Ni^0_{NH_3}/SiO_2$), the effect of several parameters (substrate/metal molar ratio, reaction atmosphere as well as gas pressure) was investigated with the aim of optimizing the hydrogenolysis yield. Then, few preliminary tests with an Organosolv lignin sample of Birch Lignin were conducted and analytical characterizations showed partial cleavage but not into small aromatic molecules.

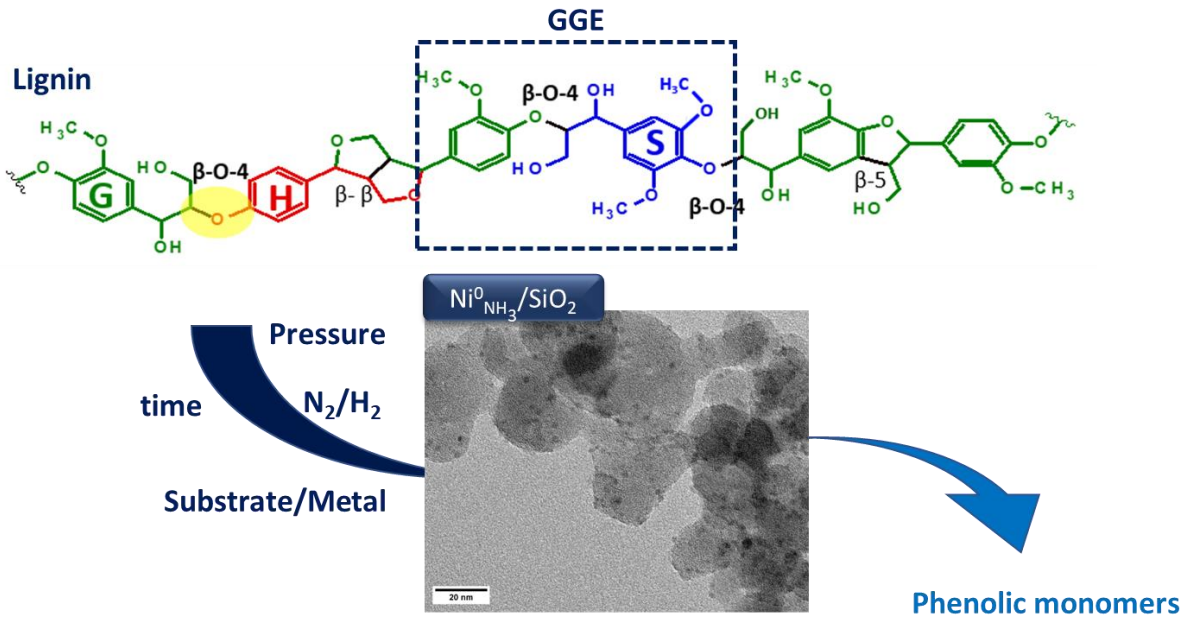

II-C.1. Introduction

The extraction process of lignin cannot be performed without any modification of the native structure. Organosolv process is known to be more environmentally friendly compared to other processes, and does lead to a partial degradation of the native structure [111].

Reductive depolymerization can be conducted under N_2 with alcohol as an H-donor solvent under an inert atmosphere [16], or with a combination of H_2 and alcohols as solvents. In the latter, a high yield of phenolic monomer was observed for the reaction of Organosolv lignin in the presence of mesoporous aluminosilica nanospheres bearing Ni NPs at 180°C under 20 bar of H_2 and for 2 h [13].

In our previous work (Chapter II – Part A1), hydrogenolysis tests of $A1_{HH}$ with $Ni^0_{NH_3}/SiO_2$ reduced at 500°C conducted in isopropanol (H-donor) under 5 bar N_2 at 180°C for 1 h, led to total conversion of all dimers and gave rise to a high phenol yield (33%$_C$). On the other hand, the same catalyst also reduced at 500°C tested on $K1_{HH}$ (a pre-oxidized β-O-4 lignin model) led to rather low activity. It has to be noted that $K1_{HH}$ conversion, but also those of the intermediates $A1_{HH}$ and $C1_{HH}$, were clearly improved (100%) by reducing Ni(II) at 650°C instead of 500°C. Hence, after only 1 h, with a substrate/metal molar ratio of 100, $K1_{HH}$ and all the dimers were converted into cleavage products giving rise to the highest phenol yield obtained from $K1_{HH}$ in this work up to now (39%$_C$ close to the theoretical maximum yield 43%$_C$). Here, guaiacylglycerol-β-guaiacyl ether (GGE) [112–114] is used to model the β-O-4 linkage of lignin.

In this work, $Ni^0_{NH_3}/SiO_2$ reduced at 650°C was chosen to conduct tests with GGE (Figure II-C.1). looking at the influence of the molar substrate/metal ratio, the reaction atmosphere as well as gas pressure on the catalytic activity and the product selectivity. Then, the conditions optimized with GGE were applied to Organosolv lignin sample of Birch Lignin (BL) dissolved in isopropanol.

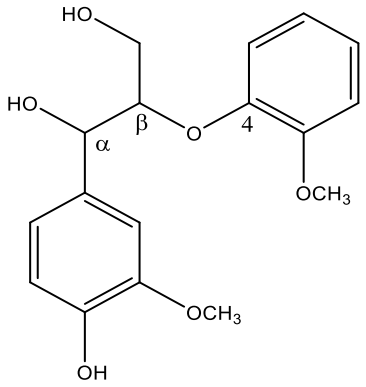

Figure II-C.1: *Guaiacylglycerol-β-guaiacyl ether (GGE).*

II-C.2. Experimental section

$Ni^{II}_{NH_3}/SiO_2$ preparation and its characterization in its dried state were detailed in the Chapter II-Part A1, paragraph II-A1.2.1 and II-A1.3.1, respectively.

Reductive cleavage of GGE

As mentioned earlier, $Ni^0_{NH_3}/SiO_2$ reduced at 650°C was chosen as a catalyst, the temperature was set at 180°C, with 15 mL of *i*-PrOH as a solvent and/or H-donor solvent. For the hydrogenolysis of GGE, its initial concentration was 0.06 M. For further details for the catalytic test, see Chapter II – Part A1, paragraph II-A1.2.2. From the reaction mixture, an aliquot of 100 µL was withdrawn and combined with H_2O/MeOH in a 10 mL flask. The resulting solution was analyzed by HPLC.

The conversion of dimers and the yields of products (expressed in % of starting carbon) were defined as follows:

$$\text{Yield } Y_j\ (\%_C) = \frac{mol\ of\ \text{"j" x number of carbons of "j"}}{initial\ mol\ of\ GGE\ x\ number\ of\ carbons\ of\ GGE} \text{ x } 100 \qquad \text{(Eq. II-C.1)}$$

$$\text{Conversion } X_i\ (\%) = \frac{mol\ of\ reacted\ of\ GGE}{initial\ mol\ of\ GGE} \text{ x } 100 \qquad \text{(Eq. II-C.2)}$$

$X_{Di}{}^*\ (\%) = X_i - \Sigma Y_{Di}$ *where Y_{Di} corresponds to the yields of molecules keeping the C-OAr bond* (Eq. II-C.3)
**X_{Di} quantifies the overall rate of cleavage of the C-OAr bond.*

Isolation of the soluble fraction of Organosolv lignin in i-PrOH

The lignin from birch lignin (BL) we have studied was graciously provided by CIMV (Compagnie Industrielle de la Matière Végétale) and has been extracted using an Organosolv process. Before use, the sample had to be purified with hot water to remove all sugars. Then, to isolate the soluble part of this lignin BL, it had been treated with *i*-PrOH. The treatment process is detailed below (Figure II-C.2).

5.0 g of BL was added in 100 mL of *i*-PrOH and the resulting mixture was heated to 80°C for 1 h. After dissolving (brown mixture), fractions of 35 mL were collected in vials for centrifugation (8000 rpm, 10 min). Afterwards, the pellet$_{(1)}$ (3.2 g) was added to 100 mL of *i*-PrOH, heated to 80°C for 1 h, then the solution was centrifuged. In both steps, the supernatants$_{(1)}$ and $_{(2)}$ were collected in a round flask, the solvent was evaporated with a rotary evaporator and the solid was dried under vaccum for 24 h in oil bath heated at 40°C. The pellet$_{(2)}$ contains BL not soluble in *i*-PrOH. The weight of the recovered solid from the first treatment (BL/*i*-PrOH$_{(1)}$) was $m_{(1)}$ = 1.8 g and the solubility yield was $Y_{(1)}$ = 1.8/5.0 x 100 = 36%, and for the second treatment (BL/*i*-PrOH$_{(2)}$), $m_{(2)}$ = 0.1 g and $Y_{(2)}$ = 0.1/3.2 = 3%, so, the solubility yield of both treatments is 39% and the weight of recovered BL/*i*-PrOH is 1.9 g. BL, BL/*i*-PrOH and BL not soluble in lignin were characterized by ^{1}H-NMR.

BL/*i*-PrOH was also analyzed by Gel Permeation Chromatography (GPC) in order to evaluate its number molecular weight. It is noteworthy that this number molecular weight is not absolute but it is relative to the PMMA standards.

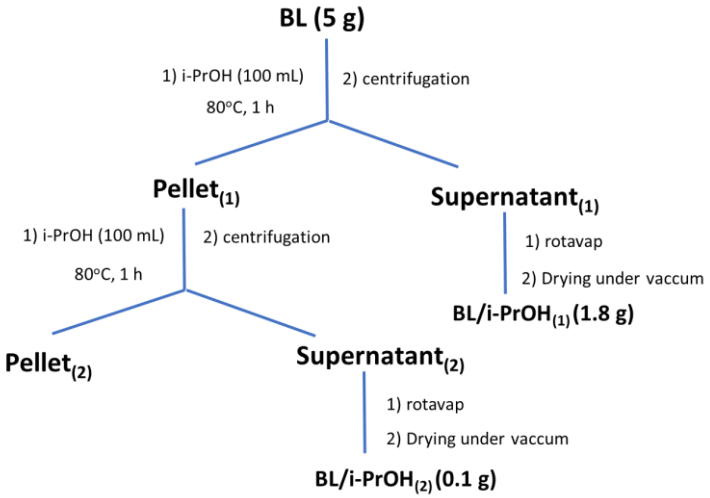

Figure II-C.2: *Treatment process of Organosolv birch lignin with i-PrOH.*

II-C.3. Results and discussion

II-C.3.1. Hydrogenolysis of GGE

For guaiacylglycerol-β-guaiacyl ether (GGE), many efforts have been deployed in order to optimize the reaction conditions.

Before that, a preliminary test was conducted with GGE at 180°C for 5 h under 5 bar of N_2 with a substrate/metal molar ratio of 100 in order to understand the scheme for the cleavage of GGE under selected conditions. The reactant and the products were not detectable by GC-MS; therefore, the reaction was monitored by HPLC (Figure II-C.3), HPLC-MS (Figure II-C.4) and 2D-NMR (Figure II-C.5).

In Figure II-C.3 A, between 7 and 25 min, several products were detected. No products were evidenced before 7 min and after 25 min in this reaction. The retention times of the main products from the cleavage of GGE (10.6 min) were mainly 7.2 min (guaiacylpropanol, GPol), 9.9 min (guaiacol, Gol), and 23.7 min attributed to an unknown product (Figure II-C.3 A). The conversion of GGE was 40%. For the detection of all possible products, a total conversion of GGE was needed. Therefore, a second test with GGE was carried out under the same reaction conditions but with a lower molar substrate/metal ratio (25). By HPLC (Figure II-C.3 B), the conversion of GGE was 100%. Between 7 and 25 min, GPol and Gol and the unknown product were detected. Two new products were evidenced at 24.6 min (4-ethylguaiacol) and at 31.4 min (4-propyguaiacol) (Figure II-C.3 B).

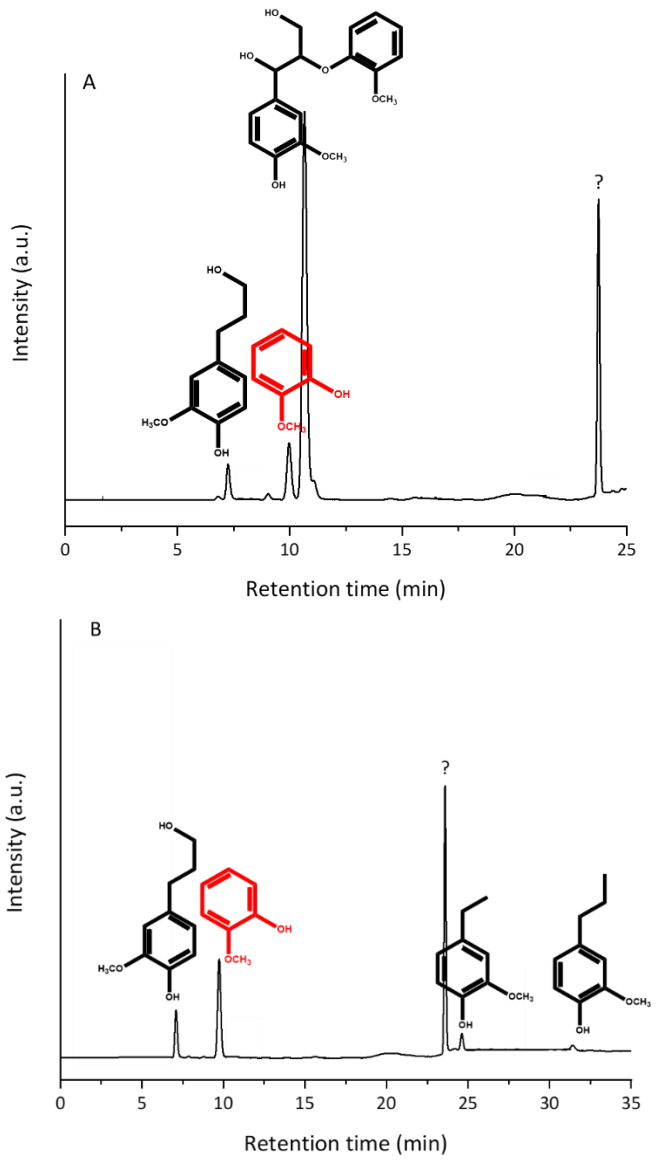

Figure II-C.3: *HPLC profiles of GGE hydrogenolysis at substrate/metal molar ratio of (A) 100 and (B) 25. (HPLC conditions: AcOH:MeOH as mobile phase with a flow rate of 0.4 mL min^{-1}).*

The last and unknown product was identified with the help of HPLC-MS (Figure II-C.4). In the range m/z 320 to 360, a signal at m/z = 343.0942 was attributed to $[GGE + Na]^+$ where molar mass of GGE = 320.1044 g mol^{-1} and M_{Na} = 22.9898 g mol^{-1} (Figure II-C.4). A second intense signal (black arrow) at m/z = 327.1203 was evidenced and the difference of these two peaks corresponds to a loss of an oxygen atom (343.0942 - 327.1203 = 15.9739). 327.1203 corresponds to [unknow product + Na]$^+$, therefore the molecular weight of the unknown product would be 327.1203 - 22.9898 = 304.1305 g mol^{-1} (Figure II-C.4). So, it is a dimer close in structure to GGE but with one less oxygen atom, it occurs by the hydrogenolysis of C-OH bond of GGE at α or γ positions.

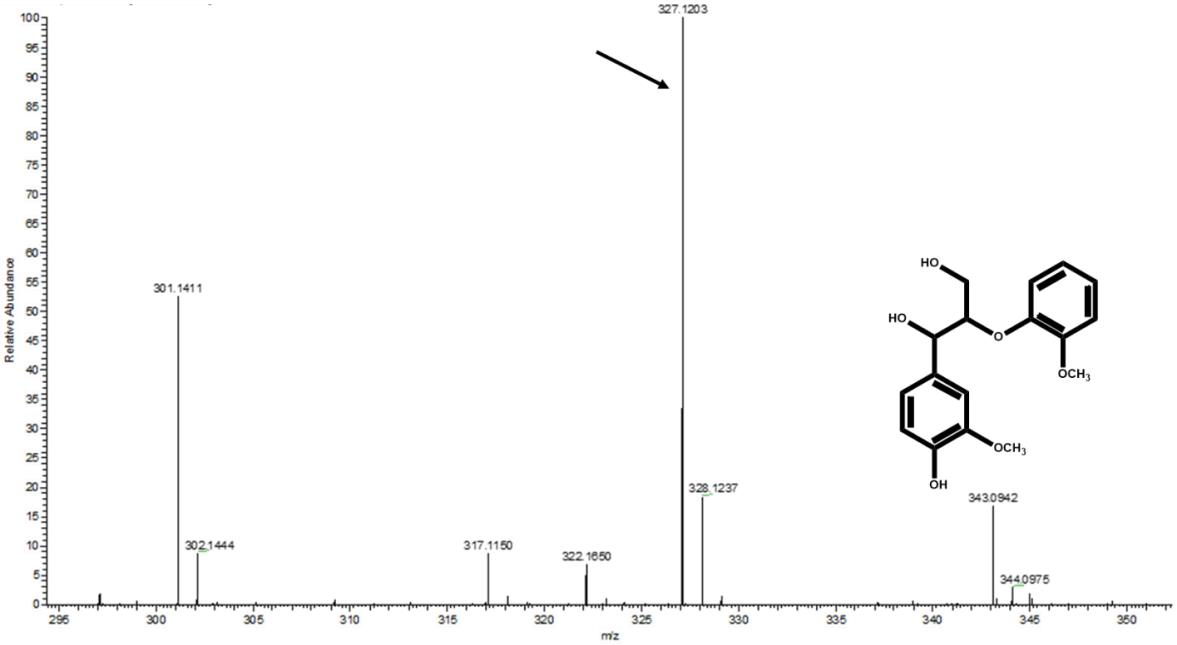

Figure II-C.4: *HPLC-MS profile in the range of m/z = 295 to 350 for the hydrogenolysis of GGE. (The heated capillary temperature, ion spray and capillary voltages were 275°C, 3.6kV and 10V, respectively).*

Herein, we will present two 2D-NMR spectra for two catalytic tests conducted with low and total conversions of GGE. 2D ^{13}C-^{1}H HMBC NMR was performed to further analyze the structural features of GGE and reaction products. Figure II-C.5 A displayed the 2D NMR spectrum after the catalytic test conducted with GGE with substrate/metal molar ratio of 100. The conversion of GGE in that case was low (40%), and it was possible to identify the correlations of Hα, Hβ and Hγ [115], as well as the correlations between H of the OH functions and the nearby carbons such as C4-OH, Cα-OH and Cγ-OH for GGE in black. The guaiacylpropanol in blue was also identified (Figure II-C.4 A). For the unknown dimer, correlations of Hβ and Hγ similar to those of GGE were identified. No correlation between H of the OH group and the carbon in Cα position which means that the loss of oxygen has occurred on α position and the dimer was 4-(3-hydroxy-2-(2-methoxyphenoxy) propyl)-2-methoxyphenol (correlations in red, Figure II-C.5 A and B).

The second catalytic test carried out with substrate/metal molar ratio of 25 with similar reaction conditions led to a total conversion of GGE. This was confirmed in Figure II-C.5 B where, clearly, no spots attributed to GGE were seen. Instead, the signals of the dimer, in red, enormously increased, as well as the GPol and the two new monomers the 4-propylguaiacol and 4-ethylguaiacol, identified in pink and green, respectively (Figure II-C.5 B). GGE as well as all mentioned products can be detected by 2D-NMR except the guaiacol due to its lack of alkyl functionalities unlike 4-ethyl or 4-propylguaiacol.

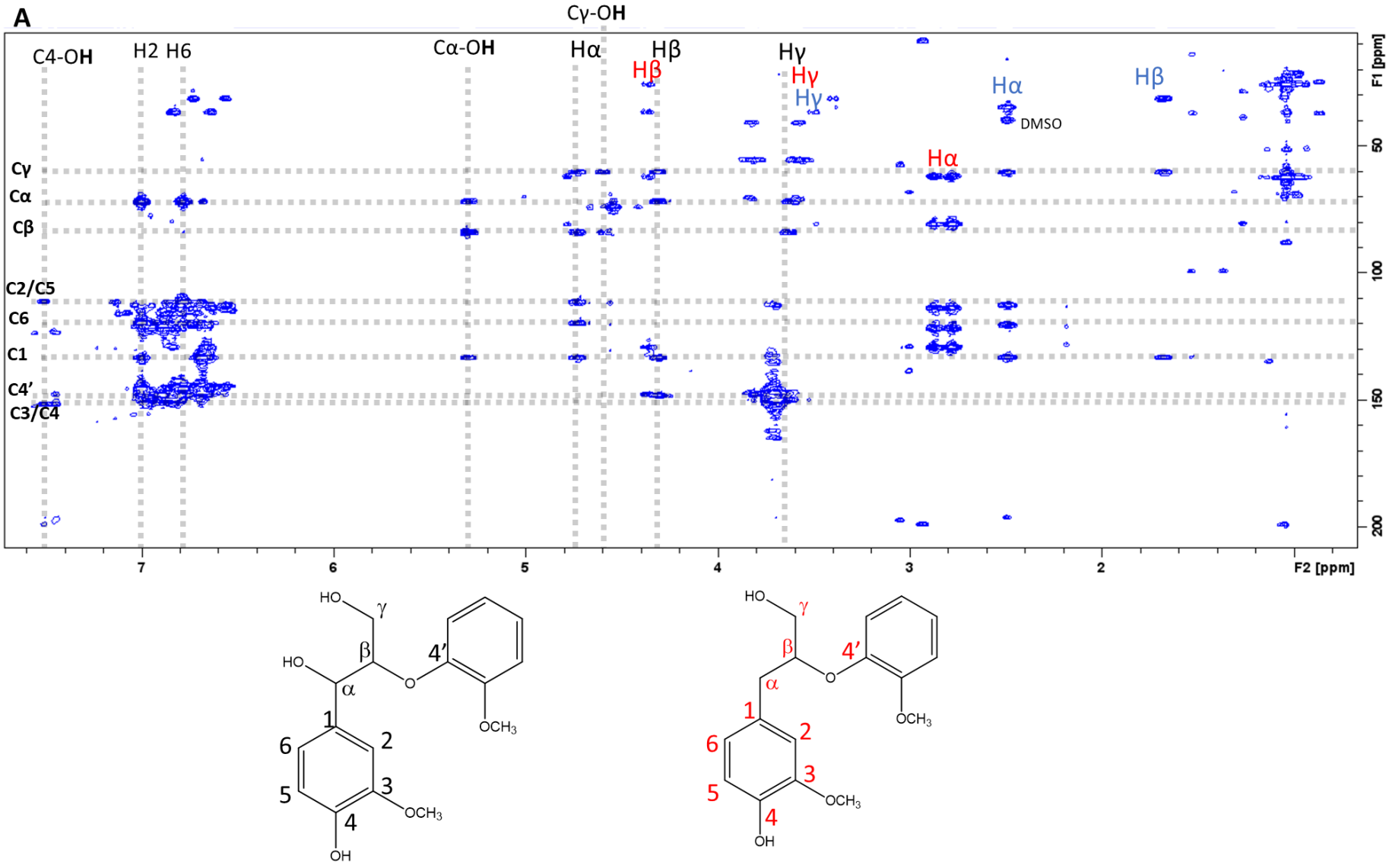
A
Cγ-OH
C4-OH
H2 H6
Cα-OH
Hα
Hβ
Hγ
Hβ
Hγ
Hγ
Hα
DMSO
Hβ
Hα
Cγ
Cα
Cβ
C2/C5
C6
C1
C4'
C3/C4
F1 [ppm]
50
100
150
200
7
6
5
4
3
2
F2 [ppm]
HO
γ
β
α
HO
4'
O
OCH3
1
2
3
4
5
6
OCH3
OH
HO
γ
β
α
4'
O
OCH3
1
2
3
4
5
6
OCH3
OH

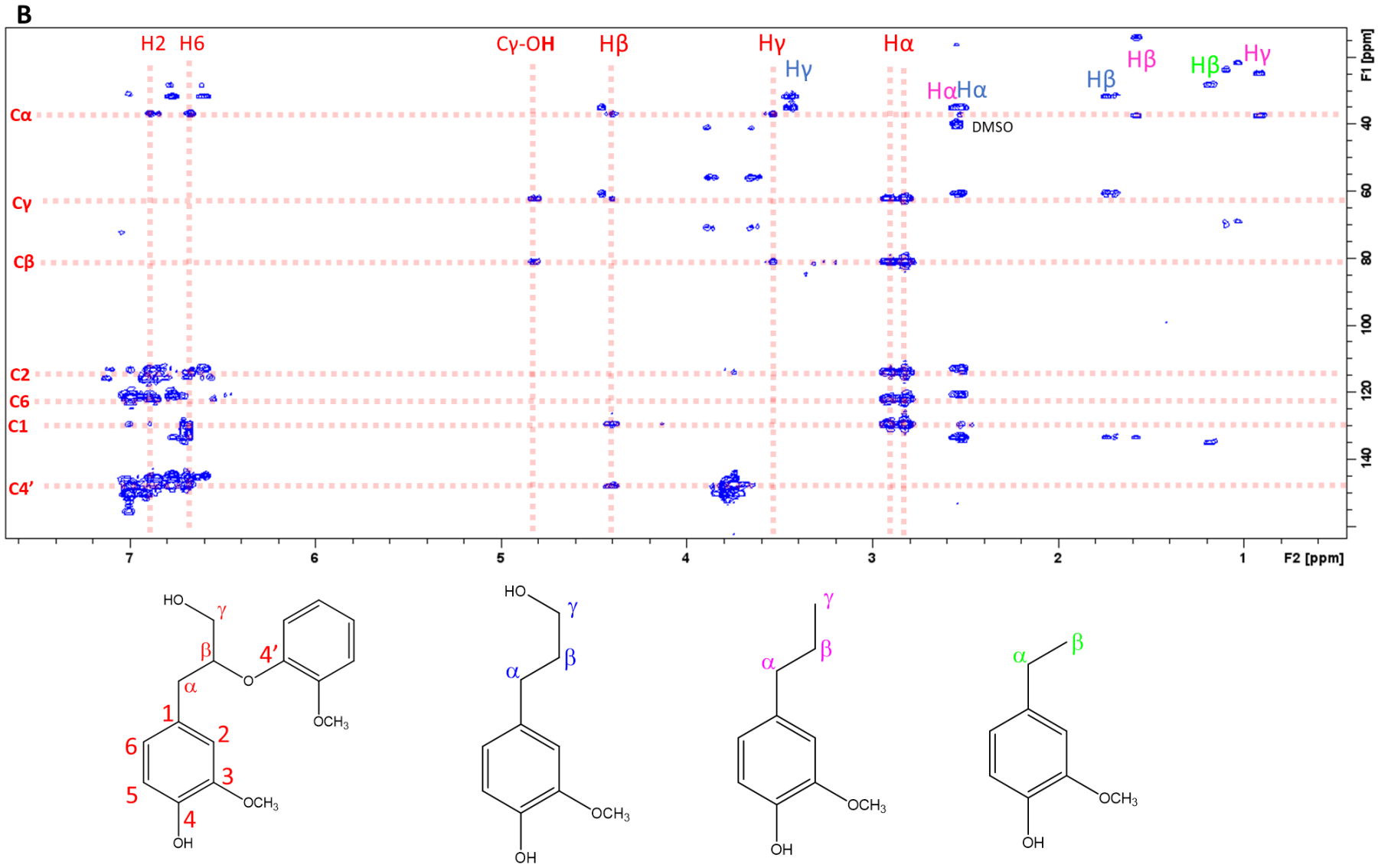

Figure II-C.5: *The 2D HMBC NMR spectra in DMSO-d6 operating at 600 MHz of the reaction mixture obtained after two catalytic tests conducted with GGE (A) with a molar substrate/metal ratio of 100 and (B) with a molar substrate/metal ratio of 25.*
Reaction conditions: $Ni^0_{NH_3}/SiO_2$*,* $[GGE]_o$ *= 0.06 M,* $V_{i\text{-}PrOH}$ *= 15 mL, 180°C, 5 h, 5 bar of* N_2*.*

With the help of all these analytical characterizations, a possible hydrogenolysis scheme of GGE can be deduced. GGE can be transformed by hydrogenolysis of Cα-OH into 4-(3-hydroxy-2-(2-methoxyphenoxy) propyl)-2-methoxyphenol. This dimer can be cleaved into monomers through hydrogenolysis, affording guaiacol and guaiacylpropanol. The latter can be transformed into 4-propylguaiacol by C-OH cleavage, then to 4-ethylguaiacol after its C-C bond cleavage (Figure II-C.6). Taking into account the total number of carbon atoms in GGE (17), the expected maximum yield of guaiacol (phenolic monomer), calculated in % C is = 7/17 = 41%$_C$. Numbers 1 and 2 indicate from which aromatic ring of GGE the monomers originate. All products could be detected and quantified by HPLC.

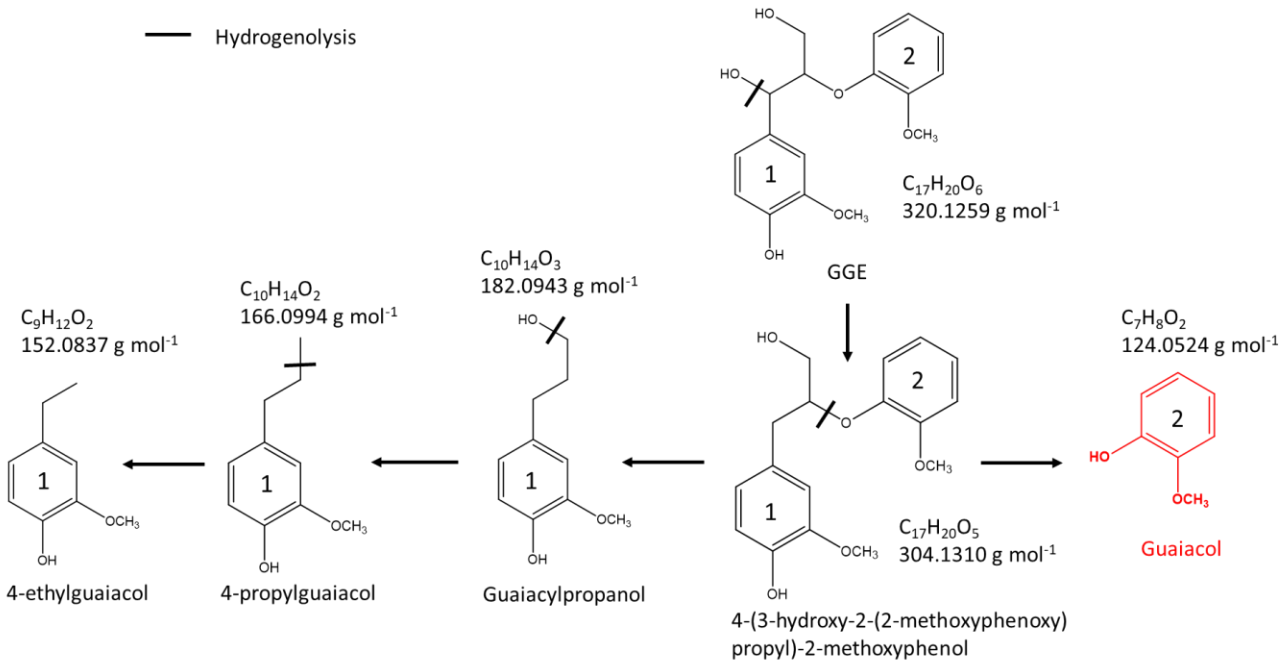

Figure II-C.6: *Expected products from the cleavage of GGE.*

In this part, the effect of several parameters, such as, substrate/metal molar ratio, reaction atmosphere as well as gas pressure was studied. So, it seemed interesting to review their influence on the catalytic activity and the product selectivity in the case of GGE which has a structure close to real lignin in order to optimize the yield of guaiacol like it was done for phenol in the case of K1$_{HH}$ and A1$_{HH}$ (Chapter II - Part A1).

II-C.3.1.a. Effect of molar substrate/metal ratio

The influence of molar substrate/metal ratio on the hydrogenolysis of GGE under an inert atmosphere (5 bar of N_2) was investigated with substrate/metal molar ratios from 10 to 100. It could be concluded from Figure II-C.7 that GGE hydrogenolysis process was highly dependent on substrate/metal molar ratio. The conversion of GGE increased from 45% to 100% (Eq. II-C.2) as well as the C-OAr bonds conversion, also increased from 15% to 70% (Eq. II-C.3) while decreasing the substrate/metal molar ratio from 100 to 25. By dividing the substrate/Ni molar ratio by two, *i.e.*, increasing the weight of the catalyst twice, the conversion of GGE doubled (64.4%) but the guaiacol yield did not greatly improve (10.5%$_C$, Eq. II-C.1) after 5 h. So, the path to enhance the GGE conversion is to decrease the substrate/Ni to 25. In this case, and by keeping the same reaction conditions, GGE was totally converted. Unfortunately, the maximum guaiacol yield is 15.4%$_C$ and the C-OAr bonds conversion remained too low. As can be seen, the guaiacol yield increased obviously with the lowest substrate/metal molar ratio (18%$_C$ with subs./M = 25). The test with a low substrate/metal molar ratio (subs./M = 10) was conducted under the same reaction conditions. In that case, results similar to those obtained with subs./M = 25 were obtained (Y_{GoI} = 22%$_C$, Eq. II-C.1, X_{GGE} = 100%, Eq. II-C.2, X_{Di} = 73%, Eq. II-C.3) (Figure II-C.7). Therefore, the next catalytic tests were conducted with substrate/metal molar ratio of 25.

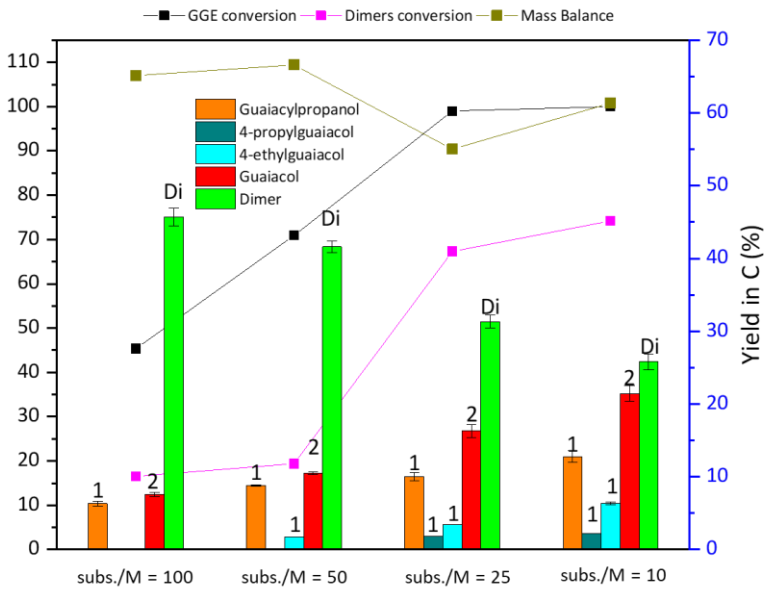

Figure II-C.7: *Effect of susbtrate:metal ratio on GGE/dimers conversion and yields of the main products obtained.*
Reaction conditions: $Ni^0_{NH_3}/SiO_2$, $[GGE]_o$ = 0.06 M, $V_{i\text{-}PrOH}$ = 15 mL, 180°C, 5 h, 5 bar of N_2.

In the work of Si *et al*. a test with GGE was conducted over Ni-based silica catalysts at 180°C in methanol under 20 bar of H_2 for 2 h. They reported a 96% conversion of GGE with 31%$_C$ of GoI over Ni/SiO_2 and etherified GGE at α or γ-OH which were not depolymerized to aromatic monomers and not detected in our case [13].

II-C.3.1.b. Effect of reaction atmosphere

GGE hydrogenolysis was also investigated under hydrogen and under nitrogen atmosphere (Figure II-C.8). The reaction results under H_2 or N_2 (including GGE conversion, C-OAr bonds conversion and guaiacol yield) were exhibited in Figure II-C.8. Addition of an external hydrogen source (H_2 gas in addition to *i*-PrOH) was not found to have a promoting effect on the GGE hydrogenolysis compared to N_2. In fact, in both cases, GGE conversion was total, C-OAr bonds conversions were very similar (76% and 70%, Eq. II-C.2) and guaiacol yield was 16%$_C$ (Eq. II-C.1) under H_2 and N_2. This indicate that the addition of H_2 do not improve the GGE hydrogenolysis reaction.

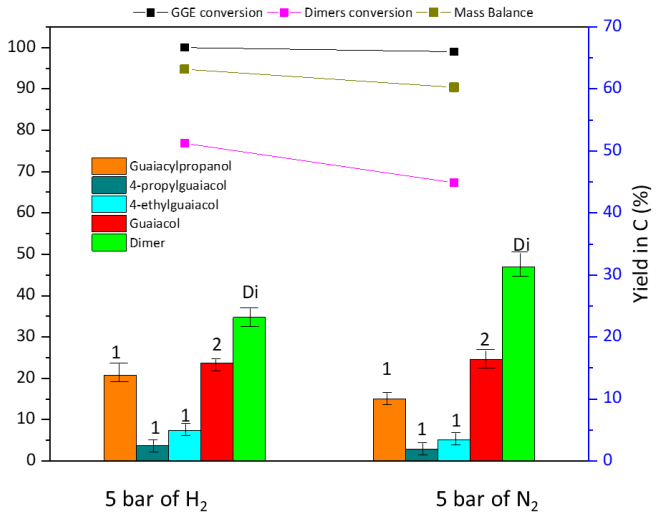

***Figure II-C.8**: Effect of reaction atmosphere (H_2 or N_2) on GGE/dimers conversion and yields of the main products obtained.*
Reaction conditions: $Ni^0_{NH_3}/SiO_2$, $[GGE]_o$ = 0.06 M, $V_{i\text{-}PrOH}$ = 15 mL, 180°C, subs./M = 25, 5 h, 5 bar of H_2 or N_2.

II-C.3.1.c. Effect of N_2 pressure

Figure II-C.9 exhibited the effect of N_2 pressure on the hydrogenolysis of GGE with a substrate/metal ratio of 25.

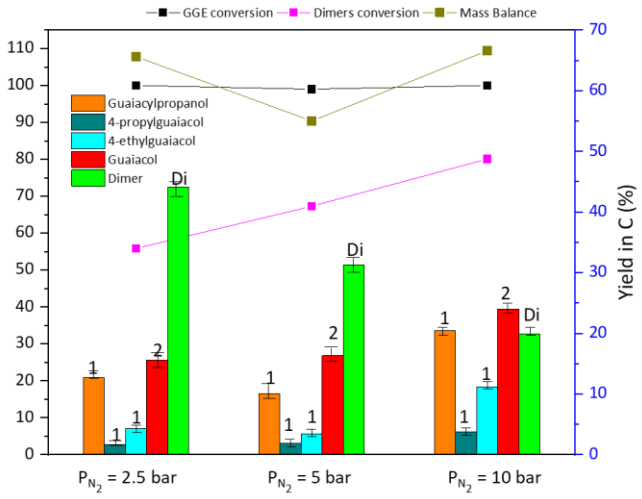

Figure II-C.9: *Effect of N_2 pressure on GGE/dimers conversion and yields of the main products obtained. Reaction conditions: $Ni^0_{NH_3}/SiO_2$, $[GGE]_o$ = 0.06 M, $V_{i\text{-}PrOH}$ = 15 mL, 180°C, subs./M = 25, 5 h.*

The hydrogenolysis reactions were carried out at a pressure range from 2.5 to 10 bar of N_2. From the results, it could be inferred that N_2 pressure was also of great importance on both C-OAr bonds conversion and guaiacol yield. An obvious promoting effect was observed during GGE hydrogenolysis when the reaction was carried out at 10 bar of N_2. Guaiacol yield increased from 15%$_C$ to 24%$_C$ with better C-OAr bonds conversions (from 55% to 80%).

II-C.3.2. Characterization of Birch Lignin and first reductive cleavage tests

The starting Birch Lignin (BL), BL soluble as well as BL not soluble in *i*-PrOH were characterized by ^{1}H NMR (Figure II-C.10 A and B a, b and c).

In Figure II-C.10 A a and b, a broad signal between 3.5 and 4 ppm could be detected and could be attributed to methoxy groups OCH_3 [116–118]. The methoxy signal was present for BL insoluble in *i*-PrOH. In that case, it was very flat and above all, there were no overlapping fine peaks (Figure II-C.10 A c). This means that only molecules with high molar mass remain and that molecules with low molar mass (monomers, dimers, trimers…) were no longer present in that fraction. This was confirmed just afterwards by the signals in the aromatic zone.

A sharp peak at 1.25 ppm was evidenced in the starting BL and in BL/*i*-PrOH (Figure II-C.10 A a and b), that was attributed to fatty acids absent in non-soluble BL (Figure II-C.10 A c). This indicate that BL/*i*-PrOH contains residual fatty acids. A shoulder at 0.85 ppm and a broad peak between 1.2 and 1.3 ppm could be attributed to aliphatics in BL and in BL/*i*-PrOH (Figure II-C.10 A a and b). In the aromatic region, oligomers or polymers were identified by very large peaks as

it is indicated in Figure II-C.10 B a, b and c. Two small sharp peaks at 6.6 ppm and 7.4 ppm could be attributed probably to aromatic cycles with low molecular mass in BL/*i*-PrOH (Figure II-C.10 B a and b).

In the end, BL/*i*-PrOH contains methoxy groups, residual fatty acids and molecules with low molecular weight, whereas non soluble BL was clear from fatty acids but was rich with molecules with high molecular weight.

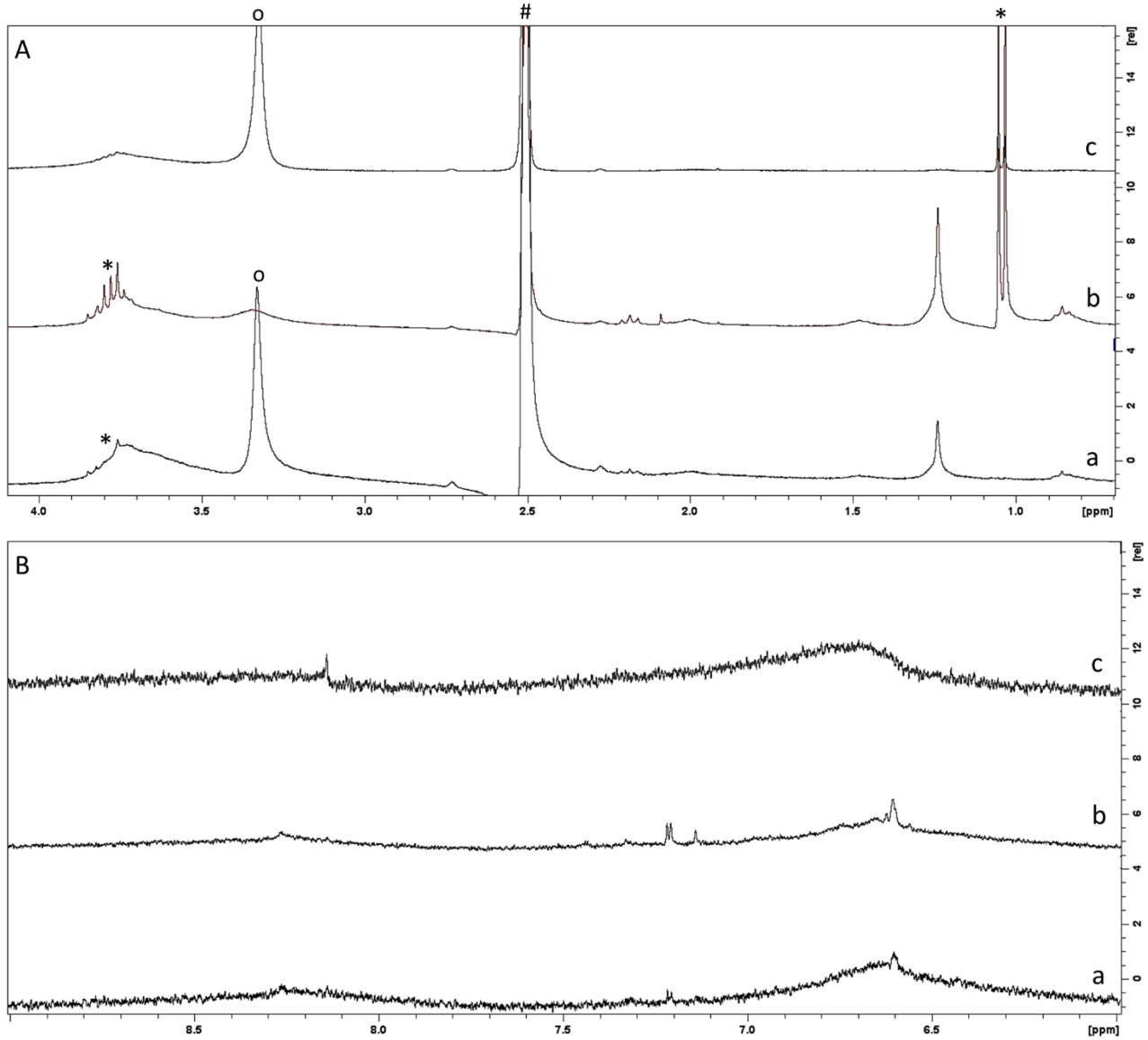

Figure II-C.10: *^{1}H NMR in DMSO operating at 300 MHz (A) from 0.8 ppm to 4.0 ppm and (B) in the aromatic region from of 6.0 ppm to 9.0 ppm of (a) BL treated with hot water only, (b) BL/i-PrOH (BL soluble in i-PrOH) and (c) BL not soluble in i-PrOH.*

** Isopropanol, $^{\#}$ DMSO-d6 and ^{o} water.*

The analysis by SEC indicated that the relative mean-number molar mass of BL/*i*-PrOH was Mn = 825 g mol^{-1}. In order to conduct catalytic tests with BL/*i*-PrOH and to keep C-O bonds to cleave /Ni ratios similar to those used with $A1_{HH}$, $K1_{HH}$ and GGE, a simple calculation was performed. In conventional tests with $A1_{HH}$, $K1_{HH}$ and GGE, the number of mol of substrate was 8.5 x 10^{-4} mol which is equivalent to 8.5 x 10^{-4} mol of C-O bonds. So, considering that BL/*i*-PrOH is composed of coniferyl alcohol units (Figure II-C.11) with a molar weight of 180.2 g mol^{-1}, the number of aromatic units per mol of BL/*i*-PrOH 825/180.2 = 4.6 ~ 5, which means that each mol of polymer contains 4 mol of C-O bonds to cleave. Therefore, for a typical catalytic test, the amount of BL/*i*-PrOH was m = (8.5 x 10^{-4} x 825)/4 = 0.175 g = 0.18 g.

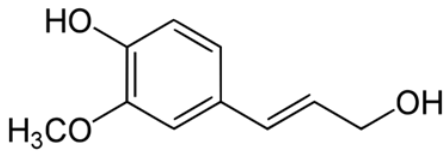

Figure II-C.11: *Coniferyl alcohol structure.*

Using $Ni^0_{NH_3}/SiO_2$ reduced at 650°C, two catalytic tests were conducted with 0.18 g of BL/*i*-PrOH for 5 h at 180°C under 5 bar of N_2. In the first one, 10 mg of the catalyst were used (C-O/Ni = 100), while in the second, the ratio was adjusted to 20 (Table II-C.1). Further details for the catalytic test in Chapter II – Part A, paragraph II-A.2.2.

Table II-C.1: *Catalytic tests performed on BL/i-PrOH for 5 h with $Ni^0_{NH_3}/SiO_2$ reduced at 650°C with two different catalyst:lignin ratios.*

Entry	Catalyst mass (mg)	Eq.bonds/Metal (mol/mol)	Catalyst/lignin (wt/wt)
1	10	100	0.055
2	50	20	0.277

Reaction conditions: $m_{BL/i\text{-}PrOH}$ = 0.18 g, $V_{i\text{-}PrOH}$ = 15 mL, 180°C, 5 h, 5 bar of N_2.

After the tests, the reaction mixture was centrifuged (8000 rpm, 10 min) and an aliquot of 100 µL of supernatant diluted by H_2O/MeOH was injected in HPLC to detect the smallest molecules, and the rest was evaporated with rotary evaporator. The resulting solid was analyzed in ^1H NMR.

In HPLC (Figure II-C.12), only small peaks, certainly not attributed to cleavage compounds produced during the reaction under these conditions were observed (Table II-C.1, entries 1 and 2).

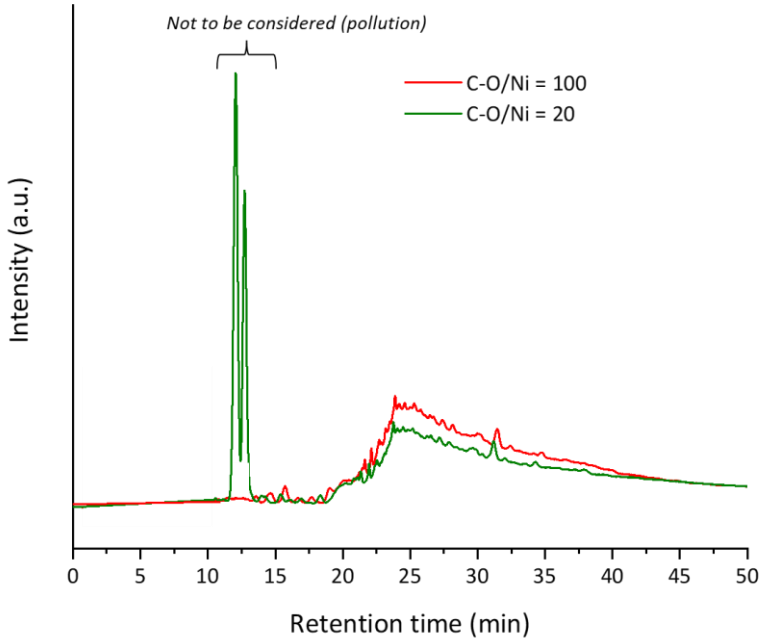

Figure II-C.12: *HPLC profiles for the reductive depolymerization of BL/i-PrOH. The two sharp peaks are not to be considered, they were attributed to benzonitrile, an impurity that occurred during a test conducted for another type of reaction.(HPLC conditions: AcOH:MeOH as mobile phase with a flow rate of 0.4 mL min^{-1}).*

Comparing ^{1}H NMR spectra, in the region between 0.8 and 4.0 ppm, of the initial BL/*i*-PrOH and of the two residues recovered after catalytic tests, no new peaks were detected despite the high catalyst:lignin mass ratio (Figure II-C.13 A a, b and c). In the aromatic region, new broad signals appeared with narrower broad peaks between 7.0 and 7.5 ppm. This could indicate the formation of molecules smaller than those of original BL/*i*-PrOH (Figure II-C.13 B b and c).

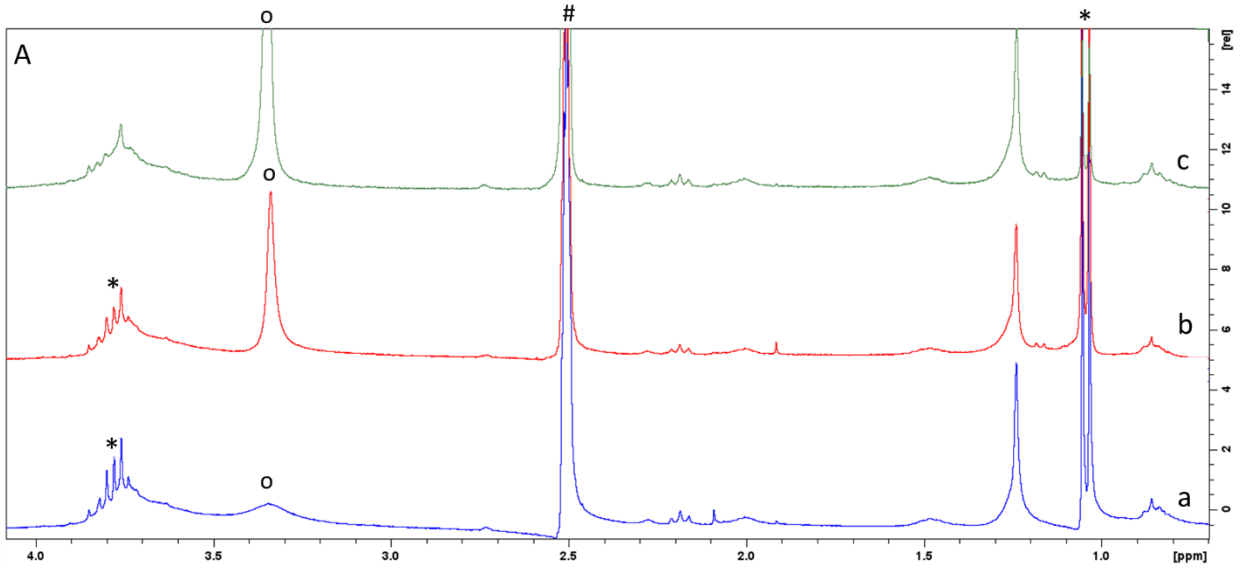

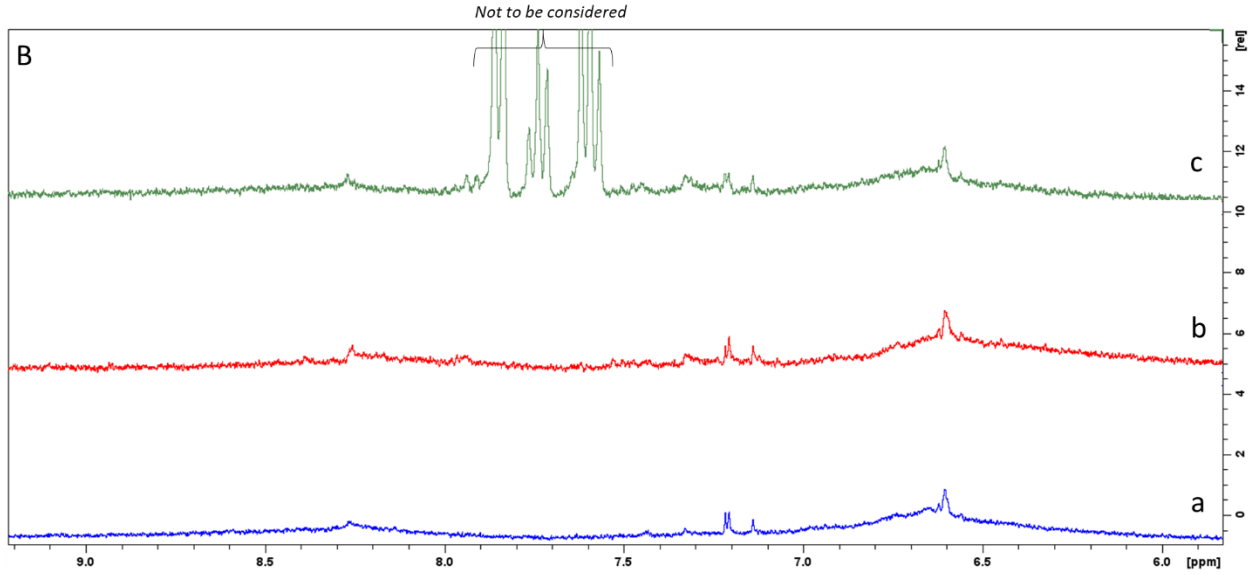

Figure II-C.13: *^{1}H NMR in DMSO-d6 operating at 300 MHz (A) from 0.8 ppm to 4.0 ppm and (B) in the aromatic region from of 6.0 ppm to 9.0 ppm of (a) BL/i-PrOH, (b) test entry 1 (C-O/Ni = 100) and (c) test entry 2 (C-O/Ni = 20).*
** Isopropanol, $^{\#}$ DMSO-d6 and ^{o} water.*
The sharp peaks are not to be considered, they were attributed to benzonitrile, an impurity that occurred during a test conducted for another type of reaction.

To determine what happened to the lignin after catalytic test, the mean-number molar mass of BL/*i*-PrOH before test was compared to that of the solid recovered after the test conducted with C-O/Ni = 20 (Table II-C.1, entry 2). The Mn value, measured by SEC, was 715 g mol^{-1}, which was lower than 825 g mol^{-1}. This small decrease could be a sign of a partial cleavage of lignin.

This let us conclude that the conditions in which the catalytic tests were carried out with BL/*i*-PrOH were not optimum and finding the optimal conditions is the main target.

II-C.4. Conclusion

In this work, the hydrogenolysis of GGE and an Organosolv lignin sample were carried out in *i*-PrOH. As it was done before for K1$_{HH}$ and A1$_{HH}$, the reaction conditions had to be optimized. Harsher conditions (a low substrate/metal molar ratio (10 or 25), under 5 or 10 bar of N_2) were necessary to improve the cleavage of GGE. The maximum carbon yield of guaiacol was 22%$_C$ with approximatively 75% of C-OAr bonds conversion. Clearly, GGE was less reactive that A1$_{HH}$. It was converted totally but not only to hydrogenolysis products. Indeed, the intermediate dimer, 4-(3-hydroxy-2-(2-methoxyphenoxy) propyl)-2-methoxyphenol, turned out to be quite stable.

With Birch Lignin (BL) extracted first in *i*-PrOH, a small decrease in the mean-number molar mass was observed after catalytic test under relatively mild conditions (in isopropanol, under 5 bar of N_2 at 180°C and in the presence of $Ni^0_{NH_3}/SiO_2$ with a C-O/Ni = 20) which could be a sign of a partial cleavage. Next step will be finding the optimal conditions to improve the catalytic hydrogenolysis. This could be done by increasing the catalyst/lignin mass ratio and performing the reaction for longer duration.

Importantly, in this chapter, the methodologies for the catalytic tests monitoring could be implemented which will be useful for further work.

II-2. Conclusion

Among Ni, Rh and Ni/Rh- based catalyst prepared in this chapter, Ni was the most active one reaching a high phenol productivity. This good catalytic performance was attributed to the formation of Ni(II) phyllosilicates intermediates after the impregnation of Aerosil 380 in the presence of NH_3. Interestingly, the use of chloride counterions instead of nitrate for Ni(II) decreased the amount of Ni-phyllosilicates. In the case of Rh-based catalysts, there was no evidence for the presence of phyllosilicates. From the catalytic activity point of view, strong differences between the use of nitrate and chloride were demonstrated for Ni-based catalysts, which provides some credibility to the important role of Ni-phyllosilicates in the formation of Ni(0) particles efficient for the hydrogenolysis of 2-phenoxy-1-phenylethanol. Using Fe as a doping agent (0.5 and 1.2 wt.%) was tested to improve the phenol selectivity. In fact, adding Fe in a low amount (0.5 wt.%) lowered the phenol selectivity, whereas adding more Fe (1.2 wt.%) decreased the catalytic activity and phenol selectivity.

For all bimetallic catalysts, the average size associated dispersions of the bimetallic nanoparticles could also be estimated from the chemisorption measurements. Also, it was demonstrated that the Rh content on the surface was lower than that of the bulk, exposing more Ni at the surface. This was confirmed by the catalytic activity of the bimetallic Ni/Rh- based catalysts. In fact, the activities and selectivities of the Ni/Rh catalysts were different from those of the monometallic Rh-based one. Actually, they exhibited intermediate activity between the monometallic Rh and Ni-based catalysts except for the one with the highest Ni content. The latter considered to be made of Rh@Ni core@shell displayed a catalytic activity very similar to monometallic Ni.

At the end, efforts have been deployed for optimizing the hydrogenolysis of the guaiacylglycerol-β-guaiacyl ether and screening the reaction conditions for the depolymerization of an Organosolv lignin sample. The more complicated structure of this model and of lignin made the original conditions used not optimal.

References

[1] W. Deng, Y. Feng, J. Fu, H. Guo, Y. Guo, B. Han, Z. Jiang, L. Kong, C. Li, H. Liu, P. T. T. Nguyen, P. Ren, F. Wang, S. Wang, Y. Wang, Y. Wang, S. S. Wong, K. Yan, N. Yan, X. Yang, Y. Zhang, Z. Zhang, X. Zeng, H. Zhou, *Green Energy Environ.* **2023**, *8*, 10–114.

[2] L. Al-Hussaini, F. Launay, E. Galvez, *Materials (Basel).* **2020**, *13*, 812–845.

[3] A. Shivhare, D. Jampaiah, S. K. Bhargava, A. F. Lee, R. Srivastava, K. Wilson, *ACS Sustain. Chem. Eng.* **2021**, *9*, 3379–3407.

[4] M. Wang, F. Wang, *Adv. Mater.* **2019**, *31*, 1–18.
[5] M. Wang, J. Lu, X. Zhang, L. Li, H. Li, N. Luo, F. Wang, *ACS Catal.* **2016**, *6*, 6086–6090.
[6] J. Lu, M. Wang, X. Zhang, A. Heyden, F. Wang, *ACS Catal.* **2016**, *6*, 5589–5598.
[7] C. Zhang, F. Wang, *Acc. Chem. Res.* **2020**, *53*, 470–484.
[8] N. Luo, M. Wang, H. Li, J. Zhang, H. Liu, F. Wang, *ACS Catal.* **2016**, *6*, 7716–7721.
[9] X. Wu, N. Luo, S. Xie, H. Zhang, Q. Zhang, F. Wang, Y. Wang, *Chem. Soc. Rev.* **2020**, *49*, 6198–6223.
[10] I. Hita, P. J. Deuss, G. Bonura, F. Frusteri, H. J. Heeres, *Fuel Process. Technol.* **2018**, *179*, 143–153.
[11] S. Rautiainen, D. Di Francesco, S. N. Katea, G. Westin, D. N. Tungasmita, J. S. M. Samec, *ChemSusChem* **2019**, *12*, 404–408.
[12] C. Zhu, J. P. Cao, X. Y. Zhao, T. Xie, J. Ren, X. Y. Wei, *J. Energy Inst.* **2019**, *92*, 74–81.
[13] X. Si, J. Chen, F. Lu, X. Liu, Y. Ren, R. Lu, H. Jiang, H. Liu, C. Miao, Y. Zhu, X. Luo, J. Xu, *ACS Sustain. Chem. Eng.* **2019**, *7*, 19034–19041.
[14] P. Chen, Q. Zhang, R. Shu, Y. Xu, L. Ma, T. Wang, *Bioresour. Technol.* **2017**, *226*, 125–131.
[15] Y. Zheng, N. Zhao, J. Chen, *Appl. Catal. B Environ.* **2019**, *250*, 280–291.
[16] B. Jiang, J. Hu, Y. Qiao, X. Jiang, P. Lu, *Energy and Fuels* **2019**, *33*, 8786–8793.
[17] M. Carrier, C. Segura, J. L. Garcia, S. Park, H. H. Lamb, N. Escalona, S. W. Peretti, *Appl. Catal. A Gen.* **2018**, *562*, 294–309.
[18] J. He, C. Zhao, J. A. Lercher, *J. Am. Chem. Soc.* **2012**, *134*, 20768–20775.
[19] A. Toledano, L. Serrano, A. Pineda, A. A. Romero, R. Luque, J. Labidi, *Appl. Catal. B Environ.* **2014**, *145*, 43–55.
[20] A. Toledano, L. Serrano, J. Labidi, A. Pineda, A. M. Balu, R. Luque, *ChemCatChem* **2013**, *5*, 977–985.
[21] O. Daoura, G. Fornasieri, M. Boutros, N. El Hassan, P. Beaunier, C. Thomas, M. Selmane, A. Miche, C. Sassoye, O. Ersen, W. Baaziz, P. Massiani, A. Bleuzen, F. Launay, *Appl. Catal. B Environ.* **2021**, *280*, 119417.
[22] O. Daoura, M. N. Kaydouh, N. El-Hassan, P. Massiani, F. Launay, M. Boutros, *J. CO_2 Util.* **2018**, *24*, 112–119.
[23] O. Daoura, S. Daher, M. N. Kaydouh, N. El Hassan, P. Massiani, F. Launay, M. Boutros, *Int. J. Hydrogen Energy* **2018**, *43*, 17205–17215.
[24] L. Delannoy, N. El Hassan, A. Musi, N. N. Le To, J. M. Krafft, C. Louis, *J. Phys. Chem. B* **2006**, *110*, 22471–22478.
[25] S. Chen, Q. Lu, W. Han, P. Yan, H. Wang, W. Zhu, *Fuel* **2021**, *283*, 119333.
[26] C. Xu, S. F. Tang, X. Sun, Y. Sun, G. Li, J. Qi, X. Li, X. Li, *Catal. Today* **2017**, *298*, 89–98.
[27] Z. Wang, X. Chen, X. Xie, S. Yang, L. Sun, T. Li, L. Chen, D. Hua, *Fuel Process. Technol.* **2023**, *248*, 107810.
[28] H. Tan, X. Li, H. Ma, X. Yang, T. Zhan, W. Xie, S. Wang, J. Zhu, *Sustain. Energy Fuels* **2022**, *6*, 2745–2754.
[29] W. Wu, H. Liu, H. Wu, B. Zheng, S. Han, K. Zhang, X. Mei, C. Xu, M. He, B. Han, *ACS Sustain. Chem. Eng.* **2021**, *9*, 11862–11871.
[30] M. Wang, X. Zhang, H. Li, J. Lu, M. Liu, F. Wang, *ACS Catal.* **2018**, *8*, 1614–1620.
[31] C. Zhang, H. Li, J. Lu, X. Zhang, K. E. Macarthur, M. Heggen, F. Wang, *ACS Catal.* **2017**, *7*, 3419–3429.
[32] C. Zhang, J. Lu, X. Zhang, K. Macarthur, M. Heggen, H. Li, F. Wang, *Green Chem.* **2016**, *18*, 6545–6555.
[33] X. Wang, R. Rinaldi, *ChemSusChem* **2012**, *5*, 1455–1466.
[34] G. Zhu, X. Qiu, Y. Zhao, Y. Qian, Y. Pang, X. Ouyang, *Bioresour. Technol.* **2016**, *218*, 718–722.
[35] J. Zakzeski, A. L. Jongerius, P. C. A. Bruijnincx, B. M. Weckhuysen, *ChemSusChem* **2012**, *5*, 1602–1609.
[36] X. Besse, Y. Schuurman, N. Guilhaume, *Appl. Catal. B Environ.* **2017**, *209*, 265–272.
[37] S. Bulut, S. Siankevich, A. P. Van Muyden, D. T. L. Alexander, G. Savoglidis, J. Zhang, V. Hatzimanikatis, N. Yan, P. J. Dyson, *Chem. Sci.* **2018**, *9*, 5530–5535.
[38] T. Klamrassamee, N. Laosiripojana, D. Cronin, L. Moghaddam, Z. Zhang, W. O. S. Doherty, *Bioresour. Technol.* **2015**, *180*, 222–229.
[39] M. Chatterjee, A. Chatterjee, T. Ishizaka, H. Kawanami, *Catal. Sci. Technol.* **2015**, *5*, 1532–1539.
[40] M. Boutros, F. Launay, A. Nowicki, T. Onfroy, V. Herledan-Semmer, A. Roucoux, A. Gédéon, *J. Mol. Catal. A Chem.* **2006**, *259*, 91–98.
[41] O. Daoura, N. El Hassan, M. Boutros, S. Casale, P. Massiani, F. Launay, *ACS Appl. Nano Mater.* **2022**, *5*, 18048–18059.
[42] M. Nowosielska, W. K. Jozwiak, J. Rynkowski, *Catal. Letters* **2009**, *128*, 83–93.
[43] W. K. Jóźwiak, M. Nowosielska, J. Rynkowski, *Appl. Catal. A Gen.* **2005**, *280*, 233–244.
[44] Y. Mao, L. Zhang, X. Zheng, W. Liu, Z. Cao, H. Peng, *Int. J. Hydrogen Energy* **2023**, *48*, 13890–13901.
[45] B. Xia, N. Cao, H. Dai, J. Su, X. Wu, W. Luo, G. Cheng, *ChemCatChem* **2014**, *6*, 2549–2552.
[46] J. Chen, Q. Yao, J. Zhu, X. Chen, Z. H. Lu, *Int. J. Hydrogen Energy* **2016**, *41*, 3946–3954.

[47] H. Duan, D. Wang, Y. Kou, Y. Li, *Chem. Commun.* **2013**, *49*, 303–305.
[48] Y. Wang, H. Arandiyan, S. A. Bartlett, A. Trunschke, H. Sun, J. Scott, A. F. Lee, K. Wilson, T. Maschmeyer, R. Schlögl, R. Amal, *Appl. Catal. B Environ.* **2020**, *277*, 1–23.
[49] P. Mirzaei, S. Bastide, A. Dassy, R. Bensimon, J. Bourgon, A. Aghajani, C. Zlotea, D. Muller-Bouvet, C. Cachet-Vivier, *Electrochim. Acta* **2019**, *297*, 715–724.
[50] M. Thommes, K. Kaneko, A. V. Neimark, J. P. Olivier, F. Rodriguez-Reinoso, J. Rouquerol, K. S. W. Sing, *Pure Appl. Chem.* **2015**, *87*, 1051–1069.
[51] P. Burattin, M. Che, C. Louis, *J. Phys. Chem. B* **1997**, *101*, 7060–7074.
[52] N. K. Zimmerli, C. R. Müller, P. M. Abdala, *Trends Chem.* **2022**, *4*, 807–821.
[53] R. S. Mulukutla, T. Shido, K. Asakura, T. Kogure, Y. Iwasawa, *Appl. Catal. A Gen.* **2002**, *228*, 305–314.
[54] M. J. F. M. Verhaak, A. J. van Dillen, J. W. Geus, *Appl. Catal. A, Gen.* **1993**, *105*, 251–269.
[55] P. Burattin, M. Che, C. Louis, *J. Phys. Chem. B* **1998**, *102*, 2722–2732.
[56] C. Louis, Z. X. Cheng, M. Che, *J. Phys. Chem.* **1993**, *97*, 5703–5712.
[57] B. He, Y. Zhang, X. Liu, L. Chen, *ChemCatChem* **2020**, *12*, 1853–1872.
[58] Y. Zhang, Q. Liu, *J. CO_2 Util.* **2021**, *50*, 101587.
[59] J. C. Park, H. J. Lee, J. U. Bang, K. H. Park, H. Song, *Chem. Commun.* **2009**, 7345–7347.
[60] Z. Bian, S. Kawi, *J. CO_2 Util.* **2017**, *18*, 345–352.
[61] Y. Kishimoto, P. Eckerle, T. Miyatake, M. Kainosho, A. Ono, T. Ikariya, R. Noyori, *J. Am. Chem. Soc.* **1999**, *121*, 12035–12044.
[62] Y. Okamoto, N. Ishida, T. Imanaka, S. Teranishi, *J. Catal.* **1979**, *58*, 82–94.
[63] M. Carvalho, L. F. Wieserman, D. M. Hercules, *Appl. Spectrosc.* **1982**, *36*, 290–296.
[64] D. Xiong, W. Li, L. Liu, *Chem. An Asian J.* **2017**, *12*, 543–551.
[65] S. R. Jiang, B. X. Feng, P. X. Yan, X. M. Cai, S. Y. Lu, *Appl. Surf. Sci.* **2001**, *174*, 125–131.
[66] S. O. Grim, L. J. Matienzo, W. E. Swartz, *J. Am. Chem. Soc.* **1972**, *94*, 5116–5117.
[67] Q. Zhang, M. Wang, T. Zhang, Y. Wang, X. Tang, P. Ning, *RSC anvances* **2015**, *5*, 94016–94024.
[68] W. E. Swartz, R. A. Alfonso, *J. Electron Spectros. Relat. Phenomena* **1974**, *4*, 351–354.
[69] D. N. Hendrickson, J. M. Hollander, W. L. Jolly, *Inorg. Chem.* **1969**, *8*, 2642–2647.
[70] J. W. E. Coenen, *Appl. Catal.* **1991**, *75*, 193–223.
[71] A. Nash, P. Nash, *Bull. Alloy Phase Diagrams* **1984**, *5*, 403–405.
[72] J. Zhang, J. Teo, X. Chen, H. Asakura, T. Tanaka, K. Teramura, N. Yan, *ACS Catal.* **2014**, *4*, 1574–1583.
[73] N. A. Eberhardt, H. Guan, *Chem. Rev.* **2016**, *116*, 8373–8426.
[74] J. Zhang, N. Yan, *Part. Part. Syst. Charact.* **2016**, *33*, 610–619.
[75] Z. Bian, S. Kawi, *J. CO_2 Util.* **2017**, *18*, 345–352.
[76] Z. Bian, S. Kawi, *Catal. Today* **2020**, *339*, 3–23.
[77] S. Das, A. Jangam, S. Jayaprakash, S. Xi, K. Hidajat, K. Tomishige, S. Kawi, *Appl. Catal. B Environ.* **2021**, *290*, 1–53.
[78] C. C. Tu, Y. J. Tsou, T. D. To, C. H. Chen, J. F. Lee, G. W. Huber, Y. C. Lin, *ACS Sustain. Chem. Eng.* **2019**, *7*, 17872–17881.
[79] M. Yang, P. Jin, Y. Fan, C. Huang, N. Zhang, W. Weng, M. Chen, H. Wan, *Catal. Sci. Technol.* **2015**, *5*, 5095–5099.
[80] J. A. Davis, R. O. James, J. O. Leckie, *J. Colloid Interface Sci.* **1978**, *63*, 480–499.
[81] T. Mizutani, Y. Fukushima, A. Okada, O. Kamigaito, *Bull. Chem. Soc. Jpn.* **1990**, *63*, 2094–2098.
[82] J. Herrero, C. Blanco, L. A. Oro, *Appl. Organomet. Chem.* **1989**, *3*, 553–555.
[83] J. Herrero, C. Blanco, M. A. Esteruelas, L. A. Oro, *Appl. Organomet. Chem.* **1990**, *4*, 157–162.
[84] S. Hans-Hebert, *J. Mol. Spectrosc.* **1963**, *11*, 483–485.
[85] W. D. Blanchard, W. Roy Mason, *Inorganica Chim. Acta* **1978**, *28*, 159–168.
[86] P. Emayavaramban, S. G. Babu, R. Karvembu, N. Dharmaraj, *Adv. Sci. Eng. Med.* **2014**, *6*, 659–666.
[87] R. Jagannadha, R. Frost, M. Dickfos, *Spectrochim. Acta Part A Mol. Biomol. Spectrosc.* **2009**, *71*, 1762–1768.
[88] C. Reber, *Can. J. Anal. Sci. Spectrosc.* **2008**, *53*, 91–101.
[89] W. Liu, A. Migdisov, A. Williams-Jones, *Geochim. Cosmochim. Acta* **2012**, *94*, 276–290.
[90] S. Kuhaudomlap, O. Mekasuwandumrong, P. Praserthdam, K. M. Lee, C. W. Jones, J. Panpranot, *ACS Omega* **2023**, *8*, 249–261.
[91] Y. Zhai, C. Li, G. Xu, Y. Ma, X. Liu, Y. Zhang, *Green Chem.* **2017**, *19*, 1895–1903.
[92] A. Laobuthee, A. Khankhuean, P. Panith, C. Veranitisagul, N. Laosiripojana, *ACS Omega* **2023**, *8*, 8675–8682.
[93] W. Wanmolee, J. N. Beltramini, L. Atanda, J. P. Bartley, N. Laosiripojana, W. O. S. Doherty, *ACS Omega*

2019, *4*, 16980–16993.
[94] R. N. Olcese, J. Francois, M. M. Bettahar, D. Petitjean, A. Dufour, *Energy and Fuels* **2013**, *27*, 975–984.
[95] Z. Vajglov, B. Gauli, P. M, N. Kumar, K. Er, W. Johan, R. Lassfolk, I. L. Simakova, I. P. Prosvirin, M. Peurla, J. Kaarle, M. Lind, H. Huhtinen, P. Paturi, D. E. Doronkin, D. Y. Murzin, *ACS Appl. Nano Mater.* **2023**, *6*, 10064–10077.
[96] H. Fang, J. Zheng, X. Luo, J. Du, A. Roldan, S. Leoni, Y. Yuan, *Appl. Catal. A Gen.* **2017**, *529*, 20–31.
[97] H. L. Huynh, J. Zhu, G. Zhang, Y. Shen, W. M. Tucho, Y. Ding, Z. Yu, *J. Catal.* **2020**, *392*, 266–277.
[98] M. M. Millet, E. Frei, G. Algara-Siller, R. Schlögl, A. Tarasov, *Appl. Catal. A Gen.* **2018**, *566*, 155–163.
[99] J. E. Benson, H. S. Hwang, M. Boudart, *J. Catal.* **1973**, *30*, 146–153.
[100] G. Corro, G. Aguilar, R. Montiel, S. Bernes, *React. Kinet. Catal. Lett.* **2001**, *73*, 317–323.
[101] M. García-Diéguez, I. S. Pieta, M. C. Herrera, M. A. Larrubia, L. J. Alemany, *Catal. Today* **2011**, *172*, 136–142.
[102] S. Damyanova, I. Shtereva, B. Pawelec, L. Mihaylov, J. L. G. Fierro, *Appl. Catal. B Environ.* **2020**, *278*, 119335.
[103] J. Wang, X. B. Zhang, Z. L. Wang, L. M. Wang, Y. Zhang, *Energy Environ. Sci.* **2012**, *5*, 6885–6888.
[104] U. Izquierdo, V. L. Barrio, K. Bizkarra, A. M. Gutierrez, J. R. Arraibi, L. Gartzia, J. Bañuelos, I. Lopez-Arbeloa, J. F. Cambra, *Chem. Eng. J.* **2014**, *238*, 178–188.
[105] H. Arandiyan, Y. Wang, J. Scott, S. Mesgari, H. Dai, R. Amal, *ACS Appl. Mater. Interfaces* **2018**, *10*, 16352–16357.
[106] T. Paryjczak, W. Jozwiak, J. Goralski, *J. Chromatogr. A* **1978**, *166*, 75–83.
[107] T. Paryjczak, J. M. Farbotko, J. Góralski, *J. Catal.* **1984**, *88*, 228–231.
[108] R. Van Hardeveld, F. Hartog, *Surf. Sci.* **1969**, *15*, 189–230.
[109] C. Bartholomew, *Catal. Letters* **1990**, *7*, 27–51.
[110] G. Bergeret, P. Gallezot, in *Handb. Heterog. Catal.* (Eds.: G. Ertl, H. Knozinger, F. Schuth, J. Weitkamp), WILEY-VCH Verlag GmbH & Co. KGaA, Weinheim, **2008**, pp. 738–765.
[111] Z. Sun, B. Fridrich, A. De Santi, S. Elangovan, K. Barta, *Chem. Rev.* **2018**, *118*, 614–678.
[112] W. Wang, J. Huang, Y. Fu, W. Jiang, Y. Chen, Y. Ma, S. Han, *Appl. Catal. B Environ.* **2023**, *333*, 122787.
[113] Q. Song, F. Wang, J. Xu, *Chem. Commun.* **2012**, *48*, 7019–7021.
[114] V. Ponnuchamy, J. Sandak, A. Sandak, *Processes* **2021**, *9*, 714–724.
[115] Y. Liu, G. Lyu, X. Ji, G. Yang, J. Chen, L. A. Lucia, *BioResources* **2016**, *11*, 5816–5828.
[116] T. Yan, Y. Xu, C. Yu, *J. Appl. Polym. Sci.* **2009**, *116*, 1896–1901.
[117] A. Bundi, C. Grathwohl, J. Hochmann, R. M. Keller, G. Wagner, K. Wüthrich, *J. Magn. Reson.* **1975**, *18*, 191–198.
[118] M. M. Schiavoni, H. G. Mack, C. O. Della Védova, *J. Mol. Struct.* **1996**, *382*, 155–162.

Chapter III

Incorporation of Ni (and Co or Fe) over mesoporous silica monoliths

III-1. Introduction

Part A of this chapter will present an original sol-gel one-pot method for the preparation of mesoporous nickel silica-based catalysts. Five samples of silica monoliths with different pore structures (wormlike, hexagonal and cubic) containing Ni were synthesized by varying the ratio between the structure directing agent and the silica precursor. Then, they were tested in the hydrogenolysis of the 2-phenoxy-1-phenylethanol ($A1_{HH}$) in the presence of isopropanol as an H-donor solvent, at 180°C and under N_2 atmosphere for 1 h. Their catalytic activities were compared to those of two materials made by the impregnation of silica supports with Ni(II) in aqueous ammonia.

The second part, B, will study the effect of the addition of a co-metal (up to 2 wt.%) to 3 wt.% Ni silica-based catalysts. A silica monolith with hexagonal mesopore structure was chosen for the incorporation of Ni and Co or Fe as co-metals with different strategies (impregnation by "two-solvents" method or by one-pot strategy). Then, Ni-Co and Ni-Fe silica-based monoliths were tested in the hydrogenolysis of 2-phenoxy-1-phenylethanol ($A1_{HH}$) in isopropanol with a substrate/metal molar ratio of 100, at 180°C and under 5 bar of N_2.

Chapter III – Part A: Exploring the effect on the structuration of mesopores in silica for the optimization of the activity of Ni-based catalysts

In this part, five samples of Ni containing silica monoliths with up to 5 wt.% Ni and wormlike, hexagonal or cubic mesopore structures ($Ni^{II}@S_x$) were successfully synthesized using a one-step sol-gel method. The resulting solids were compared to two blank materials obtained by the impregnation of either Aerosil 380 ($Ni^{II}_{NH_3}/SiO_2$) or a hexagonal silica monolith in the presence of ammonia. Deep characterization of the seven materials prepared was done by Inductively Coupled Plasma Optical Emission Spectroscopy (ICP-OES), N_2 physisorption, Transmission Electron Microscopy (TEM), Temperature-Programmed Reduction with H_2 (H_2-TPR) and X-Ray Diffraction (XRD). The desired structures were obtained by modifying only the amount of template agent in the synthesis gel. The higher the amount of template agent introduced, the larger the pore volume and the more the structures converged towards cubic phases with a progressive evolution of Ni(II) species or interactions with silica, as shown by H_2-TPR. On the other hand, silica impregnation with aqueous Ni(II) in the presence of ammonia led, after drying, to Ni phyllosilicates as shown in Chapter II – Part A1. However, impregnation of the hexagonally structured silica led to less phyllosilicates than Aerosil 380, probably as the result of its higher hydrophobicity, disfavoring the NH_3 attack of the support. After reduction at 500°C, all seven materials were found to be active in the hydrogenolysis of 2-phenoxy-1-phenylethanol, $A1_{HH}$, in the presence of isopropanol as hydrogen donor. Under the selected test conditions ($A1_{HH}$/Ni = 100 (mol/mol), 180°C, 1 h, 5 bar of N_2), the best catalyst with respect to phenol selectivity, avoiding its hydrogenation to cyclohexanol, was $Ni^0_{NH_3}/SiO_2$ reduced at 500°C. With this substrate, divergences were observed between $Ni^0@S_x$, with better yields with the more open cubic structure, all other parameters being constant.

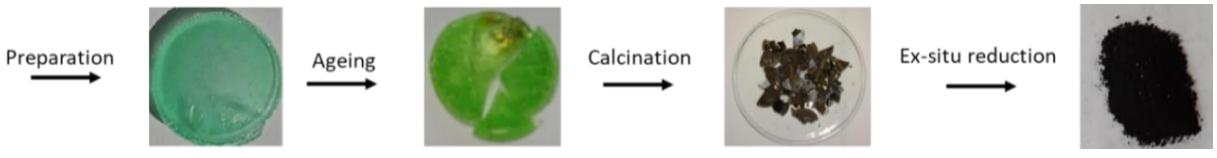

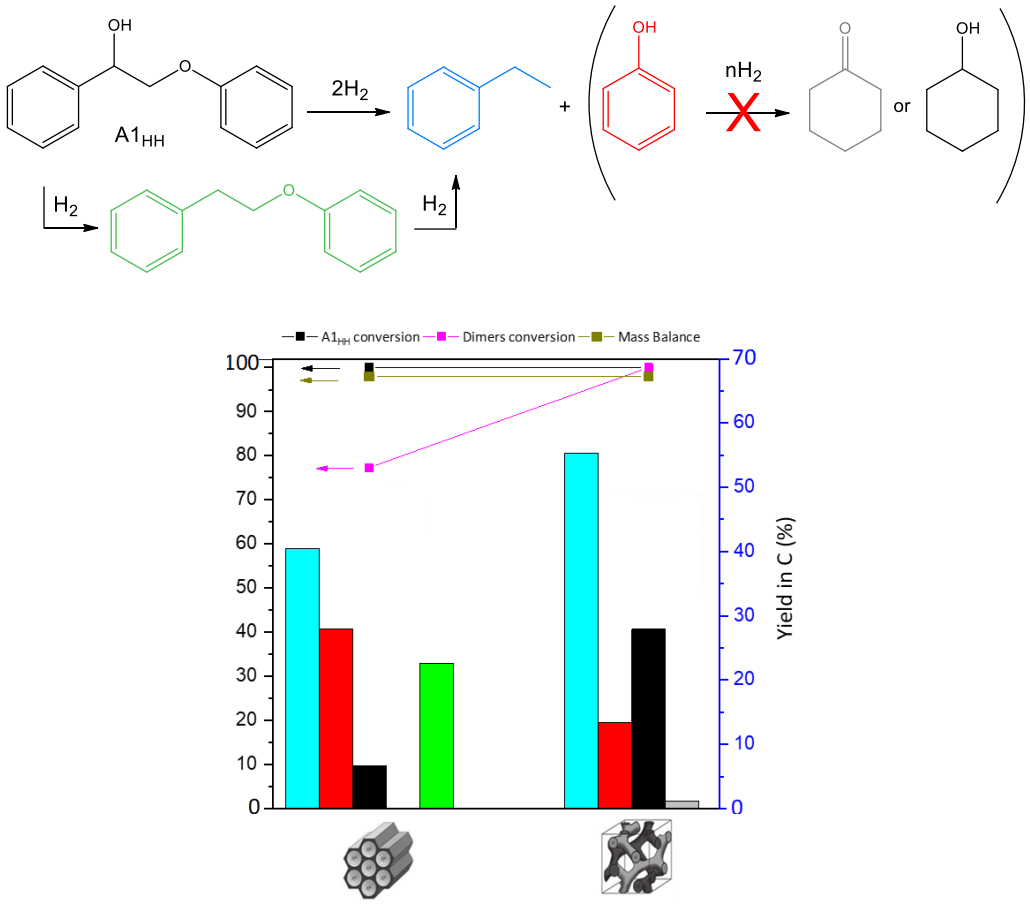

III-A.1. Introduction

Mesoporous silica are of particular interest in many fields [1–3] as well as catalysts supports [4] because of their relatively good stability and their high surface area, which allows a high concentration of active sites per weight of material. They also offer an exceptional range of highly ordered porosity (hexagonal, cubic, lamellar) [5] with a uniform pore size distribution that facilitates mass transfer control. Moreover, they can be obtained in very different forms such as powders, fibers, monoliths, thin films… Among these, SBA-15 powdered silica is well known. There are a lot of studies dealing with its functionalization with various functional groups or by adding metals [6], for example nickel(0) due to its interesting catalytic properties [7]. Several methods have been reported for zero-valent metal nanoparticles incorporation into preformed silica. However, often particles are mainly located on the outer surface of silica grains, leading to sintering and agglomerate formation [8]. Alternatively, introducing the metal salt precursor

directly into the mesoporous silica synthesis gel ("one-pot" strategy) can lead to better dispersion of the metal nanoparticles at the end. Regarding Ni, metal dispersion values of the order of 40% (measured by H_2 chemisorption) [9] could be reached (after reduction) by introducing Ni^{2+} into the synthesis gel of a mesoporous SBA-15 silica prepared in the presence of a minimal amount of water, affording monoliths instead of powder. Indeed, it is believed that the strong interaction between the structure-directing agent and the metal ion makes ions species homogeneously dispersed in the organic phase and in the end in the resulting solid recovered after calcination of the *as-synthesized* hybrid organic/inorganic material. Actually, like powders, different pores structures hosting Ni(0) nanoparticles should be obtained by varying the amount of the structure-directing agent (Pluronic P123) and keeping constant those of the silica precursor (tetramethylorthosilicate, TMOS) and of the nickel source introduced as an acidic aqueous solution [10,11]. Hence, in this contribution, $Ni^{II}@S_x$ monoliths with 5 wt.% of Ni and different pore structures were prepared with the following weight P123:TMOS ratio, x, equal to 0.3, 0.6, 0.8, 0.9 and 1. The physico-chemical properties of the supports and of the dispersed Ni^{2+} ions were studied by N_2-physisorption, TEM, H_2-TPR and XRD. The physico-chemical and catalytic properties of these Ni-containing solids, were compared to two others, $Ni^{II}_{NH_3}/S_{0.6}$ and $Ni^{II}_{NH_3}/SiO_2$, respectively obtained by the impregnation of a silica monolith with an hexagonal pores structure ($S_{0.6}$) or of Aerosil 380 with nickel(II) in aqueous ammonia. The aim of the present work was to test all these materials in the reductive depolymerization of lignin models in order to study the pore structure effect on the reaction process and the product distribution.

III-A.2. Materials preparation

Here, only the protocols concerning monoliths-based catalysts preparation are presented. They were synthesized using tetramethylorthosilicate (TMOS) as a silica source and an amphiphilic block copolymer, *i.e.*, poly(ethylene glycol)$_{70}$-block/poly-(propylene glycol)$_{20}$-block/poly(ethylene glycol)$_{70}$ (Pluronic P123, 5800 g mol^{-1}) as a structure-directing agent.

For a typical synthesis of the pure SBA-15 monolith (referred to as $S_{0.6}$), 2.4 g of P123 were added to 4 g of TMOS in a 30 mL poly-propylene vial and the solution was stirred in a water bath at 50°C until the polymer had been completely dissolved. After cooling to room temperature, 2 mL of an aqueous acidic solution (HNO_3/H_2O pH = 1.3) was quickly added to the stirred TMOS-P123 clear

mixture. The resulting solution was divided between four vials, which were closed tightly and transferred in a thermostated water bath at 23°C to be aged overnight without stirring. After removing the vial lid, the resulting viscous sol gelled within 6 h giving a translucent gel; the ageing process was continued for one additional week in order to obtain homogeneous white glassy silica–copolymer monolith. The shape of the vial determines the shape of the monolith.

For one-pot syntheses involving Ni^{2+}, five samples denoted $Ni^{II}@S_x$, where x represents the P123:TMOS mass ratio (x = 0.3, 0.6, 0.8, 0.9 and 1), were prepared following a protocol adapted from above. Depending on x values, 1.2 to 4 g of P123 were dissolved in 4 g of TMOS. Later, an adequate quantity of $Ni(NO_3)_2.6H_2O$ (395 mg corresponding to 5 wt.% Ni) dissolved in 2 mL of the aqueous acidic solution was quickly added to the P123-TMOS mixture. The remaining part of the protocol was similar to that described above.

Finally, the blank monolith $S_{0.6}$ and the five solids $Ni^{II}@S_x$ were calcined in a muffle furnace according to the procedure detailed below (Figure III-A.1) in order to free the porosity of the structure-directing agent.

It is worthy to note that for the characterization of monoliths and their reduction under H_2 for the catalytic tests, all monoliths were ground to fine powder.

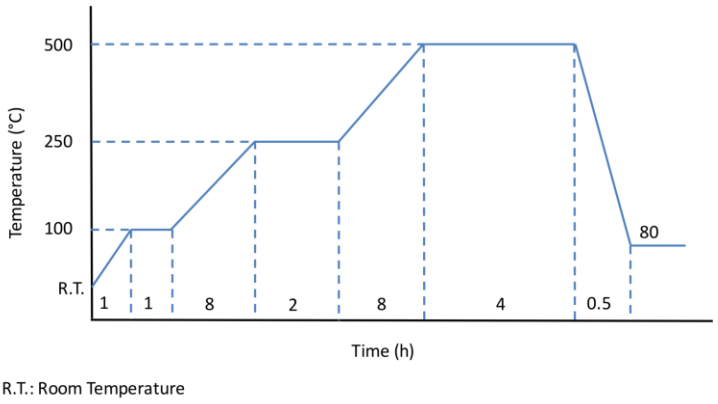

Figure III-A.1: *Calcination program used for the removal of the organic structure directing agent.*

The preparation protocol of $Ni^{II}_{NH_3}/SiO_2$ is detailed in Chapter II – Part A1, paragraph II-A1.2.1. The same was also applied for $Ni^{II}_{NH_3}/S_{0.6}$, using $S_{0.6}$ instead of Aerosil 380. In order to study the effect of adding NH_3 during impregnation on the textural properties of the support, reference

materials $S_{0.6}$-NH_3 and SiO_2-NH_3, were prepared using the same preparation protocol, but without adding the nickel precursor.

Table III-A.1 summarizes the seven Ni-containing materials prepared by one-pot strategy or by impregnation in aqueous ammonia over siliceous mesoporous monoliths or Aerosil 380.

Table III-A.1: *List of the Ni-based materials prepared by one-pot strategy or impregnated with ammonia.*

	Gel composition				
Materials	**P123 (g)**	**TMOS (g)**	**x = P123/TMOS**	**Support**	**Method**
$\mathbf{Ni^{II}@S_{0.3}}$	1.2	4	0.3	$S_{0.3}$	one-pot
$\mathbf{Ni^{II}@S_{0.6}}$	2.4	4	0.6	$S_{0.6}$	one-pot
$\mathbf{Ni^{II}@S_{0.8}}$	3.2	4	0.8	$S_{0.8}$	one-pot
$\mathbf{Ni^{II}@S_{0.9}}$	3.6	4	0.9	$S_{0.9}$	one-pot
$\mathbf{Ni^{II}@S_{1}}$	4	4	1	S_1	one-pot
$\mathbf{Ni^{II}_{NH_3}/S_{0.6}}$	2.4	4	0.6	$S_{0.6}$	NH_3 imp
$\mathbf{Ni^{II}_{NH_3}/SiO_2}$	-	-	-	SiO_2	NH_3 imp

The characterization methods and the catalytic test are detailed in the experimental part (Appendix 1) and in Chapter II – Part A1, paragraph II-A1.2.2, respectively.

III-A.3. Results and discussion

The synthesis of monoliths with different types of mesopore ordering was directly inspired by the work of Delahaye *et al.* [10]. These authors, working with cobalt at 1 wt.%, showed that the structure of the materials obtained could be wormlike, hexagonal, cubic and even lamellar as the P123 content increased. Our aim here was to prepare a few materials representative of the different structures, all with 5 wt.%. Ni. To do this, we first considered that the phase diagram with Ni is fairly similar to that obtained previously with Co. First of all, it is proposed to verify the structures of the silica obtained, as well as the quality of the textural properties of the Ni-based materials and the correct incorporation of Ni with the highest possible dispersion. After Ni(II) reduction, these solids, obtained by a one-pot strategy, will be evaluated as catalysts in the hydrogenolysis of two model lignin compounds in order to determine whether pore structuration influences catalytic activity. The proposed comparison with materials resulting from the

impregnation of silica with Ni^{2+} in ammonia aims to determine whether the mode of Ni incorporation also plays a role.

III-A.3.1. Comparison of $Ni^{II}@S_{0.6}$, $Ni^{II}_{NH_3}/S_{0.6}$ and $Ni^{II}_{NH_3}/SiO_2$

Earlier in this manuscript, it was shown that impregnation of Aerosil 380 with Ni^{2+} in ammonia, resulting in $Ni^{II}_{NH_3}/SiO_2$, leads to a strong modification of the textural properties of Aerosil 380. At that time, the generation of a significant quantity of mesopores with a broad distribution of sizes (from 5 to 40 nm) was attributed to the use of ammonia during the impregnation stage. This could be made owing to a blank test carried out in the absence of Ni^{2+} (see results with SiO_2-NH_3, Figure III-A.2 A and B).

The question was whether the same happens with supports other than Aerosil 380, such as $S_{0.6}$ here. Similarly, here, the nitrogen physisorption measurements on $Ni^{II}_{NH_3}/S_{0.6}$ were compared with those of $S_{0.6}$ and $S_{0.6}$-NH_3 (blank experiment without Ni, Figure III-A.2 A). The results (Figure III-A.2 A) indicate that $Ni^{II}_{NH_3}/S_{0.6,}$ as well as, $S_{0.6}$ and $S_{0.6}$-NH_3 are characterized by type IV (a) isotherms forming a H1 type hysteresis typical of SBA-15 [12]. Here, clearly, the changes in porosity induced by aqueous ammonia were less remarkable than those observed with Aerosil 380. As shown by the comparison of the isotherms of $S_{0.6}$ and of $S_{0.6}$-NH_3, a lower specific area and pore volume were even observed for $S_{0.6}$-NH_3. The only indication that could be linked to the effects of NH_3 attack on $S_{0.6}$ is the shift (and broadening) of the mesopores sizes distribution towards higher values, *i.e.*, 6 nm instead of 5.4 nm, with some loss of pore volume (Figure III-A.2 C). The hypothesis that can be put forward for the differences in behavior between Aerosil 380 and the solid $S_{0.6}$ is that commercial silica is more hydrophilic than $S_{0.6}$, which would make it more sensitive to the basic attack induced by aqueous NH_3. It would have been interesting to study the behavior of Aerosil 380 calcined at 550°C to see if it is closer to that of $S_{0.6}$ [13].

After impregnation of $S_{0.6}$ by nickel, the pore volume and the specific area of the support ($S_{0.6}$-NH_3) did not change to a significant extent for $Ni^{II}_{NH_3}/S_{0.6}$ (Table III-A.2). However, the pores sizes distribution of $Ni^{II}_{NH_3}/S_{0.6}$ was characterized by two maximum values at 3.8 and 4.7 nm, instead of one (Figure III-A.2 C). The decrease in the mean pore diameter given by BJH from 6.0

to 4.5 nm would mean that nickel was incorporated mainly inside the pores but probably in an inhomogeneous way which should be confirmed by TEM.

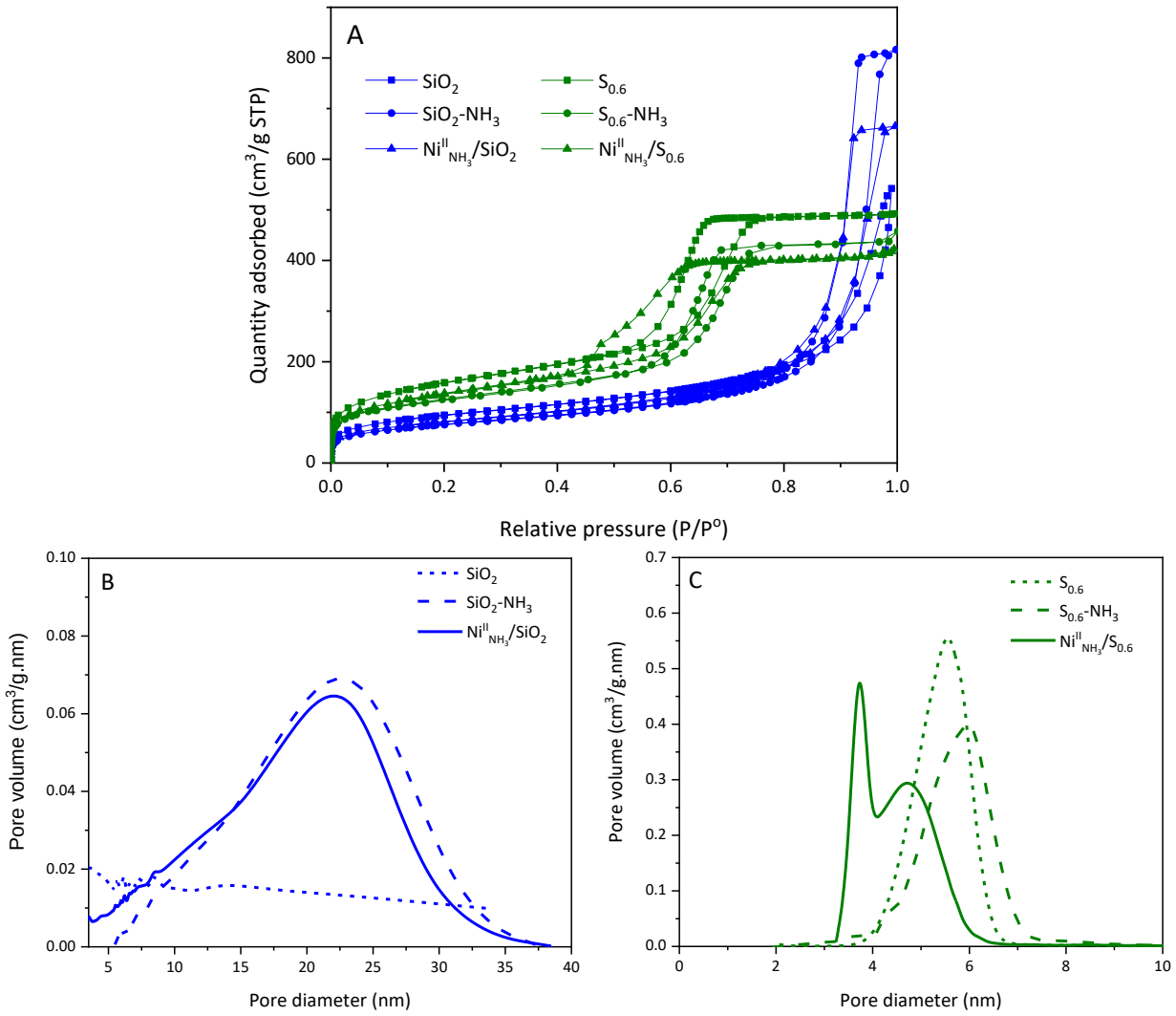

Figure III-A.2: *(A) N_2 adsorption-desorption isotherms (-196°C) of dried as-synthesized materials as well as references without metal and pore size distributions of (B) Aerosil-based samples (blue) and (C) $S_{0.6}$-based samples (green).*

$Ni^{II}@S_{0.6}$, prepared by the one pot protocol, was also characterized by type IV (a) isotherms generating a H1 hysteresis loop typical of mesoporous materials with a rather narrow range of uniform mesopores (Figure III-A.3 A and B) [12]. However, the pore volume and the mean pore diameter of $Ni^{II}@S_{0.6}$ were smaller than those of $S_{0.6}$ (shifted by 2 nm), but its specific area was significantly higher. On the contrary to $Ni^{II}_{NH_3}/S_{0.6}$ (Figure III-A.3 B and Table III-A.2) that was characterized by a non-uniform distribution of its mesopores with two maximum at 3.8 and 4.7

nm, $Ni^{II}@S_{0.6}$ displayed only one at 3.6 nm, which would emphasize a much better distribution of Ni with the one-pot approach (Figure III-A.3 B and Table III-A.2). In the end, it is important to note that all the samples based on silica monoliths were characterized by higher specific surface areas and a narrower pore size distribution than those derived from Aerosil 380.

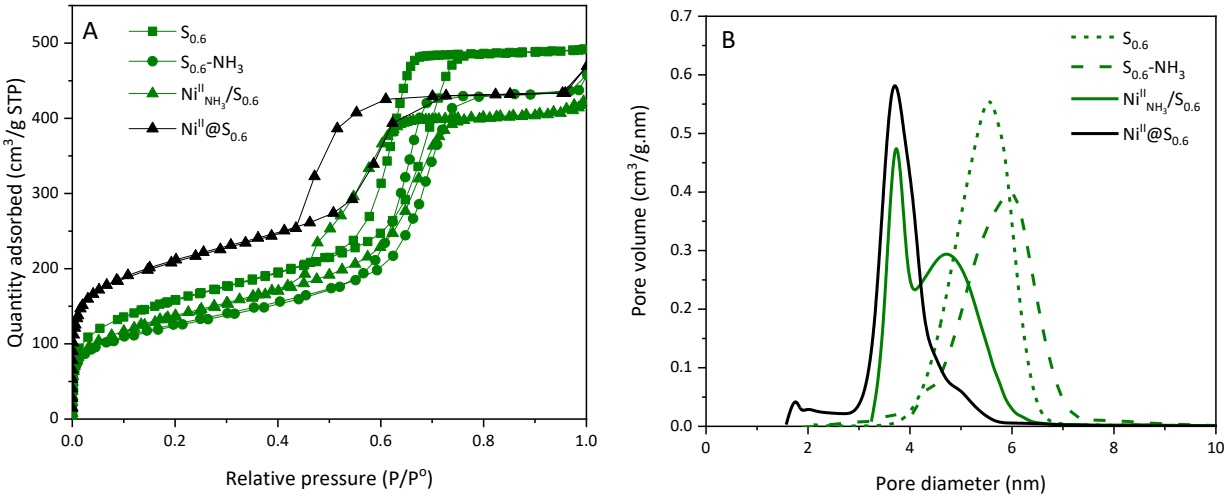

Figure III-A.3: *(A) N_2 adsorption-desorption at -196°C and (B) pores size distributions of the Ni based monolith materials: $S_{0.6}$, $S_{0.6}$-NH_3, $Ni^{II}_{NH_3}/S_{0.6}$ (green) and $Ni^{II}@S_{0.6}$ (black).*

Table III-A.2: *Physicochemical properties of the Ni 5 wt.% based monoliths and Aerosil 380 materials.*

Material	S_{BET} ($m^2\ g^{-1}$)	V^a_{Des} ($cm^3\ g^{-1}$)	Average D^b_{pores} (nm)	d^c (nm)	Ni wt.% TPR [ICP]
$S_{0.6}$	561	0.73	5.4	8.4	-
$S_{0.6}$-NH_3	451	0.69	6.0	8.5	-
$Ni^{II}_{NH_3}/S_{0.6}$	482	0.65	4.5*	8.3	4.1 [4.3]
$Ni^{II}@S_{0.6}$	760	0.63	3.6	8.1	3.8 [3.9]
SiO_2	333	0.56	10.7	-	-
SiO_2-NH_3	269	1.24	19.2	-	-
$Ni^{II}_{NH_3}/SiO_2$	288	1.00	15.8	-	4.1 [4.9]

[a] From BJH on the desorption branch (between 2 and 50 nm in diameter), [b] From the BJH desorption pore size distribution (see Figure III-A.2 B and C and Figure III-A.3 B); [c] Interplanar distance by small angle XRD calculated according to Bragg equation $n\lambda = 2d\sin\theta$; *Not meaningful because of the presence of two maximums at 3.8 and 4.7 nm; *n.d.*: not determined.

Small angle X-Ray diffractograms of the monoliths type samples studied before, $S_{0.6}$, $S_{0.6}$-NH_3, $Ni^{II}_{NH_3}/S_{0.6}$ and the $Ni^{II}@S_{0.6}$ (Figure III-A.4 A, B, C and D) exhibited the (100), (110) and (200) peaks characteristic of ordered mesoporous materials with a hexagonal (p6mm) structure (black bars) [10].

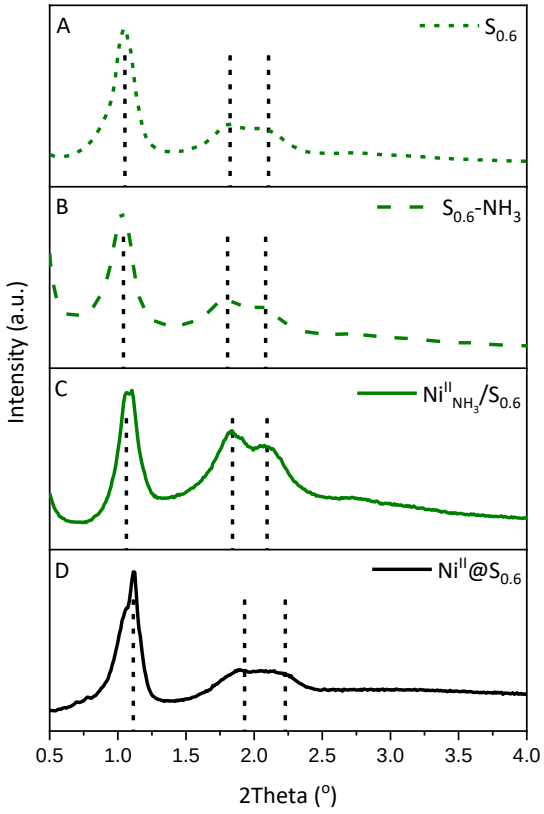

Figure III-A.4: *Small angles XRD patterns for (A) monolith incorporated with Ni by one-pot strategy, (B) in aqueous ammonia, or (C and D) references samples.*

Clearly, the preservation of good pore structuration despite the contact of $S_{0.6}$ with NH_3, assumed on the basis of N_2 physisorption data, is confirmed here (comparison of Figure III-A.4 A and B with Figure III-A.4 C). Despite the incorporation of Ni^{2+} in significant amount in its synthesis gel, $Ni^{II}@S_{0.6}$ has clearly a hexagonal structure. The proof of Ni^{2+} insertion in the silica walls is given by the shift of the diffraction peaks of $Ni^{II}@S_{0.6}$ to higher 2θ values [9,14]. Indeed, the interplanar distance of the four materials was calculated and they seemed to be similar with little decrease of $Ni^{II}@S_{0.6}$ (Table III-A.2).

Concerning the quality of Ni incorporation, some preliminary information could be provided by the wide-angle X-Ray diffractograms of calcined $Ni^{II}@S_{0.6}$ and of the *as-synthesized* dried

$Ni^{II}_{NH_3}/S_{0.6}$ and $Ni^{II}_{NH_3}/SiO_2$ samples (Figure III-A.5). All exhibited the broad peak (at 2θ = 22°) related to X-Ray diffusion by amorphous silica. No peak corresponding to crystalline NiO was observed for calcined $Ni^{II}@S_{0.6}$, suggesting the formation of small nanoparticles or clusters with the one-pot strategy. As shown earlier (Chapter II – Part A1), a nickel phyllosilicate phase (PDF 00-049-1859) was detected in the case of dried *as-synthesized* $Ni^{II}_{NH_3}/SiO_2$ by the presence of broad peaks with rather low intensity corresponding to the (200), (202) and (060) reticular planes at 2θ = 34.1, 36.4 and 60.5°, respectively. Here, it appears that nickel phyllosilicate is also formed in $Ni^{II}_{NH_3}/S_{0.6}$ but to a lower extent, which agrees with the weaker perturbations highlighted by N_2-physisorption for this sample compared to $Ni^{II}_{NH_3}/SiO_2$.

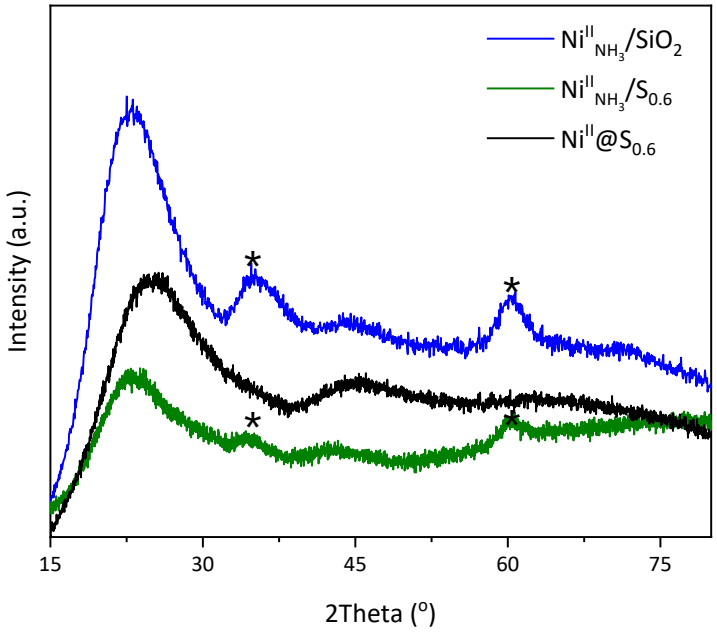

Figure III-A.5: *Wide angle XRD of calcined $Ni^{II}@S_{0.6}$ (black), dried as-synthesized $Ni^{II}_{NH_3}/S_{0.6}$ (green) and $Ni^{II}_{NH_3}/SiO_2$ (blue) samples.*

For further information, the reducibility of the nickel species was investigated by H_2-TPR (Table III-A.2). The reduction profiles of $Ni^{II}_{NH_3}/SiO_2$ (Figure III-A.6 B) and $Ni^{II}@S_{0.6}$ (Figure III-A.6 C) appeared the most different ones. Earlier in Chapter II – Part A1, it was shown that $Ni^{II}_{NH_3}/S_{0.6}$ was characterized by two peaks, *i.e.*, a minor contribution at 360°C and another, much larger one, at 765°C and it was shown that complete reduction of Ni(II) occurred after 900°C, due to the presence of Ni phyllosilicates.

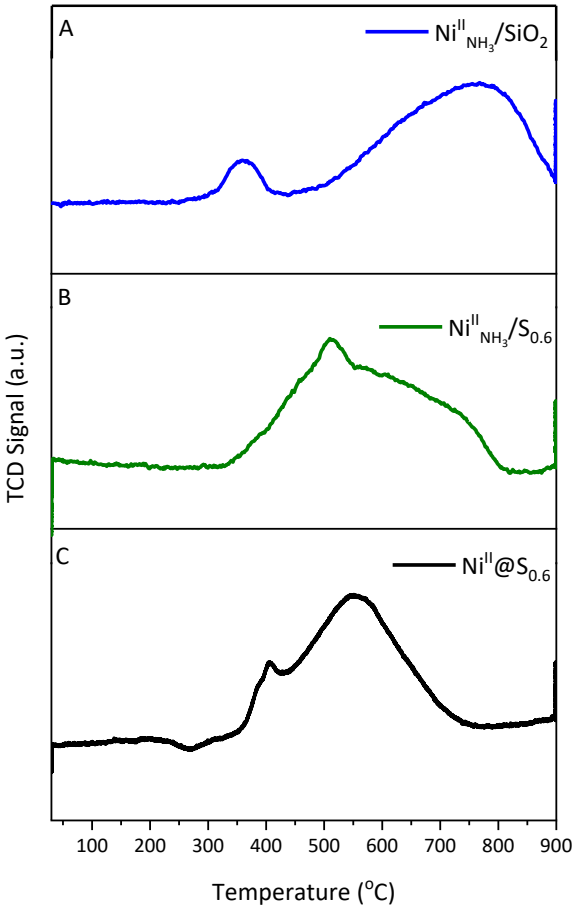

Figure III-A.6: *H_2-TPR profiles of (A) dried as-synthesized $Ni^{II}_{NH_3}/SiO_2$ (B) and $Ni^{II}_{NH_3}/S_{0.6}$ prepared by impregnation and of (C) calcined $Ni^{II}@S_{0.6}$ recorded with a H_2 5 vol.%/Ar flow of 30 mL min^{-1} and a heating rate of 10°C min^{-1}.*

On the other hand, $Ni^{II}@S_{0.6}$, obtained by one pot method, was fully reduced at lower temperature (750°C, no phyllosilicates) and showed two reduction peaks, one with a minor contribution at 517°C and the other with a larger contribution at 558°C (Figure III-A.6 C). What about $Ni^{II}_{NH_3}/S_{0.6}$? It seems that its reduction profile with a major contribution at 517°C, a minor one at 754°C and a total reduction at 800°C (Figure III-A.6 A) was a sort of intermediate between those of $Ni^{II}_{NH_3}/SiO_2$ (Figure III-A.6 B) and $Ni^{II}@S_{0.6}$ (Figure III-A.6 C). The contribution with a maximum at 754°C resembles that associated with phyllosilicates for $Ni^{II}_{NH_3}/SiO_2$ but the total reduction took place at a lower temperature than in this sample, probably due to the smaller quantities formed, as shown in particular by XRD. The other component of the profile, with a maximum at 517°C, was closer to what is observed for $Ni^{II}@S_{0.6}$ where it is suspected that the Ni species are localized in the pores of the $S_{0.6}$ support (D_{pores} = 3.6 nm). So, it can be concluded, that the differences in the reduction

behavior between the three materials with similar Ni loading (5 wt.%) studied here highlight the strong influence of the preparation method, but also of the type of silica support. It is clear that impregnation with aqueous ammonia improves the metal-support interaction by producing nickel phyllosilicates (Ni-O-Si) which should lead to the formation of smaller Ni^0 nanoparticles during the reduction step [15,16].

The nickel mass loading of $Ni^{II}_{NH_3}/S_{0.6}$, $Ni^{II}_{NH_3}/SiO_2$ and $Ni^{II}@S_{0.6}$ samples determined by H_2-TPR measurements was close to that given by ICP-OES analysis, but slightly lower (Table III-A.2). The greatest difference was found for $Ni^{II}_{NH_3}/SiO_2$ because, in that case, complete reduction of Ni^{2+} was not achieved at 900°C. The same occurred with $Ni^{II}_{NH_3}/S_{0.6}$, but to a lower extent. According to the ICP data, the most effective method for complete Ni incorporation is definitely impregnation in the presence of ammonia.

The dispersion of Ni(II) in these samples was also analyzed by TEM (Figure III-A.7). With the exception of $Ni^{II}_{NH_3}/S_{0.6}$ (Figure III-A.7 C and D) whose images showed either ordered phases with agglomerated Ni species or domains with non-ordered porosity, $Ni^{II}@S_{0.6}$ (Figure III-A.7 B) and $Ni^{II}_{NH_3}/SiO_2$ (Figure III-A.7 A) appeared to be homogeneous. For $Ni^{II}@S_{0.6}$, the TEM micrographs highlighted the ordered hexagonal mesoporosity of the support, in good agreement with small angles X-Ray diffraction measurements. After calcination of $Ni^{II}@S_{0.6}$ at 500°C, small nanoparticles, probably NiO, with an average diameter (1.5 nm) smaller than the pore diameter of $Ni^{II}@S_{0.6}$ (3.6 nm), were found to be homogeneously distributed throughout the channels of $Ni^{II}@S_{0.6}$. For $Ni^{II}_{NH_3}/SiO_2$ as well as $Ni^{II}_{NH_3}/S_{0.6}$ samples prepared by impregnation in aqueous ammonia, Ni phyllosilicates nanosheets, also proved by wide angle XRD, were observed more intense for $Ni^{II}_{NH_3}/SiO_2$. This is probably due to the fact that $S_{0.6}$ that was calcined is more hydrophobic than commercial silica which would make it less sensitive to the basic attack induced by aqueous NH_3.

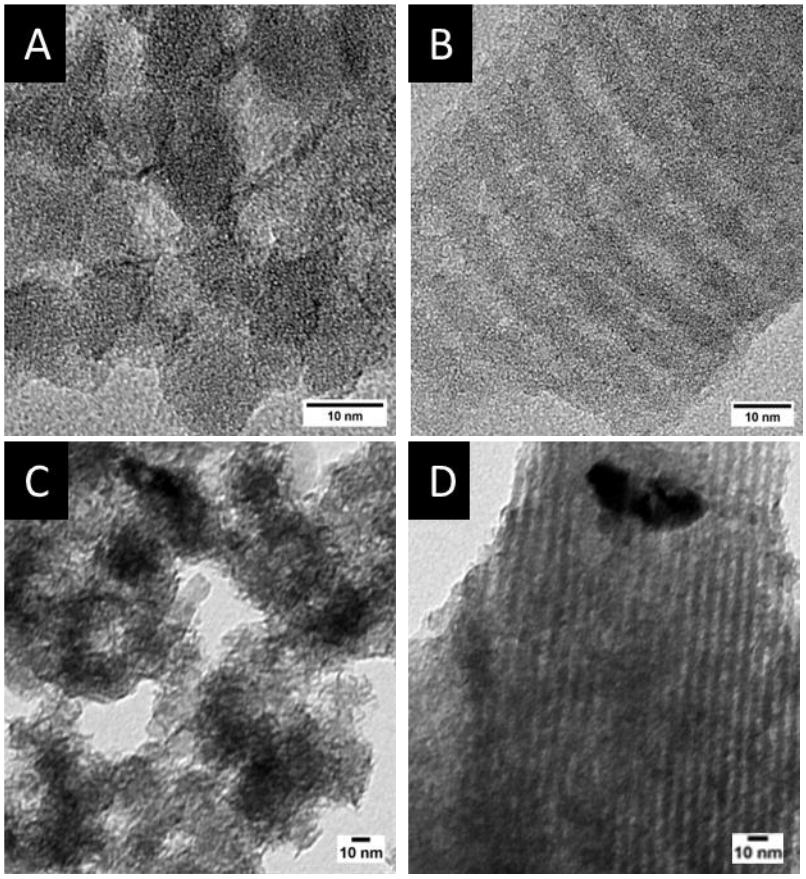

Figure III-A.7: *TEM images of (A) dried as-synthesized $Ni^{II}_{NH_3}/SiO_2$ and (C and D) $Ni^{II}_{NH_3}/S_{0.6}$) as well as (B) calcined $Ni^{II}@S_{0.6}$ (microtomy).*

TEM images, the absence of wide XRD peaks, and the H_2-TPR profiles of $Ni^{II}@S_{0.6}$ were shown go agree with the formation of small and/or highly dispersed NiO in this sample, prepared by a one-pot protocol. In the work of Daoura *et al.* [9], PDF analyses were carried out in order to check Ni species structure and Ni species particle size, even in the absence of X-Ray diffraction peaks. From the superimposition of the experimental G(r) curve of the calcined $Ni^{II}@S_{0.6}$ with that from the corresponding support $S_{0.6}$, three peaks at 2.1, 3.1 and 5.3 Å matching with NiO were revealed. From those results, it could be concluded that nickel in $Ni^{II}@S_{0.6}$ would be present as NiO clusters with 5.3 Å as size. Our idea here was to prepare similar materials with different pore structures, characterize them and then study the effect of structure on the catalytic activity of mainly confined nickel species.

III-A.3.2. Synthesis and characterization of other $Ni^{II}@S_x$ materials with different pore structures

In the work of Delahaye *et al.* [10] a phase diagram of the ternary system $Co(NO_3)_2$/TMOS/P123 as a function of the P123/TMOS weight ratio and the Co/Si percentage molar ratio was established (Figure III-A.8). This diagram shows that the organization depends, as expected, on the P123/TMOS weight ratio and, more remarkably, also on the Co/ Si molar ratio.

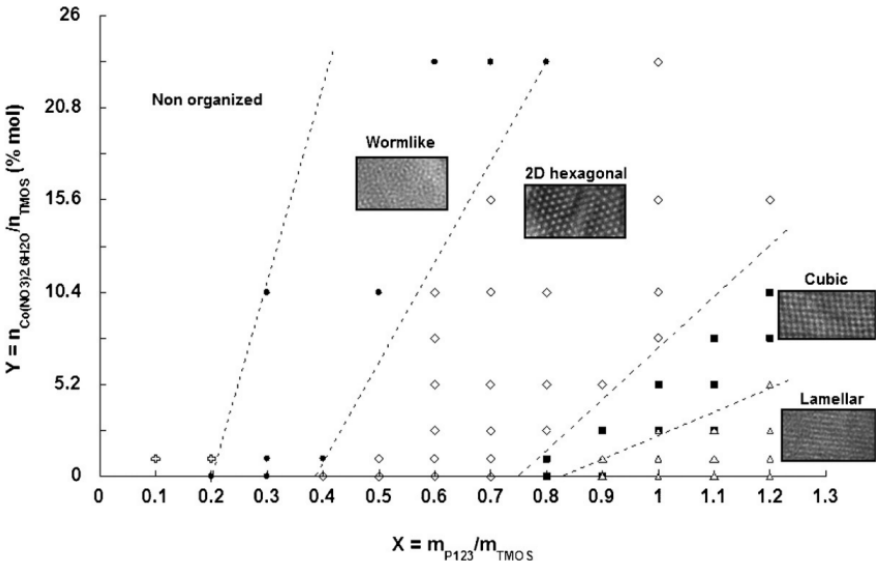

Figure III-A.8: *Phase diagram of the ternary system $Co(NO_3)_2$/TMOS/P123 [10].*

No phase diagram was established with Ni^{2+}, but it is theoretically assumed that it will exhibit the same behavior as Co^{2+}. In our case, the amount of Ni^{2+} was set constant (n_{Ni}/n_{TMOS} = 5.2% (mol) corresponding to 5 wt.% of Ni), but we only changed the x ratio (m_{P123}/m_{TMOS}), in fact with increasing the P123, a peak indicative of periodic organization appears. Obtaining structured mesoporous materials requires the formation of micelles of templating agent, around which silica is formed. Indeed, when the concentration of a surfactant reaches or exceeds the value of the critical micellar concentration, the hydrophilic and hydrophobic parts of the amphiphilic molecules organize themselves to form micelles in order to minimize Van Der Waals interactions. In the case of polar solvents, such as water or alcohols, the apolar parts of the surfactant come together to form the core of the micelle, while the hydrophilic heads point towards the surface. It is known

that at higher surfactant concentrations, these micelles aggregate into mesophases of lyotropic liquid crystals in lamellar, hexagonal or cubic form [17,18].

According to this diagram, four ordered structures can be obtained by increasing the P123 amount, from wormlike to 2D hexagonal to cubic and finally to lamellar. Five values were chosen x = 0.3 (wormlike), 0.6 (hexagonal), 0.8 (hexagonal), 0.9 (mixture of hexagonal and cubic) and 1 (cubic). It was not interesting to choose an "x" in the lamellar region due to its structure degradation after calcination.

Ni weight loadings for $Ni^{II}@S_x$ materials obtained by ICP-OES, varied from 3.9 to 4.7 wt.% with a mean value of 4.3 wt.% which is lower than the expected value, *i.e.*, 5 wt.%.

With the exception of x = 0.3, the calcined samples obtained by a one-pot strategy using values of x ranging from 0.6 to 1 were characterized by type IV (a) isotherms and hysteresis loops consistent with those of mesoporous materials (Figure III-A.9 A). The shapes of the N_2 sorption isotherms of calcined $Ni^{II}@S_x$ with x= 0.8, 0.9 and 1 were found to be relatively similar to each other and different from $Ni^{II}@S_{0.6}$. $Ni^{II}@S_{0.3}$ did not appear to be mesoporous at all, displaying type I (b) isotherms and pore sizes probably in the micropore range and possibly narrow mesopores (< 2.5 nm) [12] (Figure III-A.9 A). In fact, no significant number of pores could be detected between 2 and 8 nm for $Ni^{II}@S_{0.3}$ in Figure III-A.9 B.

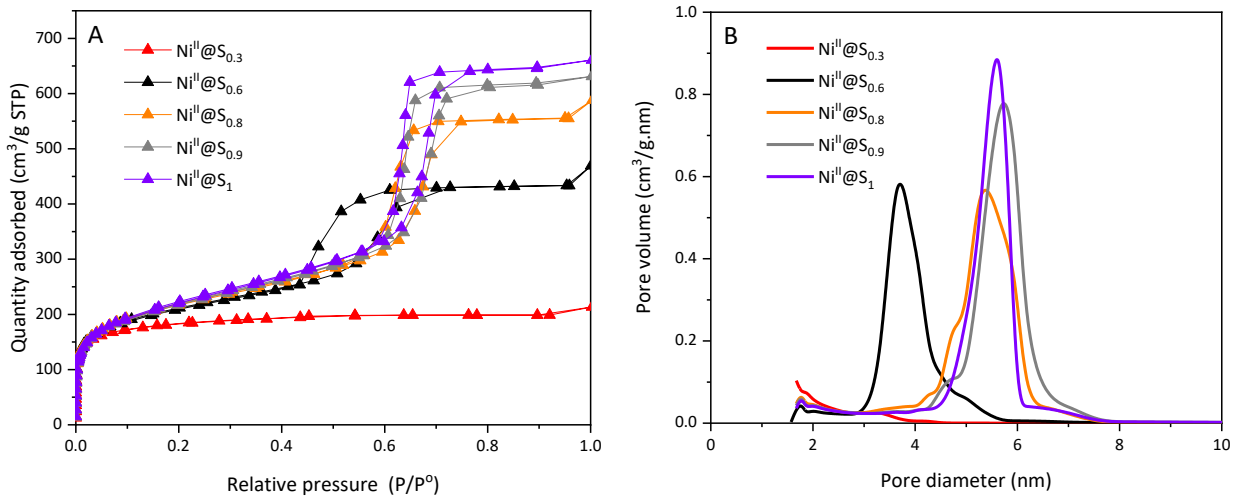

Figure III-A.9: *(A) N_2 adsorption-desorption isotherms at -196°C and (B) pores size distributions of the different calcined Ni containing silica monoliths prepared by one-pot strategy.*

By varying "x" from 0.3 to 0.6, an increase in the textural parameters was observed, with more variations between 0.3 and 0.8 (Table III-A.3). It may be recalled that such an increase has already been reported for the transition from a hexagonal structure, of the SBA-15 type, to a cubic structure, of the SBA-16 type, considering materials also prepared by a one-pot strategy with 5 wt.% of Ni [14].

Table III-A.3: *Physicochemical properties of the calcined Ni 5 wt.% based monoliths prepared with one-pot strategy.*

Material	S_{BET} ($m^2\,g^{-1}$)	V^a_{Des} ($cm^3\,g^{-1}$)	Average D^b_{pores} (nm)	d^c (nm)	Ni wt.% TPR [ICP]
$Ni^{II}@S_{0.3}$	690	0.10	1.7	8.1	4.1 [4.7]
$Ni^{II}@S_{0.6}$	760	0.63	3.6	8.1	3.8 [3.9]
$Ni^{II}@S_{0.8}$	790	0.82	5.3	8.5	4.1 [4.4]
$Ni^{II}@S_{0.9}$	794	0.92	5.7	8.4	4.4 [4.3]
$Ni^{II}@S_{1}$	799	0.98	5.7	7.9	5.0 [4.2]

[a] From BJH (desorption branch between 2 and 50 nm in diameter), [b] From the BJH desorption pore size distribution (see Figure III-A.9 B); [c] Interplanar distance by small angle XRD.

Changes in pore order as a result of variations in the amount of P123 used were revealed using small angle XRD (Figure III-A.10). First, with $Ni^{II}@S_{0.3}$, the XRD pattern showed one peak which could be attributed to a wormlike structure with a d spacing of 8.1 nm. As previously mentioned (paragraph III-A.3.2.), the hexagonal structure (P6mm) of $Ni^{II}@S_{0.6}$ has also been proven [14]. The d spacing calculated from the diffraction lines is 8.1 nm. When the amount of P123 was further increased, the XRD pattern evolved again, and for $Ni^{II}@S_{0.9}$ and $Ni^{II}@S_{1}$ samples, a cubic organization was demonstrated. Indeed, the (111), (200) and (220) diffraction peaks characteristic of cubic (fm3m) could be identified with d spacings of 8.4 and 7.9 nm for x = 0.9 and 1, respectively. Our interpretation of the diffractogram obtained for x = 0.8 (in between x = 0.6 (100% hexagonal) and x = 0.9 (100% cubic)) would be that the experimental peaks obtained correspond to a mixture of a hexagonal (P6mm) phase and a cubic (Ia3d) phase [14]. Here, the d spacing associated with the first peak is 8.5 nm. The detailed analyses were done on a Co 1 wt.% in wormlike structure x = 0.4, in 2D hexagonal structure for x = 0.6 with a d spacing of 9.9 nm , and in cubic and lamellar structures for x = 0.8 and 1 with a d spacing of 9.8 and 11.5 nm, respectively [10,17].

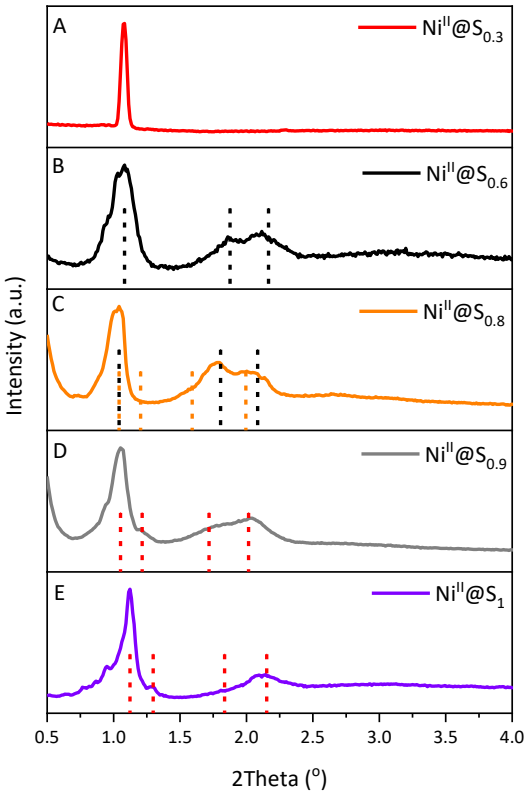

Figure III-A.10: *Small angle XRD patterns of the series of calcined Ni containing silica monoliths prepared by one-pot strategy using different amounts of P123 showing hexagonal P6mm (black bars), cubic Ia3d (orange bars) and cubic Fm3m (red bars) pore structures.*

Wide angle XRD of all $Ni^{II}@S_x$ samples (Figure III-A.11) showed similar patterns with mainly the wide peak ($2\theta = 22°$) assigned to X-Ray diffusion by amorphous silica and no diffraction corresponding to crystalline NiO, *a priori* due to the formation of clusters of small nickel oxide as shown earlier with $Ni^{II}@S_{0.6}$ [9].

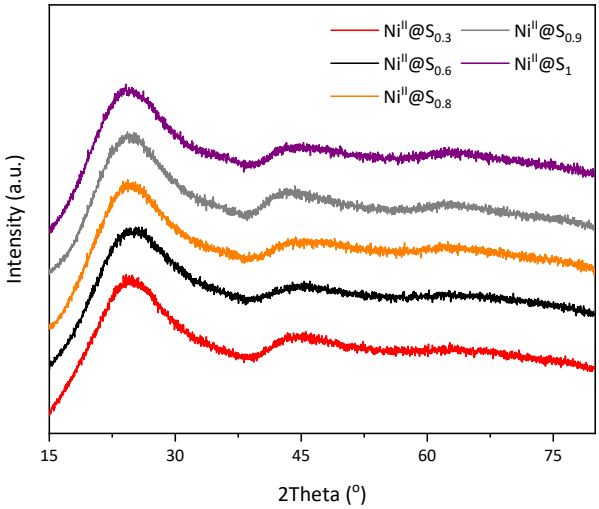

Figure III-A.11: *Wide angle XRD patterns of calcined Ni containing silica monoliths prepared by one-pot strategy using different amounts of P123.*

TEM measurements on $Ni^{II}@S_x$ samples, shown in Figure III-A.12, validate the variation of the pores structure already evidenced by small angle XRD data (Figure III-A.10). Hence, a wormlike organization was observed for $Ni^{II}@S_{0.3}$ (Figure III-A.12 A and A'). In the case of $Ni^{II}@S_{0.6}$, a honeycomb structure, characteristic of a hexagonal organization is clearly visible (Figure III-A.12 B). The SBA-15 like monolith, possesses hexagonal pores in 2D array with long 1D channels (Figure III-A.12 B') [19]. The intermediate organization for $Ni^{II}@S_{0.8}$, in between hexagonal and cubic structures could correspond to Figure III-A.12 C and C'. The TEM images of $Ni^{II}@S_{0.9}$ and $Ni^{II}@S_1$ are characteristic of the cubic structure (Figure III-A.12 D, D', E and E') with a 3D cubic arrangement of mesopores like in SBA-16 [19]. Within the series of $Ni^{II}@S_x$ samples, most of the NiO particles observed seemed to be located inside the porosity. Moreover, they were found to be homogeneously distributed. At high magnification for all samples, very small particles (Figure III-A.12 A, A', B, B', C, C' and D, D') were shown to be confined in the mesoporosity of the support. The mean particles size, from TEM, was evaluated to 2.0 nm. However, for $Ni^{II}@S_1$, other nanoparticles, small (~ 3 nm) and larger ones (~ 10 nm) were evidenced too (Figure III-A.12 E and E').

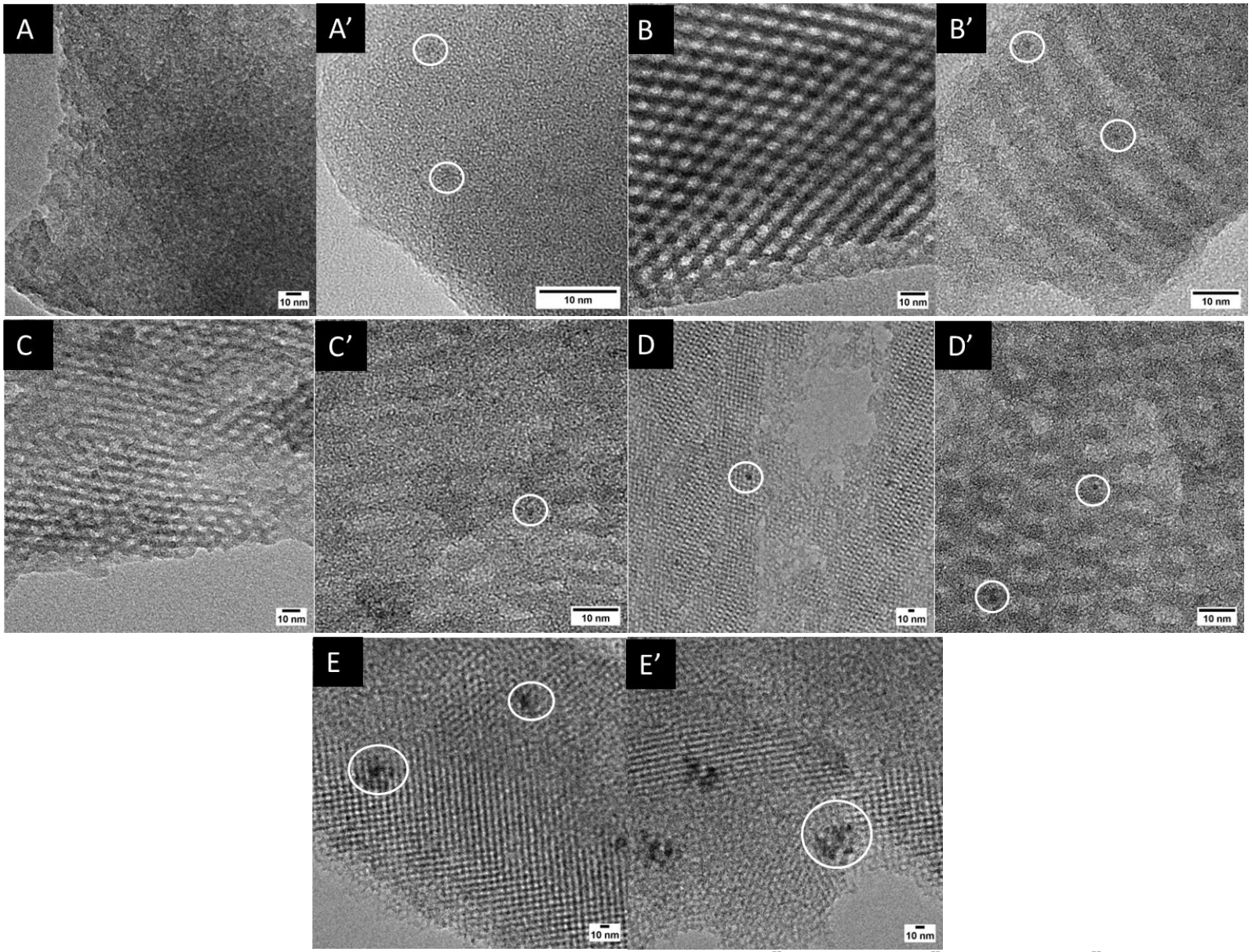

Figure III-A.12: *TEM images of microtomed samples in their calcined state, (A,A') $Ni^{II}@S_{0.3}$, (B,B') $Ni^{II}@S_{0.6}$, (C,C') $Ni^{II}@S_{0.8}$, (D,D') $Ni^{II}@S_{0.9}$ and (E,E') $Ni^{II}@S_1$.*

With regard to the interpretation of the H_2-TPR profiles, the variations are linked to the metal-support interaction [20–22]. The H_2-TPR results obtained for the series of $Ni^{II}@S_x$ materials (Figure III-A.13) clearly show that the structure of the mesoporous support influences the interaction of NiO with silica and/or the size and/or the location of NiO.

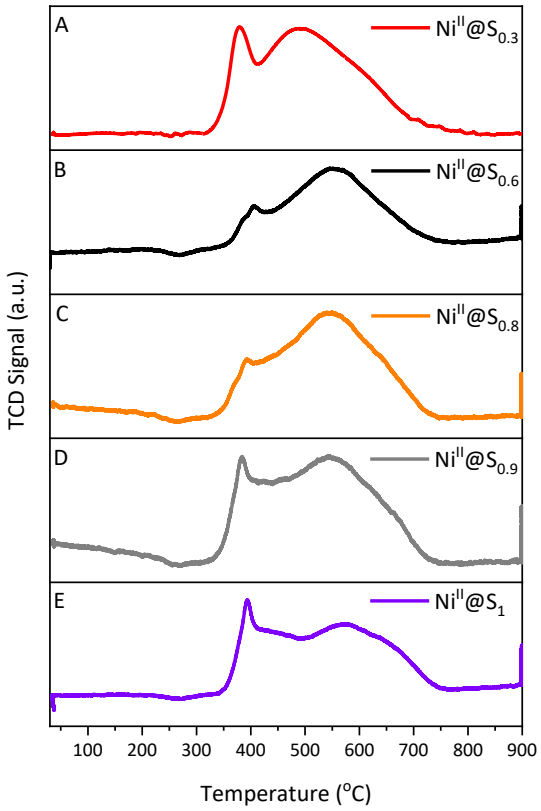

Figure III-A.13*: H_2-TPR profiles of calcined Ni containing silica monoliths prepared by one-pot strategy using different amounts of P123.*

It can be seen here that the profile of H_2 consumption evolves continuously from a two-component system with maxima at 379°C and 496°C for $Ni^{II}@S_{0.3}$, to a 4-component system for $Ni^{II}@S_1$ for which a narrow peak is found at 393°C as well as an envelope peak with two maxima at 568°C and 662°C, which are separated from the narrow peak by a continuum of H_2 consumption with no well-defined maximum (Table III-A.4). As x increases, so does the proportion of H_2 consumed at the highest temperatures for at least for $Ni^{II}@S_{0.6}$ and $Ni^{II}@S_{0.8}$ compared to $Ni^{II}@S_{0.3}$, then it seems that again, the proportion of H_2 consumed at lower temperature increases for $Ni^{II}@S_{0.9}$ and $Ni^{II}@S_{1.0}$. That could be related to the location of NiO particles at the outer surface of the support S more accessible for the reduction.

Table III-A.4: *Temperature of each maximum for H_2-TPR profiles for $Ni^{II}@S_x$.*

Material	Maxima	T (°C)
$Ni^{II}@S_{0.3}$	2	379 / 496
$Ni^{II}@S_{0.6}$	2	406 / 551
$Ni^{II}@S_{0.8}$	2	392 / 544
$Ni^{II}@S_{0.9}$	2	383 / 542
$Ni^{II}@S_1$	3	393 / 568 / 662

Nickel mass loadings estimated from H_2 consumption by TPR ranged from 3.8 to 5 wt.%, with exactly the same mean value as the ICP-OES measurements (4.3 wt.%) (Table III-A.3). The lower value determined by TPR for samples $Ni^{II}@S_{0.3}$ to $Ni^{II}@S_{0.8}$ compared with that measured by ICP may indicate that part of Ni is not reduced because it is not easily accessible, probably due to the insertion of Ni^{2+} into the silica framework. However, the opposite situation ($Ni^{II}@S_{0.9}$ and $Ni^{II}@S_1$ samples), with values determined by TPR higher than those measured by ICP, is difficult to explain. We therefore consider that the discrepancies are linked to experimental errors, particularly on the TPR side where the integration of H_2 consumption peaks is not particularly accurate due to the significant variation in the baseline on the raw measurements.

III-A.3.3. Catalytic performance of all samples in C-OAr bond hydrogenolysis in the presence of isopropanol

For the sake of comparison, the calcined Ni containing silica monoliths prepared by ammonia impregnation (one sample, $Ni^0_{NH_3}/S_{0.6}$) or by the one-pot strategy (5 samples, $Ni^0@S_x$ materials), as well as $Ni^{II}_{NH_3}/SiO_2$, were all reduced *ex-situ* at 500°C under a flow of H_2 (50 mL min^{-1}) during 3 h. The catalytic performances of all the resulting solids were investigated in the hydrogenolysis of $A1_{HH}$ or GGE using isopropanol as H-donor solvent under 5 bars of N_2 at 180°C for 1 h.

III-A.3.3.a. Case of $A1_{HH}$

The conversion and yields of products equations are presented in Chapter II – Part A1, paragraph II-A1.2.2.

With regard to the $Ni^0@S_x$ series, it can be stated that, the catalytic activity depends somewhat on the material tested (Figure III-A.14)

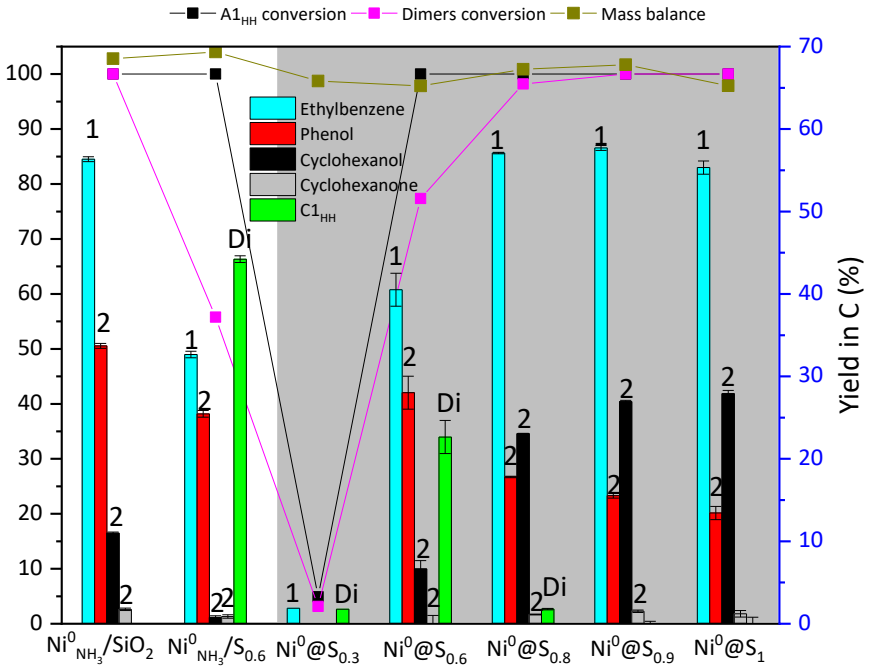

Figure III-A.14: *$A1_{HH}$ and other dimers conversions with the yields of the different products in the hydrogenolysis reaction on Ni-based silica.*
Reaction conditions: $[A1_{HH}]_o$ = 0.06 M, $A1_{HH}$ /Ni = 100 (mol/mol), i-PrOH (15 mL), 180°C, 1 h, 5 bar of N_2.

For example, $Ni^0@S_{0.3}$ (4.7 wt.% Ni) exhibited very low conversion under these conditions, while $A1_{HH}$ conversion was complete for the other four solids, *i.e.*, $Ni^0@S_{0.6}$ (3.9 wt.% Ni), $Ni^0@S_{0.8}$ (4.4 wt.% Ni), $Ni^0@S_{0.9}$ (4.3 wt.% Ni) and $Ni^0@S_1$ (4.2 wt.% Ni). It could be noted that the progress of the hydrogenolysis of the C-OAr bond was not the same since the $C1_{HH}$ dimer was still detected for $Ni^0@S_{0.6}$ and $Ni^0@S_{0.8}$, even if, for the latter, the $C1_{HH}$ yield was less than $5\%_C$. Such observations allow us to conclude that the catalytic activity increased continuously between x = 0.3 and 0.9. Next, the results obtained for $Ni^0@S_{0.9}$ and $Ni^0@S_{1.0}$ were virtually the same, which means that both materials were the most active solids of the $Ni^0@S_x$ series. The impact of the reduction temperature was tested for $Ni^{II}@S_{0.6}$, but no significant change in the cleavage of C-OAr bonds and the phenol yield could be evidenced after reduction of Ni(II) species at 650°C. (500°C, X_{Di} = 77.3%, Y = $28\%_C$, S = 85% *vs.* 650°C, X_{Di} = 82%, Y = $25\%_C$, S = 71%).

Regarding the incorporation mode of Ni, $Ni^0@S_{0.6}$ (one-pot strategy, 3.9 wt.% Ni) was more active than $Ni^0_{NH_3}/S_{0.6}$ (impregnation of pre-formed $S_{0.6}$ in the presence of ammonia, 4.3 wt.% Ni). Indeed, the C-OAr bonds conversions were 77.3% and 55.7%, respectively. This could be maybe related to the dispersion of nickel nanoparticles homogeneously into the pores of $Ni^0@S_{0.6}$ but not seen in the case of $Ni^0_{NH_3}/S_{0.6}$, where it can be clearly seen by TEM image (Figure III-A.7 D) that Ni^{2+} particles were agglomerated.

What about $Ni^0_{NH_3}/SiO_2$, the materials prepared from Aerosil 380 exhibiting a very large pore size distribution? $Ni^0_{NH_3}/SiO_2$, reduced at 500°C, was in fact a very active catalyst affording total conversions of $A1_{HH}$ and $C1_{HH}$. As mentioned in the Chapter II – Part A1, the yield of phenol decreases when all dimers are converted as the result of a competition between arene hydrogenation and C-OAr bond hydrogenolysis. In the conditions tested ($A1_{HH}$ /Ni = 100 (mol/mol), *i*-PrOH (15 mL), 180°C, 1 h, 5 bar of N_2), interestingly, $Ni^0_{NH_3}/SiO_2$ was more selective for phenol, with a yield of 33.7%$_C$ with a selectivity reaching 79%, compared to $Ni^0@S_{0.9}$ and $Ni^0@S_{1.0}$ (with yields of phenol of 15.9%$_C$ and 14.7%$_C$, with selectivity of 37% and 34% respectively) (Figure III-A.14). The two materials $Ni^0@S_{0.9}$ and $Ni^0@S_{1.0}$ are perhaps too active under the selected conditions. Could better phenol selectivity be obtained if the reaction time was shorter than 1 h? This would mean that the use of an impregnation method with ammonia combined with the use of Aerosil 380 (and not $S_{0.6}$) disadvantages the secondary reaction of hydrogenation of phenol into cyclohexanone and cyclohexanol. Increasing the reduction temperature of $Ni^0_{NH_3}/SiO_2$ to 650°C did not change to a significant extent its catalytic activity. As the matter of fact, the latter exhibited a behavior very similar to its equivalent reduced at 500°C.

Finally, the catalytic performance of $Ni^0_{NH_3}/S_{0.6}$ reduced at 500°C was very different from that of $Ni^0_{NH_3}/SiO_2$. The conversions of $A1_{HH}$ and of the produced dimer ($C1_{HH}$) under similar reaction conditions were 100 and 55.7%, respectively.

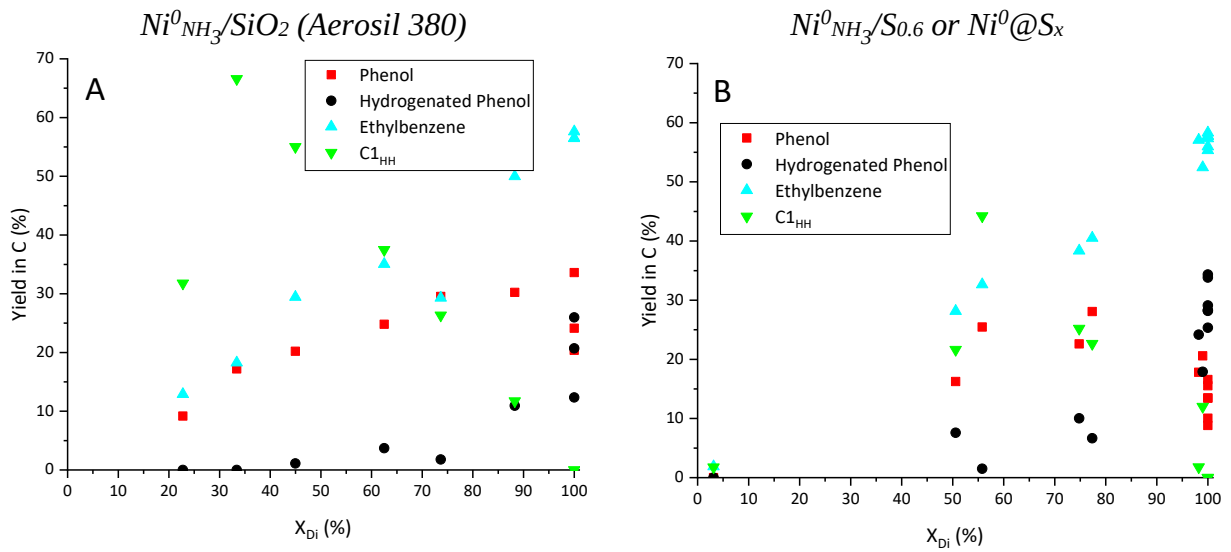

Figure III-A.15: *Yield in Carbon of each product obtained by the cleavage of $A1_{HH}$ as a function of C-OAr bonds conversion at 180°C under 5 bar of N_2 for (A) $Ni^0_{NH_3}/SiO_2$ and (B) $Ni^0_{NH_3}/S_{0.6}$ and $Ni^0@S_x$.*

It is noteworthy that with the two types of supports used (Aerosil 380 or monoliths) and both nickel incorporation methods, similar reaction profiles emphasizing the formation of $C1_{HH}$ as an intermediate was clearly seen (Figure III-A.15 A and B). Impregnation of Aerosil 380 in aqueous ammonia seems to disfavor the hydrogenation of phenol (at X_{Di} = 100%, Y_{PhOH} = 33.7%$_C$, S = 79%), red squares increasing to reach 33.7%$_C$ in (Figure III-A.15 A) whereas black circles in (Figure III-A.15 B) with monoliths.

Pore structure variation and nickel incorporation strategies turned out to influence the catalyst activity, with an improved performance with the cubic one but not the phenol selectivity compared to $Ni^0_{NH_3}/SiO_2$, as it can be clearly seen in Figure III-A.15. This was confirmed by blank experiments on the hydrogenation of phenol in the presence of a selection of the above catalysts, *i.e.*, $Ni^0_{NH_3}/SiO_2$, $Ni^0@S_{0.6}$ and $Ni^0@S_1$ and under exactly the same reaction conditions (Table III-A.5). Clearly, the cyclohexanol and, to a lower extent, the cyclohexanone formation was much more efficient with $Ni^0@S_1$, thus confirming our observations made with $A1_{HH}$.

It is noteworthy that $Ni^0_{NH_3}/SiO_2$, under the milder conditions tested in this work, showed comparable activity for $A1_{HH}$ reductive cleavage and selectivity towards phenol to nickel-based zeolite HZSM-5 in water under 50 bar of H_2 at 250°C [23]. No similar example of the use of nickel-silica based catalysts under N_2 atmosphere with $A1_{HH}$ could be found in the literature, but nickel

catalysts (supported or not) showed in some cases high selectivity towards monomers but not the highest conversion. The conversion was increased by using or adding a noble metal [24–26].

Table III-A.5: *Blank catalytic tests performed with phenol.*

Materials	X_{PhOH} (%)	$Y_{cyclohexanol}$ (%)	$Y_{cyclohexanone}$ (%)
$Ni^0_{NH_3}/SiO_2$	45.4	40.9	4.5
$Ni^0@S_{0.6}$	40.5	37.5	3.0
$Ni^0@S_1$	84.8	81.7	3.1

Reaction conditions: $[PhOH]_o$ = 0.06 M, PhOH/Ni = 100 (mol/mol), i-PrOH (15 mL), 180°C, 1 h, 5 bar of N_2.

III-A.3.3.b. Case of guaiacylglycerol-β-guaiacyl ether, GGE

The conversion and yields of products equations are presented in Chapter II – Part C paragraph II-C.2.

Earlier in this manuscript, reductive depolymerization of GGE was tested with $Ni^0_{NH_3}/SiO_2$. This substrate was found to be less reactive than $A1_{HH}$. Consequently, optimization studies had to be carried out. In the end, under 5 bar of N_2, at 180°C, the best results, *i.e.*, good guaiacol yield (Y = 25.3%$_C$) and C-OAr bonds conversion, for the GGE transformation were obtained with a substrate/Ni molar ratio of 10 with a reaction time of 1 h (Chapter II – Part C). The catalyst was reduced at 650°C.

Here, three $Ni^0@S_x$ samples were chosen, namely those with x = 0.6 (hexagonal), x = 0.8 (mix hexagonal and cubic) and x = 1 (cubic) (Figure III-A.16). Firstly, they were tested after being reduced by H_2 at 500°C for 3 h, bearing in mind that no Ni phyllosilicates were detected in their unreduced form, in this case, their calcined form obtained after the elimination of P123. GGE by hydrogenolysis of C_α-OH gives rise to 4-(3-hydroxy-2-(2-methoxyphenoxy) propyl)-2-methoxyphenol, a quite stable intermediate equivalent to $C1_{HH}$. The cleavage of this dimer affords guaiacol and guaiacylpropanol, later to 4-propylguaiacol and 4-ethylguaiacol.

$Ni^0@S_{0.6}$, $Ni^0@S_{0.8}$ and $Ni^0@S_1$ materials reduced to 500°C were found to be less active than $Ni^0_{NH_3}/SiO_2$-650°C. Like in Chapter II – Part C, they should have been reduced at 650°C. In contrast to $A1_{HH}$, with GGE, less difference was found between the performance of the $Ni^0@S_x$ catalysts (Figure III-A.16). Indeed, the conversion value of around 65% and the guaiacol yield of

around 17%$_C$ for $Ni^0@S_{0.8}$ and $Ni^0@S_1$ were slightly higher than for $Ni^0@S_{0.6}$. In all cases, unfortunately, the guaiacol yield turned out to be lower than those reported in literature [27].

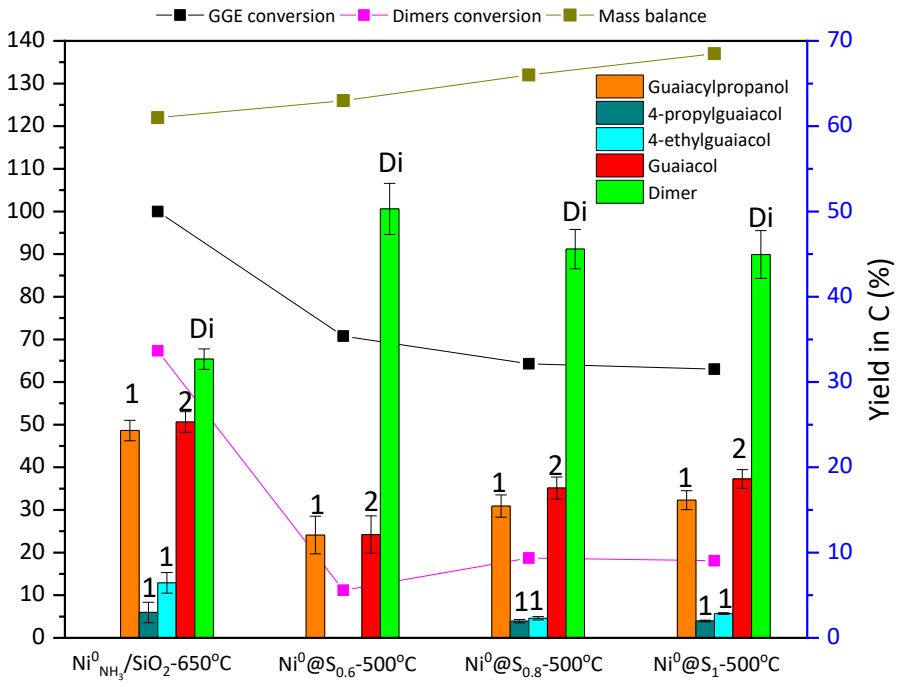

Figure III-A.16: *GGE / dimers conversion, mass balance and yields of the main products obtained with Ni-based silica catalysts.*
Reaction conditions: $[GGE]_o$ = 0.06 M, GGE/Ni = 10 (mol/mol), i-PrOH (15 mL), 180°C, 1 h, 5 bar of N_2.

III-A.4. Conclusion

In this chapter, by varying the amount of the structure directing agent (Pluronic P123), all other things being equal, it was possible to obtain, by the one-pot route, a whole series of silicic materials in the form of monoliths with controlled mesopore structures, ranging from hexagonal to cubic, and incorporating up to 5 wt.% Ni. As the amount of P123 increases, so did the pore volume and it was also found that the average pore diameter was higher for cubic structures. As expected, the range of porosity obtained and the pore sizes distribution were different from those of materials prepared from Aerosil 380 in the presence of aqueous ammonia. Another important feature is the type of Ni(II) species present before reduction. Using NH_3, it was shown previously that supported Ni(II) seems to be present exclusively in the form of phyllosilicates, whose reduction, which is rather difficult, generates very small Ni(0) nanoparticles. The one-pot route obviously did not lead to phyllosilicates because the pH range is not suitable, but, nevertheless,

small nickel oxide nanoparticles, even clusters or isolated ions have been proposed for Ni@$S_{0.6}$ in a paper published by our team [9]. Here, it was shown that the same occurs for all values of x, except x = 1, where larger objects were detected by TEM. The H_2-TPR analyses revealed a progressive evolution of the species or their location when x varies. This study also showed that impregnation of a silica monolith with an aqueous solution of nickel (II) nitrate in the presence of ammonia produces phyllosilicates less efficiently than that of Aerosil 380. It would appear that the difference is linked to the more hydrophobic nature of the monolith.

By comparing the catalytic activity of all the prepared materials, it can be concluded that the activity depends greatly on the incorporation strategy of Ni. $Ni^0_{NH_3}/SiO_2$ with Ni^0 nanoparticles in strong interaction with the support, led to the highest catalytic activity in the hydrogenolysis of lignin model compounds ($A1_{HH}$ and GGE) under reducing atmosphere and mild conditions (1 h at 180°C) with a good selectivity towards phenolic monomers. It should be noted that in the series of monoliths, it appeared that cubic structures led to more efficient catalysts than hexagonal ones in the case of $A1_{HH}$. This could not be verified for the second model, GGE, for which a Ni(II) to Ni(0) reduction temperature of 500°C is undoubtedly too low, even when working at a low molar substrate/metal ratio.

Chapter III – Part B: Bimetallic Ni-Co or Ni-Fe-silica monoliths-based catalysts with different incorporation strategies

Bimetallic Ni-Co and Ni-Fe-silica based catalysts with *c.a.* 3wt.% of Ni and 2 wt.% of co-metal were synthesized using three different strategies. The incorporation of Co or Fe was done either by co-impregnation of both metals Ni(II) and Co(II) or Fe(III) on a preformed silica monolith $S_{0.6}$ or by the introduction of Ni and Co (or Fe) in the synthesis gel of a monolith silica (Ni-Co or Ni-Fe@$S_{0.6}$) or by the impregnation of Co(III) or Fe(III) on Ni@$S_{0.6}$. The aim of this work was to study the effect of the strategy used for the second metal introduction on the hydrogenolysis of 2-phenoxy-1-phenylethanol in isopropanol with a substrate/metal molar ratio of 100, at 180°C and under 5 bar of N_2. The materials obtained by impregnation of Co(III) or Fe(III) on Ni@S, exhibited the best catalytic activity in terms of selectivity towards phenol.

III-B.1. Introduction

Non-noble metals such as Mo [28], Fe [29], Co [30] and especially Ni [31], which are quite abundant in earth, have been studied to replace noble metals [32] as catalysts in lignin depolymerization. In parallel, many research works have been conducted to enhance the stability of Ni-based catalysts by selecting the support, changing the method of catalyst synthesis and adding promoters. Ni-M bimetallic catalysts combining nickel with precious metal were used. They turned out to be efficient with lignin model compounds but display disadvantages like side hydrogenation of benzene ring at relatively harsh reaction conditions and low yield in lignin conversion [33]. Other nickel-based bimetallic materials such as Ni-Fe catalysts, have been reported for efficient hydrogenolysis of lignin [34–37]. According to some works, the synergistic effect between metal Ni and Fe would prevent the hydrogenation of aromatic rings and lead to high efficiency in ether bond cleavage [38]. In some cases, Fe-containing materials displayed high activity in selective cleavage of C−O, C−OH bonds due to enhanced interactions between Fe sites and the methoxy or hydroxyl groups [38,39]. According to Xia *et al.*, Ni and Co also exhibited a

superior hydrogenation ability compared to Ni in the transformation of lignocellulose conversion [40], greatly improving the hydrogenolysis selectivity by promoting the C-O cleavage selectively, but low selectivity towards phenols was found [41,42]. In the part A of this chapter, Ni well dispersed within a mesoporous silica matrix was obtained by a one-pot strategy. The idea here was to modify the catalytic activity of the resulting material by adding a co-metal. Three different strategies were used for Co or Fe addition to Ni. The resulting materials were tested in the hydrogenolysis reaction of $A1_{HH}$ using isopropanol as H-donor at 180°C aiming at finding relationships between the catalyst performances and their preparation methods.

III-B.2. Materials preparation

In this work, Ni and Co (or Fe) were introduced either using an impregnation protocol, named "two-solvents" impregnation or incorporated in the silica gel (like Ni before). The third strategy is a combination of both since Ni was introduced in the silica gel giving rise to $Ni^{II}@S_{0.6}$ which was further impregnated by Co or Fe employing a "two-solvents" approach.

In the case of $(Ni^{II}\text{-}Co^{II})/S_{0.6}$ and $(Ni^{II}\text{-}Fe^{III})/S_{0.6}$ monoliths where Ni and Co (or Fe) were incorporated with "two-solvents" method, a pure SBA-15 silica (monolith $S_{0.6}$) was prepared. Then, 250 mg of the $S_{0.6}$ monolith were suspended in n-heptane (with an appropriate volume to cover the solid) for a couple of minutes. A volume of water slightly lower than that of the silica pore volume (as determined by N_2 sorption) and containing an appropriate amount of $Ni(NO_3)_2.6H_2O$ (corresponding to 3 wt.% of Ni) and $Co(NO_3)_2.6H_2O$ or $Fe(NO_3)_3.9H_2O$ (corresponding to 2 wt.% of Co or Fe, respectively) was added dropwise. Due to the strong differences of solvents properties of n-heptane and water, the aqueous solution would enter preferentially into the pores of the SBA-15 monolith, leading to the confinement of iron or cobalt species. The solid was then removed from n-heptane, dried at R.T. and finally calcined, under static air, at 500°C (heating rate 5°C min^{-1}) then cooled to 80°C.

$(Ni^{II}\text{-}Co^{II})@S_{0.6}$ or $(Ni^{II}\text{-}Fe^{III})@S_{0.6}$ solids were prepared according to a one-pot method (as in Chapter III – Part A, paragraph II-A.2). $Ni(NO_3)_2.6H_2O$ (237 mg corresponding to 3 wt.% Ni) and $Co(NO_3)_2.6H_2O$ or $Fe(NO_3)_3.9H_2O$ (158 mg or 228 mg corresponding to 2 wt.% Co or Fe, respectively) were quickly added to the stirred TMOS-P123 clear mixture. The resulting solids were calcined according to the calcination program in Chapter III – Part A, paragraph III-A.2.

Solids denoted as $Co^{III}/Ni^{II}@S_{0.6}$ and $Fe^{III}/Ni^{II}@S_{0.6}$ were obtained by the impregnation of $Ni^{II}@S_{0.6}$ with 3 wt.% of Ni with an aqueous solution of Co(II) or Fe(III) using a "two-solvents" method [43]. $Ni^{II}@S_{0.6}$ (3 wt.%) was obtained as follows: $Ni(NO_3)_2.6H_2O$ was dissolved in an aqueous acidic solution before mixing with the P123-TMOS mixture. At the end, the solid was calcined according to the program of Chapter III-A, paragraph III-A.2. For the "two-solvents" method, 250 mg of the $Ni^{II}@S_{0.6}$ (3 wt.%) were suspended in n-heptane. A volume of water slightly lower than that of the silica pore volume (as determined by N_2 sorption) and containing an appropriate amount of $K_3[Co(CN)_6]$ or $K_3[Fe(CN)_6]$ (corresponding to 2 wt.% of Co or Fe, respectively) was added dropwise. The solid was then removed from n-heptane, dried at R.T. and finally calcined, under static air at 500°C (heating rate 5°C min^{-1}), then cooled to 80°C. The principle of this incorporation method for Co or Fe is based on the formation of Co(Fe)-CN-Ni-CN-Co(Fe)… coordination structures where each metal Co(Fe) and Ni is in the center of octahedra surrounded by cyanide groups which lead to an homogeneous distribution of cations [44].

It is worthy to note that all monoliths were ground to fine powder for the characterization and for their reduction under H_2 prior to the catalytic tests. The characterization methods and the conditions for the catalytic test are detailed in experimental part (Appendix 1) and in Chapter II – Part A1, paragraph II-A1.2.2, respectively.

III-B.3. Results and discussion

III-B.3.1. Physico-chemical properties of Ni-Co and Ni-Fe based monoliths

All of six prepared samples were characterized by N_2-physisorption, small-angle X-Ray scattering (SAXS) and wide angle XRD, H_2-TPR and TEM, then tested in the hydrogenolysis of the 2-phenoxy-1-phenylethanol in isopropanol at 180°C.

As shown in Figure III-B.1 A and B, all samples were characterized by type IV (a) isotherms forming a H1 hysteresis loop typical of mesoporous materials with a narrow range of uniform mesopores [12]. Compared to $S_{0.6}$, samples prepared by impregnation ($Co^{III}/Ni^{II}@S_{0.6}$ and $Fe^{III}/Ni^{II}@S_{0.6}$) or co-impregnation ((Ni^{II}-Co^{II})/$S_{0.6}$ and (Ni^{II}-Fe^{III})/$S_{0.6}$) displayed a decrease in the pore volume (14% and 21%, respectively) and in the specific area (14% and 10%, respectively) (Table III-B.1). Such modifications in the textural properties could be related to the incorporation

of oxide bimetallic particles in the porosity of these calcined materials. The specific area for samples prepared by the one-pot strategy, $(Ni^{II}\text{-}Co^{II})@S_{0.6}$ and $(Ni^{II}\text{-}Fe^{III})@S_{0.6}$, was the highest between their pore volumes the least (Table III-B.1).

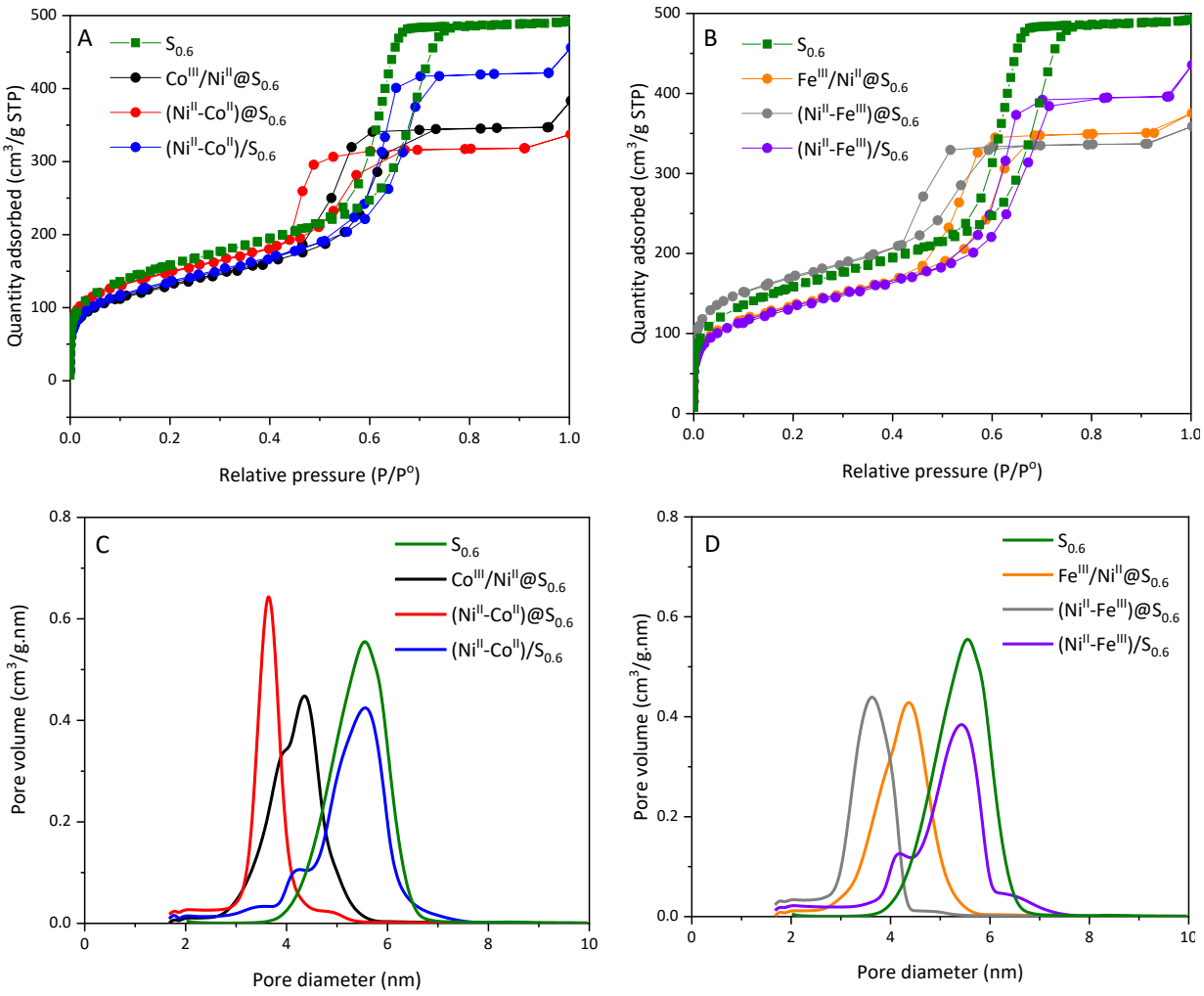

Figure III-B.1: *(A, B) N_2 adsorption-desorption isotherms (-196°C) and (C, D) pore size distributions of Ni-Co and Ni-Fe supported on hexagonal monolith $S_{0.6}$ with different incorporation strategies.*

The metal loading for Ni, Co and Fe were measured by ICP-OES (Table III.B.1). In $(Ni^{II}\text{-}Co^{II})/S_{0.6}$ and $(Ni^{II}\text{-}Fe^{III})/S_{0.6}$ samples, the experimental loadings were very close to what was expected. For $(Ni^{II}\text{-}Co^{II})@S_{0.6}$ and $(Ni^{II}\text{-}Fe^{III})@S_{0.6}$ samples, experimental values were a little bit lower with 2.7 wt.% for Ni and 1.7 wt.% for Co or Fe. The highest differences between nominal and experimental values could be emphasized with $Co^{III}/Ni^{II}@S_{0.6}$ and $Fe^{III}/Ni^{II}@S_{0.6}$ samples with only 2.4 wt.% of Ni and 0.9 wt.% of Co or Fe. In the latter case, where $K_3[Co(CN)_6]$ or $K_3[Fe(CN)_6]$ were used as

precursors for the formation of Prussian blue analogs, it appears that Ni-CN-Co or Ni-CN-Fe interactions were weaker than expected. Moreover, Ni(II) seemed to be leached out during the process.

Table III-B.1: *Physicochemical properties of bimetallic Ni-Co and Ni-Fe based monolith $S_{0.6}$ prepared by different incorporation strategies.*

Materials	S_{BET} ($m^2\ g^{-1}$)	V_{Des}[a] ($cm^3\ g^{-1}$)	D_{pores}[b] (nm)	d[c] (nm)	Ni (wt.%) Theor [ICP]	M (wt.%) Theor [ICP]
$S_{0.6}$	561	0.73	5.4	8.4	-	-
$Co^{III}/Ni^{II}@S_{0.6}$	473	0.58	4.7	7.8	3 [2.4]	2 [0.9]
$(Ni^{II}\text{- }Co^{II})@S_{0.6}$	532	0.49	3.8	7.9	3 [2.7]	2 [1.7]
$(Ni^{II}\text{- }Co^{II})/S_{0.6}$	490	0.68	5.5	8.0	3 [3.1]	2 [1.9]
$Fe^{III}/Ni^{II}@S_{0.6}$	487	0.57	4.7	7.9	3 [2.5]	2 [0.9]
$(Ni^{II}\text{-}Fe^{III})@S_{0.6}$	605	0.50	3.6	7.6	3 [2.7]	2 [1.7]
$(Ni^{II}\text{-}Fe^{III})/S_{0.6}$	481	0.64	5.3	8.2	3 [3.1]	2 [1.9]

[a] From BJH desorption (between 2 and 50 nm in diameter); [b] From the BJH desorption pore size distribution; [c] Interplanar distance by small-angle X-Ray scattering.

Small-angle X-Ray scattering analysis of the calcined samples (Figure III-B.2) exhibited the (100), (110) and (200) peaks characteristic of highly ordered hexagonal mesoporous materials of p6mm structure [9,10]. This observation attests for the pore organization of the SBA-15 monoliths. For impregnated samples, $(Ni^{II}\text{- }Co^{II})/S_{0.6}$ and $(Ni^{II}\text{-}Fe^{III})/S_{0.6}$, a slight modification in the structural parameter was observed in comparison with the naked support $S_{0.6}$ (8.0 and 8.2 nm vs. 8.4 nm) but a considerable modification could be emphasized for the other two samples ($Co^{III}/Ni^{II}@S_{0.}6$, $Fe^{III}/Ni^{II}@S_{0.6}$, $Co^{III}/Ni^{II}@S_{0.6}$ and $Fe^{III}/Ni^{II}@S_{0.6}$). However, the hexagonal structure $S_{0.6}$ was preserved for all samples.

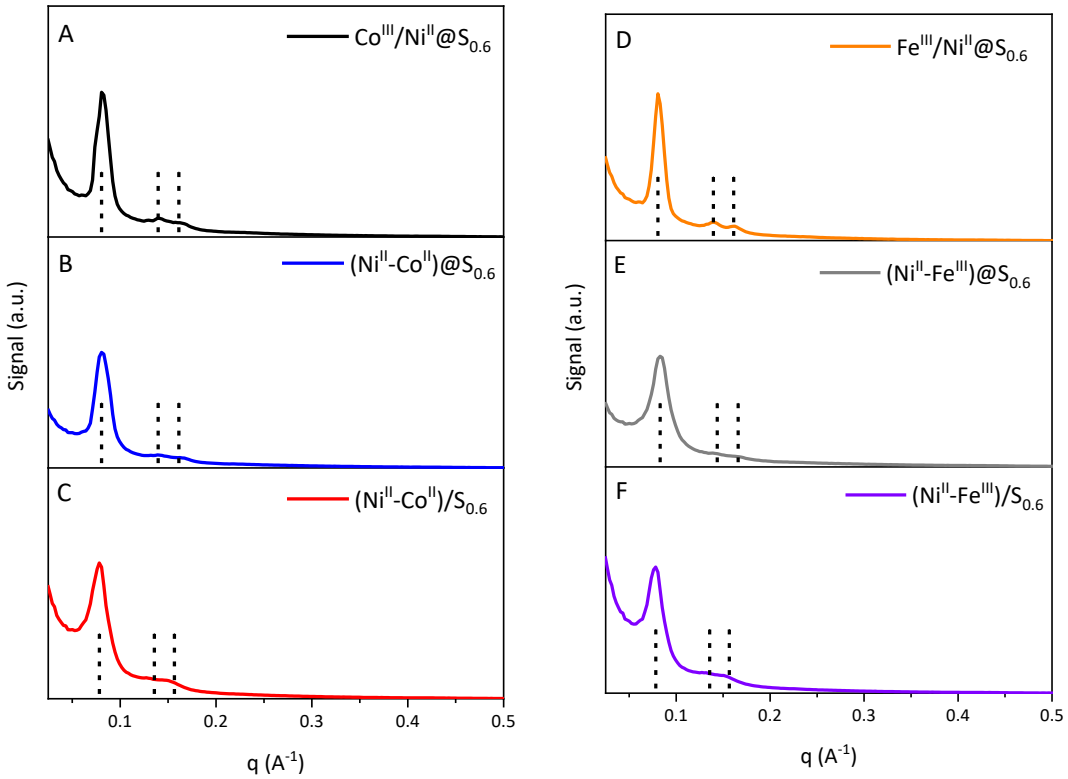

Figure III-B.2: *SAXS of bimetallic Ni-Co and Ni-Fe supported on $S_{0.6}$ monolith prepared by different incorporation methods.*

Wide angle X-Ray diffractograms of the two calcined bimetallic NiCo-based monoliths (Figure III-B.3 A), prepared by impregnation $Co^{III}/Ni^{II}@S_{0.6}$ or co-impregnation $(Ni^{II}-Co^{II})/S_{0.6}$, showed three peaks at 36.7°, 43.4° and 62.7° which were attributed to the (111), (200) and (220) crystal planes of $NiCoO_2$ (JCPDS 10-0188) [45,46]. For NiFe-based samples (Figure III-B.3 B), $Fe^{III}/Ni^{II}@S_{0.6}$ and $(Ni^{II}-Fe^{III})/S_{0.6}$, the XRD patterns exhibited three peaks at 36.3°, 43.4° and 62.3° attributed to the (311), (400) and (440) planes of a cubic phase with space group Fd3m. Actually, the obtained XRD peaks may be matched with the standard characteristics peaks of the cubic spinel lattice of $NiFe_2O_4$ reported in JCPDS 86-2267 [47]. For the samples prepared by one-pot strategy, $(Ni^{II}-Co^{II})/S_{0.6}$ and $(Ni^{II}-Fe^{III})/S_{0.6}$, no peaks corresponding to oxides were observed, which suggests the formation of small nanoparticles or clusters.

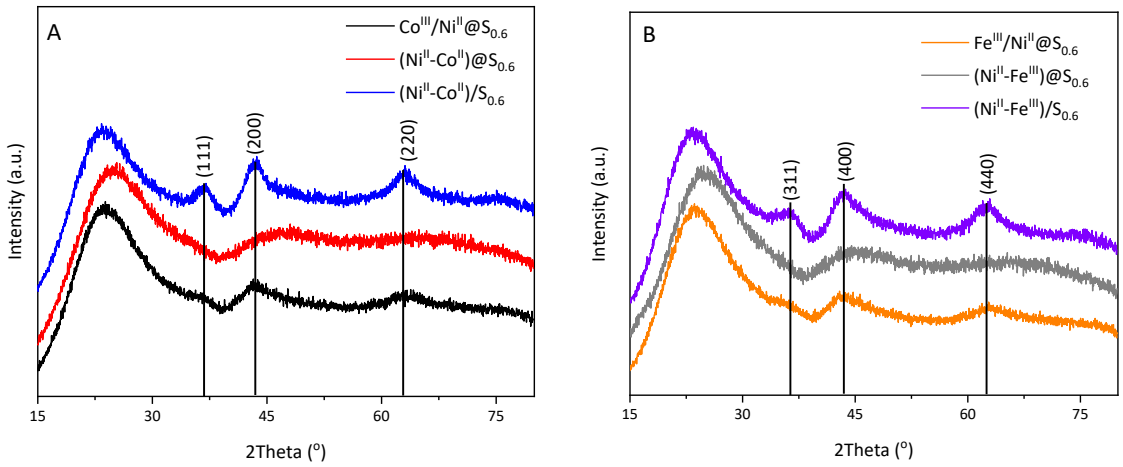

Figure III-B.3: *Wide angle XRD of bimetallic Ni-Co and Ni-Fe supported on $S_{0.6}$ monolith prepared with different incorporation methods.*

Regarding the H_2-TPR of bimetallic NiCo and NiFe materials, changes in the profiles and variation of the metal(s)-support interaction are invoked compared to monometallic $Ni^{II}@S_{0.6}$ prepared by one-pot strategy.

All of the six samples are strongly impacted by the protocol used for the metal incorporation. From the H_2-TPR profiles of $Ni^{II}@S_{0.6}$ (Figure III-B.4 A) and $Co^{III}/Ni^{II}@S_{0.6}$ (Figure III-B.4 B), it can be observed that the addition of Co(III), by impregnation, disfavored the reduction of Ni^{2+} species (temperature increased from 406ºC and 551ºC to 660ºC and 796ºC, Table III-B.2). Other authors, for example, Bian *et al*. [48] also showed with Ni-Co/SiO_2, derived from phyllosilicates, that adding Co and increasing its content shifts the reduction peaks of Ni to higher temperature. Also, promotional effect of Co enhancing the Ni-Co interaction with the support was reported (temperature increased from 600ºC to 700ºC) [49]. The profile of $Fe^{III}/Ni^{II}@S_{0.6}$ (Figure III-B.4 E) was more complex, showing two important contributions. These results indicated that introducing the second metal Co or Fe onto the Ni monometallic catalyst led to the shift of the reduction temperature, which could suggest some synergistic interaction between both metals [50].

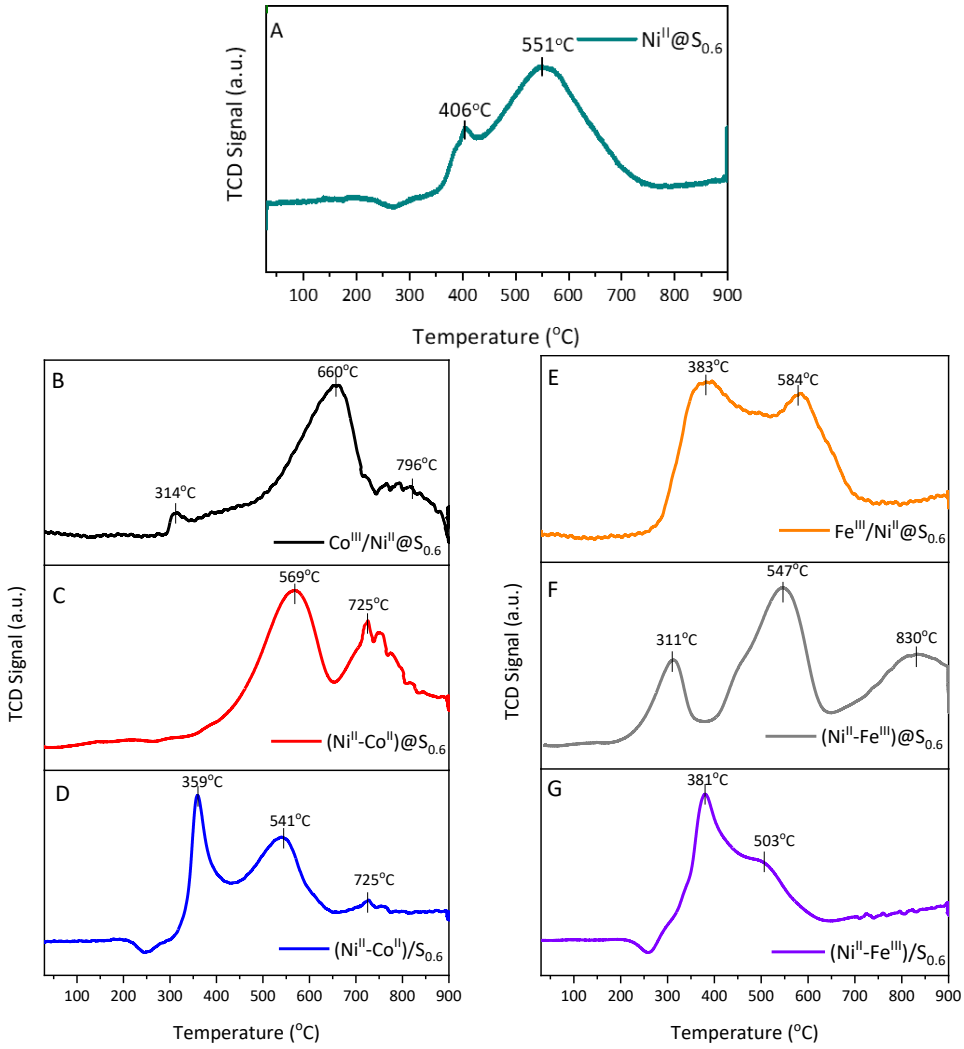

Figure III-B.4: *H_2-TPR profiles of (A) monometallic 5 wt.% $Ni^{II}@S_{0.6}$ prepared by a one-pot strategy and bimetallic (B,D,C) Ni-Co and (E,F,G) Ni-Fe supported on $S_{0.6}$ monolith prepared by different incorporation methods.*

The four remaining bimetallic materials prepared by the incorporation of both metals (Ni and Co or Fe) by a one-pot strategy or co-impregnation could also be compared together. (Ni^{II}-Co^{II})@$S_{0.6}$ exhibited two peaks at 569°C and 725°C (Figure III-B.4 C and Table III-B.2) while (Ni^{II}-Co^{II})/$S_{0.6}$ showed two main contributions at 359 and 541°C, the last one at 725°C being much smaller than its analog for (Ni^{II}-Co^{II})@$S_{0.6}$ (Figure III-B.4 D and Table III-B.2). (Ni^{II}-Fe^{III})@$S_{0.6}$ was characterized by a very broad range of temperatures for H_2 consumption from 200°C to higher than 900°C with three maxima at around 311, 547 and 830°C (Figure III-B.4 F and Table III-B.2). The peak at 547°C could suggest that the nickel and iron in the catalyst probably exist in the form of $NiFe_2O_4$ species and this agrees with the XRD studies (Figure III-B.3 B).

Table III-B.2: *Temperature of each maximum for H_2-TPR profiles of $Ni^{II}@S_{0.6}$ and the bimetallic NiCo and NiFe prepared by three different strategies.*

Material	Maxima	T (°C)
$Ni^{II}@S_{0.6}$	2	406 / 551
$Co^{III}/Ni^{II}@S_{0.6}$	3	314 / 660 / 796
$(Ni^{II}\text{-}Co^{II})@S_{0.6}$	2	569 / 725
$(Ni^{II}\text{-}Co^{II})/S_{0.6}$	3	359 / 541 / 725
$Fe^{III}/Ni^{II}@S_{0.6}$	2	383 / 584
$(Ni^{II}\text{-}Fe^{III})@S_{0.6}$	3	311 / 547 / 830
$(Ni^{II}\text{-}Fe^{III})/S_{0.6}$	2	381 / 503

The calcined bimetallic Ni-Co and Ni-Fe materials were analyzed by transmission electron microscopy in order to check the organization of the pore structure, the location and the dispersion of the metals on the support (Figure III-B.5). Definitely, all six samples exhibited well organized hexagonal pore structures. $Co^{III}/Ni^{II}@S_{0.6}$ exhibited particles in the porosity of the silica monoliths as well as outside (Figure III-B.5 A and A'). For $(Ni^{II}\text{-}Co^{II})@S_{0.6}$, clearly no particles were detected inside the porosity, instead aggregates of Ni-Co particles were deposited on the outer surface of mesoporous silica (Figure III-B.5 B and B'). $(Ni^{II}\text{-}Co^{II})/S_{0.6}$ prepared by co-impregnation of both metals exhibited particles inside the porosity (Figure III-B.5 C and C'). The behavior of Ni-Fe samples was completely different from Ni-Co samples. Clearly, most of the observed particles were located at the inner surface of the porous support and no Ni-Fe particles were detected on the external surface (Figure III-B.5 D, D', E, E', F and F'). The mean particle size for all samples was in a range between 3 and 5 nm, in good agreement with wide angle XRD, where small and broad peaks were detected.

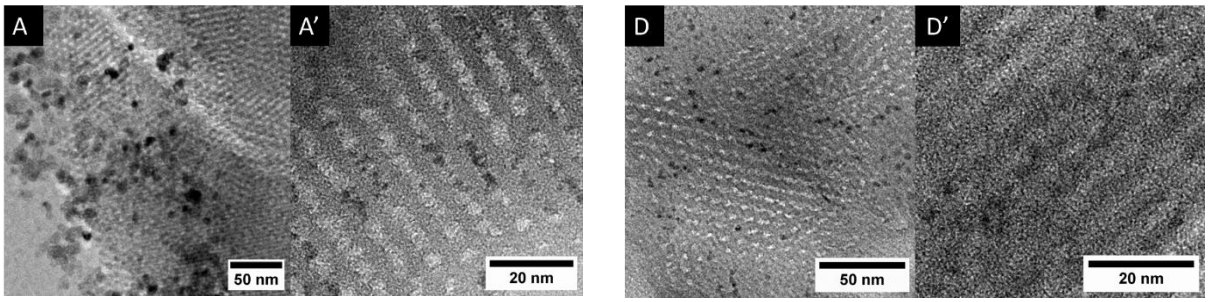

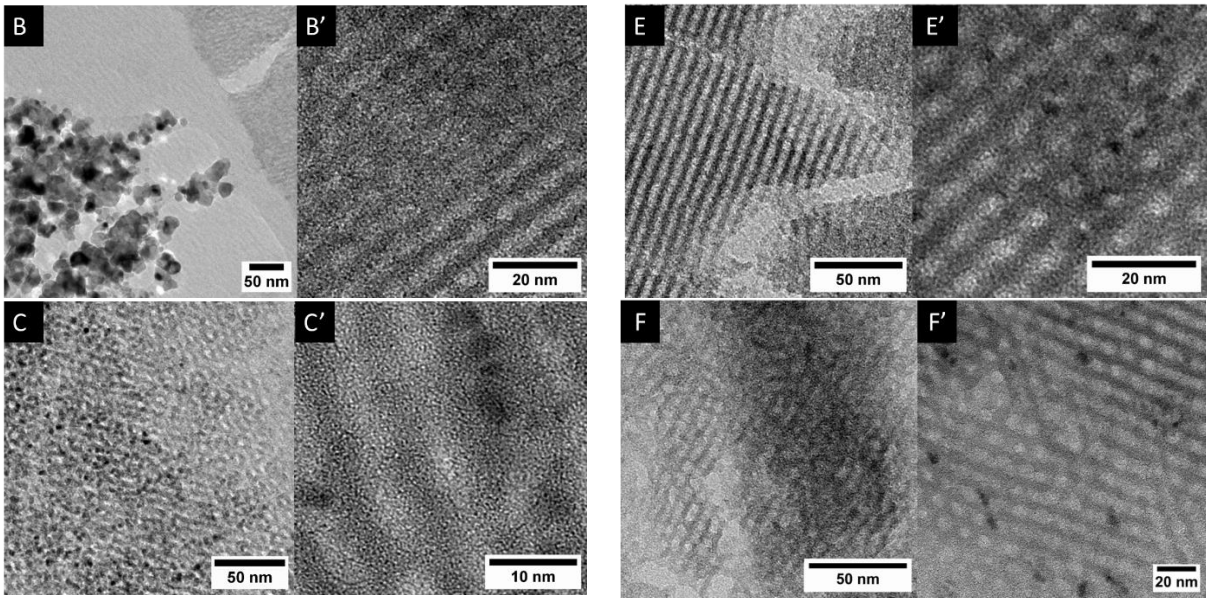

Figure III-B.5: *TEM images of microtomed samples in their calcined state for (A,A') $Co^{III}/Ni^{II}@S_{0.6}$, (B,B') $(Ni^{II}\text{-}Co^{II})@S_{0.6}$, (C,C') $(Ni^{II}\text{-}Co^{II})/S_{0.6}$, (D,D') $Fe^{III}/Ni^{II}@S_{0.6}$, (E,E') $(Ni^{II}\text{-}Fe^{III})@S_{0.6}$ and (F,F') $(Ni^{II}\text{-}Fe^{III})/S_{0.6}$ samples.*

Complementary STEM/HAADF and TEM combined with EDX/mapping were carried out on the six bimetallic Ni-M-based monolith silica in order to probe the distribution of both metals throughout the mesoporous silica. (Figure III-B.6). EDX mapping images of Ni, Co or Fe, Si and O showed that using one-pot protocol for Ni and Co (or Fe) gave rise to high dispersion of both metals. Co-impregnation would favor the formation of nano-objects made of both metals.

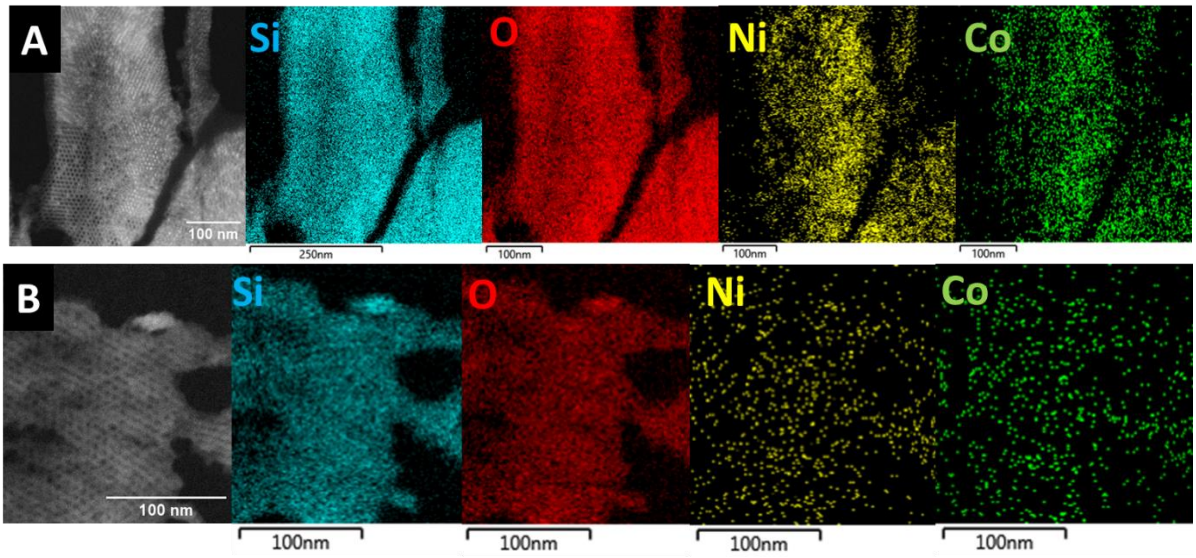

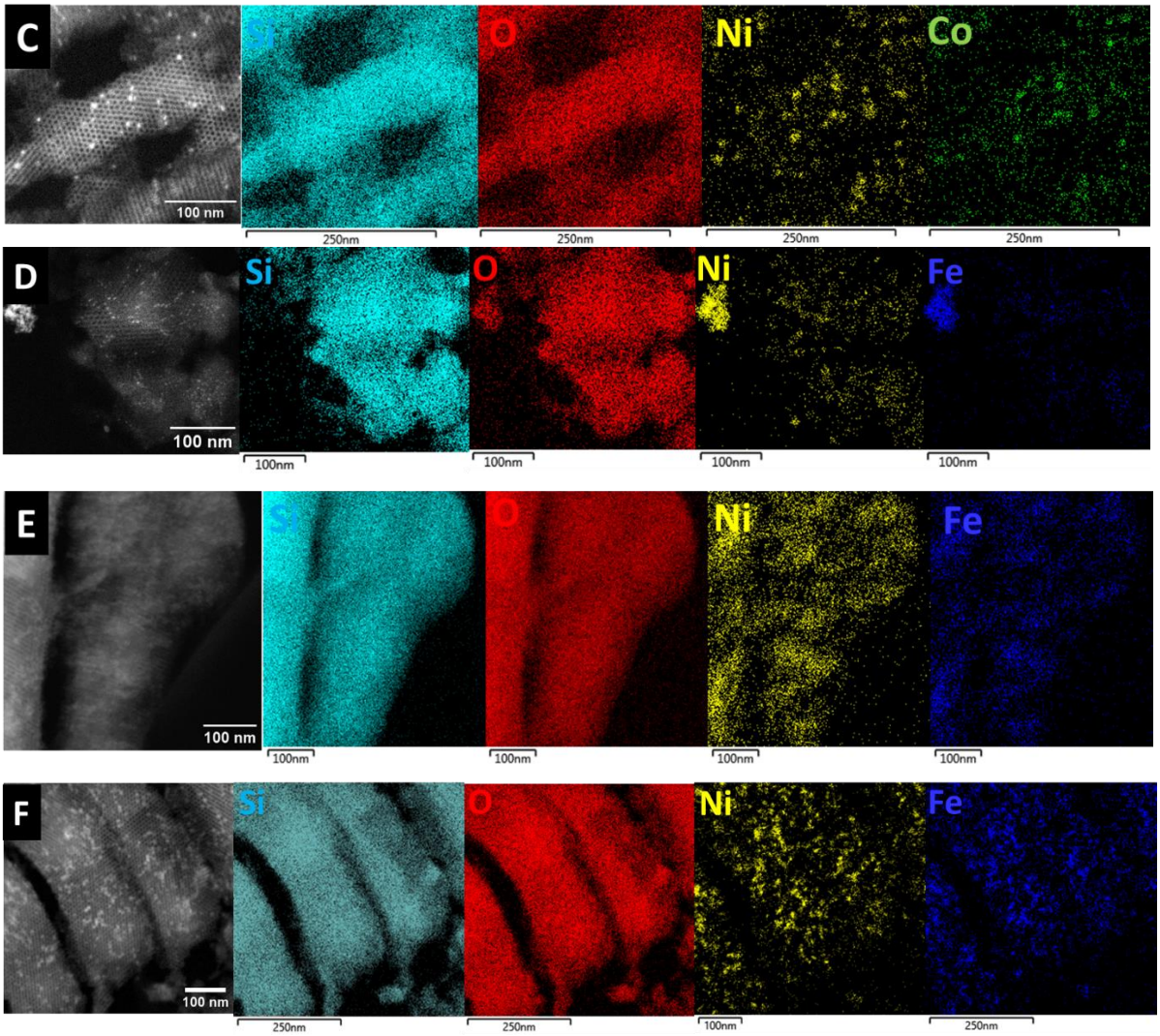

***Figure III-B.6**: STEM/HAADF images and corresponding EDX elemental mapping of calcined (A) $Co^{III}/Ni^{II}@S_{0.6}$, (B) $(Ni^{II}\text{-}Co^{II})@S_{0.6}$, (C) $(Ni^{II}\text{-}Co^{II})/S_{0.6}$, (D) $Fe^{III}/Ni^{II}@S_{0.6}$, (E) $(Ni^{II}\text{-}Fe^{III})@S_{0.6}$ and (F) $(Ni^{II}\text{-}Fe^{III})/S_{0.6}$.*

III-B.3.2. Catalytic performance of Ni-Co and Ni-Fe based monoliths in the hydrogenolysis of $A1_{HH}$

After *ex-situ* reduction at 500°C using H_2 (50 mL min^{-1}) for 3 h, the resulting Ni-Co and Ni-Fe based catalysts were tested in the hydrogenolysis of $A1_{HH}$ under 5 bar of N_2 at 180°C and using isopropanol as H-donor solvent and compared to $Ni^0@S_{0.6}$. Ethylbenzene, phenol, cyclohexanol and $C1_{HH}$ were the main products in all the tests conducted with Ni-Co and Ni-Fe monoliths as well as with $Ni^0@S_{0.6}$.

Considering the $M^0/Ni^0@S_{0.6}$ catalysts, $Co^0/Ni^0@S_{0.6}$ was more efficient for both $A1_{HH}$ (100%) and C-OAr bonds (90%) with 22%$_C$ yield in phenol (Figure III-B.5 A and Table III-B.8, entry 1), however, $Fe^0/Ni^0@S_{0.6}$ led to only 34% conversion of $A1_{HH}$ and 23% of C-OAr bonds within 1 h (Table III-B.8, entry 2). It is noteworthy that $Ni^0@S_{0.6}$ led, under similar reactions conditions, to a total conversion of $A1_{HH}$ and 77.3% conversion of C-OAr bonds producing ethylbenzene (41%$_C$), phenol (28%$_C$), cyclohexanol (7%$_C$) and $C1_{HH}$ (23%$_C$) within 1 h (Figure III-B.5 A).

After 5 h, $Co^0/Ni^0@S_{0.6}$ led to a total conversion of $A1_{HH}$ and C-OAr bonds giving rise to mainly ethylbenzene and cyclohexanol (Table III-B.8, entry 3). Similar results with $Ni^0@S_{0.6}$ were obtained with no traces of phenol (Figure III-B.5 B), whereas, $Fe^0/Ni^0@S_{0.6}$ totally converted $A1_{HH}$ with 80% conversion of C-OAr bonds leading to a yield of phenol of 27%C with a selectivity of 78% (Figure III-B.5 B and Table III-B.8, entry 4).

Such results indicate a better catalytic activity of Ni-Co based monoliths in this type of reaction after 1 h compared to Ni-Fe catalysts.

Table III-B.8: *Additional tests on $A1_{HH}$ with $M^0/Ni^0@S_{0.6}$ catalysts for 1 or 5 h.*

Entry	Catalyst	Reaction time	X_i [X_{Dimers}] (%)	Y Phenol (%$_C$) [S_{Phenol}] (%)	Y C6_ol (%$_C$)	Y EB (%$_C$)	Y $C1_{HH}$ (%$_C$)	MB[a] (%)
1	$Co^0/Ni^0@S_{0.6}$	1 h	100 [90]	22 [57]	19	49	9	99
2	$Fe^0/Ni^0@S_{0.6}$	1 h	34 [23]	10 [100]	0	14	10	100
3	$Co^0/Ni^0@S_{0.6}$	5 h	100 [100]	0 [0]	41	57	0	98
4	$Fe^0/Ni^0@S_{0.6}$	5 h	100 [80]	27 [78]	10	42	19	98

C6_ol: Cyclohexanol; EB: Ethylbenzene.
$[A1_{HH}]_o$ = 0.06 M, $A1_{HH}/M.$ = 100, $V_{i\text{-}PrOH}$ = 15 mL, 180°C, 5 bar of N_2. [a] Mass balance, $MB=\sum_i Y_i + (100 - X_{A1_{HH}})$.

Therefore, it was decided to conduct further tests with Ni-Co catalysts for 1 h (Figure III-B.5 A) and with Ni-Fe catalysts for 5 h (Figure III-B.5 B).

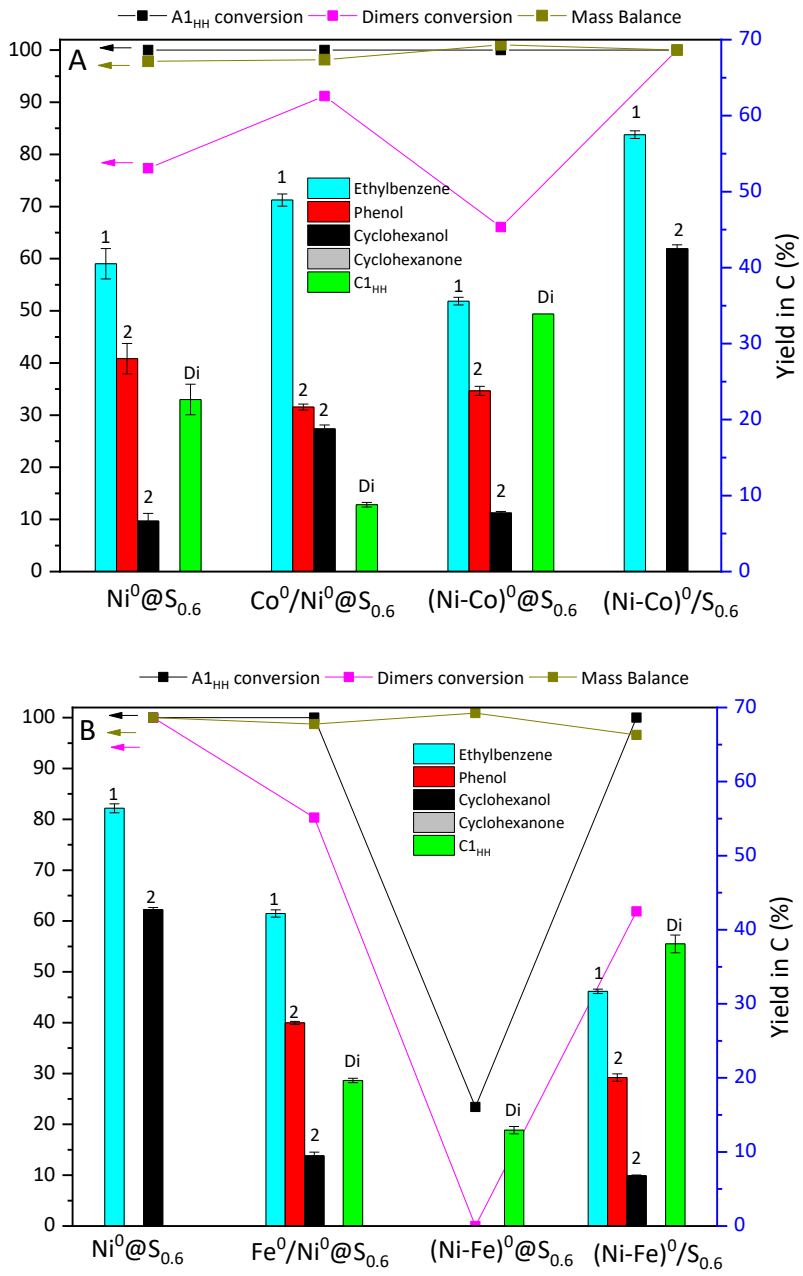

Figure III-B.7: *$A1_{HH}$ / dimers conversion, mass balance and yields of the main products obtained with (A) Ni-Co and (B) Ni-Fe based monoliths compared to 5 wt.% $Ni^0@S_{0.6}$.*
Reaction conditions: $[A1_{HH}]_o$ = 0.06 M, $A1_{HH}$/M = 100 (mol/mol), i-PrOH (15 mL), 180°C,(A) 1 h or (B) 5 h, 5 bars of N_2.

After 1 h, the catalytic activity of $(Ni\text{-}Co)^0@S_{0.6}$ was the lowest (100% and 66% for $A1_{HH}$ and C-OAr bonds conversions, respectively) compared to that of the two other Ni-Co solids. On the contrary, $(Ni\text{-}Co)^0/S_{0.6}$ prepared by co-impregnation of both Co and Ni metals over $S_{0.6}$, gave total conversion of $A1_{HH}$ and dimers after 1 h, but this catalyst showed no selectivity towards phenol.

In fact, all phenol was rapidly hydrogenated into cyclohexanol. Maybe the reaction time should be lowered or the substrate/metal molar ratio should be increased.

The worst catalyst of the Ni-Fe based monoliths series was also the one prepared with one-pot strategy, $(Ni\text{-}Fe)^0@S_{0.6}$. After 5 h, not only it gave a rather low conversion of $A1_{HH}$ but this catalyst led to a transformation of $A1_{HH}$ into $C1_{HH}$ (with no C-O bond cleavage). On the hand, the two other catalysts, $Fe^0/Ni^0@S_{0.6}$ and $(Ni\text{-}Fe)^0/S_{0.6}$, led to total conversion of $A1_{HH}$ after 5 h, but $Fe^0/Ni^0@S_{0.6}$ led to higher C-OAr bond cleavage (80% *vs.* 62%) and better phenol yield (27%$_C$ *vs.* 20%$_C$).

Finally, catalysts prepared by impregnation of $Ni^{II}@S_{0.6}$ with Co^{III} or Fe^{III} seem to be advantageous in terms of catalytic performances despite their low metal loadings compared to the four other materials (Table III.B.1). $Co^0/Ni^0@S_{0.6}$ was more efficient in converting $A1_{HH}$ and C-OAr bonds than $Ni^0@S_{0.6}$ but less selective towards phenol (57% for $Co^0/Ni^0@S_{0.6}$ *vs.* 85% for $Ni^0@S_{0.6}$) after 1h. $Fe^0/Ni^0@S_{0.6}$ was less active than $Ni^0@S_{0.6}$ but more selective towards phenol after 5 h (78% for $Fe^0/Ni^0@S_{0.6}$ *vs.* 0% for $Ni^0@S_{0.6}$).

III-B.4. Conclusion

The synthesis of mesoporous silica based materials with Ni and Co (or Fe) was achieved by using three different incorporation strategies among which a one-pot strategy involving two metals or an impregnation strategy using two solvents. Calcined bimetallic solids, thus obtained, were characterized by very different behaviors towards H_2-TPR.

After reduction at 500°C, by comparing the catalytic activity of these solids, it appeared that the incorporation method of metals is a very critical parameter. Impregnation of Co(III) or Fe(III) on Ni@S led to materials ($Co^0/Ni^0@S_{0.6}$ and $Fe^0/Ni^0@S_{0.6}$) which exhibited the best catalytic activities (in isopropanol with a substrate/metal molar ratio of 100, at 180°C and under 5 bar of N_2, 1 h for $Co^0/Ni^0@S_{0.6}$ and 5 h for $Fe^0/Ni^0@S_{0.6}$), in terms of phenol yields (22%$_C$ for $Co^0/Ni^0@S_{0.6}$ (1 h) and 27%$_C$ for $Fe^0/Ni^0@S_{0.6}$ (5 h)) which was close to 5 wt.% of $Ni^0@S_{0.6}$ (~28%$_C$, 1 h). It should be noted that probably not all active species were reduced at 500°C for 3 h. Therefore, work is in progress in order to optimize the reaction conditions maybe by increasing the reduction temperature of these solids and/or varying the substrate/metal molar ratio.

III-2. Conclusion

The catalytic activity was shown to depend greatly on the incorporation strategy of Ni. Among Ni silica based monoliths prepared by a one-pot strategy with different pore structures, or by impregnation of Aerosil 380 or of a blank monolith $S_{0.6}$ with NH_3, $Ni^0_{NH_3}/SiO_2$ led to the highest phenol production in the hydrogenolysis of $A1_{HH}$ and best catalytic activity in the hydrogenolysis of GGE at 180°C and for 1 h. The solids with cubic pore structures turned out to be more efficient than those with hexagonal and wormlike structures for the conversion of $A1_{HH}$ at 180°C within 1 h, but they were less selective toward phenol. However, hexagonal structures were efficient in converting $A1_{HH}$ but not all C-OAr bonds. Therefore, adding a co-metal (Co or Fe) to Ni with different incorporation strategies keeping a hexagonal pore structure was an idea in order to test the effect of the second metal on the reaction. It appeared that the incorporation method of metals is a very critical parameter and that impregnation of Co or Fe by the "two-solvents" method on pre-formed Ni@S led to materials which exhibited the best catalytic activity in terms of yield towards phenol. However, often highest phenol yields were obtained for incomplete conversion of C-OAr bonds.

References

[1] J. S. Beck, J. C. Vartuli, W. J. Roth, M. E. Leonowicz, C. T. Kresge, K. D. Schmitt, C. T. W. Chu, D. H. Olson, E. W. Sheppard, S. B. McCullen, J. B. Higgins, J. L. Schlenker, *J. Am. Chem. Soc.* **1992**, *114*, 10834–10843.

[2] I. Sierra, D. Pérez-Quintanilla, *Chem. Soc. Rev.* **2013**, *42*, 3792–3807.

[3] A. Walcarius, *Chem. Soc. Rev.* **2013**, *42*, 4098–4140.

[4] D. J. Mihalcik, W. Lin, *ChemCatChem* **2009**, *1*, 406–413.

[5] G. J. de A. A. Soler-Illia, C. Sanchez, B. Lebeau, J. Patarin, *Chem. Rev.* **2002**, *102*, 4093–4138.

[6] V. Chaudhary, S. Sharma, *J. Porous Mater.* **2017**, *24*, 741–749.

[7] A. Rodriguez-Gomez, R. Pereñiguez, A. Caballero, *J. Phys. Chem. B* **2018**, *122*, 500–510.

[8] M. Houalla, F. Delanny, I. Matsuura, B. Delmon, *J. Chem. Soc. Faraday Trans. 1 Phys. Chem. Condens. Phases* **1980**, *76*, 2128–2141.

[9] O. Daoura, G. Fornasieri, M. Boutros, N. El Hassan, P. Beaunier, C. Thomas, M. Selmane, A. Miche, C. Sassoye, O. Ersen, W. Baaziz, P. Massiani, A. Bleuzen, F. Launay, *Appl. Catal. B Environ.* **2021**, *280*, 119417.

[10] E. Delahaye, R. Moulin, M. Aouadi, V. Trannoy, P. Beaunier, G. Fornasieri, A. Bleuzen, *Chem. - A Eur. J.* **2015**, *21*, 16906–16916.

[11] G. Fornasieri, M. Aouadi, P. Durand, P. Beaunier, E. Rivière, A. Bleuzen, *Chem. Commun.* **2010**, *46*, 8061–8063.

[12] M. Thommes, K. Kaneko, A. V. Neimark, J. P. Olivier, F. Rodriguez-Reinoso, J. Rouquerol, K. S. W. Sing, *Pure Appl. Chem.* **2015**, *87*, 1051–1069.

[13] D. P. Serrano, G. Calleja, J. A. Botas, F. J. Gutierrez, *Ind. Eng. Chem. Res.* **2004**, *43*, 7010–7018.

[14] Y. Park, T. Kang, J. Lee, P. Kim, H. Kim, J. Yi, *Catal. Today* **2004**, *97*, 195–203.

[15] P. Burattin, M. Che, C. Louis, *J. Phys. Chem. B* **1998**, *102*, 2722–2732.

[16] C. Louis, Z. X. Cheng, M. Che, *J. Phys. Chem.* **1993**, *97*, 5703–5712.

[17] S. S. Soni, G. Brotons, M. Bellour, T. Narayanan, A. Gibaud, *J. Phys. Chem. B* **2006**, *110*, 15157–15165.

[18] P. C. A. Alberius, K. L. Frindell, R. C. Hayward, E. J. Kramer, G. D. Stucky, B. F. Chmelka, *Chem. Mater.*

2002, *14*, 3284–3294.
[19] W. J. J. Stevens, K. Lebeau, M. Mertens, G. Van Tendeloo, P. Cool, E. F. Vansant, *J. Phys. Chem. B* **2006**, *110*, 9183–9187.
[20] O. Daoura, N. El Hassan, M. Boutros, S. Casale, P. Massiani, F. Launay, *ACS Appl. Nano Mater.* **2022**, *5*, 18048–18059.
[21] X. Zhao, M. Lu, H. Li, J. Fang, L. Shi, D. Zhang, *New J. Chem.* **2017**, *41*, 4869–4878.
[22] R. Shu, Q. Zhang, Y. Xu, J. Long, L. Ma, T. Wang, P. Chen, Q. Wu, *RSC Adv.* **2016**, *6*, 5214–5222.
[23] M. Carrier, C. Segura, J. L. Garcia, S. Park, H. H. Lamb, N. Escalona, S. W. Peretti, *Appl. Catal. A Gen.* **2018**, *562*, 294–309.
[24] J. Zhang, H. Asakura, J. Van Rijn, J. Yang, P. Duchesne, B. Zhang, X. Chen, P. Zhang, M. Saeys, N. Yan, *Green Chem.* **2014**, *16*, 2432–2437.
[25] J. Zhang, J. Teo, X. Chen, H. Asakura, T. Tanaka, K. Teramura, N. Yan, *ACS Catal.* **2014**, *4*, 1574–1583.
[26] M. V. Galkin, S. Sawadjoon, V. Rohde, M. Dawange, J. S. M. Samec, *ChemCatChem* **2014**, *6*, 179–184.
[27] X. Si, J. Chen, F. Lu, X. Liu, Y. Ren, R. Lu, H. Jiang, H. Liu, C. Miao, Y. Zhu, X. Luo, J. Xu, *ACS Sustain. Chem. Eng.* **2019**, *7*, 19034–19041.
[28] T. Prasomri, M. Shetty, K. Murugappan, Y. Roman-Leshkov, *Energy Environ. Sci.* **2014**, *7*, 2660–2669.
[29] D. J. Rensel, S. Rouvimov, M. E. Gin, J. C. Hicks, *J. Catal.* **2013**, *305*, 256–263.
[30] X. Liu, L. Xu, G. Xu, W. Jia, Y. Ma, Y. Zhang, *ACS Catal.* **2016**, *6*, 7611–7620.
[31] F. Gao, J. D. Webb, J. F. Hartwig, *Angew. Chemie - Int. Ed.* **2016**, *55*, 1474–1478.
[32] S. Ogasawara, S. Kato, *J. Am. Chem. Soc.* **2010**, *132*, 4608–4613.
[33] J. Y. Kim, S. Y. Park, I. G. Choi, J. W. Choi, *Chem. Eng. J.* **2018**, *336*, 640–648.
[34] Y. Zhai, C. Li, G. Xu, Y. Ma, X. Liu, Y. Zhang, *Green Chem.* **2017**, *19*, 1895–1903.
[35] W. Wanmolee, J. N. Beltramini, L. Atanda, J. P. Bartley, N. Laosiripojana, W. O. S. Doherty, *ACS Omega* **2019**, *4*, 16980–16993.
[36] B. Yan, X. Lin, Z. Chen, Q. Cai, S. Zhang, *Bioresour. Technol.* **2021**, *321*, 124503.
[37] A. Laobuthee, A. Khankhuean, P. Panith, C. Veranitisagul, N. Laosiripojana, *ACS Omega* **2023**, *8*, 8675–8682.
[38] R. N. Olcese, J. Francois, M. M. Bettahar, D. Petitjean, A. Dufour, *Energy and Fuels* **2013**, *27*, 975–984.
[39] Z. Vajglov, B. Gauli, P. M, N. Kumar, K. Er, W. Johan, R. Lassfolk, I. L. Simakova, I. P. Prosvirin, M. Peurla, J. Kaarle, M. Lind, H. Huhtinen, P. Paturi, D. E. Doronkin, D. Y. Murzin, *ACS Appl. Nano Mater.* **2023**, *6*, 10064–10077.
[40] H. Xia, C. Chen, P. Liu, M. Zhou, J. Jiang, *Sustain. Energy Fuels* **2020**, *4*, 5709–5720.
[41] B. Chen, F. Li, G. Yuan, *Catal. Letters* **2017**, *147*, 2877–2885.
[42] M. Zhou, C. Tang, J. Li, H. Xia, P. Liu, J. Xu, C. Chen, J. Jiang, *Fuel* **2022**, *315*, 123156.
[43] M. N. Kaydouh, N. El Hassan, A. Davidson, S. Casale, H. El Zakhem, P. Massiani, *Microporous Mesoporous Mater.* **2016**, *220*, 99–109.
[44] M. B. Zakaria, T. Chikyow, *Coord. Chem. Rev.* **2017**, *352*, 328–345.
[45] Y. Liu, Y. Zhao, Y. Yu, J. Li, M. Ahmad, H. Sun, *New J. Chem.* **2014**, *38*, 3084–3091.
[46] Z. Wang, J. Hou, H. Yang, Q. Zhou, C. Xu, *J. Alloys Compd.* **2020**, *848*, 156603.
[47] P. Sivagurunathan, S. R. Gibin, *J. Mater. Sci. Mater. Electron.* **2016**, *27*, 2601–2607.
[48] Z. Bian, S. Kawi, *J. CO_2 Util.* **2017**, *18*, 345–352.
[49] X. Gao, Z. Tan, K. Hidajat, S. Kawi, *Catal. Today* **2017**, *281*, 250–258.
[50] P. Jia, X. Lan, X. Li, T. Wang, *ACS Sustain. Chem. Eng.* **2018**, *6*, 13287–13295.

General conclusion and perspectives

During the reductive depolymerization of lignin, C-O bond hydrogenolysis, that gives phenolic compounds, is accompanied by the hydrogenation of aromatics. Many studies, reported in the bibliographic section, have been published, pointing out various catalysts and reaction conditions. Wide temperature range between 80 and 350°C, wide Ni wt.% loading between 5 and 57 wt.% and low molar substrate/metal ratio were used with organic solvents such as alcohols under a broad range of gas pressure from 1 to 80 bar.

In the present study, we have focused our attention on the reactivity of three substrates bearing C-O bonds as close as possible to that in the β-O-4 linkage of lignin. Our main objective here was to develop two families of stable Ni-based catalysts with low Ni loading (5 wt.%) and high dispersion, and also, reaction conditions favorable to hydrogenolysis. Using our previous expertise for the synthesis of porous nickel-based silica catalysts with high metal dispersion [1,2], our objective was to use them for the reductive depolymerization of lignin in the presence of isopropanol in relatively mild conditions (180°C, 5 bar of N_2 and with a substrate/metal molar ratio of 100). We were also interested in investigating the influence of the pore network on the activity of the catalysts towards relatively bulky lignin models and lignin itself.

In the first part of the experimental work, the positive effect of ammonia (impregnation route) on the generation of highly dispersed Ni-silica based catalysts obtained by impregnation of Aerosil 380 (Ni_{NH_3}/SiO_2) with aqueous nickel (II) nitrate was confirmed. Similar materials bearing Rh alone or Ni and Rh at *c.a.* 5 wt.% were also prepared for the sake of comparison. PDF, as well as TEM and H_2-TPR techniques used before Ni or Rh reduction emphasized very different behavior between both metals. As shown earlier, proofs for the formation of Ni phyllosilicates could be obtained. It could be even shown here that they were of Talc structure, while Rh(III) formed isolated species. After reduction, all the materials, including the Ni-Rh bimetallic ones exhibited small nanoparticles (~ 2 nm) well dispersed over the support. The most active catalyst was the Ni-based one but it turned out to be the least selective towards phenol. The Rh-based catalyst favored phenol formation but resulted in much slower C-OAr bonds cleavage.

Bimetallic Ni-Rh catalysts could be studied in more details using an original chemisorption protocol based on oxygen-hydrogen titrations showing high dispersion of the two metals in the bimetallic catalysts and suggesting that Ni would be segregated at the surface. A better model of β-O-4 linkage in lignin, *i.e.*, guaiacylglycerol-β-guaiacyl ether was also tested. In this case, its hydrogenolysis required harsher conditions (low substrate/metal ratio (10 or 25)). Full conversion of GGE was reached but unfortunately, full C-O cleavage was not obtained in the conditions tested. Further work is required to optimize the guaiacol production and work efficiently on the reductive depolymerization of Birch Lignin extracted in *i*-PrOH.

In the second part of the experimental work, as done before in our group, nickel was introduced in the synthesis gel of SBA-15 using a minimum of water (one-pot protocol). The resulting solid, with active small Ni nanoparticles, was compared with materials prepared by the method described above using either Aerosil 380 or a SBA-15 type solid made by the one-pot protocol. It could be shown, by H_2-TPR, that the interaction between Ni and silica was improved with ammonia (presence of Ni phyllosilicates), but also depends on the type of silica used. Then, a series of siliceous materials with different pore structures, incorporating 5 wt.% of Ni, not reported before, were prepared via the one-pot sol-gel method. Our results showed that adding nickel(II) in the synthesis gel did not impact negatively the textural properties of the resulting materials. Moreover, their catalytic performance in the hydrogenolysis of the 2-phenoxy-1-phenthanol, seemed to depend on the spatial distribution of the pores.

Siliceous materials with hexagonally structured mesopores involving Ni (3 wt.%) and a second metal, Fe or Co (2 wt.%), were prepared. The impact of the methods of Ni-Fe or Ni-Co incorporation (impregnation, one-pot or co-impregnation) strategies on the dispersion/location of NPs and subsequently on the catalyst activity in the hydrogenolysis of 2-phenoxy-1-phenylethanol using isopropanol at 180ºC under 5 bar of N_2 with a molar substrate/metal ratio of 100 was investigated. The results revealed that the catalytic activity greatly relies on the incorporation strategy of the metal over the support. A high conversion of $A1_{HH}$, a relatively high yield of phenol (~ 22%$_C$ with Co and 27%$_C$ with Fe) and a selectivity reaching 57% and 78% were obtained, respectively, for Ni-Co and for Ni-Fe solids prepared by impregnation of Co or Fe over Ni@S. Low C-OAr bonds conversions could be reached with solids prepared by one-pot strategy or co-impregnation of both metals.

Last but not least, a comparison has been made between the prepared materials**.** For all lignin model compounds used, Ni_{NH_3}/SiO_2 exhibited better catalytic performances than others in the hydrogenolysis of 2-phenoxy-1-phenylethanone and 2-phenoxy-1-phenylethanol. Ni_{NH_3}/SiO_2 led to a total conversion of substrates within one hour, with high selectivity towards phenol attending 98% from $K1_{HH}$ and 79% from $A1_{HH}$.

The Ni-based catalysts prepared here, could rival with the best of the catalysts described in the literature in the hydrogenolysis of lignin and its models. A high yield of phenol (42%$_C$) as well as high selectivity (98%) could be obtained in the hydrogenolysis of lignin model compounds ($K1_{HH}$) after only 1 h of reaction time. Related studies in literature showed relatively similar results at higher temperature and/or higher reaction time [3–6].

Several perspectives can arise from the present results, among which:

1) Owing to their facile and inexpensive route of preparation which does not involve hydrothermal treatment under high pressures and temperatures [7,8], Ni_{NH_3}/SiO_2 catalysts may have a good potential for industrial applications.

2) Admittedly, the molecules used (2-phenoxy-1-phenylethanone and 2-phenoxy-1-phenylethanol) are not perfect models for the β-O-4 bond, that is why further work is being carried out with a more closely related molecule, *i.e.,* guaiacylglycerol-β-guaiacyl ether. The main factors affecting guaiacol selectivity in that case have to be further identified. High metal amount was used in that case, therefore, trying to increase the reaction temperature, the reaction time or the N_2 pressure would be interesting for GGE and also for lignin.

3) Regarding the nickel based-siliceous catalysts with different pore structures prepared by the one-pot sol-gel strategy, they provide interesting materials to investigate more systematic way the influence of the pore structure on the depolymerization and repolymerization processes after the optimization of the reaction conditions.

4) Another general outlook includes the valorization of the ferromagnetic properties of Ni^0 [9] which could be used to induce local heating upon the application of a magnetic field. Reductive lignin depolymerization could be done using local heating of the nickel particles

through the use of an oscillating magnetic field instead of the conventional heating method [10,11].

References

[1] O. Daoura, N. El Hassan, M. Boutros, S. Casale, P. Massiani, F. Launay, *ACS Appl. Nano Mater.* **2022**, *5*, 18048–18059.

[2] O. Daoura, G. Fornasieri, M. Boutros, N. El Hassan, P. Beaunier, C. Thomas, M. Selmane, A. Miche, C. Sassoye, O. Ersen, W. Baaziz, P. Massiani, A. Bleuzen, F. Launay, *Appl. Catal. B Environ.* **2021**, *280*, 119417.

[3] S. Bulut, S. Siankevich, A. P. Van Muyden, D. T. L. Alexander, G. Savoglidis, J. Zhang, V. Hatzimanikatis, N. Yan, P. J. Dyson, *Chem. Sci.* **2018**, *9*, 5530–5535.

[4] H. Tan, X. Li, H. Ma, X. Yang, T. Zhan, W. Xie, S. Wang, J. Zhu, *Sustain. Energy Fuels* **2022**, *6*, 2745–2754.

[5] C. Zhang, H. Li, J. Lu, X. Zhang, K. E. Macarthur, M. Heggen, F. Wang, *ACS Catal.* **2017**, *7*, 3419–3429.

[6] C. Zhang, J. Lu, X. Zhang, K. Macarthur, M. Heggen, H. Li, F. Wang, *Green Chem.* **2016**, *18*, 6545–6555.

[7] Z. Li, Z. Wang, B. Jiang, S. Kawi, *Catal. Sci. Technol.* **2018**, *8*, 3363–3371.

[8] Z. Bian, I. Y. Suryawinata, S. Kawi, *Appl. Catal. B Environ.* **2016**, *195*, 1–8.

[9] M. R. Knecht, J. C. Garcia-Martinez, R. M. Crooks, *Chem. Mater.* **2006**, *18*, 5039–5044.

[10] Y. Wang, X. Fan, Q. Du, Y. Shang, X. Li, Z. Cao, X. Wang, J. Li, Y. Xie, W. Gan, *Small* **2023**, *19*, 2206798.

[11] I. Mustieles Marin, D. De Masi, L. M. Lacroix, P. F. Fazzini, P. W. N. M. van Leeuwen, J. M. Asensio, B. Chaudret, *Green Chem.* **2021**, *23*, 2025–2036.

Appendixes

Appendix 1: Experimental part

1. Catalyst characterizations

Textural properties were determined from N_2 adsorption-desorption isotherms recorded on a Belsorp-max (BEL JAPAN) or ASAP 2020 (Micromeritics) apparatus. Before measurements, the samples were degassed under vacuum for 2 h at 250ºC on BelprepII-vac unit or ASAP 2020 (Micromeritics). Specific surface areas were obtained using the BET equation. Pore diameters and specific pore volumes were determined using the BJH model.

Low and wide angles XRD measurements were performed on a Bruker D8 Advance diffractometer or a Bruker D8 Discover, both operating at CuKα = 1.54 Å. Low angles data were recorded in the 2-theta range between 0.5 and 7º, a step size of 0.01º with 1 s per step and operating at 30 kV and 10 mA. Wide angles data were recorded in the 2-theta range between 5 and 80º using 30 kV and 10 mA conditions, a step size 0.03º and 1 s per step.

Small-Angle X-Ray Scattering analyses were performed on a XENOCS (XEUSS 2.0 model). It is equipped with a sealed 40 µm x 40 µm GENIX 3D microfocus tube with Cu anode and a two-dimensional detector from PILATUS 300K from DECTRIS constructor. The sample-to-detector distance used for the acquisition was 300 mm.

X-ray photoelectron spectra (XPS) were collected on an Omicron Argus X-Ray photoelectron spectrometer using a monochromatic Al Kα ($h\upsilon$ = 1486.6 eV) X-ray source with a 300 W electron beam power. The emission of photoelectrons from the sample was analyzed at the take-off angle of 45º under ultra-high vacuum conditions (1 x 10^{-8} Pa). XPS spectra were collected at pass energy of 20 eV for C 1s, Si 2p, Ni 2p, Rh 3d, O 1s, N 1s and Cl 2p core XPS levels. The charging effects were corrected by adjusting the binding energy of the C 1s peak from carbon contamination to 284.6 eV. The peak areas were determined after subtraction of a Shirley background. The atomic ratio calculations were performed after normalization using Scofield factors. Spectrum processing was carried out using the Casa XPS software package.

Temperature-Programmed Reduction (TPR), carried out on an Autochem 2019) apparatus equipped with a TCD detector, was used in order to study the metal reducibility of dried or calcined

materials. The samples (80 mg) were heated on a quartz wool in a U-Shaped quartz tube from R.T. to 900°C at a rate of 10°C min^{-1} using a 5 vol.% H_2/Ar gaseous mixture (25 mL min^{-1}). An isopropanol-liquid N_2 mixture was used before the TCD detector to trap the water molecules formed during the reduction step.

Inductive-Coupled plasma (ICP) Metal mass loadings were determined by ICP-OES spectroscopy (with an Agilent 5100 SVDV ICP-OES). 50 mg of powder was digested with 1 mL HNO_3 (Normatom, 67-69%) and 1 mL HF (Normatom, 47-51%) at 80-90°C during 4-6 h, then diluted in 50 mL of H_3BO_3 2% (20 g/L) aqueous solution to neutralize HF. 1 mL of solution was diluted in 12 mL of HNO_3 2% to obtain a final dilution factor of 12000. Three replicates were performed for each analyze. Blanks were analyzed to monitor instrument and digestion procedure contamination. Blank matrix was also analyzed in order to subtract the matrix effect. Standards solutions were prepared from pluri-elemental and mono-elemental standards solutions and analyzed for calibration and quality control (drift and accuracy). Concentration of each element was calculated from 4 wavelengths: Ni 216.555 nm, Ni 221.648 nm, Ni 230.299 nm, Ni 231.604 nm, Rh 233.477 nm, Rh 249.078 nm, Rh 343.488 nm, Rh 369.236 nm, Co 228.615 nm, Co 230.786 nm, Co 237.863 nm, Co 238.892 nm, Fe 234.350 nm, Fe 238.204 nm, Fe 239.563 nm and Fe 259.940 nm.

Transmission Electron Microscopy (TEM) analyses were performed using a JEOL 2100Plus UHR microscope operating at 200 kV. The sample powder was dispersed in ethanol using ultrasonic treatment and then two drops of the resulting suspension were deposited on a carbon-coated copper grid. Analytical investigations were performed with an energy dispersive X-rays spectrometer (EDX) attached to the microscope. The scanning mode (STEM) was used to get local and precise chemical analysis at the nanometer scale.

For microtomed solids, transmission electron microscopy (TEM) images and HRTEM images were taken on a JEOL JEM-2010 UHR operating at 200 kV. Materials were analyzed after ultramicrotomy. A few mg of powder were deposited in the bottom of a Beem capsule. Some embedding resin (AGAR 100) was added and polymerized for 48 h at 60°C. The polymerized blocks were then cut into ultrathin sections (about 70 nm thick) using a diamond knife of a Leica microtome (ULTRACUT UCT) and deposited on carbon-coated copper grids. In order to visualize

the nickel, cobalt and iron dispersion and location, STEM/HAADF and EDX/mapping were also performed on ultra-thin sections of selected samples.

Pair distribution function (PDF) analysis, X-Ray scattering measurements were performed on a Bruker D8 Advance diffractometer equipped with a molybdenum anode, a Göbel mirror and a High Energy Lynx Eye linear detector. The analysis was done in transmission: a few milligrams of powders were placed in a borosilicate capillary of 1 mm diameter that was sealed. To optimize the acquisition time, the X-Ray diagrams used for the PDF were obtained with the concentration of 7 X-Ray diagrams recorded with following parameters ($2\theta_i$ (°)- $2\theta_f$ (°)-step (°) time per step (s): 0.8-3-0.02-2, 29-61-0.04-6, 59-91-0.06-15, 89-121-0.1-40 (2 times), 119-150-0.1-100 (2 times). The XRD of the empty capillary was also recorded for subtraction. Then, the PDFGetX3 REF BILLINGE 2013 software was used to extract the experimental PDFs form XR diagrams (Q_{min} = 0.8; Q_{max} = 16.6; rpoly = 1.3). In parallel, the PDFGUI software ref billing 2007 was used to calculate the theoretical function G(r) from a structural model.

UV-Vis spectra were recorded on a UV-VIS-NIR spectrometer Cary 5000 Varian equipped for acquisition of spectra on powders in diffuse reflection on a range from 200 to 900 nm, with a source changeover at 350 nm, detector changeover at 800 nm a scan rate of 100 nm min^{-1}.

2. Analytical characterization

Mass spectrometry was performed with a OMNI^{Star} GSD 320 instrument equipped with a stainless-steel capillary set to 150°C. The latter was connected to the autoclave. Parameters of the mass spectrometer were as follows: inlet temperature of 120°C, sample gas pressure inferior to 10^{-5} mbar and detector in SEM mode.

Gas Chromatography - Mass spectroscopy (GC-MS) monitoring of the catalytic tests was carried out on a GC 2010 Plus Shimadzu gas chromatograph equipped with a RTx-5MS (**5% diphenyl/95% dimethyl polysiloxane)** column (30m*0.25mm*0.25µm) and a mass spectrometer detector (MS). The temperature of the injector was set to 250°C. The temperature program of the oven was as follows: 50 to 120°C (at 10°C min^{-1}) then 120°C (5 min);120 to 280°C (at 10°C min^{-1}) then 280°C (8 min); 280 to 300°C (at 10°C min^{-1}) then 300°C (2 min). Helium was used as the carrier gas with a constant inlet pressure (97.9 kPa). The products were detected by a Mass Spectrometer QP2010 SE. The ion source and the transfer line were heated to 200 and 280°C,

respectively and the voltage was set at 0.2 kV. The mass spectra were recorded for 35 < m/z < 300 every 0.3 s.

High Performance Liquid Chromatography (HPLC) analysis was used for the monitoring of the reaction mixtures using a Shim-pack column (4.6*100mm, 2.2 µmm, stationary phase: C18) heated to 40°C by an CT0-10AS oven. The mobile phase was constituted of aqueous AcOH (0.5 vol%) and methanol (HPLC grade, VWR Chemicals) used at a flow rate of 0.4 mL min^{-1}. The substrates and the products were detected in UV (210, 220 and 254 nm) by an SPD-M20A detector. The evolution of the volumic fraction of methanol in the eluent is given as follows:

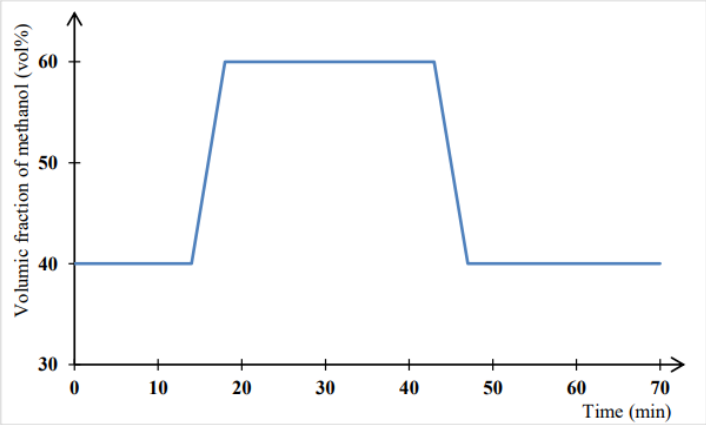

HPLC-MS was performed through direct infusion electrospray ionization (ESI) on an LTQ-Orbitrap XL Hybrid Ion Trap mass spectrometer (Thermo Fisher Scientific) at a flow rate of 60 µL.min^{-1} in MeOH. The LTQ-Orbitrap was outfitted with an ESI interface. The heated capillary temperature, ion spray and capillary voltages were 275°C, 3.6kV and 10V, respectively. The LTQ Orbitrap XL was operated in positive ions mode.

Full scan spectra (automated gain control (AGC) $2.5.10^5$) were collected in the range m/z 100–1000 at a resolution of 30,000 in the profile mode. Using MS interpretation software, the spectra were automatically and efficiently interpreted for the presence of $[M + Na]^+$, $[M + H]^+$, or $[M + NH_4]^+$ ions consistent with a compound in the mixture.

^{1}H NMR spectra were recorded on a Bruker Avance III Nanobay spectrometer operating at 300 MHz at 27°C with a 5 mm inverse probe head (^{1}H / ^{19}F, ^{31}P, ^{13}C) or a 5 mm dual probe head (^{1}H / ^{13}C)

2D NMR experiments (HSQC ^{1}H-^{13}C, HMBC ^{1}H-^{13}C, COSY ^{1}H-^{1}H) were performed using a Bruker Avance III 600 NMR spectrometer (14.1T) operating at a ^{1}H Larmor frequency of 600 MHz with a 5mm Observe broadband probe (BBFO) z-axis (^{15}N-^{31}P /^{19}F/^{1}H) at 27°C.

The NMR spectra were analyzed with TOPSPIN 3.6 (Bruker).

Size exclusion Chromatography (SEC) analyses were performed on a set of three columns (PL Gel mixed-C 5 µm, 7.5 x 300 mm, Mw range 200-2.10^{6}), connected to a pump/automatic injector system Viscotek GPC max, a UV detector (Shimadzu SPD-20AV) and a refractometer detector (VISCOTEK VE 3580). The pressure was maintained at 74 Pa and the flow rate at 1 mL min^{-1} with a run time of 35 min and the solvent used was Tetrahydrofuran (THF).

The chromatograms were analyzed with OmniSEC 5.12. The standards for calibration were Poly(methy methacrylate) (PMMA) or Polystyrene (PS).

Appendix 2: Chemicals and analyses protocols

1. Chemicals

1.1. Synthesis of lignin models

1.1.a. 2-phenoxy-1-phenylethanone ($K1_{HH}$):

2-bromoacetophenone (16.85 g, 84 mmol) and an excess of phenol (9.56 g, 101 mmol) were dissolved in 200 mL of acetone. 20 g of K_2CO_3 (145 mmol), used as a catalyst and as an acid (HBr) trap, were added to the solution. Reflux was needed during 5 h to get $K1_{HH}$. The reaction was monitored by TLC using cyclohexane/diethylether 80/20 as the eluent. After filtration and acetone evaporation, $K1_{HH}$ was recrystallized in a minimum amount of heated (65-70°C) absolute ethanol. $K1_{HH}$ was then recovered by filtration and dried by pressing. $K1_{HH}$ was characterized by ^{1}H NMR.

^{1}H NMR (CD_3CN, 300 MHz): 8.05 (m, 2H), 7.66 (m, 1H), 7.54 (m, 2H), 7.33 (m, 2H), 7.00 (m, 3H), 5.31 (s, 2H).

1.1.b. 2-phenoxy-1-phenylethanol ($A1_{HH}$):

$K1_{HH}$ (4.98 g, 23 mmol) was solubilized in 52 mL of THF and 13 mL of H_2O and reduced by $NaBH_4$ (1.32 g, 35 mmol) for 5 h. The reaction was monitored by TLC using a binary (80/20) cyclohexane/diethylether mixture. Afterwards, the reaction was quenched by 120 mL of saturated NH_4Cl (added slowly because of H_2 emission) and then diluted by 120 mL of water. Later, $A1_{HH}$ was extracted by diethyl ether (250 + 120 mL). After washing the diethylether fractions by brine (120 mL) and drying by anhydrous $MgSO_4$, the solvent was evaporated to get $A1_{HH}$ as a white solid with a yield of 96% on average. $A1_{HH}$ was characterized by ^{1}H NMR.

^{1}H NMR (CD_3CN, 300 MHz): 7.39 (m, 7H), 6.97 (m, 3H), 5.04 (dd, 1H), 4.13 (dd, H), 4.05 (dd, 1H).

1.2. Purchased compounds

Chemicals	**From**
2-bromoacetophenone (99%)	Sigma Aldrich
Phenol (99%)	Sigma Aldrich
2-phenethyl phenyl ether (98%)	TCI
Guaiacylglycerol-β-guaiacyl ether (97%)	BLDPharm
Guaiacol (99%)	Sigma Aldrich
Guaiacylpropanol	Sigma Aldrich
4-propylguaiacol (98%)	Sigma Aldrich
4-ethylguaiacol (98%)	Sigma Aldrich
Ethylbenzene (99%)	Janssen Chemicals
Acetophenone (99%)	Fluka
1-Phenylethanol (98%)	Sigma Aldrich
Cyclohexanone (98%)	Acros Organics
Cyclohexanol (98%)	Acros Organics
Anisole (99%)	Fluka
Pluronic P123	Sigma Aldrich
K_2CO_3	Acros Organics
$NaBH_4$	Sigma Aldrich
NH_4Cl	Sigma Aldrich
$MgSO_4$	Sigma Aldrich
Aerosil 380	Degussa
TMOS (98%)	Sigma Aldrich
$Ni(NO_3)_2.6H_2O$	Sigma Aldrich
$RhCl_3.3H_2O$	Strem Chemicals
$Co(NO_3)_2.6H_2O$	Sigma Aldrich
$Fe(NO_3)_3.9H_2O$	Sigma Aldrich
$K_3[Co(CN)_6]$	Sigma Aldrich
$K_3[Fe(CN)_6]$	Sigma Aldrich
NH_3 (25%)	Merck
HCl (37%)	VWR
HNO_3	Sigma Aldrich

2. Calibration curves

The main products of dimer cleavage reactions were quantified by GC-MS using internal calibration and/or HPLC using external calibration established at the UV absorption wavelength of 254 nm.

Preparation of GC-MS samples: Each authentic sample was diluted at 0.06 M in isopropanol (15 mL). Then, two daughter solutions (S_1 and S_2) were prepared as follows: In S_1, 150 µL of the mother solution and 300 µL of a solution of anisole, used as internal standard (0.06 M in 15 mL of isopropanol) were introduced in a 10 mL volumetric flask and the volume completed with dichloromethane. S_2 was obtained in a similar way using 300 µL of the mother solution.

Calibration curves for GC-MS:

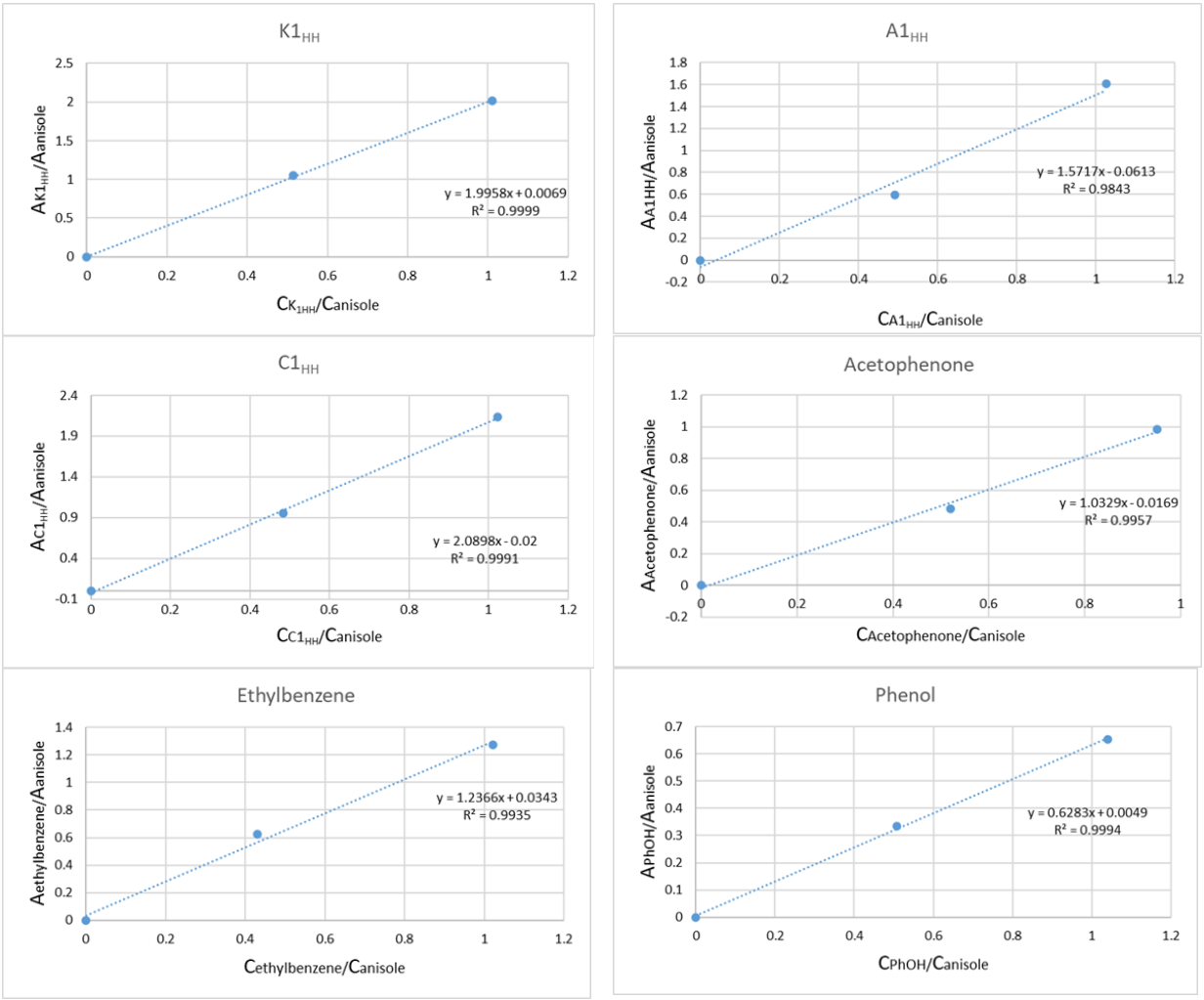

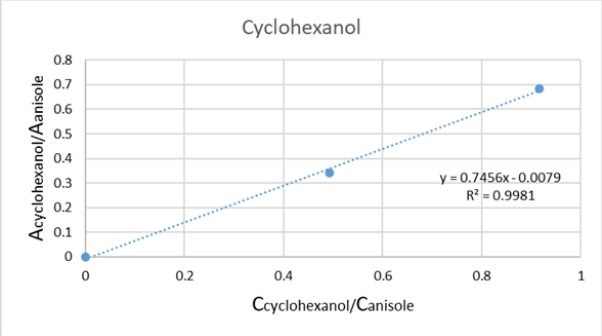

Figure Ap2.1: *Calibration curves of the products and reactants in GC-MS.*

Preparation of HPLC samples: 0.06 M mother solutions of authentic samples were prepared in 15 mL of isopropanol. Two daughter solutions were prepared in volumetric flasks by diluting 100 µL or 200 µL of the mother solutions to 10 mL using the HPLC eluent as solvent (H_2O/MeOH:60/40).

Calibration curves for HPLC:

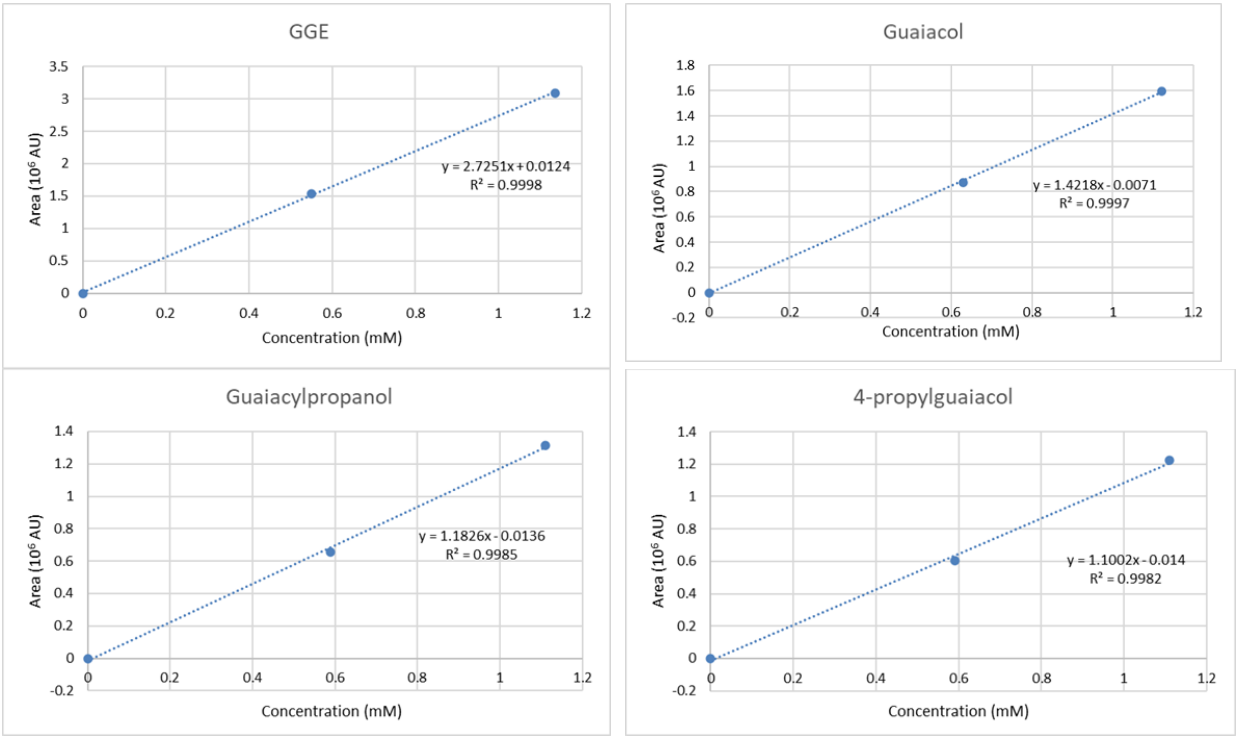

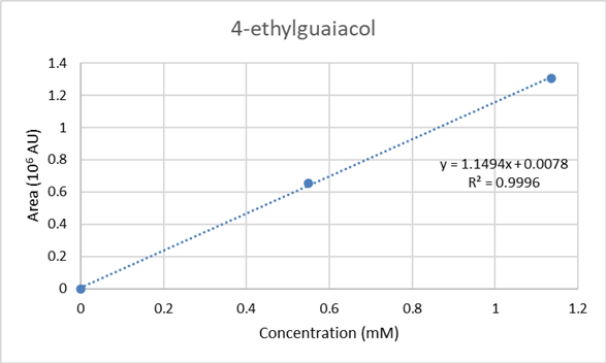

Figure Ap2.2: *Calibration curves of the reactants and products in HPLC at 254 nm.*

Scientific production

Publications

- R. Raachini, F. Ben Romdhane, C, Sassoye, M. Boutros and F. Launay, *Controlling C-OAryl hydrogenolysis vs aryl hydrogenation in lignin model depolymerization using Ni-, Rh- or Ni/Rh- based silica catalysts*, **ChemCatChem**, 2024, 16, e202300948 (https://doi.org/10.1002/cctc.202300948).

Conferences

- French Conference on Catalysis (FCCat), Ronce-les-Bains, France 2022, ***Towards silica supported bimetallic Ni/Rh catalysts for the optimization of phenols production through lignin hydrogenolysis. Presented by: Rita RAACHINI.***
- Société Chimique de France (SCF), Nantes, France 2023, ***Modifying nickel-on-silica catalysts for a more selective hydrogenolysis of lignin. Presented by: Franck LAUNAY.***

List of figures

List of tables

List of abbreviations

Abbreviations	Stands for
AC	Activated Carbon
Ar	Aromatic
BDE	Bond-dissociation Energy
BET	Brunauer-Emmett-Teller
BJH	Barrett Joyner Halenda
BL	Birch Lignin
BPE	Benzyl phenyl ether
C	Carbon
CAGR	Compound Annual Growth Rate
CB	Carbon Black
DPE	Diphenyl ether
Di	Dimers
DMSO	Dimethyl sulfoxide
DRM	Dry Reforming of Methane
EO	Ethylene Oxide
EDX/EDS	Energy-dispersive X-ray Spectroscopy
GC	Gas Chromatography
GGE	Guaiacylglycerol-β-guaiacyl ether
Gol	Guaiacol
GPol	Guaiacylpropanol
HAADF	High-Angle Annular Dark-Field imaging
HMBC	Heteronuclear Multiple Bond Correlation
HPLC	High Performance Liquid Chromatography
HRTEM	High Resolution Transmission Electron Microscopy

ICP-OES	Inductively Coupled Plasma Optical Emission Spectroscopy
IUPAC	International Union of Pure and Applied Chemistry
IWI	Incipient Wetness Impregnation
kDa	Kilo Dalton
MCM	Mobil Composition of Matter
MS	Mass Spectroscopy
MSN	Mesoporous Silica Nanospheres
NP	Nanoparticle
n.d.	Not determined
NDC	Nitrogen Doped Carbon
NMR	Nuclear Magnetic Resonance
PDF	Pair Distribution Function
PO	Propylene Oxide
P123	Pluronic P123
PS	Phyllosilicate
R.T.	Room Temperature
SAXS	Small-Angle X-Ray Scattering
SBA	Santa Barbra Amorphous
STEM	Scanning Transmission Electron Microscopy
TEOS	Tetraethylorthosilicate
TEM	Transmission Electron Microscopy
Theor.	Theoretical
TO	Tetrahedral Octahedral sheet
TOT	Tetrahedral Octahedral Tetrahedral sheet
TMC	Total Metal Content
TPR	Temperature Programmed Reduction
US	United States
UV	UltraViolet

WI	Wet Impregnation
wt	Weight
XPS	X-Ray Photoelectron Spectroscopy
XRD	X-Ray Diffraction
ZSM	Zeolite Socony Mobil

List of symbols

Abbreviations	Stands for
$A1_{HH}$	2-phenoxy-1-phenylethanol
$C1_{HH}$	2-phenethyl phenyl ether
CD_3CN	Acetonitrile
DMSO	Dimethyl sulfoxide
HCOOK	Potassium formate
i-PrOH	isopropanol
$K1_{HH}$	2-phenoxy-1-phenylethanone
Ph	Phenyl
PhOH	Phenol